Semiconductors, Vol. 38, No. 9, 2004, pp. 1001–1004. Translated from Fizika i Tekhnika Poluprovodnikov, Vol. 38, No. 9, 2004, pp. 1039–1042.

ELECTRONIC AND OPTICAL PROPERTIES OF SEMICONDUCTORS

Elementary Blue-Emission Bands in the Luminescence Spectrum of Undoped Gallium Nitride Films

A. N. Gruzintsev*^, A. N. Red'kin*, V. I. Tatsiĭ*, C. Barthou, and P. Benalloul****

** Institute of Microelectronics Technology and High-Purity Materials, Russian Academy of Sciences, Chernogolovka, Moscow oblast, 142432 Russia*

^e-mail: gran@ipmt-hpm.ac.ru

*** Université P. et M. Curie, 75252 Paris, France*

Submitted January 8, 2004; accepted for publication January 12, 2004

Abstract—Inhomogeneous broadening of the blue-emission band in the luminescence spectrum of nominally undoped gallium nitride films grown on substrates of sapphire with orientation (0001) and silicon with orientation (001) using chemical vapor deposition is observed. Studies of the emission spectra under different conditions of excitation of GaN films made it possible to detect three elementary bands with peaks at 2.65, 2.84, and 3.01 eV in the blue region of luminescence of these films at room temperature. Assumptions are made about the types of intrinsic and impurity defects involved in the formation of various centers in GaN as sources of blue emission. © *2004 MAIK "Nauka/Interperiodica".*

1. INTRODUCTION

The contemporary state of optoelectronics requires a search for materials with predominant emission in the blue and ultraviolet spectral regions [1]. Gallium nitride and solid solutions based on this compound are now thought to be the most promising for the formation of structures that emit in these regions of the spectrum. It is especially important to obtain $Al_xGa_{1-x}As$ semiconductor compounds and the structures based on these compounds with monochromatic emission in the excitonic region. To this end, it is necessary to obtain thin films of wide-gap semiconductors with a high crystal quality, since intrinsic crystal-lattice defects and uncontrolled impurity donors or acceptors can give rise to a shift of the edge luminescence to longer wavelengths and to broad (inhomogeneously broadened) emission bands in the so-called impurity region of the spectrum [2, 3].

Gallium nitride—a direct-gap semiconductor whose hexagonal modification has a band gap of 3.39 eV—is the most promising material for fabricating light-emitting diodes and other sources of light in the blue and ultraviolet regions of the spectrum. Ultraviolet emission of GaN is caused by excitonic recombination that involves the free and bound excitons in the hexagonal phase. According to published data [4, 5], the blue emission with a peak at 2.7 eV is caused by radiative recombination within donor–acceptor pairs (DAPs). The shift of the blue-emission peak to shorter wavelengths as the excitation intensity increases is evidence that the origin of the blue-emission band in the luminescence spectrum is DAP-related. Further evidence for this origin of blue luminescence is based on the observation of a line emission spectrum that consists of separate, closely spaced, narrow lines [6]. As a rule, the position of the peak and the half-width of the blue-emission line differ in the various studies published so far. This circumstance indicates that the blue-emission band is broadened inhomogeneously, which may be caused both by the difference in the average distance between a donor and an acceptor of a pair in the crystal lattice and by the large number of different types of donors and acceptors in the samples under study. In each case, the type of prevailing centers involved in the blue-emission radiative recombination depends on the technology used to fabricate the films [7].

In this study, we used optical spectroscopy to resolve the blue-luminescence band of undoped GaN films into several elementary components related to different emitting centers.

2. EXPERIMENTAL

The gallium nitride films were synthesized using a modified chloride–hydride method of chemical vapor deposition. In contrast to the conventional method, we used metallic gallium (with 99.999% purity) and ultrahigh-purity ammonium chloride. High-purity nitrogen (PNG brand) served as the carrier gas. The samples were grown in a two-zone horizontal quartz reactor. Gallium heated to a temperature of 400°C interacted with ammonium chloride in the first zone. The resulting vapors of gallium trichloride monoammoniate were transported by nitrogen flow to the second zone, where these vapors were decomposed with the formation of gallium nitride. The pyrolysis temperature was 950°C. Silicon with orientation (111) and sapphire with orientation (0001) were used as substrates. According to the data of electron microscopy, the GaN films obtained

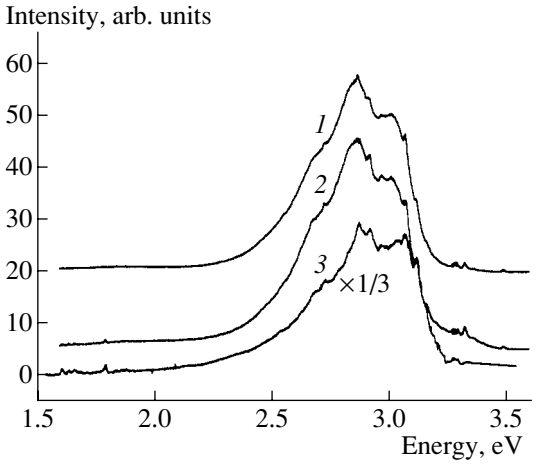

Fig. 1. Spectra of photoluminescence excited by a nitrogen laser for GaN films grown on Si (curve *1*) and sapphire (curve *2*) substrates; the spectra were measured at temperature $T = 300$ K. Curve *3* shows the spectrum measured at $T = 80$ K for a GaN film grown on a sapphire substrate.

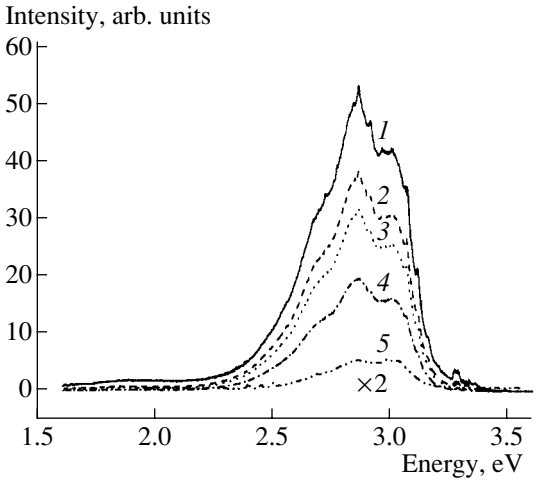

Fig. 2. Photoluminescence spectra of a GaN film grown on a Si substrate with orientation (111) for intensities I of excitation radiation of a nitrogen laser; $I = (1)\ I_0$, $(2)\ 0.47I_0$, $(3)\ 0.31I_0$, $(4)\ 0.12I_0$, and $(5)\ 0.01I_0$ (here, $I_0 = 2$ MW/cm^2 is the highest peak intensity). The spectra were measured at $T = 300$ K.

had a polycrystalline structure with average sizes of separate crystallites of about 0.4 μm and with clearly pronounced crystal faces. The films had *n*-type conductivity with rather low resistivity (10 Ω cm).

The luminescence was excited using either a Photonics LN 1000 nitrogen laser (wavelength 337.1 nm, pulse width 0.6 ns, and energy in a pulse 1.4 mJ) or a tunable xenon-lamp emission passed through a monochromator. Luminescent emission from the sample was collected perpendicularly to the surface of the sample using an optical waveguide positioned 10 mm from the surface, and it was analyzed using a Jobin-Yvon HR460 spectrometer and a PM Hamamatsu R5600U multichannel detector. The photoluminescence (PL) spectra of GaN films were recorded with the films placed in an optical cryostat at 80 and 300 K.

3. RESULTS AND DISCUSSION

Two typical PL spectra of the studied GaN films grown on silicon and sapphire substrates are shown in Fig. 1; the spectra were recorded with the PL excited by a nitrogen laser. As can be seen from Fig. 1 (curves *1*, *2*), two peaks at 2.85 and 3.0 eV, as well as a long-wavelength shoulder at 2.68 eV, can be recognized in the PL spectrum measured at room temperature, irrespective of the substrate used in the synthesis of the film. A decrease in the measurement temperature to 80 K (Fig. 1, curve *3*) leads to a considerable shift of the short-wavelength peak to 3.05 eV and to an increase in the intensity of all bands. Note immediately that the complex structure of the blue-emission band in the PL spectrum of GaN films is not caused by the interference of light at the film boundaries. The point is that the samples under consideration had a developed grain structure that gave rise to pronounced scattering of light. As a result, the films appeared matte to the eye, and there was no interference in the films. The aforementioned special features of the PL spectra cannot be attributed to phonon replicas of the short-wavelength peak because of the large (compared to the energies of phonons) spacing between the peaks. The temperature dependence of the energy positions of the blue-emission peaks (curves *2*, *3*) is indicative of differences between corresponding centers of radiative recombination.

In order to resolve the complex blue-emission band in GaN into elementary components, we studied the dependence of the shape of the PL-spectrum on the intensity of the laser-induced excitation (Fig. 2). It can be seen that the band with a peak at 2.85 eV is prevalent in the PL spectrum at the highest excitation intensity (curve *1*).

As a result of the decrease in the intensity of PL excitation by the nitrogen laser by two orders of magnitude (Fig. 2, curve *5*), the short-wavelength peak at 3.0 eV becomes prevalent in the PL spectrum and the long-wavelength shoulder in the emission curve almost disappears. Such behavior of the blue luminescence in GaN films indicates that there are at least three elementary components in the PL spectrum. If these elementary bands do not overlap at any wavelength (all three bands simultaneously), we can use the Alentsev–Fok mathematical procedure to separate these bands in the spectrum. However, we used a purely experimental spectral method of selective excitation of elementary bands to resolve these bands in the complex spectrum. The point is that different emitting centers necessarily have dissimilar excitation spectra. Therefore, the use of a tunable xenon-lamp emission that is passed through a monochromator makes it possible to excite a fraction of

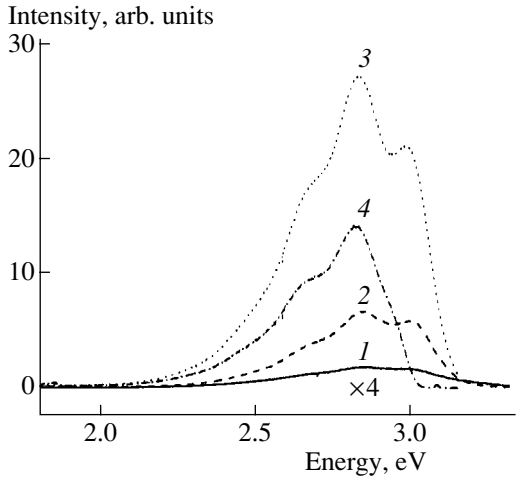

Fig. 3. Photoluminescence spectra of a GaN film grown on a sapphire substrate with orientation (0001) for energies of excitation photons equal to (*1*) 4.96, (*2*) 3.57, (*3*) 3.31, and (*4*) 3.1 eV. A xenon lamp was used for excitation. The spectra were measured at $T = 300$ K.

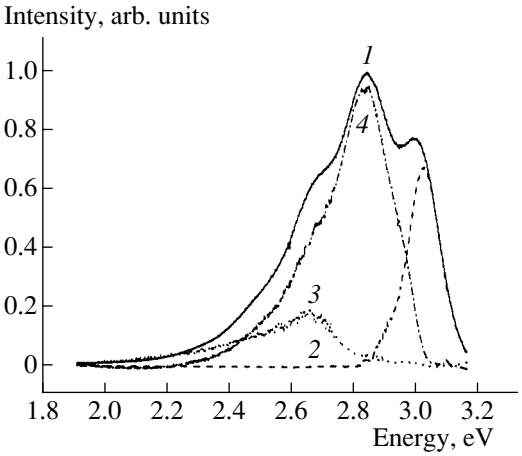

Fig. 4. (*1*) Photoluminescence spectrum of a GaN film grown on a sapphire substrate with orientation (0001); the photoluminescence was excited by the light of a xenon lamp with a photon energy of 3.31 eV. Curves *2*, *3*, and *4* represent the resolution of spectrum *1* into elementary component bands. The spectrum was measured at $T = 300$ K.

the luminescent centers rather than all of them (as in the case of band-to-band excitation by a nitrogen laser).

As a result, the blue-emission band in the GaN luminescence spectrum may become narrower owing to the disappearance of some components of the emission bands in this spectrum (Fig. 3). It can be clearly seen that a decrease in the energy of the excitation photons leads not only to a variation in the ratio between the intensities of the blue-emission bands, but also to the complete disappearance of the short-wavelength band when the PL is excited with 3.1-eV photons (curve *4*). This behavior is related to the fact that excitation of gallium nitride films by photons with energies lower than the band-gap energy induces the onset of selective direct excitation of particular emitting centers. If the excitation-photon energy is decreased further, recombination involving only specific centers proceeds, and only the emission bands related to these centers appear in the corresponding PL spectra. For example, only two blue-emission bands with peaks at 2.68 and 2.85 eV are involved in the formation of spectrum *4*. In this case, by subtracting spectrum *4* from spectrum *3* normalized to the peak at 2.85 eV, we can obtain the elementary short-wavelength spectral component with a peak at 3.01 V (Fig. 4, curve *2*). Similarly, subtracting curve *2* from curve *3* (Fig. 3) yields the long-wavelength component of the blue-emission band of GaN films; this component is peaked at 2.65 eV (Fig. 4, curve *3*). Finally, subtracting the previously found short- and long-wavelength bands (curves *2*, *3*) from the PL spectrum under excitation with the light of a xenon lamp with a photon energy of 3.31 eV (Fig. 4, curve *1*) yields the third elementary band of blue luminescence with a peak at 2.84 eV (Fig. 4, curve *4*). Thus, Fig. 4 represents the resolution of the blue-emission luminescence band for GaN film into three elementary components caused by different recombination centers in undoped gallium nitride.

As mentioned above [5–8], the blue emission from gallium nitride is mostly related to radiative recombination within DAPs, where intrinsic (nitrogen vacancies) or extrinsic (for example, silicon or chlorine atoms) defects act as donors. In the GaN films under study, the presence of donors is also indicated by the rather low resistivity of the material (10 Ω cm). It is notable that nitrogen vacancies are caused by deviation of the film's composition from the stoichiometry, whereas the silicon impurity can appear from the quartz tubes used in the growth process and the chlorine impurity can be introduced from the gas used as the carrier in the chloride–hydride method of CVD. Note that, according to the results obtained in this study (Figs. 1, 2), the short-wavelength band with a peak at 3.01 eV has temperature and excitation-intensity dependences that differ from those of the other three blue-emission bands. For example, the bands with peaks at 2.65 and 2.84 eV shift by 0.01–0.02 eV to longer wavelengths when the temperature is decreased to 80 K, whereas the band peaked at 3.01 eV shifts by 0.05 eV (Fig. 1). In this case, the small temperature-related shifts of the position of the band peak are characteristic of radiative recombination involving donor–acceptor pairs. The recombination of excited electrons from the conduction band at an acceptor level is more dependent on temperature. In our opinion, the peak located at the shortest wavelength among all the observed PL peaks corresponds to the latter type of recombination. The other two peaks can be attributed to DAP-related emission.

Our previous studies [8, 9] of the effect of annealing in an activated nitrogen atmosphere on the emission spectrum of gallium nitride show that the doubly charged gallium vacancy is most likely the acceptor

involved in the formation of blue-emission centers. The singly charged state of this vacancy gives rise to the centers of ultraviolet edge luminescence. If we assume that the short-wavelength luminescence band with a peak at 3.01 eV is related to the transition of electrons from the conduction band to the level of the gallium vacancy, the position of this level in reference to the valence band will be E_V + 0.38 eV. This result agrees well with the data reported by Boguslavsky *et al.* [10]. The origin of donor defects involved in the formation of DAPs that are responsible for elementary blue-emission bands with peaks at 2.65 and 2.84 eV can be related either to intrinsic defects (nitrogen vacancies) or to the silicon and chlorine impurities that enter the GaN films uncontrollably during synthesis.

4. CONCLUSION

Thus, the studies of emission spectra of GaN films at various intensities and wavelengths of optical excitation showed that the emission bands were broadened inhomogeneously. Selective optical spectroscopy in the blue region of emission of undoped GaN films was used to separate three elementary luminescence bands with peaks at 2.65, 2.84, and 3.01 eV. It was also shown that different mechanisms of radiative recombination give rise to the above photoluminescence bands. The bands with peaks at 2.65 and 2.84 eV are related to the recombination of charge carriers within the donor–acceptor pairs, whereas the short-wavelength band with a peak at 3.01 eV is related to the recombination of electrons from the conduction bands at the acceptor level of gallium vacancy V_{Ga}.

ACKNOWLEDGMENTS

This study was supported by the "Low-Dimensional Quantum Structures" program of the Russian Academy of Sciences and by INTAS (project no. 2002-0796).

REFERENCES

1. S. Nakamura, T. Mukai, and M. Senoh, Jpn. J. Appl. Phys. **30**, L1998 (1991).
2. S. J. Xu, G. Li, and S. J. Chue, Appl. Phys. Lett. **72**, 2451 (1998).
3. E. R. Glaser, T. A. Kennedy, and K. Doverspike, Phys. Rev. B **51**, 13326 (1995).
4. U. Kaufmann, M. Kunzer, and M. Maier, Appl. Phys. Lett. **72**, 1326 (1998).
5. J. P. Basrur, F. S. Choa, and P. L. Liu, Appl. Phys. Lett. **71**, 1385 (1997).
6. A. N. Gruzintsev, U. Kaiser, I. I. Khodos, and W. Richter, Neorg. Mater. **37**, 1 (2001).
7. U. Kaiser, A. N. Gruzintsev, I. I. Khodos, and W. Richter, Neorg. Mater. **36**, 720 (2000).
8. A. N. Georgobiani, A. N. Gruzintsev, U. A. Aminov, *et al.*, Fiz. Tekh. Poluprovodn. (St. Petersburg) **36**, 149 (2002) [Semiconductors **36**, 141 (2002)].
9. A. N. Georgobiani, A. N. Gruzintsev, U. A. Aminov, *et al.*, Fiz. Tekh. Poluprovodn. (St. Petersburg) **35**, 725 (2001) [Semiconductors **35**, 695 (2001)].
10. P. Boguslavsky, E. L. Briggs, and J. Bernholc, Phys. Rev. B **51**, 17255 (1995).

Translated by A. Spitsyn

Semiconductors, Vol. 38, No. 9, 2004, pp. 1005–1011. Translated from Fizika i Tekhnika Poluprovodnikov, Vol. 38, No. 9, 2004, pp. 1043–1049.

ELECTRONIC AND OPTICAL PROPERTIES OF SEMICONDUCTORS

Determination of the Minority-Carrier Lifetime in Silicon Ingots by Photoconductivity Relaxation Measured at Microwave Frequencies

P. A. Borodovskiĭ, A. F. Buldygin, and A. S. Tokarev^

Institute of Semiconductor Physics, Siberian Division, Russian Academy of Sciences, pr. Akademika Lavrent'eva 13, Novosibirsk, 630090 Russia

^e-mail: tokarev@isp.nsc.ru

Submitted December 15, 2003; accepted for publication January 20, 2004

Abstract—A new method for determining the bulk lifetime of minority carriers in single-crystal silicon ingots is proposed. A photoconductivity signal measured at a microwave frequency and normalized to its initial value is compared with the results of calculating the total number of excess charge carriers $N(t)/N_{st}$, where N_{st} corresponds to the quasi-steady-state photoconductance. The location of the point of intersection of the photoconductivity-relaxation curve and the dependence $N(t = \tau)/N_{st}$ determines the bulk lifetime $\tau = \tau_V$. The measurements were performed on silicon ingots with different resistivities grown by cruciibleless zone melting and the Czochralski method. The experimental data obtained agree well with the results of calculation. © *2004 MAIK "Nauka/Interperiodica".*

1. INTRODUCTION

The quality of Si single crystals is controlled by the lifetime of minority carriers. This parameter is more sensitive to defects than resistivity and carrier mobility. In high-quality undoped silicon ingots, the minority-carrier lifetime $\tau \geq 1$ ms. Significantly smaller values of τ indicate either the poor quality of the initial material or violation of the crystal-growth conditions. Therefore, a fairly simple and reliable method should be used for determining the minority-carrier lifetime directly in the grown ingots, without cutting wafers and preparing samples with ohmic contacts to measure photoconductivity.

In Si ingots with resistivity $\rho = 0.5$–$500\ \Omega$ cm, the minority-carrier lifetime τ is measured by conductivity modulation at a point contact [1]. When certain requirements are satisfied that make it possible to disregard the effects of surface recombination and diffusion of minority carriers, the measurement error should not exceed ±20% for $\tau \geq 2.8$ μs for *p*-Si ingots and $\tau \geq 7.7$ μs for *n*-Si ingots (GOST [State Standard] 19658-81).

As is well known, the minority-carrier lifetime can be determined using contactless (optical and microwave) methods based on the absorption of electromagnetic energy by free charge carriers. The optical method was proposed almost 50 years ago [2]. In this method, minority carriers generated by a pulse of visible light are analyzed using IR light. The optical method based on lasers is now used to measure the parameters of Si wafers with scanning and computer processing of the measurement results. This technique and the results of measurements were reported in [3, 4], where a solid-state pulsed laser ($\lambda = 1.064$ μm) was used to generate minority carriers and a gaseous laser ($\lambda = 3.39$ μm) was used for probing. In [5], a source of light with very low absorption was used to generate minority carriers: a solid-state laser operating on F_2^- enters in LiF ($\lambda = 1.17$–1.18 μm). The low absorption of light made it possible to measure the carrier lifetimes almost at any point of the ingot bulk (infrared tomography). However, such systems are fairly expensive and their application is reasonable only in particular cases when a Si ingot of high structural quality and volume homogeneity is required.

The method in which microwave frequencies are used to study photoconductivity in germanium and silicon was proposed more than 40 years ago [6, 7]. Since that time, a large number of studies have been published that consider the possibilities and advantages of the microwave method for studying the properties of semiconductors and semiconductor structures. We refer here only to [8–12], where the theory of microwave measurements and the methods for determining the minority-carrier lifetime with regard to surface recombination in Si wafers were studied in considerable detail. The use of microwave oscillators based on Gunn diodes and semiconductor light-emitting diodes (LEDs) (light sources) made it possible to develop compact inexpensive systems for express control of the minority-carrier lifetime, which can also be used in production conditions. For example, the standard ASTM F 1535-94 for the microwave method of measuring the recombination lifetime in Si wafers has been developed in the United States. This standard describes

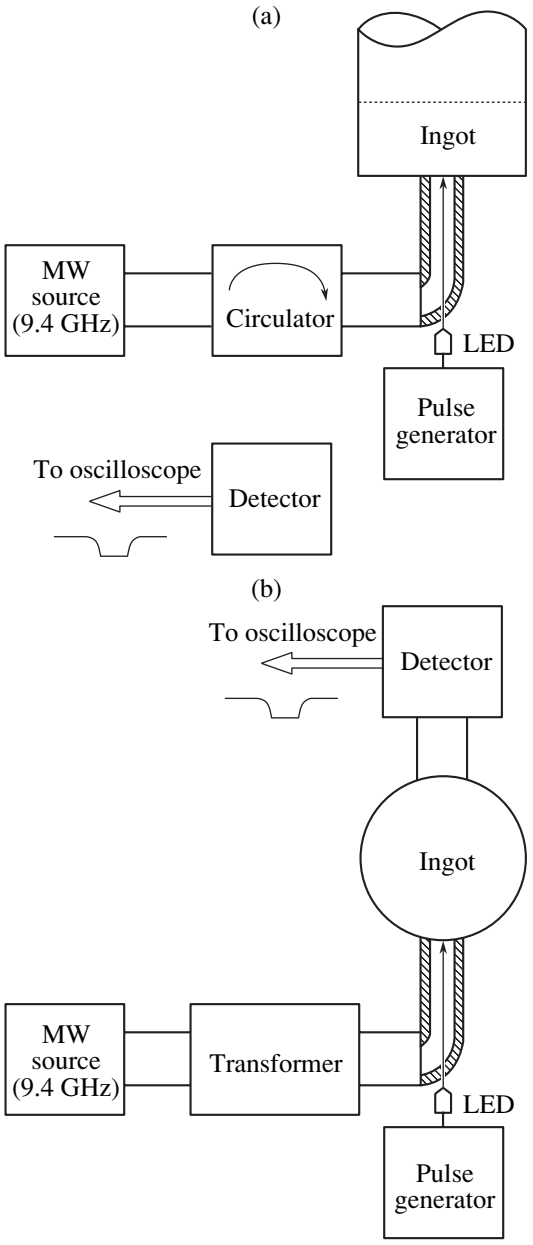

Fig. 1. Schematics of the setups for measuring the photoconductivity of Si ingots by recording microwave power in (a) reflection and (b) transmittance modes.

the measurement procedure and lists the requirements for the treatment and preparation of the wafer surface. A supplement to this standard (ASTM STP 1340) was published in 1998.

We should note that the microwave method has a higher sensitivity than the optical method based on the absorption of IP light by free carriers. For example, for high-resistivity (>100 Ω cm) Si wafers, the microwave method allows one to measure minimum drops in concentration up to $\Delta n_{min} = 4 \times 10^9$ cm^{-3} [10], while the limit for the optical method is $\Delta n_{min} \approx 10^{11}$ cm^{-3} [3].

In this study, we analyze the microwave method as applied to determining the minority-carrier lifetime in Si ingots: at faces of the ingot and on different parts of the lateral surface along the axis of the ingot. A new technique is proposed for determining the minority-carrier lifetime by measuring the photoconductivity relaxation signal upon generation of minority carriers by a fairly long pulse of light with a small absorption coefficient ($\alpha \approx 10$ cm^{-1}). For theoretical analysis, this is the case of a semi-infinite sample, and, if minority carriers are located at a sufficiently large distance from the surface, the effect of surface recombination decreases. Theoretically, even for a short light pulse, the photoconductivity relaxation time becomes similar to the bulk lifetime when a fairly long time passes after the pulse. However, the signal magnitude in this case becomes lower than the noise level in the microwave measurements, and τ cannot be reliably determined.

The effect of surface recombination can be disregarded when a pulsed source of light with low absorption and a quasi-steady mode of photoconductivity (until the end of the pulse) are used. In this case, the photoconductivity relaxation cannot be described by one exponential function either, but, comparing the calculated dependence of the total number of minority carriers with the measured photoconductivity signal obtained with a long light pulse, one can easily determine the minority-carrier lifetime. Microwave measurements were carried out and the minority-carrier lifetime determined for Si ingots of different resistivity. For ingots with $\rho < 500$ Ω cm, the results obtained by the method proposed have been compared with the data obtained by the method of conductivity modulation in the point contact [1].

2. MEASUREMENT OF MICROWAVE PHOTOCONDUCTIVITY AND DETERMINATION OF MINORITY-CARRIER LIFETIME

Schematics of the systems for measuring pulsed photoconductivity of Si ingots are shown in Fig. 1. A sample (ingot face) is pressed against a waveguide. The microwave power reflected from the sample passes through a circulator and is measured by a microwave detector (Fig. 1a). The surface of the sample in the waveguide is illuminated through a small aperture at a bend in the waveguide by an LED connected to a pulsed oscillator. A microwave source with an output power of 20–30 mW at a frequency of 9.4 GHz makes it possible to obtain a pulsed PL signal with an amplitude of several tens of millivolts at the output of the microwave detector, i.e., to observe a photoconductivity signal on the screen of a pulsed oscilloscope without amplification. For undoped ingots with a resistivity $\rho > 100$ Ω cm, microwave power passed through an ingot can be measured (an ingot is clamped between two coaxial waveguides in this case) (Fig. 1b). Using a matching transformer, one can also obtain a sufficiently high pho-

toconductivity signal at the microwave-detector output to observe it on the oscilloscope screen.

The schematic shown in Fig. 1a was considered theoretically in [8] and subsequent studies [9, 11] for a sample in a waveguide. This analysis can be applied to a system consisting of a thin plate pressed against the waveguide and a metal reflector behind the plate, with a variable distance between them [10, 11]. A simple analysis for a high-resistivity Si wafer with a quarter-wave short circuit was also performed in our previous study [13].

In our case, when the thickness of the sample is comparable with the microwave wavelength or exceeds it, theoretical analysis of microwave measurements becomes much more difficult. Below, we will dwell briefly only on certain features that must be taken into account in analyzing microwave measurements of photoconductivity. The propagation constant for a high-resistivity semiconductor is $\gamma = a + ib$, where the damping constant a and the phase constant b are determined by the approximate relations [7]

$$a \approx 60\pi/(\rho\sqrt{\varepsilon_r}), \quad (1)$$

$$b \approx \frac{2\pi\sqrt{\varepsilon_r}}{\lambda}\left[1 + \frac{1}{8}\left(\frac{60}{\rho\varepsilon_r}\right)^2\right], \quad (2)$$

where ε_r is the semiconductor permittivity and λ is the microwave wavelength. The damping constant determines the penetration depth of the microwave field in the semiconductor, i.e., the skin depth:

$$\delta = \frac{1}{a} = \frac{\rho\sqrt{\varepsilon_r}}{60\pi}.$$

In undoped silicon, $\rho > 100\ \Omega$ cm, $\varepsilon_r = 12$, and the skin depth $\delta > 18.3$ mm. Light-generated minority carriers are located in the region determined by the diffusion length $L_D = \sqrt{D\tau}$, which, even at lifetimes $\tau \geq 1$ ms, does not exceed several millimeters. This circumstance means that the conductivity inhomogeneity $\Delta\sigma(z, t)$ and the inhomogeneity of the microwave field $E(z)$ must be taken into account in calculations. Within the theory of microwave measurements considered in [8–12], we analyze the case when a relative change $\Delta P/P$ in the microwave power reflected from the illuminated surface of a semiconductor is determined as

$$\Delta P(t)/P = \int A(z)\Delta\sigma(z, t)dt, \quad (3)$$

where $A(z)$ is the sensitivity coefficient, which is proportional to the squared amplitude of the microwave field.

When the surface recombination velocity is low, the spatial distribution of minority carriers practically does not change with time, and one may suppose that the pulse photoconductivity signal corresponds to the relaxation of the total number of minority carriers, which is determined after a light pulse as $N(t) \propto \exp(-t/\tau)$. However, in reality, the surface recombination velocity is high, the peak of the minority-carrier concentration shifts into the bulk of the sample, and the photoconductivity-relaxation time continuously changes. At an instant t after a short light pulse, we have [14]

$$\frac{1}{\tau} = \frac{1}{\tau_v} + \frac{\pi^2}{4t}.$$

The bulk lifetime is approximately equal to the photoconductivity relaxation time when $t \geq 5\tau_v$. In addition, when there is a significant change in the spatial distribution of minority carriers (a shift of the peak) in a highly inhomogeneous microwave field, the relaxation of the photoconductivity signal does not correspond to the time dependence of the total number of minority carriers after the light pulse. Calculating the distribution of minority carriers at different instants of time [14] and using Eq. (3), one can simulate this effect on a computer.

In order to reliably determine the minority-carrier lifetime, one has to find the theoretical time dependence of the total number of minority carriers when the sample is exposed to pulsed illumination. A general solution to the continuity equation, which determines the change in the minority-carrier concentration during the light pulse and after the pulse, has not been obtained. For a low injection level (linear recombination), with regard to the diffusion and the surface recombination, this solution was obtained for the first time by Lashkarev *et al.* [15] for a semi-infinite sample.

The total number of minority carriers is determined by the equation

$$N(t) = \int_0^\infty n(z, t)dz$$

$$= \eta\frac{(1-R)I}{1-\alpha D/S}\left\{\frac{1-\exp(-t/\tau)W(\alpha\sqrt{Dt})}{1/\tau - \alpha^2 D}\right.$$

$$-\frac{\alpha D/S}{1/\tau - S^2/D}[1-\exp(-t/\tau)W(S\sqrt{t/D})] \quad (4)$$

$$\left.-\alpha^3 D\sqrt{D\tau}\frac{1-(S/\alpha D)^2}{(1/\tau-\alpha^2 D)(1/\tau - S^2/D)}\right.$$

$$\left.\times[1-\exp(-t/\tau)W(\sqrt{t/\tau})]\right\},$$

$$W(u) = \frac{2}{\sqrt{\pi}}\exp(u^2)\int_u^\infty \exp(-u^2)du,$$

where η is the quantum yield of internal photoionization; R is the reflection coefficient; I and α are the intensity and the absorption coefficient of light incident on the semiconductor, respectively; D is the bipolar diffu-

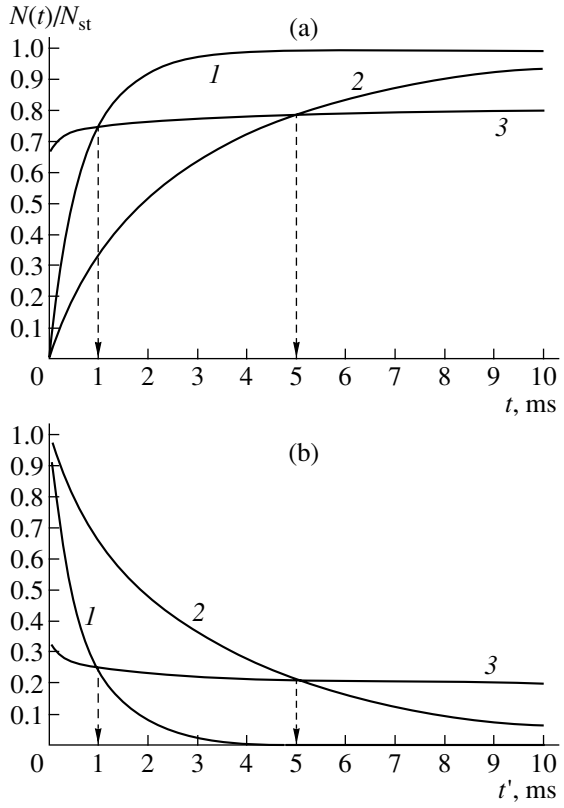

Fig. 2. Calculated dependences of the total number of minority carriers $N(t)/N_{st}$ (a) during a light pulse ($0 < t < t_{pulse}$) and (b) after the pulse ($t' > t - t_{pulse}$) for the minority-carrier lifetime τ = (*1*) 1 and (*2*) 5 ms. Dependences (*3*) are calculated for $t = t' = \tau$. The diffusivity $D = D_p = 13$ cm^2/s and $\alpha = 10$ cm^{-1}.

sion coefficient; τ is the minority-carrier lifetime; and S is the recombination rate.

Analysis of Eq. (4) shows that, at $S = 0$, as well as when $\alpha\sqrt{D\tau} \ll 1$, the time dependence of the total number of minority carriers after the light pulse, and, accordingly, the photoconductivity relaxation, is described by an exponential function. It is difficult to implement these cases in practice for high-resistivity Si ingots with a long lifetime. However, when the light absorption coefficient is sufficiently low ($\alpha \approx 10$ cm^{-1}), it is easy to implement the case when $\alpha D/S \ll 1$ and $S^2/D \gg 1/\tau$. These conditions allow us to disregard the second term in Eq. (4) and obtain the following calculation formulas for normalized values of the total number of minority carriers:

$$\frac{N(t)}{N_{st}} \approx \frac{1 - e^{-\frac{t}{\tau}}W(\alpha\sqrt{Dt}) - \alpha\sqrt{D\tau}\left[1 - e^{-\frac{t}{\tau}}W(\sqrt{t/\tau})\right]}{1 - \alpha\sqrt{D\tau}} \quad (5)$$

during the light pulse from $t = 0$ to $t = t_{pulse}$ and

$$\frac{N(t')}{N_{st}} \approx \exp(-t'/\tau)\left[\frac{W(\alpha\sqrt{Dt'}) - \alpha\sqrt{D\tau}W(\sqrt{t'/\tau})}{1 - \alpha\sqrt{D\tau}}\right] \quad (6)$$

after the pulse at $t' > t - t_{pulse}$.

N_{st} is the value of $N(t)$ at $t \longrightarrow \infty$, i.e., the total number of minority carriers at the end of a long light pulse, when saturation and transition to steady-state photoconductivity are observed.

Using Eqs. (5) and (6), one can calculate the normalized values of $N(\tau)/N_{st}$ at $t = \tau$ and $t' = \tau$.

During the pulse ($t \le \tau_{pulse}$),

$$\frac{N(\tau)}{N_{st}} = \frac{1 - 0.3679W(\alpha\sqrt{D\tau}) - 0.8427\alpha\sqrt{D\tau}}{1 - \alpha\sqrt{D\tau}}, \quad (7)$$

and, after the pulse ($t \ge \tau_{pulse}$),

$$\frac{N(\tau)}{N_{st}} = 0.3679\frac{W(\alpha\sqrt{D\tau}) - 0.4276\alpha\sqrt{D\tau}}{1 - \alpha\sqrt{D\tau}}. \quad (8)$$

Note also that the function $W(\alpha\sqrt{D\tau}) = W(u) = \exp(u^2)[1 - \mathrm{erf}(u)]$, where $\mathrm{erf}(u)$ is the probability integral.

Figure 2 shows the dependences calculated for the two lifetimes: $\tau = 10^{-3}$ and 5×10^{-3} s at $D = D_p = 13$ cm^2/s and $\alpha = 10$ cm^{-1}.

The dependences calculated by formulas (5) and (7) (Fig. 2a) and by formulas (6) and (8) (Fig. 2b) and plotted on the same time scale intersect each other. The point of their intersection determines the bulk lifetime of minority carriers. This circumstance means that, comparing a normalized measured signal of photoconductivity relaxation $\Delta U(t)/\Delta U(t_{pulse})$ with the result of calculation by formula (8), one can determine the bulk lifetime of minority carriers from the point of intersection. It also follows from Fig. 2a that the mode of steady-state or quasi-steady-state photoconductance (i.e., $N(t)/N_{st} \approx 1$) is obtained at $t \gtrsim 5\tau$. Thus, at $\tau =$ 5 ms, the duration of the light pulse should be no less than 25 ms. One should also note that, with an increase in the minority-carrier lifetime, the difference between the values determined by the conventional technique from the decrease by a factor of e ($\tau_v = \tau_{1/e}$) and our measurements (Fig. 2b) increases. For example, for $\tau =$ 1 and 5 ms, this difference is ~25 and 78%, respectively.

3. RESULTS OF MEASUREMENTS OF MICROWAVE PHOTOCONDUCTIVITY IN Si INGOTS

Measurements of photoconductivity in *n*-Si ingots with different resistivities ρ (from 4.5 to 1000 Ω cm or higher) were performed on the microwave setup described in our previous research [13]. A prototype of an LED with $\lambda \approx 1.064$ μm was used as the pulsed light source.

Figure 3 shows the results of microwave measurements of the minority-carrier lifetime for a high-resistivity (1640 Ω cm) Si ingot with a diameter of 76 mm and a length of 72 mm. The measurements were per-

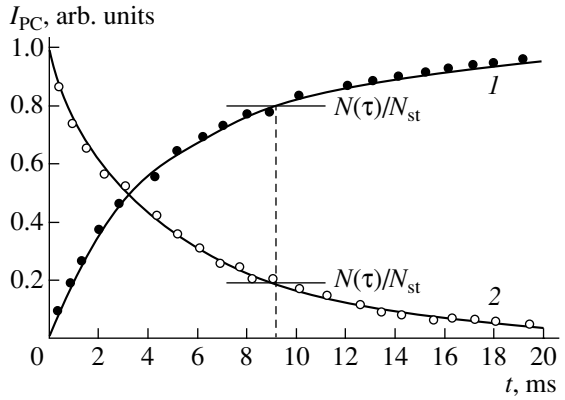

Fig. 3. Pulsed photoconductivity signal I_{PC} and its relaxation measured from the change in the transmitted microwave power under pulsed illumination of an *n*-Si ingot (ρ = 1640 Ω cm, diameter 76.5 mm, length 71.5 mm). The pulse duration is τ_{pulse} = 30 ms. The calculated dependences $N(t)/N_{st}$ (solid lines) are obtained at τ = 9.5 ms, D = 13 cm^2/s, and α = 10 cm^{-1} from expressions (5) and (6) (curves *1* and *2*, respectively). The values of $N(t)/N_{st}$ are calculated according to (7) and (8) (upper and lower straight segments, respectively).

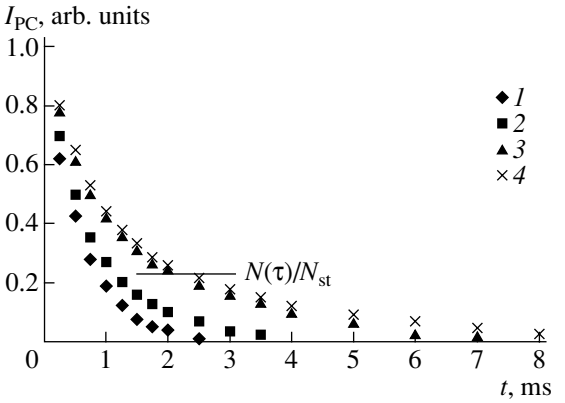

Fig. 4. Photoconductivity relaxation (microwave measurements) for light pulses ($\alpha \approx 10$ cm^{-1}) of duration t_{pulse} = (*1*) 0.1, (*2*) 1, (*3*) 10, and (*4*) 100 ms in a portion of an *n*-Si ingot (ρ = 2760 Ω cm, diameter 80 mm, length 14.5 mm). The measurement scheme is shown in Fig. 1a; the metal reflector is at the upper face.

formed according to the schematic shown in Fig. 1b; waveguides with a cross section of 10×23 mm^2 were pressed against the ingot faces. The matching transformer was tuned to the maximum photoconductivity signal. At the end of a pulse (τ_{pulse} = 30 ms), the pulse amplitude was ~93 mV. To compare the experimental data with the results of calculation, the measured signal was normalized: during the pulse up to t = 20 ms and after the pulse. The lifetime $t = \tau$ was determined at the points of intersection with the values calculated by formulas (7) and (8). In Fig. 3, the calculated values are shown by segments in the vicinity of $t \approx \tau$. The results of the calculations by formulas (5) and (6) for $D = D_p$ = 13 cm^2/s, α = 10 cm^{-1}, and τ = 9.5 ms agree well with the experimental data. Certain discrepancies observed at the beginning of the relaxation process (at $t \lesssim 4$ ms) are apparently due to the effect of spatial inhomogeneity of the microwave field, as was noted above.

The results of microwave measurements of the photoconductivity relaxation using light pulses of different duration are shown in Fig. 4 for an *n*-Si ingot with a resistivity of 2760 Ω cm. A portion of the ingot 14.5 mm long and 80 mm in diameter was installed at the open end of the waveguide, and a reflector (a metal plate) was mounted on the upper face. The skin depth δ was about 50 mm; thus, a significant fraction of the microwave power was reflected to form a spatial inhomogeneity of the field $E(z)$ along the length of the sample. In our case, the distribution of the microwave field will be such as to make the peak of minority carriers diffuse to the region of stronger field, and the effect of the microwave-field inhomogeneity will be negligible at long pulse durations. As can be seen from Fig. 4, the photoconductivity-relaxation curves differ significantly at pulse durations below 10 ms but almost coincide at $t_{pulse} \geq 10$ ms. In this case, the calculation formulas can be used at $t_{pulse} > 10$ ms and the found value of the lifetime τ = 2.25 ms corresponds to the region where the measured signal (at pulse duration t_{pulse} = 0.1 ms) does not exceed 2% of the initial value (Fig. 4, curve *1*). This fact once again confirms that the method proposed can be used when the condition $t_{pulse} > 5\tau$ is satisfied.

The microwave measurements were performed with a large number of high-resistivity Si ingots grown by crucibleless zone melting and a few ingots grown by the Czochralski method. In our opinion, interesting results were obtained for a KÉF-4.5 (*n*-Si:P with a resistivity of 4.5 Ω cm) ingot (see Fig. 5).

At τ = 0.5 ms, D = 12 cm^2/s, and α = 10 cm^{-1}, the calculated dependence agrees well with the experiment, especially at $t > 0.5$ ms. At $t < 0.5$ ms, the falloff of the experimental curve is clearly sharper than that of the

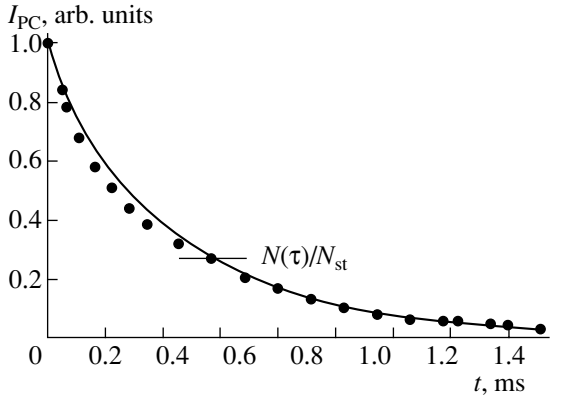

Fig. 5. Photoconductivity relaxation (microwave measurement) for a KÉF-4.5 (*n*-Si:P with a resistivity of 4.5 Ω cm) ingot. The calculated dependence $N(t)/N_{st}$ (solid line) is obtained for τ = 0.5 ms, α = 10 cm^{-1}, and D = 12 cm^2/s.

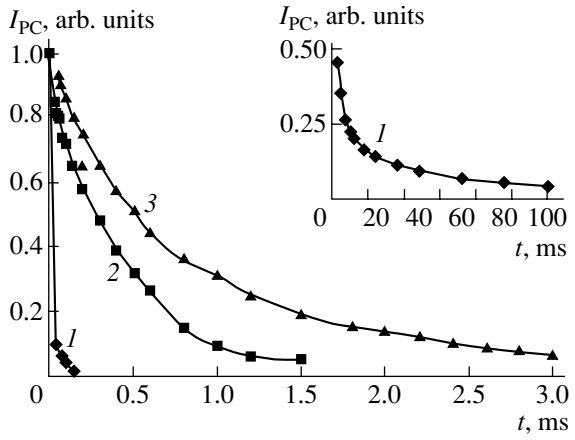

Fig. 6. Photoconductivity relaxation (microwave measurements) for different light sources used to generate minority carriers: (*1*) an LPI-12 semiconductor laser (τ_{pulse} = 0.15 μs, $\lambda \approx 0.91$ μm; see inset); (*2*) an AL 123A LED (τ_{pulse} = 10 ms, $\lambda \approx 0.94$ μm); and (*3*) a semiconductor laser (τ_{pulse} = 10 ms, $\lambda \approx 1.064$ μm).

theoretical dependence $N(t)/N_{st}$ (see also Fig. 3). Apparently, the reason for this discrepancy is not only in the surface recombination but also in the microwave field inhomogeneity, as was mentioned above. At ρ = 4.5 Ω cm, the skin depth at a frequency of 9.4 GHz is ~1.3 mm and, therefore, the peak of minority carriers will shift to the region of weaker field $E(z)$, which enhances the photoconductivity relaxation.

The choice of the light source for the generation of minority carriers is important for the reliable determination of their lifetime. This statement is illustrated by the results of measurements shown in Fig. 6. The position of the Si ingot with ρ = 230 Ω cm was not changed and the light spot was in the central area of the ingot face pressed against the waveguide (Fig. 1a). When an LPI-12 semiconductor laser with short light pulses was used (t_{pulse} = 0.15 μs, $\lambda \approx 0.91$ μm, intensity up to 10 W/cm^2), a very fast photoconductivity relaxation was observed (Fig. 6, curve *1* and inset). The effect of surface recombination was very significant in this case, and the time constant τ_1 was 80 μs. As was noted above, the effect of surface recombination can be minimized by carrying out measurements when the photoconductivity signal decreases to about 1% of the initial value [14–16]. Such a decrease was not observed in our experiments (Fig. 6), apparently because, when an ingot is cut, a damaged layer is formed with a high density of defects. Measurements with a polished sample showed that, in the region of falloff by less than 3%, it is possible to determine $\tau \approx 1$ ms, which is close to the bulk lifetime of minority carriers (1.25 ms). When an AL-123A LED ($\lambda \approx 0.94$ μm, t_{pulse} = 10 ms) is used, photoconductivity relaxation is observed even in the range below 2 ms (Fig. 6, curve *2*). Finally, when we used an LED operating at $\lambda \approx 1.064$ μm with t_{pulse} = 10 ms, the photoconductivity relaxation was observed in the range below 5 ms (curve *3*) and the minority-carrier lifetime was determined as τ = 1.25 ms. For curve *2*, the point of intersection was found using the curve $N(t)/N_{st}$ calculated for D = 13 cm^2/s and α = 190 cm^{-1}. The value obtained (τ = 0.78 ms) is significantly smaller than that for curve *3*. The value of τ determined theoretically from the point of intersection should be the same at α = 10 and 190 cm^{-1} since the conditions $\alpha D/S \ll 1$ and $S^2/D \gg 1/\tau$ are satisfied at high surface recombination velocities ($S \geq 10^4$ cm/s).

Table 1

Ingot no.	Cone			Tail		
	ρ, Ω cm	$\tau_{1/e}$, ms	τ_v, ms	ρ, Ω cm	$\tau_{1/e}$, ms	τ_v, ms
Ap231	2210	6.1	9.2	1250	7	11.2
		(4.1)	(6.7)		(7.5)	(12.5)
Ap232	1860	9.8	17	660	5.5	7.5
		(8.2)	(13.5)		(6)	(10)
Ap233	3140	10.7	17.8	2110	7.5	14
		(3.2)	(5.5)		(8)	(14)
Ap234	1840	6.5	11.2	1780	4.8	8
		(6)	(11)		(4.5)	(7)

Note: The values obtained from microwave measurements after scalping of ingots are given in brackets.

The above method for determining the minority-carrier lifetime in Si ingots makes it possible to carry out rapid analysis immediately after growth of the ingot before cutting off the cone and the tail and scalping (which is required to equalize the diameter of the ingot). The results of measurements for four high-resistivity Si ingots from the same set grown by crucibleless zone melting on an FZ-20 growth system at the Institute of Semiconductor Physics (Siberian Division, Russian Academy of Sciences) are listed in Table 1. The microwave measurements were performed according to the schematic shown in Fig. 1b at the two ingot faces before and after scalping.

It can be seen from the data of Table 1 that all the ingots studied have rather high quality ($\tau_v \gtrsim 5$ ms), but there is also a significant spread of the values of τ_v both for the opposite faces of an ingot and from ingot to ingot, although the same initial material (polysilicon) and the same growth technique were used. The values of $\tau_{1/e}$ listed in Table 1, as was mentioned above, are clearly smaller than τ_v. However, on the whole there is a correlation between these values, and for simplicity the conventional method for determining τ_v from the decrease in the photoconductivity signal by a factor of e can be used in rapid analysis.

The ingots were subjected to neutron transmutation doping, after which τ_v was measured by modulating the conductivity in the point contact, and the results were compared with the data obtained by the microwave

Table 2

Ingot no.	ρ, Ω cm	MCPC method**		Microwave measurements			
		τ_v^*, μs		$\tau_{1/e}$, μs		τ_v, μs	
		Cone	Tail	Cone	Tail	Cone	Tail
F224	40	170	200	340	450	460	620
F225(3)	220	150	190	320	430	410	580
F227(1)	220	190	150	500	260	650	330
F227(2)	40	120	150	390	800	500	1140
F227(3)	40	180	200	330	230	420	310
M230	230	190	170	540	275	750	350

* The average values were determined from measurements at three points: in the center and on the opposite faces of the ingot.

** MCPC denotes modulating conductivity in the point contact;

method. The data for six ingots are listed in Table 2. The values of τ_v measured by modulating the conductivity are even smaller than $\tau_{1/e}$, while the values of τ_v obtained from the microwave measurements exceed $\tau_{1/e}$ by a factor of 3–4. It should be noted that, in the measurements by modulating conductivity in the point contact, the surface of the ingot's face was not ground and the smaller values of τ_v may be due to the presence of a damaged layer formed during cutting. However, this question requires special research, like the question of the possible replacement of the method documented by GOST 19658-81 with the microwave method proposed here.

4. CONCLUSIONS

A new method for determining the minority-carrier lifetime in Si ingots from microwave measurements of pulsed photoconductivity is proposed. The known solution of the one-dimensional continuity equation in the approximation of linear recombination in a semi-infinite sample is used to calculate the total number of minority carriers generated by a light pulse. It is shown that, for sufficiently long light pulses ($t_{\text{pulse}} \geq 5\tau$) with a low absorption coefficient ($\alpha \approx 10$ cm^{-1}), the effect of surface recombination can be disregarded and a good agreement between the time dependence of the total number of minority carriers and the measured photoconductivity signal can be obtained. This statement is confirmed by the microwave measurements performed with portions of *n*-Si ingots with different resistivities. The bulk lifetime τ_v is determined from the point of intersection of the measured photoconductivity-relaxation curve with the calculated time dependence $N(t = \tau)/N_{\text{st}}$ obtained for the given values of the absorption coefficient and the minority-carrier diffusivity. The experiments were carried out using two modes of microwave measurements: the detection of transmitted microwave power for high-resistivity Si ingots and the measurement of reflected microwave power using a circulator for ingots with $\rho < 1000$ Ω cm.

The proposed method of microwave measurements of minority-carrier lifetimes can be used for rapid analysis of the quality of undoped Si ingots to optimize the growth conditions and to certify doped ingots instead of the method of modulating conductivity in a point contact.

REFERENCES

1. L. P. Pavlov, *Methods for Measuring Parameters of Semiconductor Materials* (Vysshaya Shkola, Moscow, 1987), Chap. 3, p. 105 [in Russian].
2. N. J. Harrick, J. Appl. Phys. **27**, 1439 (1956).
3. V. Grivickas, J. Linnros, A. Vigelis, *et al.*, Solid-State Electron. **35**, 299 (1992).
4. J. Linnros, J. Appl. Phys. **84**, 275 (1998).
5. D. V. Akhmetov and N. V. Fateev, Fiz. Tekh. Poluprovodn. (St. Petersburg) **35**, 40 (2001) [Semiconductors **35**, 40 (2001)].
6. A. M. Ramsa, H. Jacobs, and F. A. Brand, J. Appl. Phys. **30**, 1054 (1959).
7. H. A. Alwater, J. Appl. Phys. **31**, 938 (1960).
8. M. Kunst and G. Beck, J. Appl. Phys. **60**, 3558 (1986); **63**, 1093 (1988).
9. A. Sanders and M. Kunst, Solid-State Electron. **34**, 1007 (1991).
10. C. Swiatkowski, A. Sanders, K.-D. Buhre, and M. Kunst, J. Appl. Phys. **78**, 1763 (1995).
11. M. Schöfthaler and R. Brendel, J. Appl. Phys. **77**, 3162 (1995).
12. J. Schmidt and A. G. Aberle, J. Appl. Phys. **81**, 6186 (1997).
13. P. A. Borodovskiĭ, A. F. Buldygin, and A. S. Tokarev, Avtometriya, No. 6, 43 (2000).
14. M. S. Tyagi and J. F. Nus, Solid-State Electron. **25**, 411 (1982).
15. V. E. Lashkarev, É. I. Rashba, V. A. Romanov, and Z. A. Demidenko, Zh. Tekh. Fiz. **28**, 1853 (1958) [Sov. Phys. Tech. Phys. **3**, 1707 (1958)].
16. K. Misiakos, F. A. Lindholm, and A. Neugroshel, J. Appl. Phys. **58**, 1647 (1985).

Translated by Yu. Sin'kov

Semiconductors, Vol. 38, No. 9, 2004, pp. 1012–1017. Translated from Fizika i Tekhnika Poluprovodnikov, Vol. 38, No. 9, 2004, pp. 1050–1055.

SEMICONDUCTOR STRUCTURES, INTERFACES, AND SURFACES

Interfaces and Roughness in a Multilayer Silicon Structure

A. I. Belyaeva^, A. A. Galuza, and S. N. Kolomiets

National Technical University "Kharkov Polytechnical Institute", Kharkov, 61002 Ukraine

^e-mail: belyaeva@kharkov.com

Submitted December 4, 2003; accepted for publication January 8, 2004

Abstract—The results of spectral ellipsometric studies of a complex multilayer system consisting of a Si substrate, a SiO_2 layer, and a layer of polycrystalline Si are reported. A method for analysis of the multilayer structure is suggested; the method is based on a heavy dependence of experimental data of spectral ellipsometry on the depth of penetration of probing radiation at various wavelengths in the visible region of the spectrum. The actual structure of the system and the parameters of the layers are determined. Processing the ellipsometry data made it possible to identify a natural rough surface oxide SiO_2 layer and also a transition layer at the interface between the layer of polycrystalline Si and the layer of natural oxide. The composition and thickness of these layers are determined. It is shown that the deposited Si layer consists of a mixture of the crystalline and the amorphous phases; the percentage of these phases is determined. © *2004 MAIK "Nauka/Interperiodica".*

1. INTRODUCTION

At present, interest in multilayer coatings based on silicon is primarily related to the development of nanotechnologies that form the basis of contemporary microelectronics. At the same time, it is undoubtedly necessary to refine our fundamental ideas about the actual structure of complex multilayer systems and the origin of the surface and transition layers and clarify the effect of these layers on the properties of the system as a whole. Crystalline silicon (*c*-Si) is the main material in modern microelectronics. Multilayer thin-film structures containing silicon layers are widely used in integrated electronics [1], in particular, for the production of integrated circuits and liquid-crystal (LC) displays. Studies of the origin of transition layers and the effect of these layers on optical and other properties of multilayer solid-state structures are extremely important for improving the current technology of production of these structures. Systematized data in this field of research are lacking. All the above facts prompted us to undertake this study, whose aim was to clarify the origin of the surface and transition layers in a complex multilayer system that consisted of a *c*-Si substrate, a SiO_2 layer, and a film of polycrystalline Si (*poly*-Si); this system is used in the production of LC displays.

2. TECHNOLOGY OF FORMATION OF A SYSTEM CONSISTING OF A *c*-Si SUBSTRATE, A SiO_2 LAYER, AND A *POLY*-Si FILM

Typically, a layer of amorphous silicon (*a*-Si) is deposited onto a glass-substrate surface in order to form thin-film transistors. It is tempting to form control microcircuits in the same system. Unfortunately, silicon in the amorphous phase does not possess the requisite properties for the formation of complex logic circuits. Polycrystalline silicon can be considered a compromise between amorphous and crystalline silicon; the technology of formation of *poly*-Si is much simpler than that of single-crystal silicon. However, there are also a number of problems here. The amorphous phase is also formed during production of polycrystalline silicon; the proportion of *c*-Si and *a*-Si depends heavily on the deposition temperature. The system considered in this study belongs to precisely this type of system.

Crystalline silicon *c*-Si is used as the material for substrates in the production of semiconductor integrated circuits (ICs). Layers are formed on the Si substrates after mechanical lapping and polishing. Oxidation is one of the main processes in the production of ICs. Silicon dioxide SiO_2 is a very stable material; it is used as the mask in the formation of the IC pattern and is grown in an atmosphere of oxygen or an atmosphere of water vapor according to one of the following reactions:

$$Si + O_2 \longrightarrow SiO_2,$$

$$Si + 2H_2O \longrightarrow SiO_2 + 2H_2.$$

At present, much attention is being given to studying the properties and origin of the interfacial layer between crystalline *c*-Si and its oxide (natural or deposited thermally). This interest is caused not only by the wide practical use of these structures but also by the fact that the *c*-Si–SiO_2 structure is the simplest semiconductor–oxide system that can be treated from the fundamental standpoint.

In order to attain the desired parameters of ICs, it is necessary to have thorough knowledge of the system characteristics, such as the thickness of the layers and their composition and the quality of the surface and the interfaces between the phases. The Si–SiO_2 system deserves the most attention among the materials for

microelectronics. Specifically, ellipsometric measurements showed that the effective refractive index of SiO_2 increased with decreasing film thickness, which was related to the existence of a transition region (interface) at the Si–SiO_2 boundary [2]. In modern devices, the thickness of the natural oxide SiO_2 film is $\lesssim$5 nm. It is still unclear whether it is important to take into account the transition region and its structure in this case.

In this study, we paid most attention to the *c*-Si substrate. As is well known [3], optical constants of the Si substrate depend heavily on the method used for preparation of the surface for measurements of these constants. The substrates were commercial wafers of *c*-Si single crystals with orientation (100), *p*-type conductivity, and a roughness of ~0.5 nm. Prior to the deposition of the SiO_2 layer, the natural oxide layer was removed from the Si surface by immersing the sample for a short time in concentrated hydrofluoric acid.

Polycrystalline Si films were formed using pyrolysis of high-purity silane ($SiH_4 \longrightarrow Si + 2H_2$) under conditions of chemical vapor deposition at a low pressure (0.3 Torr) and temperature $T = 635$°C in a system produced by Sematech and Prometrix. The films were formed on silicon wafers 150 mm in diameter; the wafers were preliminarily coated with a thermally deposited layer of amorphous SiO_2 31.1 nm thick. The *poly*-Si films were not doped. The deposition temperature was chosen so that the formation of large grains of *c*-Si and a decrease in the fraction of the *a*-Si phase were ensured [4].

3. EXPERIMENTAL

Since the layers under consideration had a thickness of tens of nanometers or less, we used spectral ellipsometry (SE) and cross-sectional transmission electron microscopy (XTEM) as the main experimental methods. The use of SE in quantitative studies of a multilayer silicon system is based physically on the strong dependence of the penetration depth of probing radiation on the wavelength. The study includes a simulation of the system under consideration in order to interpret the SE data and compare them to the XTEM data. The parameters of the surface roughness and other structure parameters (the thickness and composition of the layers) were determined by fitting the parameters of various physically justified multilayer models to experimental ellipsometric spectra. Each layer (the surface, transition, and silicon layers) was simulated by a physical mixture using the Bruggeman effective-medium approximation (BEMA) [5]. We suggested and justified the physical model of various layers.

The ellipsometry method is based on the fact that the light changes its state of polarization as a result of reflection from some surface. Specifying the state of polarization prior to reflection from the sample and measuring this state after reflection, we can obtain information about the reflecting surface. A variation in the polarization ellipse can be described using two parameters. As a rule, ellipsometric angles Ψ and Δ are used to this end; these angles characterize relative variations in the amplitude and phase of the light wave. Ellipsometric angles can be determined experimentally. As is well known, a variation in the state of polarization as a result of reflection from a surface with specified optical parameters can be calculated theoretically using the Fresnel coefficients R_p and R_s. The basic ellipsometry equation relates the ellipsometric angles Ψ and Δ to the physical parameters of the surface in terms of R_p and R_s [6]:

$$\tan\Psi \exp(i\Delta) = \frac{R_p}{R_s}. \quad (1)$$

The main problem of ellipsometry consists in determining the optical parameters of a system, provided that the experimental values of ellipsometric angles Ψ and Δ are known. In order to solve the basic problem of ellipsometry, one has to choose an adequate model of the surface (specify the explicit form of R_p and R_s) and solve the basic equation of ellipsometry (1) in the context of the chosen model. There are comparatively simple models; these are applicable to a clean surface and a homogeneous single-layer film. The multilayer model is the most general.

If a film is a mixture of several components, the BEMA approach is used. This approximation makes it possible to determine the effective refractive index of a mixture of several materials. According to the BEMA, the effective complex refractive index of the aforementioned mixture is defined by the expression

$$\sum_j v_j \frac{N_j - N}{N_j + 2N} = 0, \quad \sum_j v_j = 1,$$

where $N_j = n_j - ik_j$ is the complex refractive index of the jth component and v_j is the volume fraction of this component.

In order to devise physical models of the system, we studied the same samples using the XTEM method. The samples for these studies were prepared using the conventional technology [7]. The samples were cut, polished mechanically, and then thinned using layer-by-layer ion etching. The flux of 6-keV Ar^+ ions was incident on the sample surface at a small angle (~12°). The resulting thickness of the sample was ~800 Å.

Ellipsometric angles were measured using an unconventional spectral ellipsometric setup that was described in detail in [8].

4. EXPERIMENTAL RESULTS AND SIMULATION OF THE SURFACE AND TRANSITION LAYERS IN THE SILICON FILM

In Fig. 1 we show the details of the microstructure of the damaged surface layer in the polycrystalline Si film of the system under study. The size of the grains in

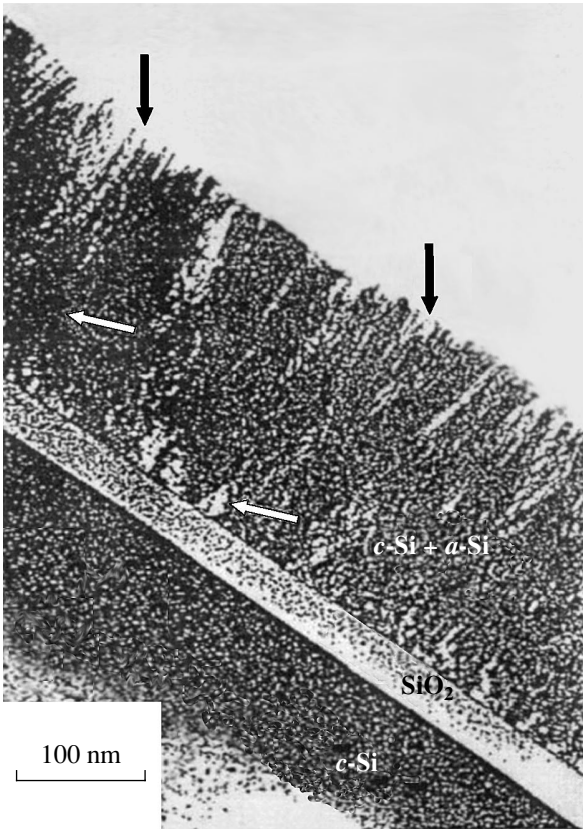

Fig. 1. Structure of the system consisting of the *c*-Si substrate, a SiO_2 layer, and a Si film as imaged in an electron microscope (XTEM).

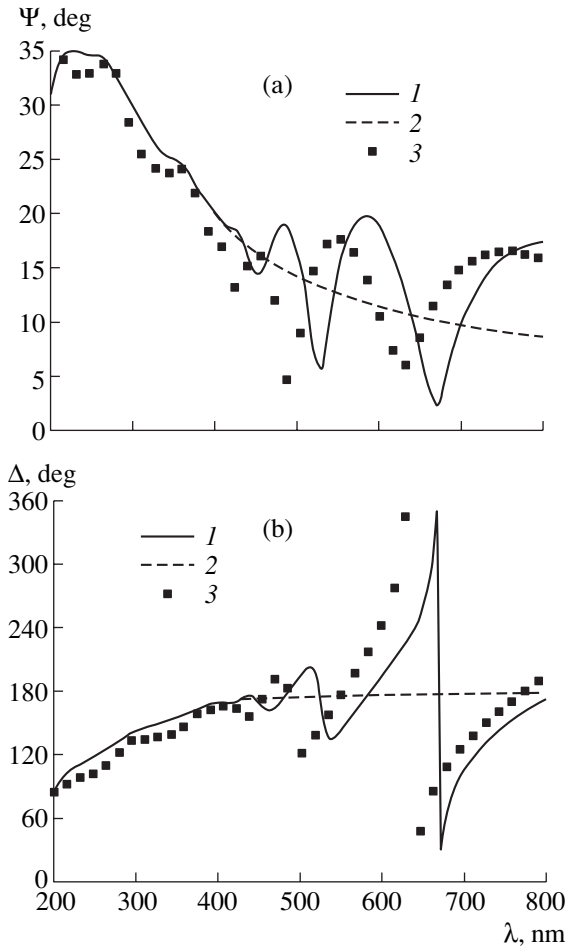

Fig. 2. Experimental and simulated spectra of ellipsometric parameters (a) Ψ and (b) Δ: (*1*) the technology (design) model; (*2*) the model of the *poly*-Si surface; and (*3*) experiment. Spectra *1* and *2* coincide at $\lambda < 400$ nm.

the polycrystalline Si film is ~100 Å. The structure as a whole consisted of a single-crystal silicon (*c*-Si) substrate, a silicon dioxide (SiO_2) film, and a polycrystalline silicon (*poly*-Si) film. However, the XTEM data (Fig. 1) showed that the structure of the sample was complicated by the presence of an appreciable surface roughness (black arrows) and a nonuniformity of the *poly*-Si layer thickness (white arrows).

An analysis of ellipsometric spectra made it possible to gain additional quantitative information about the composition and thickness of different layers in the system under study. In Figs. 2a and 2b, we show the experimental spectra of Ψ and Δ (the angle of incidence is equal 70°) and the spectra calculated on the basis of the design-related model. It can be seen that the difference between the experimental and calculated spectra is not only quantitative but even qualitative.

In order to determine unambiguously an adequate model, we used primarily physical concepts and XTEM data. All the considered models included a *poly*-Si layer that was simulated as a mixture of amorphous and/or crystalline silicon (*a*-Si and/or *c*-Si) and voids. Physical grounds for describing the optical properties of *poly*-Si as due to a mixture of *a*-Si and *c*-Si was discussed previously [9], and the fruitfulness of this approach is now beyond doubt. In this context, in order to gain information about the crystal structure of the silicon film, we used the BEMA approximation in processing the experimental results of spectral ellipsometry. The optical parameters *n* and *k* (the refractive and absorption indices) calculated using the known parameters ε_1 and ε_2 (the real and imaginary parts of the dielectric constant) appear in this approximation [10].

An analysis of the spectrum of penetration of probing radiation into the sample served as a physical basis for devising the models of a multilayer surface structure. The term "penetration depth" requires an explanation. For simplicity, let us consider a system that consists of a single-layer absorbing film and a substrate. In this case, we are interested mainly in the possible effect of reflection from the substrate on the ellipsometric parameters Ψ and Δ rather than in the depth of penetration of radiation into the system. This question is not trivial since this effect depends on the optical constants of the film and the substrate, the thickness of the film, and the angle of incidence of the probing radiation; i.e.,

it is necessary to study preliminarily the system in detail. At the same time, if the film parameters are such that the radiation does not reach the substrate, the contribution of the latter to reflection will undoubtedly be zero.

Thus, in the case of reflection ellipsometry, we are interested in the largest film thickness for which reflection from the substrate still affects the ellipsometric angles Ψ and Δ. This depth differs considerably from the depth to which the radiation penetrates into the film; i.e., we are dealing in fact with the "sensitivity depth" rather than the "penetration depth." Evidently, the sensitivity depth cannot exceed the penetration depth. This means that the penetration depth can be used as the upper-bound estimate of the sensitivity depth.

In order to estimate the depth h of penetration of radiation into a homogeneous semi-infinite layer of a material, one as a rule uses the classical approach based on the Bouguer law [11]:

$$h = \frac{\lambda}{4\pi k}, \qquad (2)$$

where λ is the wavelength of radiation and k is the absorption index.

In the case under consideration, we can use dependence (2) to estimate the largest possible depth of penetration of radiation into the silicon wafer and, thus, devise the effective model of the system. Since the phase composition of the film is initially unknown, as was mentioned above, the penetration depth was studied in three limiting cases that corresponded to the single-crystal, polycrystalline, and amorphous films (Fig. 3). It can be seen from Fig. 3 that the penetration depth does not exceed 10 nm in the wavelength range from 200 to 350 nm for all three cases. This means that, in this spectral range, the initial system under consideration can be treated as homogeneous since the film thickness is 200 nm.

Nevertheless, the simulation shows (Fig. 2) that a model of a homogeneous *poly*-Si layer with a homogeneous surface does not adequately describe the experimental spectrum even in the short-wavelength region, which is especially pronounced for the spectrum of Δ. At the same time, the ellipsometric spectra for the *poly*-Si surface and the design system coincide at $\lambda <$ 400 nm. It then follows that the sensitivity depth for the design system at $\lambda < 400$ nm is smaller than 200 nm (the film thickness). It can be seen from Fig. 2 that ellipsometric spectra of the *poly*-Si surface are smooth in the entire spectral region, whereas the experimental spectra of the samples are significantly oscillatory at $\lambda > 400$ nm. It is reasonable to conclude that the appearance of oscillations in the spectrum in the long-wavelength region is related to an increase in the depth of penetration of the radiation into the sample and to involvement of new layers; i.e., these oscillations are none other than a result of interference of radiation at internal boundaries. In contrast, differences between

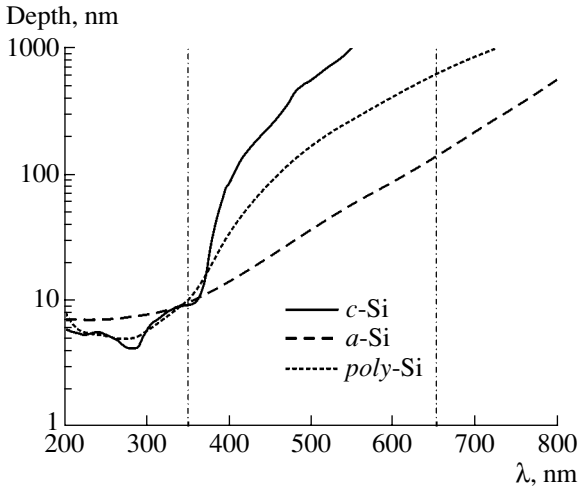

Fig. 3. Spectra of the depth of penetration of the probing radiation into single-crystal (*c*-Si), polycrystalline (*poly*-Si), and amorphous (*a*-Si) silicon. Vertical lines indicate the boundaries between separate spectral regions.

the spectra in the short-wavelength region indicate that, first, the phase composition of the film differs from that of pure *poly*-Si and, second, additional layers (a layer related to roughness or an oxide layer) can exist at the surface.

Attempts to describe the experimental spectra in a model that differs from the design-related model only in the phase composition of the silicon film made it possible to improve the quality of approximation, but not significantly. This circumstance gives grounds to conclude that it is necessary to take into account the interface and surface layers (the roughness-related layer is clearly seen in the XTEM image). We considered a number of physically plausible models for the surface structure of the sample; the parameters of the model that corresponds most closely to experimental data are listed in the first column of the table.

Actual structure and composition of the system under study

Layer	Composition		Thickness, nm
1) Rough oxide	SiO_2	66%	3
	Voids	34%	
2) Transition	*a*-Si	15%	9
	c-Si	75%	
	SiO_2	10%	
3) Polycrystalline silicon	*a*-Si	14%	188
	c-Si	74%	
	Voids	12%	
4) Oxide	SiO_2	100%	31
5) Substrate	*c*-Si	100%	–

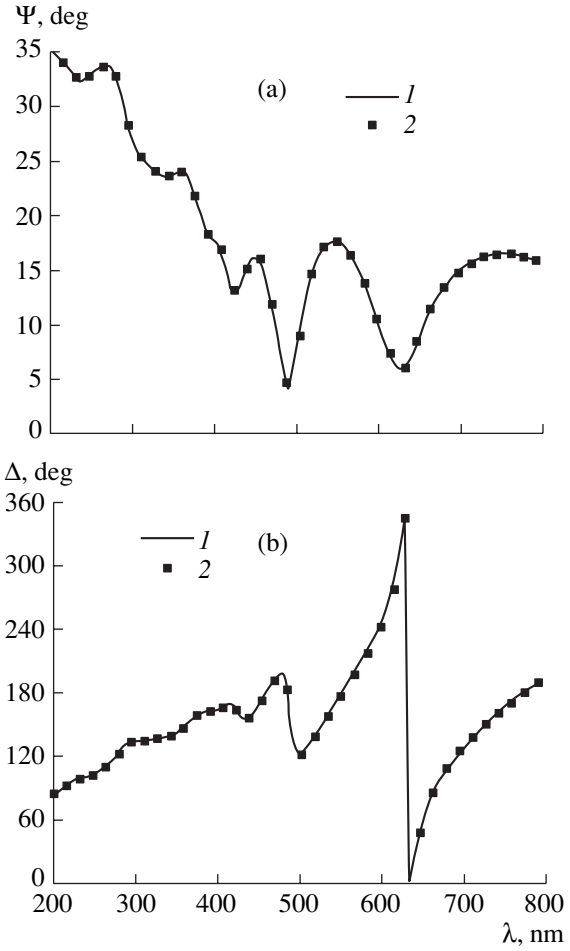

Fig. 4. (*1*) Experimental spectra and (*2*) spectra calculated using the optimized model (see table) for ellipsometric parameters (a) Ψ and (b) Δ.

Simulation of the damaged silicon layer, transition layers, oxide layer, and surface-roughness layer (according to the SE data) was based on the following considerations. The spectrum shown in Fig. 2 was divided into three portions taking into account the depth of penetration of the probing radiation into *a*-Si, *c*-Si, and *poly*-Si (see Fig. 3): (i) the region of short wavelengths ($\lambda < 350$ nm), where the depth of penetration of the probing radiation is certain not to exceed 10 nm; (ii) the middle (transition) spectral region ($350 \text{ nm} < \lambda < 650$ nm); and (iii) the long-wavelength portion of the spectrum, where the radiation is certain to penetrate the system as far as the substrate ($\lambda > 650$ nm).

The SE data in the short-wavelength region of the spectrum carry information about only the surface layers of the system, i.e., about the rough natural-oxide layer and the interface between the surface oxide and the Si film. This circumstance makes it possible to treat the system as a single-layer structure, which considerably reduces the number of adjustable parameters and makes it possible to solve the problem mathematically.

The structure of experimental ellipsometric spectra in the range $350 \text{ nm} < \lambda < 650$ nm is indicative of the profound effect of the interfacial layers. The interference effects related to the reflection at the boundary between the interfacial layer and the Si film also contribute to the spectrum. In this case, the system is physically a two-layer structure; however, since the parameters of the upper layers are already known, the system is still equivalent to a single-layer structure.

An analysis of the spectra in the region $\lambda > 650$ nm made it possible, first, to ensure that there were no significant transition layers at the interfaces between the substrate and SiO_2 and between SiO_2 and the Si film and, second, to clarify the phase composition of the Si film. The thickness of the Si film was considered known from the XTEM data and equal to 200 nm.

In order to make the three portions of the spectrum consistent with each other, we repeated the fitting procedure once again, this time for the spectrum as a whole.

As a result of this procedure, we determined the parameters of the model (the first column of the table) that described best the experimental data of spectral ellipsometry. In Fig. 4 we show the Ψ and Δ spectra calculated in the context of this model and experimental spectra. The quality of the approximation is so high that the experimental spectra fit the simulation spectra to within ~0.1°, which is close to the measurement error (±0.01° for Ψ and ±0.05° for Δ [8]).

Thus, the resulting structure (see table) differs from the nominal (design) structure, first, in the phase inhomogeneity of the Si film composition and, second, in the presence of a significant complex oxide layer at the surface of the Si film. In addition, the oxide layer itself consists of a surface-roughness layer and a transition layer with a nonuniform composition at the interface between the oxide and the Si film.

The thickness of the layers and the volume fractions of each of the materials composing the mixture (the parameters that are independent of the probing-radiation wavelength) were used as adjustable parameters in the analysis of the system under consideration. The refractive and absorption indices (n_j and k_j) of the components (*a*-Si and *c*-Si) were calculated using known values of ε_1 and ε_2 [10].

The parameters corresponding to the resulting model are listed in the table. The following conclusions can be drawn from the data of the table. (i) The natural-oxide layer exhibits microscopic roughness levels at the surface (there are ~34% voids). (ii) A transition layer exists between the oxide and a ~9-nm-thick silicon layer in which there are no voids; a comparison of the composition of this layer with that of the Si layer makes it possible to conclude that voids (12%) are filled with SiO_2 (10%) in the case of a transition layer. (iii) The silicon layer contains a large amount of both crystalline and amorphous phases, as well as a certain number of defects (voids) in the microstructure of this layer.

Finally, (iv) the interphase processes in a composite medium consisting of crystalline Si and voids in SiO_2 may be similar to the processes in the composite formed of SiO_2 and voids, i.e., in porous silica.

As is well known, the content of amorphous *a*-Si in a Si film depends heavily on the deposition temperature. In this context, the obtained value of a 14% fraction for *a*-Si in the silicon layer is quite reasonable for the deposition temperature used in our study (T = 635°C) [4].

Evidently, the SE data are in good qualitative agreement with the results of the direct XTEM measurements.

5. CONCLUSION

The combined use of XTEM and SE and information about the depth of penetration of probing radiation into the sample made it possible to perform a layer-by-layer analysis of a complex structure of polycrystalline silicon. We revealed the presence of surface and transition layers and determined their physical origin and structure; we also established the appreciable porosity of these layers. It is shown that the SE and BEMA methods can be used successfully in simulating and determining the parameters of a multilayer silicon system. We determined the composition, thickness, and parameters of the surface roughness of both the Si film and the Si natural oxide.

Using the SE data and a detailed analysis of them in terms of simulation of the multilayer structure, we managed to gain (i) information about the depth profile of the multilayer structure, (ii) quantitative data on the thickness of each layer, (iii) information about the structure (crystalline or amorphous) of each layer, and (iv) the characteristic of the natural oxide layer and its roughness.

All the above data agree well with the results of direct measurements by electron microscopy.

REFERENCES

1. T. I. Kamins, *Polycrystalline Silicon for Integrated Circuit Applications* (Academic, Boston, 1988).
2. C. Zhao, P. R. Lefevre, and E. A. Irene, Thin Solid Films **313–314**, 286 (1998).
3. V. I. Gavrilenko, A. M. Grekhov, D. V. Korbutyak, and V. G. Litovchenko, *Optical Properties of Semiconductors* (Naukova Dumka, Kiev, 1987) [in Russian].
4. A. Borghesi, M. E. Giardini, and M. Marazzit, Appl. Phys. Lett. **70**, 892 (1997).
5. D. A. G. Bruggeman, Ann. Phys. (Leipzig) **5**, 636 (1935).
6. R. M. Azzam and N. M. Bashara, *Ellipsometry and Polarized Light* (North-Holland, Amsterdam, 1977; Mir, Moscow, 1981).
7. O. W. Holland, B. R. Appleton, and J. Narayan, J. Appl. Phys. **54**, 2295 (1983).
8. A. I. Belyaeva and A. A. Galuza, Adv. Cryog. Eng. A **46**, 435 (2000).
9. G. E. Jellison, Opt. Mater. **1**, 41 (1992).
10. G. E. Jellison, M. F. Chisholm, and S. M. Gorbatkin, Appl. Phys. Lett. **62**, 3348 (1993).
11. G. S. Landsberg, *Optics* (Nauka, Moscow, 1976), p. 563 [in Russian].

Translated by A. Spitsyn

Semiconductors, Vol. 38, No. 9, 2004, pp. 1018–1022. Translated from Fizika i Tekhnika Poluprovodnikov, Vol. 38, No. 9, 2004, pp. 1056–1060.

SEMICONDUCTOR STRUCTURES, INTERFACES, AND SURFACES

Photosensitive Structures Based on Single-Crystal Silicon and Phthalocyanine CuPc: Fabrication and Properties

G. A. Il'chuk*, N. V. Klimova, O. I. Kon'kov*, S. E. Nikitin*, Yu. A. Nikolaev*, L. I. Rudaya**, V. Yu. Rud'***, Yu. V. Rud'*, E. I. Terukov*, V. V. Shamanin****, and T. A. Yurre****

** Ioffe Physicotechnical Institute, Russian Academy of Sciences, St. Petersburg, 194021 Russia*
e-mail: yuryrud@mail.ioffe.ru
*** St. Petersburg State Technological Institute (Technological University), St. Petersburg, 190013 Russia*
**** St. Petersburg State Polytechnical University, St. Petersburg, 195251 Russia*
***** Institute of High-Molecular Compounds, Russian Academy of Sciences, St. Petersburg, 199004 Russia*
Submitted January 13, 2004; accepted for publication January 14, 2004

Abstract—Vacuum thermal deposition of phthalocyanine CuPc onto the surface of crystalline silicon and subsequent magnetron sputtering of ZnO:Al are used to form *n*-ZnO:Al–*p*-CuPc–*n*-Si photosensitive structures for the first time. The highest photosensitivity of these structures $S_U^m \approx 20$ V/W is attained if the ZnO side of the structure is illuminated and is observed in the photon-energy range 1–3.2 eV at $T = 300$ K. An induced photopleochroism is observed if the linearly polarized light is incident obliquely on the ZnO side; the magnitude of the photopleochroism oscillates as a result of the interference of linearly polarized light in the ZnO film. It is concluded that the suggested structures have prospects for use in broadband photoconverters of natural light and in rapidly tunable photoanalyzers of linearly polarized light. © *2004 MAIK "Nauka/Interperiodica".*

The fabrication and study of various types of heterostructures are very important for the further development of contemporary electronics [1–3]. In recent years, organic materials of both natural and synthetic origin have found increasing use in the formation of heterojunctions [4–7]. In particular, the quantum efficiency of thin-film solar photoconverters based on organic materials is now as high as 3.6% [6]. It is expected that further progress in the field of solar cells will be achieved on the basis of compositions of donor and acceptor materials of organic origin [8]. In this paper, we report the results of the first attempt to use the contact between thin films of phthalocyanine CuPc (an organic semiconductor with *p*-type conductivity) and crystalline *n*-Si to fabricate photosensitive structures.

1. In order to fabricate the structures under study, we used *n*-Si(111) substrates with a thickness of ~300 μm, an area of up to 2 cm^2, and a resistivity of 1 Ω cm at T = 300 K. The phthalocyanine CuPc films were formed on the polished surface of a silicon substrate using vacuum thermal deposition at a temperature of ~50°C. These films were uniformly blue in color, had a specular-smooth surface, and exhibited fairly good adhesion to the surface of the *n*-Si substrate.

In order to form heterostructures, we used magnetron sputtering of a pressed target of undoped ZnO with the addition of 2.5% of pure Al in an argon atmosphere to deposit the high-conductivity ZnO:Al film ($n \approx 10^{20}$ cm^{-3} at T = 300 K) [9]. The substrate temperature was no higher than 50°C during the deposition of ZnO:Al for 2–4 h; the argon pressure was 0.5 Pa. The surface of the *n*-ZnO:Al films grown by the method described above was specular-smooth and dark green when exposed to the white light of an incandescent lamp. It is worth noting that the specular state of the surface, the adhesion, and the interference-related coloring of the ZnO:Al films deposited simultaneously in the same process onto the surfaces of the organic film and the crystalline substrate were practically identical. This observation makes it possible to assume that chemical interaction of ZnO with CuPc does not occur in the course of formation of the ZnO:Al film.

2. The measured steady-state current–voltage (*I–V*) characteristics of the obtained *n*-ZnO:Al–*p*-CuPc–*n*-Si structures exhibit a pronounced rectification effect (Fig. 1). The forward portion of the *I–V* characteristics for all the structures obtained corresponds to the application of a negative voltage to the *n*-ZnO:Al film. The forward dark current exceeds the reverse current by a factor of ~3×10^3 (T = 300 K) in the best structures at the bias voltages $|U| \approx 10$ V. Exposure of the ZnO side of structures to the light of an incandescent lamp with a power density of $P \approx 10$ mW/cm^2 leads to an increase in the reverse current by two orders of magnitude at U = –10 V; at the same time, the shape of the *I–V* characteristic remains unchanged.

At forward bias voltages as high as 1.1 V, the dark current of the structure satisfies the well-known diode equation

$$I = I_s[\exp(eU/\beta kT) - 1], \quad (1)$$

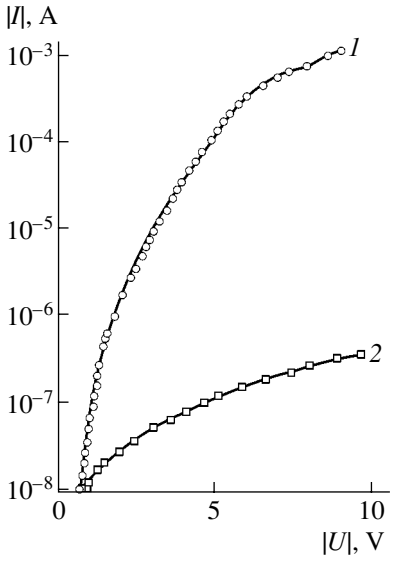

Fig. 1. Forward (curve *1*) and reverse (curve *2*) portions of the current–voltage characteristic of the *n*-ZnO:Al–*p*-CuPc–*n*-Si structure (sample no. 1-2) at $T = 300$ K. The conducting direction corresponds to the negative sign of external bias at the *n*-ZnO:Al film.

where the saturation current I_s is typically in the range of 10^{-9}–10^{-10} A at $T = 300$ K and the coefficient β varies from 5 to 17. As the forward-bias voltage increases ($U > 5$ V), the dark current obeys a linear law:

$$I = \frac{U - U_0}{R_0}, \qquad (2)$$

where the cutoff voltage $U_0 \approx 4.5$ V and the residual resistance $R_0 = 500$–$9000\ \Omega$ for different structures.

In the wide bias range from 2 to 25 V, reverse currents of the studied structures follow the power-law dependence $I \propto U^m$, where the exponent $m = 1.8$. This dependence of current on the bias voltage is almost quadratic and may indicate that we are dealing here with currents limited by the space charge (the trap-free quadratic law) [10, 11]:

$$I = U^2 \frac{9\varepsilon\varepsilon_0\mu A}{8L^3}, \qquad (3)$$

where ε and ε_0 are the dielectric constants of the medium and free space, respectively; μ is the mobility of holes in the organic film; and A and L are the area and the thickness of the structure, respectively.

3. A photovoltage is observed between the contacts *a* and *b* (see Fig. 2, inset) if the *n*-ZnO:Al–*p*-CuPc–*n*-Si structures under study are illuminated. The sign of this photovoltage is independent of the position of the light beam (0.3 mm in diameter) at the surface of the sample, the energy of incident photons, and the illumination intensity. In all the experiments, a negative photovoltage sign is observed at contact *a*, which, in turn, is consistent with the rectification direction in the structures

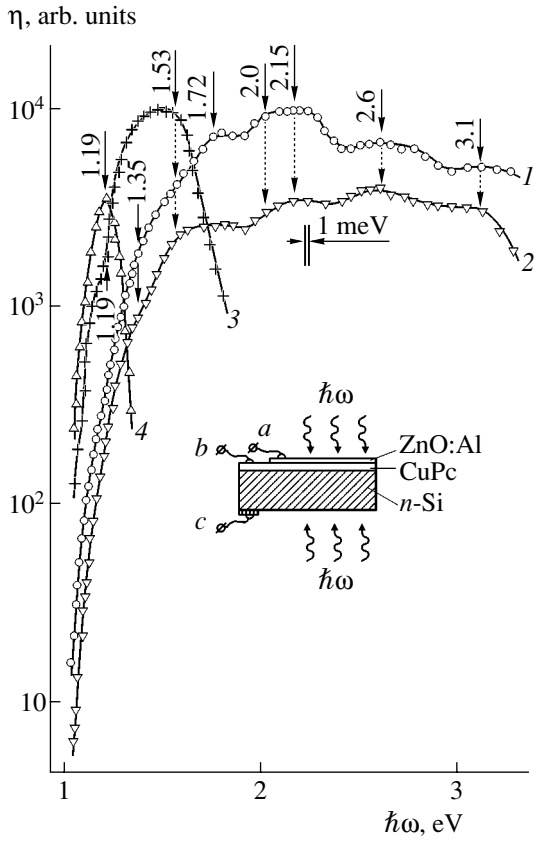

Fig. 2. Spectral dependences of relative quantum efficiency of photoconversion in the *n*-ZnO:Al–*p*-CuPc–*n*-Si structure (curve *1*, the *n*-ZnO:Al side is exposed to light) and the heterojunctions *n*-ZnO:Al–*p*-CuPc (curve *2*, the *n*-ZnO:Al side is exposed to light) and *p*-CuPc–*n*-Si (curves *3* and *4* with the *p*-CuPc and *n*-Si sides exposed to light, respectively) at $T = 300$ K; nonpolarized light was used. Sample no. 1-1. The spectra are shifted along the η axis in order to avoid their superposition. Inset: schematic representation of the structure and the geometry of irradiation with nonpolarized light; the letters *a*, *b*, and *c* designate the contacts.

under consideration. Our studies show that a maximum open-circuit photovoltage of ~40 mV and a short-circuit current of ~0.1 mA are attained at an incident-radiation intensity of ~10 mW/cm^2. The highest voltage photosensitivity of the best of the *n*-ZnO:Al–*p*-CuPc–*n*-Si structures is $S_U^m \approx 20$ V/W at $T = 300$ K and is invariably attained if the *n*-ZnO:Al side of the structure is illuminated.

A typical spectral dependence of the relative quantum efficiency of photoconversion $\eta(\hbar\omega)$ is shown in Fig. 2 (curve *1*) for the *n*-ZnO:Al–*p*-CuPc–*n*-Si heterostructures exposed to nonpolarized light. This efficiency is calculated as the ratio between the short-circuit current and the number of incident photons. For comparison, the $\eta(\hbar\omega)$ spectra of the component heterojunctions *n*-ZnO:Al–*p*-CuPc and *p*-CuPc–*n*-Si are also shown (Fig. 2, curves *2–4*). It is worth noting that the voltage photosensitivity of the *n*-ZnO:Al–*p*-CuPc

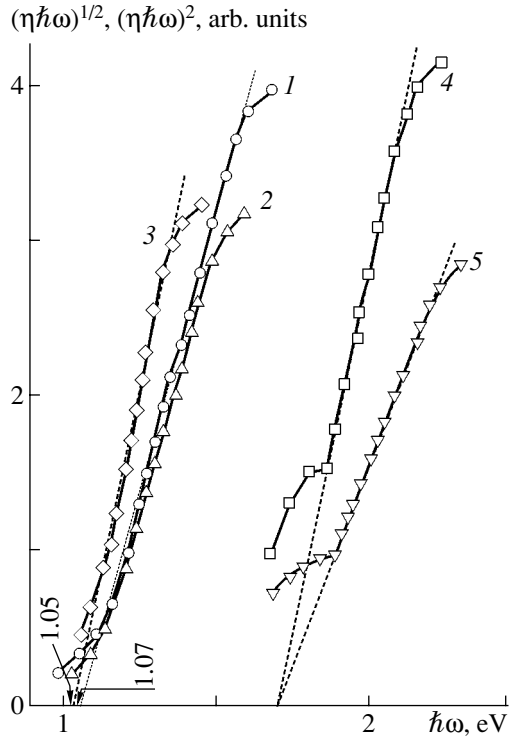

Fig. 3. Dependences $(\eta\hbar\omega)^{1/2} = f(\hbar\omega)$ (curves *1–3*) and $(\eta\hbar\omega)^2 = f(\hbar\omega)$ (curves *4*, *5*) for the structures (*1*, *4*) *n*-ZnO:Al–*p*-CuPc–*n*-Si, (*2*, *5*) *n*-ZnO:Al–*p*-CuPc, and (*3*) *p*-CuPc–*n*-Si at $T = 300$ K. Sample no. 1-1.

heterojunction is close to the values of S_U^m for the *n*-ZnO:Al–*p*-CuPc–*n*-Si heterostructure as a whole. Polarities of the photovoltage coincide in the above two cases; i.e., the *n*-ZnO:Al film is always charged negatively. As can be seen from Fig. 2 (curves *1*, *2*), the photosensitivity spectra of the structures under comparison are almost the same if the *n*-ZnO:Al side of the structure is illuminated. Indeed, the photosensitivity is observed in a wide spectral range (1–3.2 eV) in these structures; the full width of the photosensitivity spectra at the half-maximum (FWHM) $\delta \approx 1.3$–1.7 eV. One should also note the qualitative agreement between the energies that correspond to special features in the $\eta(\hbar\omega)$ spectra of the two structures under consideration (points of inflection and peaks that are indicated by arrows at the spectral curves; see Fig. 2, curves *1*, *2*). Generally, the observed similarity of the $\eta(\hbar\omega)$ spectra and the close agreement between the values of S_U^m for the *n*-ZnO:Al–*p*-CuPc–*n*-Si structure and the *n*-ZnO:Al–*p*-CuPc heterojunction suggest that the main contribution to the photosensitivity of these structures is made by the ZnO–CuPc heterojunction.

The energy position of the onset of the long-wavelength increase in the photosensitivity at $\hbar\omega \gtrsim 1$ eV for the *p*-CuPc–*n*-Si heterojunction (Fig. 2, curves *3*, *4*) was found to be independent of the illumination geometry and coincident with that for the *n*-ZnO:Al–*p*-CuPc–*n*-Si and *n*-ZnO:Al–*p*-CuPc heterostructures (Fig. 2, curves *1*, *2*). At the same time, the $\eta(\hbar\omega)$ spectra for the *p*-CuPc–*n*-Si heterojunction were found to have a small width. For example, if the *n*-Si substrate (with a thickness of ~300 μm) side of the structures is illuminated, the photosensitivity spectra exhibit a pronounced short-wavelength falloff at $\hbar\omega > 1.19$ eV, which is caused by an increase in the optical-absorption coefficient for *n*-Si. As a result, the layer containing the photogenerated charge carriers moves progressively further from the active region of the heterojunction with a consequent falloff of η (Fig. 2, curve *4*). In this situation, the quantity $\delta \approx 0.15$ eV.

If the side of the *p*-CuPc–*n*-Si heterojunction corresponding to its wide-gap component CuPc is exposed to light [6], the FWHM of the $\eta(\hbar\omega)$ spectrum increases by approximately a factor of 2 compared to the FWHM in the above conditions of illumination, and it can be as large as $\delta \approx 0.3$ eV. The short-wavelength falloff at $\hbar\omega > 1.53$ eV (Fig. 2, curve *3*) is caused by an increase in the coefficient of optical absorption in thin *p*-CuPc films (with thickness $d \approx 1$ μm) as the photon energy increases. As a result, the zone of photogenerated charge carriers moves further from the active region of the *p*-CuPc–*n*-Si heterojunction.

It is important to note that the energy position of the short-wavelength falloff of $\eta(\hbar\omega)$ under conditions of illumination of the CuPc side of the *p*-CuPc–*n*-Si heterojunction (Fig. 2, curve *3*) corresponds to the onset of a drastic increase in η in the *n*-ZnO:Al–*p*-CuPc–*n*-Si structure (Fig. 2, curve *1*). This circumstance is caused by differences in the location of the active region in the barriers being compared. Indeed, in the case of the *n*-ZnO:Al–*p*-CuPc–*n*-Si structure, the active region is located at the ZnO–CuPc heterocontact rather than at the *p*-CuPc–*n*-Si heterojunction. If the *n*-ZnO side of the structure is exposed to light, an increase in the optical absorption in the bulk of the phthalocyanine CuPc film is accompanied by an approach of the zone of photogenerated charge carriers to the active region of the heterocontact. As a result, the spectral photosensitivity band extends widely to shorter wavelengths of up to 3.1 eV, which was not attained in the case of two-layer CuPc–C_{60} heterojunctions [8].

In Fig. 3 we show the results of the analysis of the photoactive-absorption spectra for the studied structures based on a phthalocyanine CuPc film. It follows from this analysis that the falloff of photoactive absorption in the *n*-ZnO:Al–*p*-CuPc–*n*-Si structure (Fig. 3, curve *1*) and also the *n*-ZnO:Al–*p*-CuPc and *p*-CuPc–*n*-Si heterojunctions (Fig. 3, curves *2*, *3*) is linearized if represented as $(\eta\hbar\omega)^{1/2} = f(\hbar\omega)$. The extrapolation $(\eta\hbar\omega)^{1/2} \longrightarrow 0$ yields values of $\hbar\omega$ that are close to the silicon band gap [12]. Taking into account the shape of the above dependences and the theory of interband absorption [13], we can attribute the long-wavelength

edge of photosensitivity in the structures under consideration to the direct interband transitions in silicon.

As can be seen from Fig. 3 (curves *4*, *5*), the short-wavelength portion of the spectra of relative quantum efficiency of photoconversion in the structures under study is described adequately by the quadratic dependence $(\eta\hbar\omega)^2 \propto \hbar\omega$ and can be attributed to the direct band-to-band optical transitions [13] in films of the organic semiconductor CuPc. As can be seen from Fig. 3, the extrapolation $(\eta\hbar\omega)^{1/2} \longrightarrow 0$ yields values of the cutoff energy that are the same for the *n*-ZnO:Al–*p*-CuPc–*n*-Si structure and the *n*-ZnO:Al–*p*-CuPc heterojunction incorporated into this structure. Finally, the onset of the short-wavelength falloff of photosensitivity at $\hbar\omega >$ 3.1 eV for the *n*-ZnO:Al–*p*-CuPc–*n*-Si structure and the *n*-ZnO:Al–*p*-CuPc heterojunction incorporated into this structure (Fig. 2, curves *1*, *2*) may be related to the onset of high optical absorption in the ZnO film [14].

4. Studies of the *n*-ZnO:Al–*p*-CuPc–*n*-Si structures exposed to linearly polarized light along the normal to the surface of the *n*-ZnO:Al film suggest that variations in the spatial orientation of the electric-field vector *E* of the optical wave only slightly affect the photosensitivity of these structures. Consequently, natural photopleochroism is not observed in the structures under study, which is directly related to the isotropy of absorption in materials incorporated into the structures under consideration [6].

The photopleochroism in the structures is observed only under conditions of oblique incidence of linearly polarized light on the ZnO surface. For example, Fig. 4 shows the dependences of the short-circuit photocurrents i^p (**E** ∥ IP, where IP is the plane of incidence of linearly polarized light) and i^s (**E** ⊥ IP), as well as the induced-photopleochroism coefficient [17]

$$P_I = \frac{i^p - i^s}{i^p + i^s}, \qquad (4)$$

on the angle of incidence θ of the beam of linearly polarized light on the active surface of ZnO at $\hbar\omega$ = const in the range of photosensitivity of the structures under study. Angular dependences of i^p and i^s shown in Fig. 4 are consistent with the Fresnel relations [18], and the coefficient of induced photopleochroism follows the square law [19]

$$P_I \propto \theta^2; \qquad (5)$$

experimental values of P_I agree with the theoretical estimate if the refractive index of ZnO is taken into account [14].

It is important to note that this agreement was observed only in the vicinity of certain energies of incident photons. As the distance from these energies increased, the angular dependences of photocurrents became anomalous and the experimental values of P_I became smaller than the theoretically expected values [14]. In addition, oscillations of induced photopleochroism are observed (Fig. 5), which are related to the interference of linearly polarized light in the thin-film component of the structures under consideration [17]. The angular dependences of photocurrents and the P_I coefficient (see Fig. 4) take place only at the peaks of $P_I(\hbar\omega)$ dependences, whereas the angular dependences $i^p(\theta)$ and $i^s(\theta)$ become anomalous at the minima of $P_I(\hbar\omega)$. According to Kesamanly *et al.* [17], the observed minima in the spectra of induced photopleochroism correspond to the condition for the highest transmission $P_I \longrightarrow 0$. An estimate of the thickness of *n*-ZnO:Al films on the basis of oscillations observed in

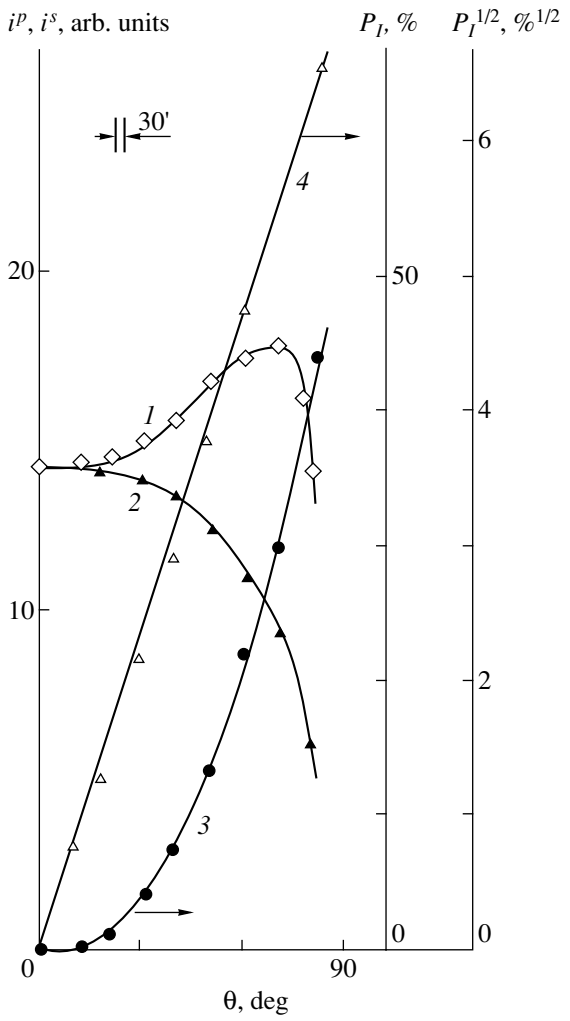

Fig. 4. Dependences of the short-circuit currents (*1*) i^p and (*2*) i^s and the induced-photopleochroism coefficient P_I (curve *3* for P_I and curve *4* for $P_I^{1/2}$) on the angle of incidence of linearly polarized light θ on the surface of the ZnO film in the *n*-ZnO:Al–*p*-CuPc–*n*-Si structure at T = 300 K. Sample no. 1-2; $\hbar\omega$ = 2.7 eV. The ZnO side of the structure was exposed to light.

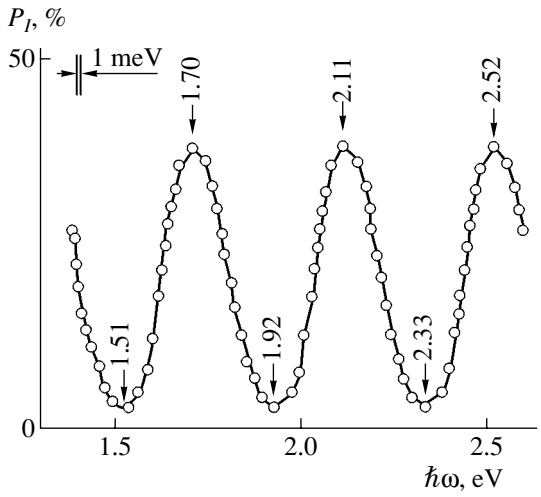

Fig. 5. Spectral dependence of the induced-photopleochroism coefficient for the *n*-ZnO:Al–*p*-CuPc–*n*-Si structure at T = 300 K. Sample no. 1-2, $\theta = 75°$. The ZnO side of the structure was exposed to light.

the spectra of P_I (Fig. 5) coincides with the results of direct measurements.

The observed oscillations of the photopleochroism coefficient in the structures under consideration allow us to draw the important conclusion that the *n*-ZnO:Al films obtained by magnetron-sputtering deposition onto films of phthalocyanine CuPc are of fairly high quality.

5. The window effect characteristic of ideal heterojunctions [15] is clearly pronounced in the spectral dependences of photosensitivity for the photosensitive *n*-ZnO:Al–*p*-CuPc–*n*-Si structures and *n*-ZnO:Al–*p*-CuPc heterojunctions obtained for the first time. This effect manifests itself when the energy positions of the long- and short-wavelength edges of photosensitivity are governed by the interband absorption in the components of the structures and high photosensitivity is attained for energies that are in the range limited by the band gaps of these components. The results of our studies of photoelectric properties of the heterocontact of the organic and inorganic semiconductors indicate that this contact can be used to advantage in broadband photoconverters of natural light and in selective photoanalyzers of linearly polarized light.

REFERENCES

1. Zh. I. Alferov, Fiz. Tekh. Poluprovodn. (Leningrad) **32**, 3 (1988) [Sov. Phys. Semicond. **32**, 1 (1988)].
2. N. N. Ledentsov, IEEE J. Sel. Top. Quantum Electron. **8**, 1015 (2002).
3. N. N. Novikov, M. V. Maksimov, Yu. M. Shernyakov, *et al.*, in *Abstracts of VI Russian Conference on the Physics of Semiconductors* (Fiz.–Tekh. Inst., St. Petersburg, 2003).
4. V. Yu. Rud', Yu. V. Rud', and V. Kh. Shpunt, Fiz. Tekh. Poluprovodn. (St. Petersburg) **31**, 129 (1997) [Semiconductors **31**, 97 (1997)].
5. C. W. Tang, Appl. Phys. Lett. **48**, 183 (1986).
6. P. Peumans and S. R. Forrest, Appl. Phys. Lett. **79**, 126 (2001).
7. R. Rinaldi, E. Branca, R. Cingolani, *et al.*, Appl. Phys. Lett. **78**, 3541 (2001).
8. P. Peumans, S. Uchida, and S. R. Forrest, Nature **425**, 158 (2003).
9. S. U. Nikitin, Yu. A. Nikolaev, I. K. Polushina, *et al.*, Fiz. Tekh. Poluprovodn. (St. Petersburg) **37**, 1329 (2003) [Semiconductors **37**, 1291 (2003)].
10. E. Hernander, Cryst. Res. Technol. **33**, 285 (1998).
11. M. A. Lampert and P. Mark, *Current Injection in Solids* (Academic, New York, 1970; Mir, Moscow, 1973).
12. S. Sze, *Physics of Semiconductor Devices*, 2nd ed. (Wiley, New York, 1981; Mir, Moscow, 1984).
13. Yu. A. Ukhanov, *Optical Properties of Semiconductors* (Nauka, Moscow, 1977) [in Russian].
14. *Physicochemical Properties of Semiconductors*, Ed. by A. V. Novoselova, V. B. Lazarev, Z. S. Medvedeva, N. P. Luzhina, and A. A. Levin (Nauka, Moscow, 1979) [in Russian].
15. A. G. Milnes and D. L. Feucht, *Heterojunctions and Metal–Semiconductor Junctions* (Academic, New York, 1972; Mir, Moscow, 1975).
16. Yu. V. Rud', Izv. Vyssh. Uchebn. Zaved., Fiz. **29**, 68 (1986).
17. F. P. Kesamanly, V. Yu. Rud', and Yu. V. Rud', Fiz. Tekh. Poluprovodn. (St. Petersburg) **30**, 1921 (1996) [Semiconductors **30**, 1001 (1996)].
18. G. S. Landsberg, *Optics* (Nauka, Moscow, 1976) [in Russian].
19. G. A. Medvedkin and Yu. V. Rud', Phys. Status Solidi A **67**, 333 (1981).

Translated by A. Spitsyn

Semiconductors, Vol. 38, No. 9, 2004, pp. 1023–1029. Translated from Fizika i Tekhnika Poluprovodnikov, Vol. 38, No. 9, 2004, pp. 1061–1067.

SEMICONDUCTOR STRUCTURES, INTERFACES, AND SURFACES

Interaction of C_{60} Molecules with the (100)W Surface: Adsorption, Initial Stages of Film Growth, and Thermal Transformation of the Adsorption Layer

N. R. Gall', E. V. Rut'kov, and A. Ya. Tontegode

Ioffe Physicotechnical Institute, Russian Academy of Sciences, Politekhnicheskaya ul. 26, St. Petersburg, 194021 Russia
e-mail: gall@ms.ioffe.rssi.ru

Submitted January 28, 2004; accepted for publication February 2, 2004

Abstract—Adsorption, initial stages of film growth, and transformation of the adsorption layer of C_{60} molecules on the (100)W surface on heating are investigated in ultrahigh-vacuum conditions. It is shown that the C_{60} molecules from the first adsorption layer undergo substantial transformation even at room temperature, whereas the molecules in the second and subsequent adsorption layers retain their nature in the adsorbed state up to 700 K. The layer-by-layer growth of a fullerite film is observed at room temperature. It is found that a considerable quantity of fullerenes, which corresponds to approximately two monolayers, remain at the surface during thermal desorption. A physical model explaining this phenomenon is suggested. © *2004 MAIK "Nauka/Interperiodica".*

1. INTRODUCTION

Fullerenes belong to a new relatively recently found form of existence of carbon. They are individual molecules of strictly defined dimensions with compositions C_{60}, C_{70}, C_{84}, C_{100}, and others. All fullerene molecules consist of carbon atoms only. The carbon network forms a closed cage, and there is a void free of material inside the molecule. The C_{60} molecule is most available for research. This molecule comprises a sphere with a diameter of 7.08 Å, which passes through the centers of constituting carbon atoms [1].

For both practical and scientific purposes, it is necessary to understand the way in which fullerene molecules interact with the material; any such an interaction starts from the surface. Now there are at least several tens of studies in which such research was carried out by different methods, both theoretically and experimentally for silicon [1–7], noble metals [8–12], and refractory metals [13–16].

We previously showed that C_{60} molecules adsorbed at room temperature retain their structure at the surface of Ir [11], Re [14], and Mo [15]. However, fullerene molecules on the surface of tungsten undergo a substantial transformation even at room temperature [16, 17]. At elevated temperatures, the fullerite film grows on the surfaces of silicon, rhenium, and molybdenum by the island mechanism, while at room temperature it grows on the surface of molybdenum by the layer-by-layer mechanism. It seemed important to understand the ways of transformation of the known mechanisms of interaction of fullerenes with the substrate on going to a more chemically active surface: (100)W.

2. EXPERIMENTAL

The experiments were carried out in a high-resolution Auger spectrometer [18] under ultrahigh vacuum ($p \approx 10^{-10}$ Torr). It was possible to record the Auger spectra immediately from the samples heated to 300–2100 K. The Auger spectra were measured at an angle of ~5° to the normal to the surface. The samples were straight-channel tungsten ribbons $0.02 \times 1 \times 40$ mm^3 in size, which were sequentially cleaned by heating in oxygen ($p \approx 10^{-7}$ Torr, $T = 1500$ K, 30 min) and in ultrahigh vacuum ($p \approx 10^{-10}$ Torr, $T = 2600$ K, 3 h). After cleaning, the sample surface yielded only Auger signals of tungsten. Simultaneously with the cleaning, the ribbon was textured, and a (100) facet was formed on the surface. The work function of the surface was $e\varphi = 4.65$ eV, and the surface was homogeneous with respect to the value of $e\varphi$. According to electron microscopy data, the average grain size was ~20 μm. We previously found that the energy of the Auger peak C_{KVV} for the C_{60} molecules is 269 eV, which is almost 3 eV lower than that for, e.g., graphite, metal carbides, or adsorbed carbon clusters. The energy of the Auger peak is the same for both thick films of adsorbed C_{60} molecules (5–10 monolayers) and submonolayer coatings. We used this phenomenon to distinguish fullerenes adsorbed at the surface from other possible states of carbon.

The C_{60} molecules were deposited onto the entire ribbon surface at an angle of 65° to its normal from the Knudsen cell. The charge of the C_{60} molecules (~0.05 g) with a purity of 99.5% was placed into the cell. After training, the cell provided a stable and easily controlled flux of fullerene molecules with a density of 10^{10}–10^{13} mol/(cm^2 s). For the absolute calibration of the flux density, the iridium ribbon was arranged near

1063-7826/04/3809-1023$26.00

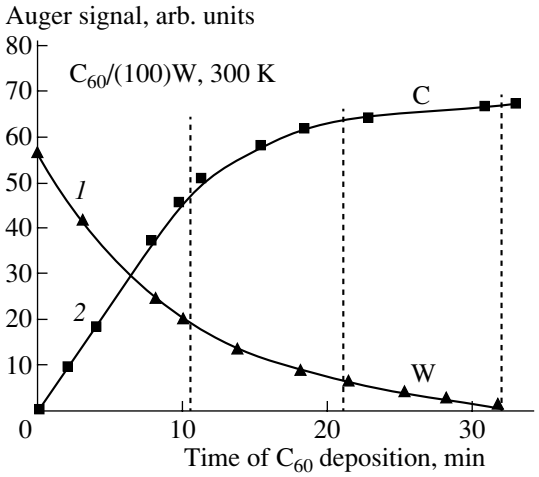

Fig. 1. Deposition of C_{60} molecules on the (100)W surface; flux density $\nu_{C_{60}} = 2.4 \times 10^{11}$ molecule/(cm^2 s). (*1*) Auger signal of W and (*2*) Auger signal of C; vertical dotted lines indicate the boundaries of filling of fullerene monolayers.

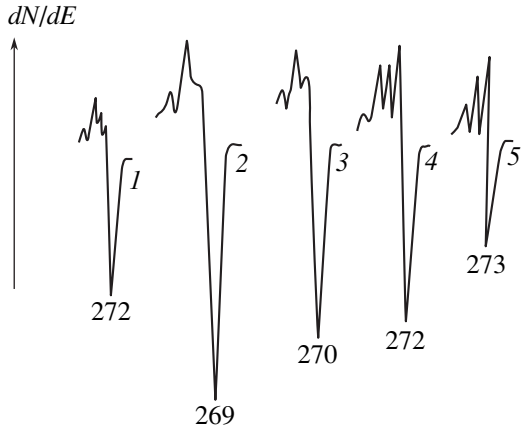

Fig. 2. Shapes of the Auger line C_{KVV} of various adsorption states of C_{60} molecules on W. (*1*) 0.5 monolayer (ML) at 300 K; (*2*) multilayer (~3 ML) fullerene films deposited at 300 K; (*3*) the same film annealed at 900 K (1 min); (*4*) the same film annealed at 1100 K (1 min); and (*5*) the same film annealed at 1400 K (surface carbide). Numbers at the bottom denote the energy of the Auger peaks (eV).

the tungsten one and in parallel to it, as we suggested in [16]. The accuracy of the absolute calibration was 15–20%.

3. ADSORPTION AT ROOM TEMPERATURE

Figure 1 shows the changes of the Auger signals of carbon and tungsten during adsorption of a constant flux of C_{60} molecules at the (100)W surface at room temperature. One can see that the Auger signal of tungsten decreases steadily and drops to zero, while the Auger signal of carbon increases almost linearly up to the deposition time $t \approx 650$ s. Then the rate of the signal increase diminishes, and the signal magnitude saturates rather abruptly. This means that, starting from $t = 650$ s, the newly incoming C_{60} molecules screen both the substrate and the Auger signal of carbon from previously adsorbed molecules. Thus, we may suggest that the first monolayer was filled during this deposition time, and subsequent layers started to grow. During deposition of the C_{60} molecules, the shape of the Auger line C_{KVV} gradually transforms from spectrum *1* in Fig. 2, obtained for ~300 s of deposition, into spectrum *2* in Fig. 2, obtained for 30 min of deposition.

What is the monolayer of C_{60} molecules on the (100)W surface? One can see that the energy of the Auger signal from the first monolayer of C_{60} molecules is 272 eV; the shape of this signal is not in the least like that of fullerene, which is completely consistent with our data [16, 17]. As one can see from the plot, the first monolayer reduces (screens) the Auger signal of the substrate very strongly, specifically, by a factor of ~2.8! This magnitude is very close to the degree of screening that was effected by fullerene monolayers at the surfaces (100)Mo [15], (100)Si [7], and $(11\bar{1}0)$Re [14]. It significantly exceeds the degrees of screening effected by carbon monolayers in other chemical states. Thus, the surface carbide and a two-dimensional graphite film reduce the Auger signal of tungsten by a factor of 1.2 and 1.6, respectively. It seems likely that the fullerene molecule, when contacting with a highly active tungsten surface, significantly transforms rather than lose its individuality and structure completely. This enables some of the carbon atoms to be involved in strong chemisorption interaction with the metal surface. This phenomenon apparently accounts for the carbide-like shape of the Auger line for submonolayer and monolayer adsorbed films consisting of C_{60} molecules (Fig. 2, spectrum *1*). Somewhat conditionally, we suggest characterizing this state as a "flat ball" or, perhaps, a "hemisphere," which is illustrated in Fig. 3a in the schematic diagram of processes on the (100)W surface at 300 K during the deposition of fullerenes. Assuming that the screening ability of fullerene molecules varies weakly during the transformation described above, we can estimate their concentration in the first monolayer. According to calculations carried out in [15], it is $N_{\text{cl-packed}} \approx (1.5\text{–}1.6) \times 10^{14}$ mol/cm^2. On the basis of our absolute calibration of the flux, we can suggest that $\sim 1.5 \times 10^{14}$ mol/cm^2 will fall onto the surface in 11 min, which agrees well with the estimate given.

And how do the films grow further? Certain estimates can be obtained from the Auger spectroscopy data. Let us assume that the concentration of the C_{60} molecules in the second layer is the same as in the first one, i.e., $\sim 1.5 \times 10^{14}$ mol/cm^2. To deposit this layer, a further 11 min will be necessary, and the substrate after completion of its formation should be screened by a factor of $2.8 \times 2.8 = 7.9$. As one can see from Fig. 1, the Auger signal from the substrate decreases by a factor of

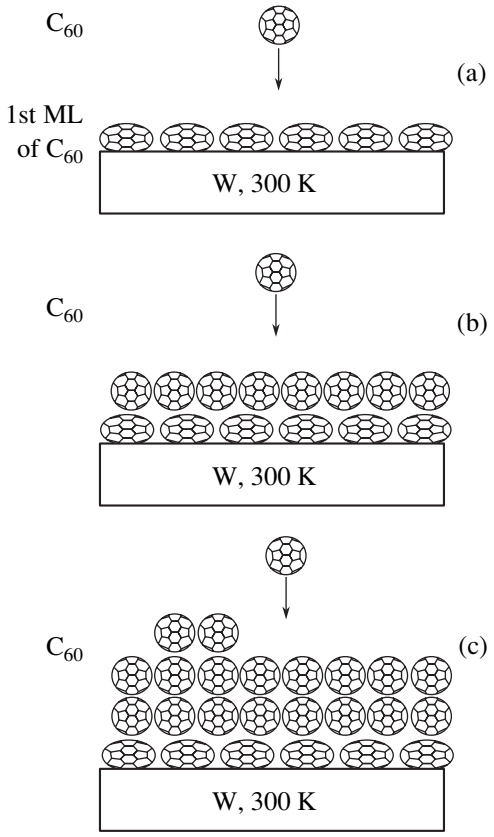

Fig. 3. Schematic diagrams of processes during deposition of C_{60} molecules onto the (100)W surface at room temperature. (a) Filling of the first monolayer ($\theta_{C_{60}} = 1$) and (b, c) filling of the second and subsequent layers, respectively.

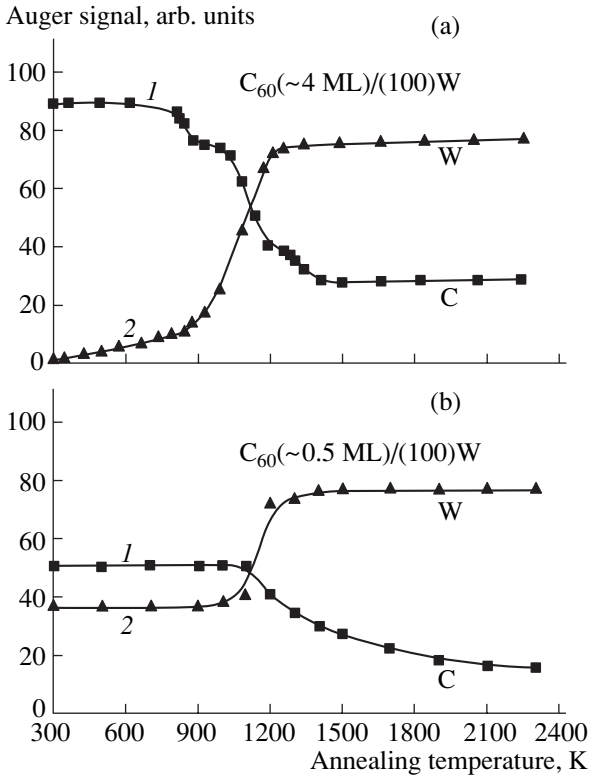

Fig. 4. Variations in the Auger signals of (*1*) C and (*2*) W during thermal treatment of the film of C_{60} molecules on the (100)W surface. The initial state is the film of C_{60} molecules deposited at room temperature; the film thickness is (a) ~4 and (b) ~0.5 ML; the time of thermal treatment at each point is 20 s.

~8 due to screening for a deposition time of 22 min and by a factor of ~24 for a deposition time of 33 min, which corresponds to the formation of the third layer. Note that $2.8^3 = 22$, which is very close to the given value. These data are indicative of the layer-by-layer growth of the fullerite film on the (100)W surface at room temperature.

In addition, note that, until the first monolayer is completed, the shape of the Auger line of carbon does not vary. This line is present in spectrum *1* in Fig. 2. In contrast, the shape of the Auger line starts to vary simultaneously with the growth of the second layer. This line is apparently the superposition of signals that have different shapes for the first and subsequent layers. For a film three to four layers thick, the line shape is typically that of fullerene (Fig. 2, spectrum *2*), since the Auger signal from the first layer is strongly reduced due to screening and virtually does not contribute to the total signal. The sequence of processes described here is schematically illustrated in Figs. 3b and 3c.

Using our model, we estimate the expected intensity of the Auger signal of carbon for two monolayers consisting of C_{60} molecules. Let us assume that the transformation of fullerene molecules only slightly affects the probability of the Auger transition *KVV* in the carbon atom [19] and that the fullerene monolayer screens the Auger signals of carbon and tungsten to the same extent, since the corresponding mean free paths are close [20]. We can then calculate the Auger signal from two fullerene monolayers I_2 by an almost evident formula:

$$I_2 = I_1 + I_1/\delta, \quad (1)$$

and the Auger signal from three layers I_3 by the formula

$$I_3 = I_1 + I_1/\delta + I_1/\delta^2, \quad (2)$$

where I_1 is the Auger signal from the first monolayer, and δ is the degree of screening of the Auger signal of the substrate by the first fullerene monolayer. Substituting the experimental data $I_1 = 48$ and $\delta = 2.8$, we obtain $I_2 = 65$ and $I_3 = 71$, which should be compared with the experimental values 64 and 71, respectively.

4. THERMAL TRANSFORMATION OF THE FULLERITE FILM ON THE (100)W SURFACE

Figure 4a shows the variation in the Auger signals of carbon and tungsten during annealing of a multilayer

fullerite film. According to the estimate, the film thickness is ~4 ML. One can see that, up to 700 K, the Auger signal of the adsorbate varies only slightly, whereas the signal of the substrate increases. This observation is indicative of the reconstructions in the adsorption layer. The energy of the Auger peak of carbon remains constant (269 eV), which indicates that precisely C_{60} molecules are present on the surface. The adsorption layer is rapidly reconstructed in the range 750–800 K. The Auger signal of carbon decreases, whereas the Auger signal of the substrate increases drastically. For all previously studied substrates (Mo, Re, Ir, Si, and SiC), thermal desorption of fullerenes from a multilayer film was observed in this temperature range. It is logical to assume that the Auger signals vary due to the same phenomenon in our case. In fact, other possible causes, for example, dissolution in the substrate, chemical reactions, or surface migration seem to be unlikely. At the temperatures mentioned, even single carbon atoms do not yet dissolve in the tungsten bulk [21]. There are no impurities potentially capable of reacting on the surface. C_{60} molecules are deposited uniformly over the entire ribbon surface, and escape of particles due to migration seems to be unlikely. Consequently, thermal desorption is the only possible cause of the escape of C_{60} molecules.

Up to 900 K, a certain carbon coating, which decreases the Auger signal from the substrate by a factor of ~4.7 (Fig. 4a), remains on the surface in the experiment described. This coating does not consist of fullerenes, since the energy of the Auger peak is 270 eV, although the shape of the Auger peak is similar to the fullerene peak (Fig. 2, spectrum *3*). It seems likely that the main portion of the C_{60} molecules desorb, and only the layer of transformed carbon cages of the fullerene molecules remains on the surface. At $T > 900$ K, the Auger line exhibits a further pronounced transformation (Fig. 2, spectrum *4*), specifically, the line acquires a more "carbide" character. This is apparently associated with the further decomposition of fragments of fullerene molecules and substitution of C–W chemisorption bonds for a considerable part of C–C bonds. In this temperature range, single carbon atoms are already actively dissolved in the tungsten bulk. It seems likely that precisely the decomposition of fragments of C_{60} molecules prevents the dissolution and formation of the equilibrium concentration of C atoms at the surface. The final considerable transformation is observed at $T \gtrsim 1300$ K. At this temperature, the Auger signal of carbon abruptly decreases once more, and its shape becomes purely carbide (Fig. 2, spectrum *5*). We previously showed that there is a diffusion-related equilibrium between the surface and the substrate bulk at these temperatures [21]. In this case, it is already not important in which form carbon was adsorbed at the surface, since all the molecules and their remains are decomposed, and there are only individual C atoms in the adsorption layer. Their surface concentration corresponds to the formation of the surface carbide layer [22], which is supported by the dissolution and segregation of carbon atoms.

Figure 4b shows the data on the thermal treatment of a submonolayer film consisting of C_{60} molecules (~0.5 ML). One can see that the character of the processes is generally the same. The low-temperature region of thermal stability of the adsorption layer can be distinguished. This region is alternated by a region where the cages of fullerene molecules decompose, while the released atoms dissolve in the substrate bulk. It follows from the reasoning above that no region of thermal desorption is observed in the case of the submonolayer film. All adsorbed molecules reside on the surface up to 1100 K, when their active fragmentation sets in. The final state of the adsorption layer is the surface carbide with a concentration lower than that of WC. It seems likely that the total amount of carbon that enters the substrate during the thermal treatment of half the fullerene monolayer is insufficient to provide its thermal stability, since the carbon atoms are distributed between the tungsten bulk and the surface [23]. The estimation shows that the composition of the obtained surface carbide is close to W_2C relative to surface metal atoms at the (100) facet.

5. THE STRUCTURE OF THE ADSORPTION LAYER AT 700–900 K

Let us again discuss the structure of the adsorption layer after thermal desorption of fullerenes in more detail. For all previously studied substrates (Mo, Re, Ir, Si, and SiC), all C_{60} molecules desorbed, excluding those in direct contact with the metal surface. These molecules remained in the adsorption layer and were transformed and then atomized on further heating. However, in the case of the (100)W surface, it turns out that the amount of fullerenes that remained on the surface after desorption is much larger than in the first layer. The corresponding estimate based on the degree of screening of tungsten indicates that $\sim 2 \times 10^{14}$ mol/cm^2 (~1.5 ML) remained on the surface in our experiment. Moreover, it turns out that this quantity is not constant. It varies from one experiment to another in the range $(2–3.5) \times 10^{14}$ mol/cm^2 (1.5–2.5 ML) and depends on the history of the sample, the amount of initially deposited molecules, the duration of intermediate thermal treatment, and so on.

It seems likely that a complex combination of processes occurs during heating of the fullerite film on tungsten to 700–750 K. The C_{60} molecules from the first layer, which have already formed strong chemisorption bonds with the substrate, undergo further transformation; as a result, a fraction of carbon bonds becomes dangling. These bonds are partially saturated due to the C_{60} molecules from the second and even the third layers. Thus, during heating, these molecules can either have time to leave the substrate due to thermally activated desorption or to form strong bonds with the fragments of molecules from the first layer, and later

from subsequent layers. These molecules thus lose their fullerene nature. On subsequent heating, such molecules already cannot desorb. They remain in the adsorption layer and decompose into carbon clusters. As the temperature increases, they can also decompose into atoms.

It is interesting to compare the results described above with a direct deposition of C_{60} molecules onto a heated tungsten substrate. These data are shown in Fig. 5. One can see that the Auger signal of carbon, which corresponds to the accumulation of adsorbate in the first monolayer, grows linearly at the first stage. After t = 14 min of deposition, this growth levels off. A decrease in the Auger signal of tungsten ceases simultaneously; during the further heating, both Auger signals remain constant. Note that the total amount of C_{60} molecules that are incident on the surface to this instant coincides with the amount necessary for the formation of the first monolayer at 300 K (Fig. 1). The shape of the Auger line of carbon corresponds to spectrum *3* in Fig. 2 and is close to that of the fullerene line. However, there is a shift in energy by ~1 eV. On attaining the plateau, the Auger signal of tungsten turns out to be reduced by a factor of ~2.9. Thus, the concentration of fullerenes corresponds to a monolayer similar to that formed by deposition at room temperature. The intensity of the Auger signal of carbon also coincides with that of the signal from the monolayer formed at lower temperatures.

It is interesting that deposited fullerenes do not accumulate on the surface on top of the already formed monolayer, although they remain on the surface of a thick film during its thermal treatment in a noticeably higher concentration (see previous section). It seems likely that a single C_{60} molecule that is incident on the surface cannot form strong chemisorption C–C bonds with carbon cages of fullerenes in the first layer. Accordingly, this molecule does not transform; it retains its structure and "prefers" to escape; i.e., the probability of desorption of such molecules is 100%.

The thermal treatment of the formed coating up to 950 K does not lead to any variations in the intensity or shape of the Auger lines. At higher temperatures, the Auger line of carbon becomes more similar to that of carbide and decreases in amplitude, whereas the Auger signal of tungsten increases. At $T > 1400$ K, both Auger signals are stabilized at amplitudes characteristic of the surface tungsten carbide. It seems likely that the processes in the adsorption layer are the same as those in the thick film. Carbon cages of fullerene molecules are gradually destroyed, and the C atoms formed actively diffuse into the substrate bulk.

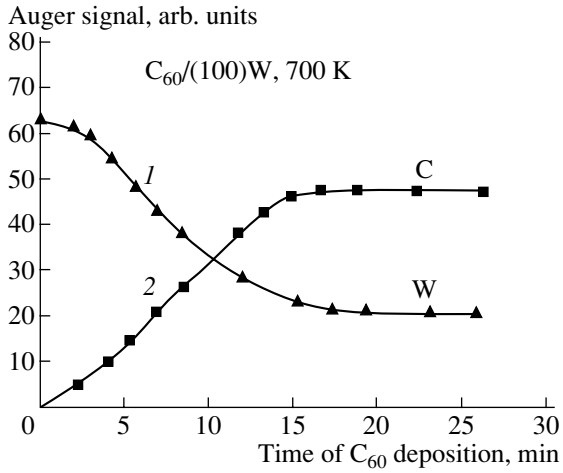

Fig. 5. Deposition of C_{60} molecules onto the (100)W surface at 700 K. The flux density $\nu_{C_{60}} = 1.5 \times 10^{11}$ mol/(cm^2 s); (*1*) Auger signal of tungsten and (*2*) Auger signal of carbon.

6. THE USE OF OXYGEN TO PROBE THE STRUCTURE OF THE ADSORPTION LAYER OF FULLERENES

We previously showed [23] that keeping fullerite films on a (100)Mo surface in oxygen leads to the adsorption of oxygen only in the regions of the metal substrate free of fullerenes rather than on the surface of the adsorbed C_{60} molecules themselves. In principle, this circumstance permits us to use the adsorption of oxygen as a probe to indicate the part of the metal surface free of adsorbed fullerenes in absolute units.

We carried out a series of special experiments with adsorption of oxygen on a fullerene-coated tungsten surface. On a pure (100)W substrate or on tungsten with a surface carbide, oxygen adsorbs in a dissociative form of O atoms up to a concentration of $N_O^{ML} = 9 \times 10^{14}$ cm^{-2} [24, 25]. No adsorption of oxygen is observed on a film consisting of C_{60} molecules three or more monolayers thick.

Figure 6a shows the largest amount of oxygen that can adsorb on the surface against the degree of its coverage with C_{60} molecules $\theta_{C_{60}}$. The degree of coverage $\theta_{C_{60}}$ was determined from the time of adsorption of the C_{60} molecules on the (100)W surface at room temperature using the data shown in Fig. 1. The inflection of the curve at t = 650 s was considered as corresponding to $\theta_{C_{60}} = 1$. This point corresponds to the surface concentration of adsorbed fullerenes $N_{C_{60}} \approx 1.5 \times 10^{14}$ cm^{-2}.

One can see that the amount of adsorbed fullerenes decreases linearly as the amount of fullerenes deposited on the surface decreases. For example, about 65% of the sample surface remains accessible for the adsorp-

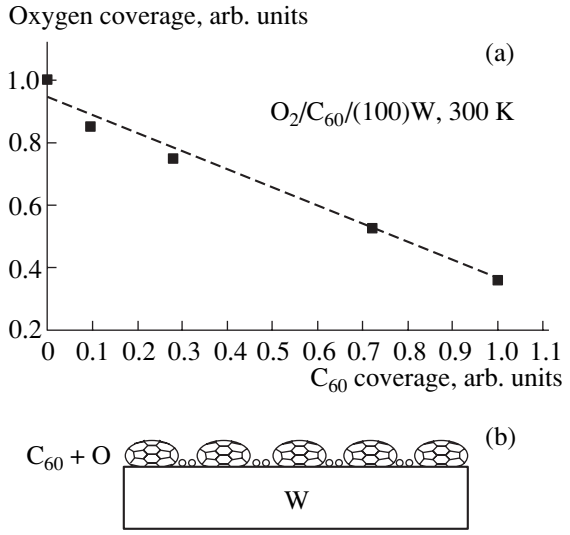

Fig. 6. Adsorption of oxygen on the (100)W surface covered with a fullerite film. (a) Variation in the largest amount of oxygen capable of being adsorbed on the surface depending on the degree of its coverage with fullerenes; $\theta_O = 1$ corresponds to $N_O = 9 \times 10^{14}$ cm^{-2} and $\theta_{C_{60}} = 1$ corresponds to $N_{C_{60}} \approx 1.5 \times 10^{14}$ cm^{-2}. (b) Schematic diagram of the process of accumulation of oxygen on a surface covered with a layer of C_{60} molecules.

tion of oxygen at $\theta_{C_{60}} = 0.5$. A schematic diagram of the assumed processes is shown in Fig. 6b. Let us estimate the part of the surface that remains accessible for the adsorption of O_2 molecules at $\theta_{C_{60}} = 0.5$ from structural considerations. The structural-chemical diameter of a C_{60} molecule $d = 8.4$ Å [1], and, accordingly, the area occupied by a single molecule $s = 55$ Å^2. Disregarding in the first approximation the variation in the shape of the C_{60} molecule during adsorption ("deflated ball," see Section 3), we can easily find that the surface occupied by a half-monolayer of the molecules arranged on 1 cm^2 is ~0.4 cm^2. Thus, the sample surface remains about 60% free, which agrees well with the experimental value of 65% given above.

It should be noted that still about 30% of the surface remains accessible for the adsorption of oxygen for the monolayer coating of the surface with C_{60} molecules ($\theta_{C_{60}} = 1$). As the second layer grows, the part of the surface accessible for the adsorption of oxygen becomes progressively smaller. When this layer is filled completely, this part is no larger than 5%, most likely due to the growth defects.

7. DISCUSSION

Let us compare the results obtained for tungsten with the dependences of interaction of fullerenes with other metal substrates. The most significant and interesting differences are in the fact that the molecules from the second and even subsequent layers rather than from the first layer remain on the surface during thermal desorption of fullerenes. In our opinion, this is associated with the destruction of the fullerene structure of the molecules arranged in the adsorption layer. Initially, we observe the destruction of the molecules from the first layer, which form strong chemisorption C–W bonds. Then we also observe the destruction of the molecules of subsequent layers, which form C–C bonds with carbon cages of underlying molecules. No similar induced decomposition of adsorbed molecules was observed in other adsorptive systems. Of all the studied substrates (namely, Ir, Re, Si, SiC, and Mo) tungsten is most active catalytically [26], which apparently accounts for the differences observed.

8. CONCLUSIONS

We studied the special features of interaction between C_{60} molecules and the (100)W surface in detail. We showed that the deposition of fullerites at room temperature lead to layer-by-layer growth of the fullerite film. The layer immediately adjoining the surface consists of strongly transformed molecules with changed electron and, possibly, chemical structures. Deposition at 700–900 K leads to the growth of a monolayer coating only, and all newly arriving molecules do not adsorb. Heating a multilayer film leads to thermal desorption of some of the C_{60} molecules. However, a large amount (more than 2 ML) of these molecules, which are transformed and are not capable of thermal desorption, remain on the surface. This effect, specifically, the induced transformation of molecules from the second and subsequent adsorption layers, is apparently observed for the first time. One would expect such a phenomenon to be typical of the interaction of fullerenes with chemically and catalytically active substrates, for example, niobium or zirconium.

ACKNOWLEDGMENTS

This study was supported by the "Controlled Synthesis of Fullerenes" program, project 8C78, and the "Low-Dimensional Quantum Structures" program, project 9G19.

REFERENCES

1. C. Gripon, L. Legrand, I. Rosenman, and F. Boue, Fullerene Sci. Technol. **4**, 1195 (1996).
2. Xu Hang, D. M. Chen, and W. N. Creager, Phys. Rev. Lett. **70**, 1948 (1993).
3. Y. Z. Li, M. Chander, J. C. Partin, and J. H. Weaver, Phys. Rev. B **45**, 13837 (1992).
4. T. Sato, T. Sueyoshi, and M. Iwatsuku, Surf. Sci. Lett. **321**, L137 (1994).
5. D. Chen and D. Sarid, Surf. Sci. **318**, 74 (1994).

6. P. H. Beton, A. W. Dunn, and P. Moriarty, Surf. Sci. **361/362**, 878 (1996).
7. N. R. Gall', E. V. Rut'kov, and A. Ya. Tontegode, Fiz. Tekh. Poluprovodn. (St. Petersburg) **36**, 1084 (2002) [Semiconductors **36**, 1008 (2002)].
8. T. Hashizume, K. Motai, X. D. Wang, *et al.*, J. Vac. Sci. Technol. A **12**, 2097 (1994).
9. T. Chen, S. Howelles, M. Gallager, *et al.*, J. Vac. Sci. Technol. B **9**, 2461 (1991).
10. D. K. Kin, Y. D. Suh, K. H. Park, *et al.*, J. Vac. Sci. Technol. A **11**, 1675 (1993).
11. E. V. Rut'kov, A. Ya. Tontegode, and Yu. S. Grushko, Pis'ma Zh. Éksp. Teor. Fiz. **57**, 712 (1993) [JETP Lett. **57**, 724 (1993)].
12. E. V. Rut'kov, A. Ya. Tontegode, and M. M. Usufov, Phys. Rev. Lett. **74**, 758 (1995).
13. G. K. Wertheim, Solid State Commun. **88**, 97 (1993).
14. N. R. Gall, E. V. Rut'kov, A. Ya. Tontegode, and M. M. Usufov, Mol. Mater. **7**, 187 (1996).
15. N. R. Gall', E. V. Rut'kov, A. Ya. Tontegode, and M. M. Usufov, Zh. Tekh. Fiz. **69** (11), 117 (1999) [Tech. Phys. **44**, 1371 (1999)].
16. N. R. Gall, E. V. Rut'kov, and A. Ya. Tontegode, Fullerene Sci. Technol. **9** (2), 111 (2001).
17. N. R. Gall', E. V. Rut'kov, and A. Ya. Tontegode, Pis'ma Zh. Tekh. Fiz. **28** (4), 1 (2002) [Tech. Phys. Lett. **28**, 126 (2002)].
18. N. R. Gall, S. N. Mikhailov, E. V. Rut'kov, and A. Ya. Tontegode, Surf. Sci. **191**, 185 (1987).
19. *Electron and Ion Spectroscopy of Solids*, Ed. by L. Fiermans, J. Vennik, and W. Dekeyser (Plenum, New York, 1978; Mir, Moscow, 1981).
20. M. L. Tarug and G. K. Wehner, J. Appl. Phys. **44**, 1534 (1973).
21. N. D. Potekhina, N. R. Gall', E. V. Rut'kov, and A. Ya. Tontegode, Fiz. Tverd. Tela (St. Petersburg) **45**, 742 (2003) [Phys. Solid State **45**, 782 (2003)].
22. N. R. Gall', E. V. Rut'kov, and A. Ya. Tontegode, Ross. Khim. Zh. **47** (2), 13 (2003).
23. N. R. Gall, E. V. Rut'kov, A. Ya. Tontegode, and M. M. Usufov, Fullerene Sci. Technol. **6**, 721 (1998).
24. N. P. Vas'co, Yu. G. Ptushinskii, and B. A. Chuikov, Surf. Sci. **14**, 448 (1969).
25. N. R. Gall', E. V. Rut'kov, A. Ya. Tontegode, and G. V. Plekhotkina, Poverkhnost, No. 10, 22 (2000).
26. G. K. Boreskov, *Heterogeneous Catalysis* (Nauka, Moscow, 1986; Nova Sci., Hauppauge, N.Y., 2003).

Translated by N. Korovin

Semiconductors, Vol. 38, No. 9, 2004, pp. 1030–1035. Translated from Fizika i Tekhnika Poluprovodnikov, Vol. 38, No. 9, 2004, pp. 1068–1073.

SEMICONDUCTOR STRUCTURES, INTERFACES, AND SURFACES

Radiative Recombination in a Silicon MOS Tunnel Structure

N. Asli*, M. I. Vexler, I. V. Grekhov**, P. Seegebrecht*, S. E. Tyaginov**, and A. F. Shulekin**^**

** Technische Fakultät der Christian-Albrechts-Universität zu Kiel, D-24143 Kiel, Germany*

*** Ioffe Physicotechnical Institute, Russian Academy of Sciences, St. Petersburg, 194021 Russia*

^ e-mail: shulekin@pop.ioffe.rssi.ru

Submitted January 30, 2004; accepted for publication February 2, 2004

Abstract—Recombination luminescence spectra of tunnel Al/SiO_2/*p*-Si MOS structures have been studied experimentally. A mathematical reconstruction of these spectra taking into account the loss by photon reabsorption is carried out. For the first time, the experimental data are presented in absolute units (W eV^{-1}). A relationship is shown between the shape of the spectrum and the energy of injected electrons, which is defined by the applied voltage. The rate of energy loss by photon emission has been estimated. The effect of the oxide degradation on the luminescence characteristics of MOS structures is considered. © *2004 MAIK "Nauka/Interperiodica".*

1. INTRODUCTION

By MOS tunnel structure is understood a metal–oxide–semiconductor structure in which charge can be transferred across the structure via direct tunneling [1]. In recent years, these structures became one of the most important objects of study in applied semiconductor physics [2], since it became obvious [3, 4] that tunnel-thin (1–3 nm) SiO_2 can be used as a gate insulator in field-effect transistors.

It has been shown [5, 6] that, under certain conditions, a MOS diode emits light when current flows across it, although the light intensity is low. Evidently, an analysis of spectra can provide very useful information on the behavior of hot carriers in this interesting and commercially important structure. However, until now only electrical properties of MOS tunnel structures have been studied, and their luminescent properties remained nearly untouched. Therefore, the goal of this study was to investigate the luminescence of a MOS tunnel structure, which is still a relatively little known aspect of its operation.

Earlier, we reported some luminescence spectra of MOS structures [5, 7, 8]. In this study, we offer new experimental data, and for the first time it became possible to present the spectra in absolute units and to reconstruct the net photon emission spectrum. Separate sections discuss the modification of optical characteristics in SiO_2 degradation and the determination of the rate of energy loss by photon emission. Interest in the recombination component of the luminescence is due to the fact that this component is responsible for most of the spectral range of MOS structure emission accessible to experimental study.

2. RECOMBINATION LUMINESCENCE SPECTRA OF Al/SiO_2/*p*-Si STRUCTURES

When the positive bias V is applied to the substrate of a MOS tunnel structure, monoenergetic hot electrons are injected into silicon [9]. For the case of Al/SiO_2/*p*-Si structures, which operate in the accumulation mode at $V > 0$, we can introduce the characteristic energy of electrons, E, as the energy difference between the Fermi level in metal, E_{Fm}, and the edge of the conduction band in the quasi-neutral region of Si (Fig. 1b). Electrons pass the region of the near-surface band bending ballistically [9]. The relation between E and V is simple; specifically, $E \approx qV - E_g$ when the substrate is doped quite heavily.

Since the electron energy is defined by the applied voltage, and not by the oxide thickness d_{ox}, the latter can be chosen for reasons of experimental convenience. Thus, samples with relatively thick SiO_2 layer, which allow the application of higher V (at lower currents), are more convenient for studies with higher E, and samples with a thin oxide layer should be used at low E.

One of the mechanisms of energy relaxation is by radiative electron transitions, which are usually preceded by the emission of a certain number of phonons with phonon energy $\hbar\omega_0 = 0.063$ eV [7]. Accordingly, the energy of an electron immediately before photon emission lies in the range between E and kT. The emission of photons can occur via intraband [10] or recombination electron transitions, and the recombination emission is characterized by the shortest wavelength. The energy of "recombination" photons $\hbar\omega_{RR}$ lies approximately between E_g and $E + E_g$, taking into account the fact that holes in the valence band exist only near the band maximum.

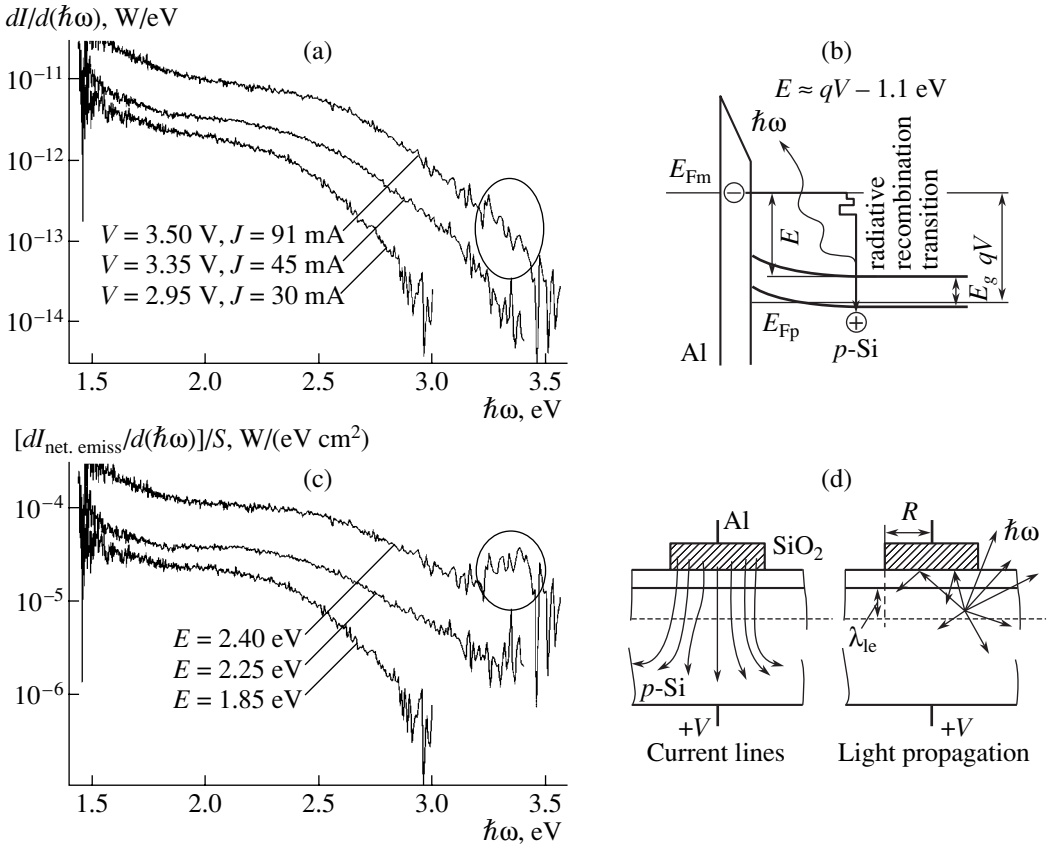

Fig. 1. (a) Experimental electroluminescence spectra of Al/SiO_2/*p*-Si MOS structures with a tunnel-thin insulator. $N_A = 2 \times 10^{18}$ cm^{-3}, $T = 300$ K. The data are presented in absolute units. (b) The band diagram. (c) Spectra reconstructed taking into account reabsorption of photons. (d) Configuration of the device ($R = 200$ μm). We assumed that $\lambda_{le} = 10$ nm and that no current spreading occurs at this depth.

Figure 1a shows the observed luminescence spectra of Al/SiO_2/*p*-Si structures ($N_A = 2 \times 10^{18}$ cm^{-3}) in units of W eV^{-1}. As follows from these data, the measured intensity of light from the structures under study (Fig. 1b) is nearly 11 orders of magnitude lower than the power *VJ* introduced into the sample; i.e., the emission is very weak. Note, however, that these spectra were recorded in a specific, though frequently used, device configuration, which allows the detection of light emitted only by regions localized near the border of a circular metal electrode.

Figure 1a clearly demonstrates the existence of the blue "recombination" edge in all the spectra. Its position corresponds to $E + E_g$. In the left part of the figure, the intensity increases owing to the contribution of thermalized electrons (this range is not related to the injection energy). At $E > 2.3$ eV, a certain feature is observed at about $\hbar\omega \approx 3.4$ eV (encircled in Fig. 1a) that is attributed to direct recombination transition at the Γ point of the Brillouin zone. Note that this feature was considerably more pronounced in the structures studied earlier [8].

Basing on the recorded spectra, we mathematically reconstructed (see Appendix I) the net photon emission spectra taking into account photon reabsorption (Fig. 1c). It was assumed that the "current lines" are concentrated within a cylinder with the electrode in its base, and a significant spreading occurs only in the Si bulk at distances exceeding the depth from which emitted photons emerge. Indeed, tunneling is a very strong factor that orientates electrons, and electrons pass across the region of high electric field ballistically [9].

As can be seen in Fig. 1c, the net emission spectra differ from the measured spectra. The deformation is due to the frequency dependence of the Si absorption coefficient [11]. The spectral feature related to direct recombination emission of a MOS tunnel structure becomes clearly evident after the reconstruction.

3. RELATIONSHIP BETWEEN DEGRADATION AND LUMINESCENCE

Unlike the thoroughly studied impact of oxide degradation on the electrical characteristics of devices [2, 12], little is known about changes in the luminescence of thin MOS structures during an overload. Below, we discuss the new data we obtained.

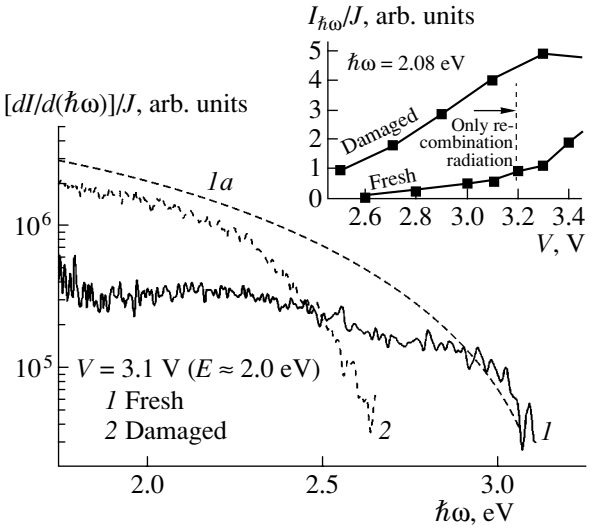

Fig. 2. Quenching of the blue edge of recombination emission upon damage of SiO_2. (*1*, *2*) recorded spectra; (*1a*) the spectrum at the initial stage of degradation (schematic). Inset: typical dependence of intensity at the given wavelength: (lower curve) before damage and (upper curve) after damage.

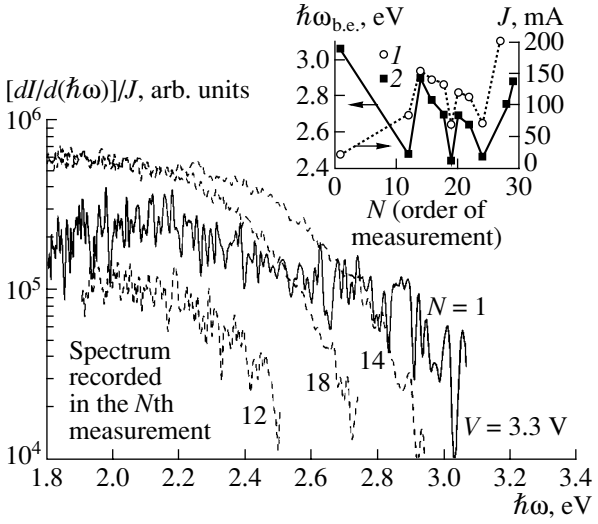

Fig. 3. Example of the observed restoration of the blue edge in the course of degradation. Inset: (*1*) evolution of current J and (*2*) position of the spectral edge $\hbar\omega_{b.e.}$ in the course of measurements. $\hbar\omega_{b.e.} = \hbar\omega$ at $[dI/d(\hbar\omega)]/J = 3 \times 10^4$.

Figure 2 shows luminescence spectra of a MOS tunnel structure recorded at different stages of its degradation. As a rule, "fresh" structures demonstrated a virtually flat (on a logarithmic scale) spectrum and relatively low luminescence intensity (curve *1*). If the bias and the duration of its application are large enough, both the intensity $dI/d(\hbar\omega)$ and current J across the structure increase with time. In this case, the luminescence intensity increased more rapidly (the ratio $[dI/d(\hbar\omega)]/J$ increases), especially in the relatively long-wavelength range. The spectral position of the blue edge (shown schematically by line *1a* in Fig. 2) was retained, because the voltage V and, hence, the energy of injected electrons remained unchanged.

Further degradation of the structure as a result of prolonged current flow or the application of stresses[1] resulted in a shift of the blue edge of radiative recombination to lower $\hbar\omega$ (Fig. 2, curve *2*). This effect was followed by a gradual decrease in intensity $[dI/d(\hbar\omega)]/J$ and current J across the device, compared to values reached at the stage 1 $\longrightarrow$ 1*a*. It seems that the shift of the edge is caused by the loss of energy by tunneling electrons in their interaction with defects. As can be seen, after stress the luminescence in a specific spectral range completely disappears (1*a* $\longrightarrow$ 2). We believe that the shift of the spectral edge can be attributed to a gradual accumulation of defects in the oxide and at the interfaces.

The decrease in current J at the final stages of degradation is not surprising: at high bias, the resistance of shunts formed in degradation may well exceed the tunneling resistance [13].

An increase in the luminescence "efficiency" $[dI/d(\hbar\omega)]/J$ (or $I_{\hbar\omega}/J$ if the measurements are done at a fixed photon energy; see Fig. 2, inset), which is observed in the course of degradation, may occur for two reasons. First, degradation gives rise to shallow centers in the Si band gap, which significantly raises the probability of transitions with the emission of relatively low-energy photons. Furthermore, the current density and, consequently, the "pace" of degradation on the periphery of the electrode are higher than in the inner regions. Therefore, the current density on the periphery (i.e., in the region from which the emission recorded in the experiment is collected) increases to a greater extent than that averaged over the whole structure.

The evolution of the luminescence characteristics (Fig. 2) is typical, at the qualitative level, for any type of stress. However, short but "hard" (~5 V) overloads sometimes caused not only the gradual red shift of the blue edge described above; in some cases, the edge almost completely returned to its initial position (Fig. 3 and inset). This shift to lower energies and back could occur several times in the same sample. The figure shows some selected spectra recorded before the Nth application of stress, including the spectrum of a "fresh" structure (N = 1), and those before the 12th, 14th, and 18th stresses. The inset shows the position of the blue edge for $\hbar\omega_{b.e.}$ for a large number of records. The stress described above was applied to the sample prior to each recording, but the edge was recovered in only a few cases (records 14, 20, and 25). After the restoration of the edge, a "standard" degradation was observed, with the shift of the blue edge and usually a decrease in current (Fig. 3, inset).

[1] A structure was stressed by applying a 4 to 5-V bias for 1–2 s.

The nature of the observed effect is not quite clear. It may be related to specific features of the breakdown in the structures under study, in which the damaged regions are excluded from the current transfer and replaced with others. At the same time, we can also make the trivial assumption that at some stresses Al "burned out" along the perimeter, and the next spectrum was recorded from regions that were not on the periphery during the preceding measurements. It remains unclear, however, why this burning-out occurred only in three out of approximately 30 similar stresses (Fig. 3).

4. ESTIMATION OF THE RATE OF PHOTON EMISSION IN SI BASED ON THE RECORDED LUMINESCENCE SPECTRA OF MOS STRUCTURES

The luminescence of Al/SiO_2/*p*-Si diodes can be used for a quantitative analysis of the radiative processes in Si.

The relaxation of hot electrons is characterized by the rate of energy loss via different mechanisms. For example, the rates of phonon emission $\tau_{ph}^{-1}(E)$, impact ionization $\tau_{ii}^{-1}(E)$, and photon emission $\tau_{le}^{-1}(E)$ can be introduced. They are the sums of probabilities of electron transitions in unit time, which are accompanied by the generation of a phonon, an electron–hole pair, or a photon, respectively, averaged over all the possible initial states of an electron of energy E. Since not only the very fact of emission of a photon but also its energy $\hbar\omega$ are important in analyzing optical transitions, we must introduce the quantity $d\tau_{le}^{-1}/d(\hbar\omega) = f(E, \hbar\omega)$, which has the meaning of the rate of energy loss by photon emission in the given spectral range from $\hbar\omega$ to $\hbar\omega + \delta\hbar\omega$.

A method for determining the photon emission rate $d\tau_{le}^{-1}/d(\hbar\omega) = f(E, \hbar\omega)$ was proposed in our earlier study [14] (see also Appendix II). It is based on the mathematical processing of the reconstructed luminescence spectra of a MOS tunnel structure in absolute units (W eV^{-1}). The approbation of the method has now become possible owing to (i) better reproducibility of the data obtained with different samples, (ii) calibration of the experimental setup, and (iii) mathematical consideration of the reabsorption of photons.

Figure 4 shows an example of the results obtained. The range of combinations of electron (E) and photon ($\hbar\omega$) energies corresponds to radiative recombination. As one might expect, the photon emission is much less probable than scattering on phonons. The values of $\tau_{ph}^{-1}(E)$ are in the range 10^{13}–10^{14} s^{-1} [15], whereas the estimates for $\tau_{le}^{-1}(E)$ give ~10^6 s^{-1} ($\tau_{le}^{-1} \approx [d\tau_{le}^{-1}/d(\hbar\omega)]\Delta\hbar\omega$, where $\Delta\hbar\omega \approx 2$ eV is the range under study). At $E < \hbar\omega - E_g$,

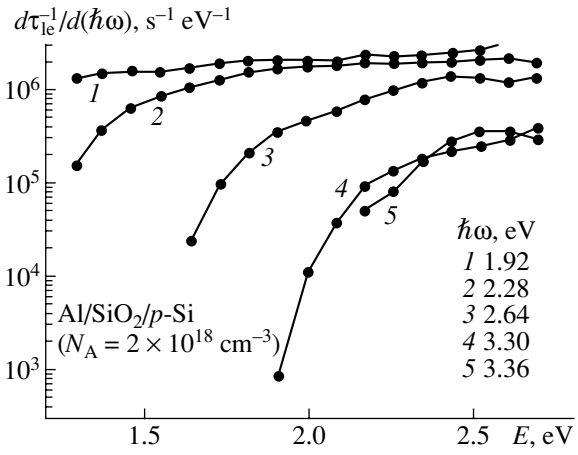

Fig. 4. Rate of energy loss by photon emission; calculated from the measured luminescence spectra of MOS tunnel structures by the method proposed in [14].

the rate of loss $d\tau_{le}^{-1}/d(\hbar\omega) = f(E, \hbar\omega)$ becomes zero, because for a given E the energy of the emitted photons is limited by the value $E + E_g$.

The notion of "quantum yield" P_{le} (the number of photons emitted per hot electron) is not always adequate as applied to photon emission (unlike, for example, the case of impact ionization), because it does not reflect the spectral composition of light. Nevertheless, this quantity can be roughly estimated as $(\tau_{le}^{-1}/\tau_{ph}^{-1})(E/\hbar\omega_0)$, where the first and second factors describe the probability of an optical transition and the number of scattering events in the course of relaxation, respectively. Assuming $\tau_{le}^{-1} = 10^6$ s^{-1} and $\tau_{ph}^{-1} = 10^{13}$–10^{14} s^{-1}, we obtain $P_{le} \approx 10^{-6}$. This value is comparable with those reported in the literature for Si (e.g., ~10^{-5} for prebreakdown luminescence [16]), although one should emphasize that P_{le} fundamentally depends on the parameters of a specific device.

5. CONCLUSION

We present for the first time experimentally obtained luminescence spectra of Si MOS tunnel structures in absolute units, as well as after reconstruction taking the reabsorption loss into account. All the spectra demonstrate a pronounced blue recombination edge, whose position is defined by the energy of injected electrons. The direct radiative recombination transition with $\hbar\omega = 3.4$ eV was reliably recorded. The rate of energy loss by emission was estimated using the reconstructed spectra; it was ~10^6 s^{-1}, which was seven to eight orders of magnitude less than the phonon emission rate. The relationship between the degradation of structures and the modification of luminescence characteristics was considered. It was shown that the application of electric stress to a structure results in the

quenching of the blue part of the spectrum (edge shift), which is related to energy loss in the transport of electrons across the damaged oxide. In some cases, the initial spectral shape was virtually restored, with a subsequent repeated quenching of the edge.

ACKNOWLEDGMENTS

This study was supported by the "Physics of Solid-State Nanostructures" program, a grant from the Russian president for the Support of Leading Scientific Schools (grant no. NSh-758.2003.2), the Russian Science Welfare Social Fund, and the Soros International Science Foundation.

Appendix I

RECONSTRUCTION OF THE EMISSION SPECTRUM

In the device configuration under study (Fig. 1d), each point in Si within a circular semi-infinite cylinder with an electrode in its base is regarded as an isotropic source of photons. The distribution of the intensity density along the depth z is given by

$$f(z) = \frac{1}{\lambda_{le}}\exp\left(-\frac{z}{\lambda_{le}}\right), \quad \text{(A.I.1)}$$

where the parameter λ_{le} is chosen on the order of the electron free path (10 nm) [17].

The portion of the intensity of light that reaches the front surface of the sample can be found as

$$\nu = \frac{1}{\pi R^2}\int_0^R 2\pi r\,dr\int_0^{+\infty} f(z)\,dz \times\left(\frac{1}{4\pi}\int_0^{2\pi} d\varphi\int_{\theta_{min}}^{\pi/2}\sin\theta\exp\left(-\frac{\kappa(\hbar\omega)z}{\cos\theta}\right)d\theta\right), \quad \text{(A.I.2)}$$

where

$$x = -r\cos\varphi + \sqrt{R^2 - r^2\sin^2\varphi}, \quad \text{(A.I.3)}$$

$$\theta_{min} = \arccos[z(x^2+z^2)^{-1/2}], \quad \text{(A.I.4)}$$

and κ is the absorption coefficient of Si [11]. The origin of this expression can be easily understood if it is kept in mind that φ is the angle reckoned from the straight line that connects the projection of the point source (r, z) onto the electrode surface with the center of the electrode; the vertex of the angle lies at this projection point.

With the calculated $\nu(\hbar\omega)$ dependence, we can reconstruct the net emission spectrum:

$$\frac{dI_{net.emiss}}{d(\hbar\omega)} = \frac{dI}{d(\hbar\omega)}\nu^{-1}(\hbar\omega). \quad \text{(A.I.5)}$$

Due to the strong dependence of the absorption coefficient κ on $\hbar\omega$, this spectrum differs appreciably from the measured spectrum. If we are interested in the "specific" intensity, the result must be additionally divided by the area of the electrode, πR^2:

$$\frac{dI_{net.emiss}}{d(\hbar\omega)S} = \frac{1}{\pi R^2}\frac{dI_{net.emiss}}{d(\hbar\omega)}. \quad \text{(A.I.6)}$$

These spectra (expressed in W eV^{-1} cm^{-2}) are shown in Fig. 1c.

Appendix II

CALCULATION OF THE PHOTON EMISSION RATE

As follows from a simple model of luminescence in a MOS tunnel structure [7], the net photon emission spectrum proper has the form

$$\frac{dI_{net.emiss}(E,\hbar\omega)}{d(\hbar\omega)} = \frac{J}{q}\frac{\hbar\omega}{\hbar\omega_0}\int_0^E\frac{1}{\tau_{ph}^{-1}(\tilde{E})}\frac{d}{d(\hbar\omega)}\tau_{le}^{-1}(\tilde{E},\hbar\omega)d\tilde{E}, \quad \text{(A.II.1)}$$

where J is the current and $\hbar\omega_0 = 0.063$ eV. If the reconstructed experimental spectra (A.I.5) are measured with small enough increments in the electron energy E, the relation (A.II.1) can be applied to process the data in order to determine $d\tau_{le}^{-1}(E,\hbar\omega)/d(\hbar\omega)$.

After the transposition of preintegral factors to the left-hand side and differentiation with respect to the electron energy E, we obtain

$$\frac{d\tau_{le}^{-1}(E,\hbar\omega)}{d(\hbar\omega)} = \tau_{ph}^{-1}(E)\left(\frac{q\hbar\omega_0}{\hbar\omega}\right)\frac{\partial}{\partial E}\left(J^{-1}(E)\frac{dI_{net.emiss}(E,\hbar\omega)}{d(\hbar\omega)}\right). \quad \text{(A.II.2)}$$

The rate of the phonon emission $\tau_{ph}^{-1}(E)$ can be taken, for example, from [15].

The obtained rates $d\tau_{le}^{-1}(E,\hbar\omega)/d(\hbar\omega)$ depend on the doping level, because it defines the density of states in the valence band that are accessible to electron transitions. Therefore, a correction factor with the Fermi functions must be introduced:

$$\left.\frac{d\tau_{le}^{-1}(E,\hbar\omega)}{d(\hbar\omega)}\right|_{new} \approx \left.\frac{1-f_{new}(E-\hbar\omega)}{1-f_{meas}(E-\hbar\omega)}\frac{d\tau_{le}^{-1}(E,\hbar\omega)}{d(\hbar\omega)}\right|_{meas}, \quad \text{(A.II.3)}$$

where the quantities with subscripts "meas" and "new" correspond to the conditions of experiment and to the

doping level for which the obtained data will be used, respectively.

If necessary, the total rate of photon emission can be obtained by integration:

$$\tau_{le}^{-1}(E) = \int \frac{d\tau_{le}^{-1}(E, \hbar\omega)}{d(\hbar\omega)} d(\hbar\omega). \qquad \text{(A.II.4)}$$

More details concerning the data processing and the model that yields expression (A.II.1) can be found in [14].

REFERENCES

1. *Direct Tunneling*, http://semiconductorglossary.com/.
2. F. Monsieur, in *Abstract Book of INFOS'03* (Barselona, Spain, 2003), IT-1.
3. H. S. Momose, M. Ono, T. Yoshitomi, *et al.*, IEEE Trans. Electron Devices **43**, 1233 (1996).
4. H. S. Momose, S. Nakamura, T. Ohguro, *et al.*, IEEE Trans. Electron Devices **45**, 691 (1998).
5. M. I. Veksler, I. V. Grekhov, S. A. Solov'ev, *et al.*, Pis'ma Zh. Tekh. Fiz. **21** (13), 81 (1995) [Tech. Phys. Lett. **21**, 530 (1995)].
6. E. Cartier, J. C. Tsang, M. V. Fischetti, and D. A. Buchanan, Microelectron. Eng. **36**, 103 (1997).
7. N. Asli, M. I. Vexler, A. F. Shulekin, and P. Seegebrecht, Semicond. Sci. Technol. **18**, 147 (2003).
8. N. Asli, M. I. Vexler, A. F. Shulekin, *et al.*, Microelectron. Reliab. **41**, 1071 (2001).
9. I. V. Grekhov, E. V. Ostroumova, A. A. Rogachev, and A. F. Shulekin, Pis'ma Zh. Tekh. Fiz. **17** (13), 44 (1991) [Sov. Tech. Phys. Lett. **17**, 476 (1991)].
10. J. Bude, N. Sano, and A. Yoshii, Phys. Rev. B **45**, 5848 (1992).
11. D. F. Edwards, in *Handbook of Optical Constants of Solids*, Ed. by E. D. Palik (Academic, New York, 1985), p. 547.
12. K. R. Farmer, M. O. Andersson, and O. Engström, Appl. Phys. Lett. **58**, 2666 (1991).
13. A. F. Shulekin, S. É. Tyaginov, R. Khlil, *et al.*, Fiz. Tekh. Poluprovodn. (St. Petersburg) **38**, 753 (2004) [Semiconductors **38**, 724 (2004)].
14. N. Asli, S. V. Gastev, I. V. Grekhov, *et al.*, Mater. Sci. Semicond. Process. **3**, 539 (2000).
15. Y. Wang and K. F. Brennan, J. Appl. Phys. **75**, 313 (1994).
16. *Electroluminescence Light Sources*, Ed. by I. K. Vereshchagin (Énergoatomizdat, Moscow, 1990) [in Russian].
17. S. Sze, *Physics of Semiconductor Devices*, 2nd ed. (Wiley, New York, 1981; Mir, Moscow, 1984), Vol. 1, Chap. 2.

Translated by D. Mashovets

Semiconductors, Vol. 38, No. 9, 2004, pp. 1036–1040. Translated from Fizika i Tekhnika Poluprovodnikov, Vol. 38, No. 9, 2004, pp. 1074–1078.

SEMICONDUCTOR STRUCTURES, INTERFACES, AND SURFACES

Potential Barrier Formation at a Metal–Semiconductor Contact Using Selective Removal of Atoms

B. A. Gurovich, B. A. Aronzon, V. V. Ryl'kov, E. D. Ol'shanskiĭ, E. A. Kuleshova, D. I. Dolgiĭ, D. Yu. Kovalev*, and V. I. Filippov

Russian Research Centre Kurchatov Institute, pl. Kurchatova 1, Moscow, 123182 Russia

**e-mail: kovalev@imp.kiae.ru*

Submitted February 3, 2004; accepted for publication February 11, 2004

Abstract—The possibility of forming a potential profile in a semiconductor by forming a metal film on its surface via selective removal of oxygen atoms from a deposited metal oxide layer was studied. Selective removal of atoms (SRA) was performed using a beam of accelerated protons with an energy of about 1 keV. Epitaxially grown GaAs films with a thickness of ~100 nm and an electron concentration of 2×10^{17} cm^{-3} were chosen as the semiconductor material, and W obtained from WO_3 was used as the metal. The potential profile appeared due to the formation of a Schottky barrier at the metal–semiconductor interface. It was found that the Schottky barrier formed at W/GaAs contacts made by the SRA method is noticeably higher (~1 eV) than the barrier formed at the contacts made by conventional metal deposition (0.8 eV for W/GaAs). The data presented indicate that there is no damaged layer in the gate region of the structures, which is most strongly affected by the proton irradiation. Specifically, it was shown that the electron mobility in this region equals the mobility in bulk GaAs with the same doping level. © *2004 MAIK "Nauka/Interperiodica".*

1. INTRODUCTION

The mainstream development of microtechnologies and nanotechnologies relies mainly on the improvement of optical lithography, which constitutes the basis of modern microtechnology. In fact, the transformation of microtechnology into nanotechnology through gradual advances in optical lithography is now envisaged [1].

However, in certain areas of technology where the drawbacks and limitations of optical lithography are most evident, its replacement with alternative, more efficient methods for manufacturing nanodevices is justified. This applies primarily to the case of fabricating multilayer nanodevices in which an alignment of elements located in different layers of the structure with accuracy better than 5–7 nm is required. This accuracy cannot be achieved by methods that use consecutive fabrication. It is desirable to introduce methods suitable for parallel fabrication of nanodevices, when all the layers are formed beforehand and elements of the structure with the required properties are created simultaneously in different layers using the same mask.

A new method for fabricating nanostructures that allows a transition from consecutive to parallel fabrication schemes in manufacturing multilayer nanodevices and, thus, provides a means for aligning elements in different layers of the structure with an accuracy as high as 1 nm was proposed in [2]. This method is based on the previously observed phenomenon of "selective removal of atoms" (SRA) from thin films under irradiation with particles accelerated to certain energies, which results in a major modification of the atomic composition of solids. Such a modification is accompanied by changes in the physical properties of the material and makes it possible to convert insulators into metals or semiconductors, nonmagnetic materials into magnetic ones, and optically transparent materials into opaque ones. It is also important that, using this effect, a pattern of a given design with nanometer-scale spatial resolution can be formed on the surface of a solid [2, 3].

In this paper we investigate the possibility of forming a potential relief in a semiconductor material with high charge-carrier mobility using the SRA method, with the aim of fabricating nanoscale electronic elements. The essence of this approach is as follows. It is known that a Schottky potential barrier can form at a metal–semiconductor contact; the height of the barrier, for example, in the case of GaAs, is 0.72–0.88 eV [4]. Consider a fairly thin (quasi-two-dimensional) semiconductor film coated with a patterned metal layer containing a gap. A potential well for electrons appears in the region of the semiconductor beneath the gap, forming a one-dimensional conductive channel whose configuration is determined by the design of the pattern in the metal layer. This method for fabricating nanostructures looks rather promising: technology for obtaining two-dimensional surface layers has now been well developed, and the method for creating a conductive pattern developed by us possesses high spatial resolution. At the same time, certain problems may arise in implementing this method, such as the possible effect of protons on the semiconductor material and its degradation, which leads to a decrease in the charge-carrier mobility. In addition, it was necessary to examine

1063-7826/04/3809-1036$26.00 © 2004 MAIK "Nauka/Interperiodica"

whether the Schottky barrier formed by the SRA technique is well controlled and sufficiently high (with the typical size-quantization scale of 10 nm, one needs a potential-profile amplitude of 1 eV). Thus, the main goals of this study were the following:

(a) to fabricate Schottky gate transistor structures based on metal–semiconductor contacts formed either by the SRA method or by the conventional method, where the gate is formed by evaporation of pure metal;

(b) to investigate the main characteristics of these structures, in particular, to determine the height of the Schottky barrier and the mobility of the charge carriers in the gate region, which is most affected by the proton radiation.

2. SAMPLES

Two types of transistor structures were fabricated on the basis of epitaxially grown GaAs with a donor concentration in the active region of $\sim 2 \times 10^{17}$ cm^{-3}. Tungsten was used as the gate material. In the structures of the first type, the metal was deposited by evaporation of pure W. Note that the height of the Schottky barrier at the contact of GaAs with evaporated W is well known and equals 0.8 eV [4]. In the second case, tungsten oxide was deposited in the gate area and was subsequently deoxidized into pure W by selective removal of oxygen atoms. It was established in the preliminary experiments that irradiation of WO_3 with low-energy protons (~1 keV) results in the formation of a W film whose conductivity is typical of quasi-amorphous (ultradisperse) metals. Transistor structures of both types were prepared in the same Corbino-disk ring geometry, which allows us to measure the mobility in the active layer by the geometric magnetoresistance method [5].

Standard GaAs wafers used in the production of Schottky gate FETs served as templates for the structures under study. Such a wafer consists of (1) a high-resistivity GaAs substrate, (2) a 1-μm-thick pure GaAs buffer layer, (3) a 150-nm-thick active GaAs layer, and (4) a 100-nm-thick n^+-GaAs contact layer with a donor concentration of $\sim 10^{19}$ cm^{-3}.

The structures were fabricated by the following sequence of technological operations. First, contact regions of source and drain covered by a metal Au film were made. Then, a gate window was formed using a burst-type photoresist. Next, a pure W film 80 nm thick and a WO_3 film 40–45 nm thick were deposited onto wafers of the first and the second type, respectively. On the wafers of the second type, selective removal of oxygen atoms from tungsten oxide with the formation of metallic tungsten was performed by irradiation with low-energy protons. The irradiation process was monitored in situ by measuring the change in the electrical resistance of a control WO_3 film; irradiation was terminated as soon as the resistance reached values typical of metallic tungsten. After the resist was removed and the wafers rinsed, they were cut into separate structures.

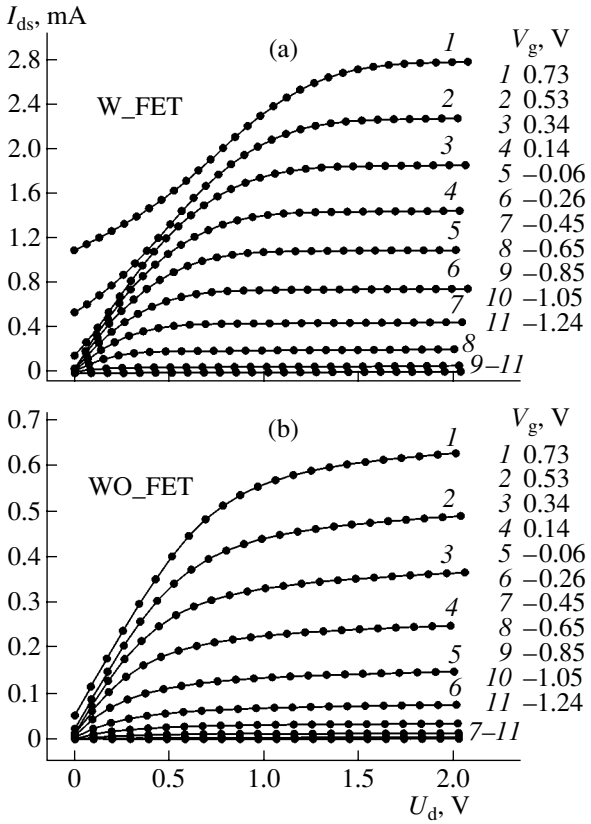

Fig. 1. Output (drain) characteristics of GaAs structures (a) with the gate obtained by W evaporation and (b) with the gate obtained by reduction of WO_3 to W using selective removal of atoms.

The transistor structures obtained had an inner diameter of the source region of 75 μm and an outer diameter of the drain region of 150 μm. Between the source and the drain, a 40-μm-wide gate was located at a distance of 20 μm from the drain.

Experiments were carried out at room temperature. They included measurements of output and transfer characteristics of the transistor structures, magnetic-field dependences of the drain current at different gate voltages, and bias-voltage dependences of the gate–drain differential capacitance at a frequency of 1 MHz.

3. RESULTS AND DISCUSSION

Output characteristics (dependences of the drain current I_{ds} on the source–drain voltage U_d) for different gate voltages V_g are shown in Figs. 1a and 1b and correspond to transistors with a gate made of evaporated tungsten (referred to below as W_FET structures) and tungsten obtained from WO_3 by selective removal of oxygen atoms (referred to below as WO_FET structures), respectively. In both cases, the shape of these characteristics is typical of long-channel Schottky gate

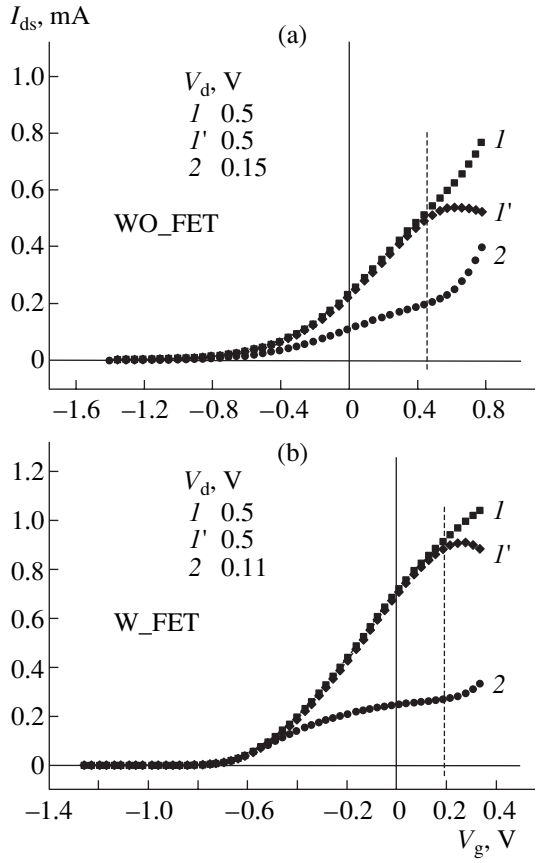

Fig. 2. Transfer (drain–gate) characteristics of (a) WO_FET and (b) W_FET GaAs transistor structures for different drain voltages U_d. Curves *1'* are obtained by subtracting the gate leakage current.

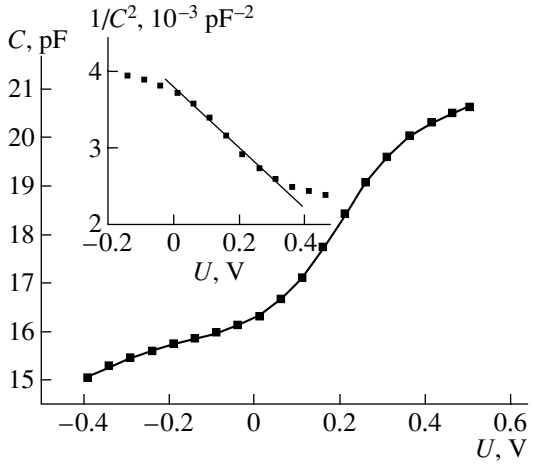

Fig. 3. Dependence of the gate–drain differential capacitance C on the bias voltage U in the WO_FET structure. Inset: relationship between $1/C^2$ and U and the result of fitting its linear segment by a first-degree polynomial.

FETs based on GaAs [4]. The drain current steadily increases with an increase in the pulling voltage U_d and tends to saturation at voltages exceeding $U_d \approx 0.5$ V. In the saturation region, the current is highest for positive gate voltages. In W_FET structures, gate leakage current manifests itself already at rather low gate voltages ($V_g > 0.2$ V): the residual drain current differs noticeably from zero for a near-zero source–drain voltage (see Fig. 1a). In WO_FET structures, gate leakage current is not observed up to $V_g \approx 0.7$ V. In the structures of both types, the drain current drops at negative gate voltages (by more than two orders of magnitude at $V_g \approx -1$ V). In W_FET structures, this is usually accompanied by a reversal of the sign of the current, which is caused by gate leakages.

Observation of strong modulation of the channel conductivity in WO_FET structures indicates that the height of the surface potential barrier changes considerably. Consequently, there is no Fermi-level pinning, which could take place if a large number of defects (localized electronic states) appeared at the interface of GaAs with W obtained by WO_3 reduction. Another indication of this fact is given by the shape of the transfer characteristics of WO_FET structures (dependences of the drain current I_{ds} on the gate voltage V_g), which are shown in Fig. 2a for different values of the pulling voltage U_d. For comparison, transfer characteristics of W_FET structures are shown in Fig. 2b. One can see that there are no clearly pronounced inflection points in the region of negative V_g in these dependences, whose presence could be caused by the existence of a large number of discrete interface states [4]. Note that the presence of an inflection region at positive V_g is not related to the interface states. Indeed, in this region the width of the conducting channel reaches its limiting value (equal to the thickness of the GaAs active layer), which should be accompanied by the saturation of the current. At the same time, the Schottky contact is forward-biased in this case, which leads to the onset of gate leakage currents, i.e., to an additional increase in the drain current. It is the combination of these two factors that gives rise to the inflection point in the transfer characteristics. Curves *1'* represent the dependences $I_d(V_g)$ obtained after subtracting the gate leakage currents. No inflection regions are seen in these curves. It should be noted that, for the WO_FET structure, the saturation region in curve *1'* is shifted by more than 0.2 V along the voltage axis as compared to the W_FET structure. This fact means that the height φ of the barrier at the interface of GaAs with W formed from the oxide exceeds by 0.2 eV the height of the barrier at the interface of GaAs with directly evaporated W and, thus, reaches a value of $\varphi \approx 1$ eV. This inference is also confirmed by the data from measurements of the gate–drain differential capacitance C at a frequency of 1 MHz as a function of the bias voltage U (see Fig. 3). The C–U curve contains a region with a clearly pronounced decrease in capacitance with decreasing U, which is related to the increase in the width of the Schottky layer in the region of negative bias voltages. It is known that φ can be determined from this depen-

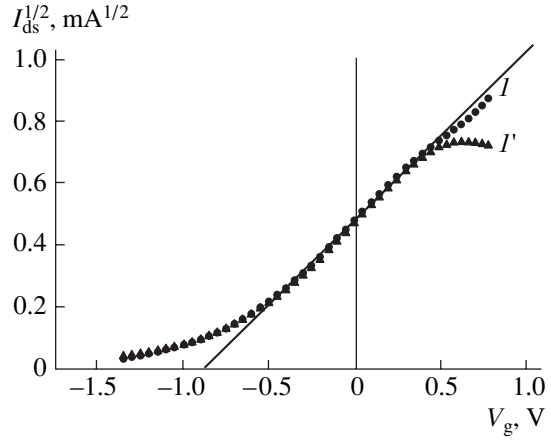

Fig. 4. Transfer characteristic of a WO_FET GaAs transistor structure plotted in $\sqrt{I_{ds}}$–V_g coordinates. Curve *1'* is obtained by subtracting the gate leakage current; drain voltage U_d = 0.5 V.

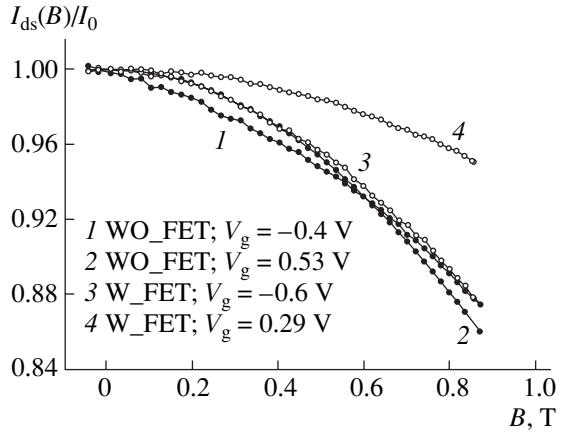

Fig. 5. Magnetoresistance effect for WO_FET and W_FET transistor structures (curves *1*, *2* and *3*, *4*, respectively), taken for drain voltage U_d = 0.12 V and different gate voltages; I_0 is the drain current in zero magnetic field.

dence plotted as $1/C^2$ vs. U [4]. This curve is shown in the inset in Fig. 3. Its linear portion can be fitted as

$$1/C^2[10^{-3}\ \text{pF}^{-2}] = 3.82 - 3.99U[\text{V}].$$

The value $1/C^2 = 0$ corresponds to the cutoff $U = U_i$ = 0.96 V. The value φ = 0.96 eV agrees well with the above estimate of the barrier height $\varphi \approx 1$ eV.

An increase in the barrier height by 0.2 eV is significant because, for covalent semiconductors like GaAs, surface defects of the crystal structure introduced upon deposition of a metal have a decisive effect on the formation of Schottky barriers, and the height of the barrier is almost independent of the chemical nature of the metal. In the case of GaAs, the barrier height amounts to 0.8 eV on average [4]. One possible explanation for the noticeable increase in the barrier height attained by using the SRA technique is the introduction of hydrogen (protons) in the surface region, which is known to result in the passivation of such defects as dangling bonds. Specifically, this fact is widely used for producing high-quality amorphous silicon (*a*-Si:H) (see [6, 7] and references therein) and for obtaining a lower density of localized states at a Si–SiO_2 interface.

The quality of transistor structures with a Schottky barrier is often estimated judging by the value of the threshold gate voltage V_t corresponding to the cutoff of the conductive channel. For an ideal structure with a uniform distribution of the doping impurity over the depth of the active layer, V_t is determined from the condition $d = w$, where d is the thickness of the active layer and w is the width of the Schottky layer:

$$w = \sqrt{\varepsilon(\varphi + eV_t)/2\pi e^2 N_d}. \quad (1)$$

Here, ε is the permittivity (ε = 13.1 for GaAs), φ is the height of the Schottky barrier at the metal–semiconductor contact, and N_d is the donor density in the active layer of the structure. The value of V_t can be determined experimentally from a transfer characteristic by plotting it as a $\sqrt{I_{ds}}$ vs. V_g dependence and extrapolating the linear portion of the curve to zero (the drain voltage should correspond to the saturation region of the output characteristics) [4]. Such a dependence is shown in Fig. 4; it can be seen that the threshold voltage is ~1 V. Substituting this value in (1) and assuming that φ = 1 eV, we obtain w = 120 nm; this virtually coincides with the technological setting for the width of the active GaAs layer (~150 nm).

Next, we consider the magnetic-field dependence of the drain current of the structures. For samples shaped like a Corbino disk, the magnetoresistance is related to the mobility of the charge carriers μ by the following simple expression [5]:

$$\Delta R/R_0 \approx (\mu B)^2, \quad (2)$$

where B is the field strength. In the samples under study, the presence of a ring-shaped gate makes it possible to measure electron mobility in the gate region, since, with quite high depleting voltages, it is this region that determines the resistance of the sample.

Figure 5 shows the magnetic-field dependences of the drain current I_{ds} recorded at pulling voltage U_d = 0.12 V and different gate voltages for WO_FET (curves *1*, *2*) and W_FET (curves *3*, *4*) structures. Depending on the choice of gate voltage, the channel is either fully conducting (curves *2*, *4*) or partially depleted, so the drain current drops six- to sevenfold compared to the open state (curves *1*, *3*). One may assume that the structure resistance is determined by the gate region in the latter case; at the same time, in the former case, there may be a significant contribution to the magnetoresistance from the regions between the gate, the source, and the drain, as far as their total width (35 μm) is comparable with the width of the gate (40 μm).

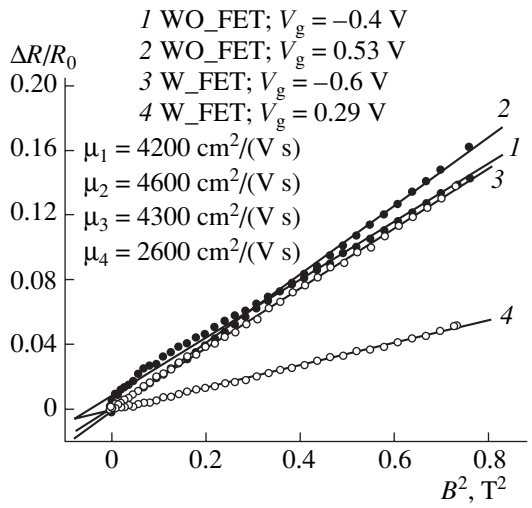

Fig. 6. Magnetoresistance-effect dependences for WO_FET and W_FET transistor structures (curves (*1*, *2*) and (*3*, *4*), respectively) for different gate voltages.

Note that these regions were protected from proton irradiation by the resist and, thus, one would expect a considerable magnetoresistance for the WO_FET structure. However, measurements show that the magnetoresistance of this structure in a 9-kOe field for conducting and partially depleted channels is the same within 10%. Meanwhile, a considerable reduction in the magnetoresistance in the case of a completely conducting channel is observed for the W_FET structure. Magnetoresistance dependences, calculated from $I_{ds}(B)$ curves, are shown in Fig. 6 in $\Delta R/R_0 = f(B^2)$ coordinates. It can be seen that these dependences are nearly linear, in agreement with (2). For the W_FET structure, the magnetoresistance in the conducting state decreases by a factor of 2.6. This fact is explained by the appearance of significant gate-leakage currents (see Fig. 1a), which causes shunting of the Hall current by the metal electrode of the gate (in the open state, part of the current flows through the gate). For the WO_FET structure, this effect is insignificant. The mobilities for this structure, obtained from the slope of curves *1* and *2*, are μ = (4200–4600) cm^2 V^{-1} s^{-1}; for the W_FET structure, we obtain from curve *3* (taken under conditions of a partially depleted channel) μ = 4300 cm^2 V^{-1} s^{-1}. This agrees well with the data on the mobility in single-crystal GaAs ($\mu \approx 4500$ cm^2 V^{-1} s^{-1} for $N_d = 2 \times 10^{17}$ cm^{-3} at $T \approx 300$ K) [4].

4. CONCLUSION

Thus, the data presented indicate that there is no damaged layer at the interface of GaAs with W obtained from the oxide and, for the chosen conditions of the SRA process, proton irradiation has an insignificant effect on the properties of GaAs. A comparison of the two types of W/GaAs FETs also indicates that the Schottky barrier formed in the structures obtained by the method of selective removal of atoms is noticeably (by 0.2 eV) higher than the barrier in the structures obtained by conventional metal deposition (0.8 eV for a W/GaAs contact). This is important for the fabrication of electronic elements of nanoscale dimensions (in particular, "conductive" patterns with ballistic charge-carrier transport) and for the use of Schottky diodes in solar cells.

ACKNOWLEDGMENTS

This study was supported in part by the Russian Foundation for Basic Research (project no. 01-02-16420).

REFERENCES

1. C. Wyon, Nucl. Instrum. Methods Phys. Res. B **186**, 380 (2002).
2. B. A. Gurovich, D. I. Dolgiĭ, E. A. Kuleshova, *et al.*, Usp. Fiz. Nauk **171**, 105 (2001) [Phys. Usp. **44**, 95 (2001)].
3. B. A. Gurovich, D. I. Dolgy, E. A. Kuleshova, *et al.*, Microelectron. Eng. **69**, 358 (2003).
4. S. Sze, *Physics of Semiconductor Devices*, 2nd ed. (Wiley, New York, 1981; Mir, Moscow, 1984), Vol. 1.
5. K. Seeger, *Semiconductor Physics* (Springer, Berlin, 1974; Mir, Moscow, 1977).
6. O. A. Golikova, Fiz. Tekh. Poluprovodn. (St. Petersburg) **31**, 281 (1997) [Semiconductors **31**, 228 (1997)].
7. I. V. Antonova, Ĭ. Stano, D. V. Nikolaev, *et al.*, Fiz. Tekh. Poluprovodn. (St. Petersburg) **36**, 65 (2002) [Semiconductors **36**, 60 (2002)].

Translated by M. Skorikov

Semiconductors, Vol. 38, No. 9, 2004, pp. 1041–1046. Translated from Fizika i Tekhnika Poluprovodnikov, Vol. 38, No. 9, 2004, pp. 1079–1083.

SEMICONDUCTOR STRUCTURES, INTERFACES, AND SURFACES

Special Features of Radiation-Defect Annealing in Silicon *p–n* Structures: The Role of Fe Impurity Atoms

B. A. Komarov

Institute of Solid-State and Semiconductor Physics, Belarussian Academy of Sciences, ul. Brovki 17, Minsk, 220072 Belarus
e-mail: murin@ifttp.bas-net.by

Submitted October 20, 2003; accepted for publication February 18, 2004

Abstract—Deep-level transient spectroscopy is used to study the formation of complexes that consist of a radiation defect and a residual impurity atom in silicon. It is established that heat treatment of the diffused Si p^+–n junctions irradiated with fast electrons lead to the activation of a residual Fe impurity and the formation of the FeVO ($E_{0.36}$ trap) and FeV_2 ($H_{0.18}$ trap) complexes. The formation of these traps is accompanied by the early (100–175°C) stage of annealing of the main vacancy-related radiation defects: the A centers (VO) and divacancies (V_2). The observed complexes are electrically active and introduce new electron ($E_{0.36}$: $E_t^e = E_c - 0.365$ eV, $\sigma_n = 6.8 \times 10^{-15}$ cm^2) and hole ($H_{0.18}$: $E_t^h = E_v + 0.184$ eV, $\sigma_p = 3.0 \times 10^{-15}$ cm^2) levels into the silicon band gap and have a high thermal stability. It is believed that the complex FeVO corresponds to the previously observed and unidentified defects that have an ionization energy of $E_t^e = E_c - (0.34–0.37)$ eV and appear as a result of heat treatment of irradiated diffused Si p^+–n junctions. © *2004 MAIK "Nauka/Interperiodica".*

1. INTRODUCTION

The control of highly diffusible impurities remains one of the most important problems in silicon microelectronics and nanoelectronics. These impurities, primarily, the atoms of transition metals (Fe, Cu, Ni, etc.), can be introduced in significant amount during high-temperature technological treatment [1–3]. Due to the high mobility of these impurities, they interact actively with various lattice defects with the subsequent formation of new electrically active centers in a number of cases. One might expect that the presence of transition metals in silicon structures subjected to a high-temperature treatment would also manifest itself in the course of production and annealing of radiation defects.

It was established in the early studies of the thermal stability of radiation defects introduced by irradiation with γ-ray photons or fast electrons that the most important radiation defects, such as the A centers (VO) and divacancies (V_2), are stable in float-zone silicon (FZ-Si) up to a temperature $T_{ann} \approx 350$°C, whereas divacancies V_2 are stable up to 250°C in silicon grown by the Czochralski method (Cz-Si) and are annealed out without giving rise to new electrically active defects with appreciable concentrations [4–8].

It was shown in subsequent studies that annealing the A centers in diffused p–n junctions can be complex and can give rise to new electron traps whose origin is unknown [9–11]. For example, Kimerling [9] observed the appearance and disappearance of electron traps with a level at $E_c - 0.35$ eV ($E_{0.35}$) in diffused p–n junctions irradiated with 1-MeV electrons and then annealed at temperatures of 150–300°C. In these conditions, the A centers were annealed out steadily at temperatures higher than 100°C. Brotherton and Bradley [10] studied the radiation defects produced by irradiation with 12-MeV electrons and observed a similar pattern of annealing of the A centers with the resulting formation of traps with a level at $E_c - 0.36$ eV ($E_{0.36}$). The generation of $E_{0.36}$ defects in the Schottky barriers has not been observed. Barnes [11] studied the annealing of radiation defects produced in diffused junctions by ^{60}Co γ-ray photons and observed an early stage (at $T_{ann} \geq 170$°C) of partial annealing of the $E_{0.18}$ traps (VO) with simultaneous generation of new electron traps $E_{0.35}$ with a concentration equal to that of annealed VO centers. At higher temperatures, the annealing of the A centers and the $E_{0.35}$ traps occurred simultaneously up to temperatures $T_{ann} \geq 370$°C. It is assumed that the early stage of partial annealing of the A centers is caused by the interaction of these centers with mobile defects or with an impurity with the subsequent transformation of the A center into a more complex center.

An anomalously early stage ($T_{ann} \approx 120$°C) of complete annealing of the VO defect was observed both in the Cz-Si single crystals subjected to a preliminary heat treatment [12, 13] and in p–n junctions [14–17]. It is believed that residual technological impurities of rapidly diffusing metals (Fe, Ni, etc.) may be involved in the defect-formation processes in crystals subjected to preliminary heat treatment [12, 13].

The early stage of annealing of VO centers ($T_{ann} >$ 100°C) in p–n junctions was accompanied by the for-

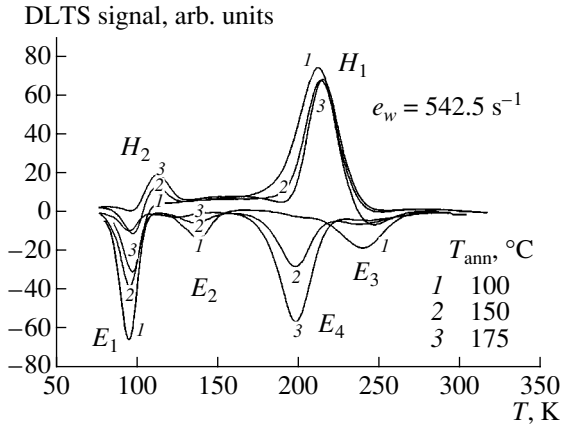

Fig. 1. DLTS spectra of radiation defects in Si p^+–n junctions (structures II) irradiated with fast electrons (E = 7 MeV, $F = 3 \times 10^{14}$ cm^{-2}); the transformation of these spectra as a result of initial heat treatment is shown.

mation of new electron traps $E_{0.37}$ [14] or $E_{0.34}$ [15] with a concentration equal to that of annealed *V*O canters and with levels at $E_c - 0.37$ eV and $E_c - 0.34$ eV, respectively. The reverse transformation of the $E_{0.34}$ trap into an *A* center was observed at $T > 200$°C. It was assumed that an unknown mobile defect was involved in the formation of the $E_{0.34}$ trap.

It was established by You *et al.* [16] that the interaction of Fe atoms with radiation defects in *p*–*n* junctions gives rise to the early stage ($T_{ann} \approx 100$°C) of annealing of *A* centers with the simultaneous formation of $E_{0.36}$ traps with a concentration equal to that of annealed *A* centers. This trap was identified as the Fe*V*O complex. The early stage of annealing of divacancies was also observed.

Anomalous early stages of annealing of the *A* centers and divacancies and also the appearance of new traps for electrons ($E_{0.36}$) and holes ($H_{0.18}$) were observed in studies of the formation and annealing of radiation defects in the lightly doped base of Si p^+–n junctions [17].

Thus, the objective of this study was to clarify the interaction of radiation defects with a residual impurity and identify this impurity by studying the special features of annealing of radiation defects in diffused Si *p*–*n* junctions.

2. EXPERIMENT AND RESULTS

We studied Si p^+–n structures formed by diffusion of boron ($T_{dif} = 1150$°C) into *n*-Cz-Si:P with $\rho = 2$ Ω cm (structures I) and $\rho = 20$ Ω cm (structures II). The samples were irradiated with fast electrons (energy E = 7 MeV, doses $F = 3 \times 10^{14}$–3×10^{15} cm^{-2}) at room temperature. Deep-level transient spectroscopy (DLTS) was performed using a DLS-83D system produced by Semitrap [18].

The DLTS method is based on the relation between the time variation in the barrier capacitance of a *p*–*n* junction or a Schottky barrier with the temperature-dependent rate of thermal emission of charge carriers $e_n(T)$ from the deep level of the defect as the bias voltage applied to the structure is varied. This relation is described by the expression $\Delta C(t) = \Delta C(0)\exp[-e_n(T)t]$, where $\Delta C(0)$ is the variation in the barrier capacitance at the initial point in time $t = 0$. In the DLS-83D spectrometer, the pulse corresponding to the filling of the trap is repeated periodically with the frequency ν. The used variations in the capacitance $\Delta C(t)$ are amplified using a synchronous amplifier and are then integrated using a quadratic wave weighting function. For a discrete center, the temperature corresponding to the peak in the signal amplitude T_{peak}, the thermal-emission rate e_n, and the repetition rate ν of filling pulses are related by the simple expression $e_n(T_{peak}) = 2.17\nu$. Performing the necessary number of thermal scans at various frequencies, we obtain the corresponding number (i) of pairs $T_{peak}^{(i)} - e_n^{(i)}$ used in the conventional procedure for plotting the Arrhenius relation. The defect concentration N_t is equal to the amplitude of the peak $\Delta C(T_{peak})$ multiplied by the correlation coefficient for the system under consideration. Other parameters of the trap are determined using procedures typical of the DLTS methods.

Electron traps were not found in the upper half of the band gap in the reference (unirradiated) samples. A band with a peak at about 225 K ($H_{0.38}$, $N_{0.38} \geq 2 \times 10^{11}$ cm^{-3}) was observed in the lower half of the band gap in structures II.

Both the energy spectrum and the formation efficiency of the main radiation defects are nearly the same in structures I and II. In Fig. 1, we show a typical DLTS spectrum of radiation defects and its transformation in the early stages of isochronous annealing of structures II. Irradiation with electrons gave rise to the following electron traps in the upper half of the band gap: trap E_1 (0.166 eV; $\sigma_n = 1.1 \times 10^{-14}$ cm^2; the *A* center, C_iC_s) [4–11, 19]; trap E_2 (0.241 eV; $\sigma_n = 5.0 \times 10^{-15}$ cm^2; V_2^{-2}) [6, 7, 9]; and trap E_3 (0.424 eV; $\sigma_n = 2.1 \times 10^{-15}$ cm^2; the *E* center, V_2^{-1}) [6–9]. The hole trap H_1 (0.363 eV, $\sigma_p = 1.5 \times 10^{-15}$ cm^2; C_iO_i) was introduced into the lower half of the band gap [20].

Appreciable differences between the behavior of the radiation defects introduced into structures I and II were observed in performing an isochronous (30 min) annealing in the temperature range 100–400°C.

The main radiation defects (*A* centers and divacancies) are annealed out in a single stage (T_{ann} = 300–350°C) in structures I (with a higher level of doping of the base) (Fig. 2). As can be seen from Fig. 2, the trap E_1 is stable up to a temperature of 350°C, and the contribution of C_iC_s complexes (whose annealing occurs at

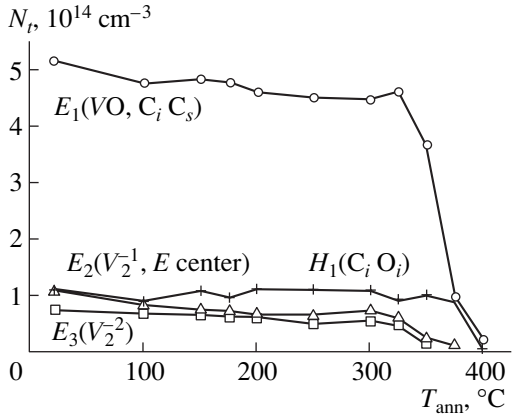

Fig. 2. Annealing of radiation defects in Si p^+–n junctions (structures I) irradiated with fast electrons with E = 7 MeV and $F = 3 \times 10^{15}$ cm^{-2}.

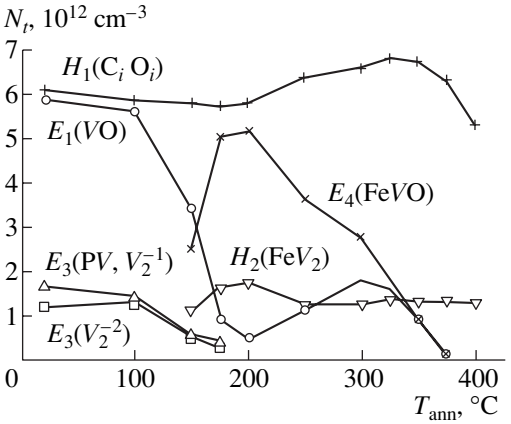

Fig. 3. Annealing of radiation defects in Si p^+–n junctions (structures II) irradiated with fast electrons (E = 7 MeV, $F = 3 \times 10^{14}$ cm^{-2}). The levels are located at $E_1 = E_c - 0.166$ eV, $E_2 = E_c - 0.241$ eV, $E_3 = E_c - 0.424$ eV, $E_4 = E_c - 0.365$ eV, $H_1 = E_v + 0.363$ eV, and $H_2 = E_v + 0.184$ eV.

$T_{ann} \approx 250$°C [19]) to the concentration of the defects E_1 is small. Therefore, the features of annealing of the defects with level E_1 are governed by the thermal stability of the A center. We did not observe formation of new electrically active centers with significant concentrations. In addition, it is worth noting that the divacancy levels are stable up to 350°C. The concentration of the E centers (the PV complexes) was low in the structures we studied.

The early (T_{ann} = 100–175°C) stage of annealing of the traps $E_1(VO)$, $E_2(V_2^{-2})$, and $E_3(V_2^{-1})$ is observed in structures II with a lightly doped base (Figs. 1, 3). New traps E_4 (0.365 eV, $\sigma_n = 6.8 \times 10^{-15}$ cm^2) and H_2 (0.184 eV, $\sigma_p = 3.0 \times 10^{-15}$ cm^2) are formed simultaneously. The annealing of the E_1 center is accompanied by a buildup of the same concentration of the E_4 trap. These traps are annealed out to a certain extent at T = 250–300°C; this annealing is accompanied by a partial recovery of the E_1 traps (the stage of reverse annealing). At higher temperatures, the traps E_1 and E_4 are annealed out synchronously up to 350°C. The annealing of the traps E_2 and E_3 (divacancies) coincides with the appearance of the new trap H_2 with a concentration equal to that of annealed E_2 traps. The H_2 trap is stable up to 400°C (we did not perform heat treatment at higher temperatures). The stage of formation of the trap H_2 correlates in temperature with that of the stage of formation of the trap E_4.

We did not observe any appreciable differences between the characteristics of annealing of interstitial-containing radiation defects (C_iO_i complexes) in structures I and II. However, a certain increase in the concentration of the trap H_1 is observed in structures II as the E_4 traps are annealed out. In our opinion, this annealing of H_1 traps is related to the transformation of other carbon-containing defects into the C_iO_i complex rather than to the dissociation of the trap E_4.

3. DISCUSSION

We assumed above that residual rapidly diffusing impurities introduced during technological operations can interact with radiation defects. The phenomenon of passivation of radiation defects in silicon with hydrogen is well known. However, the absence of hydrogen-containing defects (VOH [21] and MRH [22–24]) in the structures under study and the fact that the parameters of new traps determined in this study are close to those reported in previous publications [16] allows us to consider below the interaction of Fe atoms with radiation defects.

3.1. The Role of the Fe Impurity

Iron is an important fast-diffusing technological impurity of transition metals, which can be introduced unintentionally (but efficiently) into crystals both during their growth and in the course of production of semiconductor devices [1–3, 16, 25–28]. As a result of rapid cooling after a high-temperature treatment, electrically active iron atoms reside mostly at interstitial sites (Fe_i) in the crystal and are hole traps with the donor level located at E_v + (0.38–0.41) eV. According to electron spin resonance (ESR) data, the concentration of Fe_i^0 in the crystal can be as high as ~10^{14} cm^{-3} if conventional procedures for purification are used. Studies [25, 26] have shown that the Si–Fe solid solution is more stable in n-Si than in p-Si. This behavior is related to the fact that interstitial Fe atoms in p-Si are charged positively, so there is a high probability of Coulomb interaction with an acceptor impurity, e.g., Fe_i^+–B^- [2, 3]. Iron atoms in n-Si are neutral, so there is no Coulomb interaction of these atoms with acceptor-type defects [26].

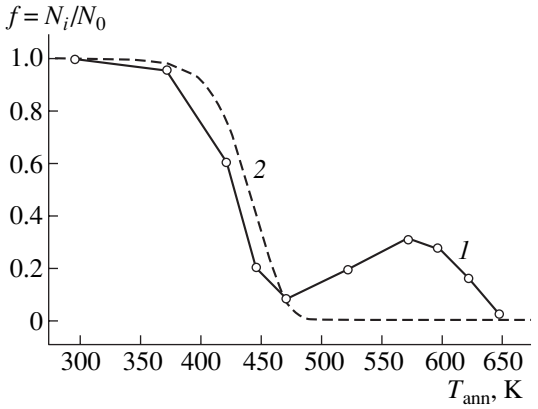

Fig. 4. Fragment of the early stage of annealing of the defects *V*O. Curve *1* corresponds to experimental data; curve *2* represents the results of calculation of the fraction of unannealed defects *V*O according to formula (1). For clarity, we do not show here the stage of formation and annealing of the trap $E_{0.36}$ (T = 150–350°C).

Lebedev and Urunbaev [26] studied in detail the decomposition kinetics for a solid solution of Fe in *n*-Cz-Si using capacitance-based methods. Isochronous annealing was performed in the temperature range from 50 to 200°C. An appreciable variation in the Fe concentration was observed at $T_{ann} \geq 130$°C; the iron-related levels were annealed out completely as a result of annealing at 200°C [26]. The established stage of annealing of the levels at $E_v + 0.41$ eV agrees well with the results of studying the annealing of the Fe_i^0 state in Si using ESR [27, 28].

Earlier studies of thermal stability of Fe_i [25] in the presence of radiation defects showed that the transformation of the level $E_c - 0.17$ eV (*V*O) into a level $E_c - 0.30$ eV was observed in irradiated samples at T_{ann} = 100°C; this transformation occurred only in the Si samples saturated with Fe.

In Fig. 4, we show a fragment of the early stage of *A*-center annealing (curve *1*) and also the stage of reverse annealing reported by Komarov *et al.* [17]. The experimental curve of promoted annealing is described adequately by the following expression:

$$f = \exp[-2.8 \times 10^5 t\beta \exp(-0.78/kT_i)]. \quad (1)$$

Here, $f = N_i/N_0$ is the fraction of unannealed defects, N_i is the concentration of defects *V*O at an annealing temperature $T_{ann} = T_i$, N_0 is the concentration of *V*O defects before annealing, $t = t_{ann}$ is the isochronous-annealing duration (expressed in seconds), E_a = 0.78 eV is the activation energy for annealing, and the preexponential factor $\beta = 2.8 \times 10^5$ s^{-1}. Assuming that the early stage of annealing of *A* centers is related to the capture of mobile interstitial Fe atoms by the *V*O complexes, we chose process parameters equal to those for annealing Fe^+ centers in Si [26] (the results of the calculation are represented by curve *2* in Fig. 4). The above mechanism of annealing is supported by the following observations:

(i) the presence of the early annealing stage for the *A* centers and the transformation of the trap $E_{0.17}$ into the traps $E_{0.3}$ [25], $E_{0.34}$ [15], $E_{0.36}$ [16, 17], and $E_{0.37}$ [14];

(ii) this transformation could be observed in Si crystals that contained the Fe impurity [16, 25].

We relate the experimental spread in the position of the trap energy level after transformation to the use of different methods in the studies (the Hall effect, photocapacitance method, isothermal capacitance transient spectroscopy, and DLTS). In our opinion, the origin of the phenomenon is the same in all the studies cited.

It is most probable that the trap E_4 ($E_{0.36}$), whose formation is observed in the structures under consideration (Figs. 1, 3), is also the Fe*V*O complex. This inference is supported by both the identity of the $E_{0.36}$-center parameters observed previously [16, 17] and the similar behavior of these centers in the course of annealing. Furthermore, the appearance of the $H_{0.38}$ trap in the starting (unirradiated) samples also indicates that there are interstitial Fe atoms in the crystal (according to Istratov *et al.* [3], the donor level of Fe_i is located at about $E_v + 0.38$ eV).

Taking into account the facts above, we may conclude the following. The early stage of annealing of the trap E_1 (*V*O) and the formation of a new electron trap $E_{0.36}$ (Fe*V*O) that we observed are related to the capture of mobile Fe_i atoms by the *V*O complex. The fact that the activation energy (E_a = 0.78 eV) obtained by us for the early annealing stage of the *A* center is close to $E_a \approx$ 0.7 eV [15] and to the data reported in [26] further verifies the above capture mechanism.

We draw attention to the fact that the parameters of the trap E_4 ($E_{0.36}$) in this study coincide with those of the traps $E_{0.36}$ (0.363 eV, $\sigma_n = 1.4 \times 10^{-15}$ cm^2) [10], $E_{0.36}$ (0.36 eV, $\sigma_n = 4 \times 10^{-15}$ cm^2) [16], and $E_{0.34}$ (0.34 eV, $\sigma_n = 10^{-15}$ cm^2) [15]. We also note that there is a common stage of appearance and annealing of the traps $E_{0.36}$ and $E_{0.34}$ at $T_{ann} \approx$ 150–350°C [9–11, 15–17]. Furthermore, we should mention the presence of a partial [11] or complete early stage of annealing of the *A* centers and their transformation into new $E_{0.36}$ or $E_{0.37}$ traps [11, 14–17, 25]. We also note that the aforementioned phenomena were observed in diffused junctions some of which were specially doped with Fe. All these facts indicate that the structure of the new defect is the same in all the cases mentioned above; i.e., this is the Fe*V*O complex.

3.2. Annealing of Divacancies

A divacancy introduces two levels ($E_c - 0.23$ eV and $E_c - 0.39$ eV) into the upper half of the silicon band gap. Both divacancy levels are produced with the same rate (~0.01 cm^{-1}) and are annealed out at the same temperature (~330°C) in float-zone silicon in the case of irra-

diation with electrons. The annealing can be described using a single exponential function with an activation energy of 1.47 eV and preexponential factor $\beta = 1.1 \times 10^9$ s^{-1} [29].

Recent Laplace DLTS studies of thermal stability of divacancies [30] showed that the annealing of the centers V_2^{-2} at $T_{ann} > 170$°C in *n*-Cz-Si was accompanied by the transformation of divacancies into complexes V_2O with equal concentration and nearly the same parameters of thermal emission of electrons. This complex is stable up to $T_{ann} \approx 300$°C.

You *et al.* [16] studied the interaction of Fe atoms with radiation defects in Si *p–n* junctions and reported an early annealing stage ($T_{ann} > 80$°C) of divacancies; however, new traps were not observed.

In contrast to [16], where the traps in the lower half of the Si band gap were not studied, we observed a new trap H_2 (Figs. 1, 3). The temperature of formation of this trap correlates with the early stage of annealing of divacancies, which is accompanied by the generation of the E_4 trap (Fe*V*O). Apparently, divacancies are also efficient traps for mobile Fe atoms.

An ESR study of iron-related centers in silicon [28] showed that a divacancy can be involved in the formation of the $Fe_{2i}V_2$ complex, which consists of two interstitial Fe atoms in the vicinity of V_2. This complex is annealed out at a temperature of 250°C.

However, the trap H_2 is stable up to an annealing temperature of 400°C (the highest annealing temperature used in this study). We do not rule out that the trap H_2 may be related to the formation of the complex Fe_iV_2, which is possibly more stable than the complex $Fe_{2i}V_2$.

In conclusion, we note the following. In previous research [9–11, 14–17], the concentration of the majority doping impurity and that of radiation defects were $N \leq 10^{14}$ cm^{-3}. Therefore, we believe that, in conventional diffused Si *p–n* junctions or in the Si *p–n* junctions doped intentionally with Fe so that the concentration of radiation defects is comparable with that of iron, we should expect a promoted annealing of the *A* centers and divacancies with the resulting formation of new thermally stable defects under corresponding thermal conditions of treatment or service of commercial structures exposed to severe radiation. Such a promoted annealing of the vacancy-related complexes *V*O and V_2 and the formation of new traps $E_{0.36}$ and $H_{0.18}$ indicate that the residual Fe_i impurity interacts with radiation defects. These changes in the types of radiation defects can lead to a degradation of the electrical characteristics of commercial devices.

4. CONCLUSION

The interaction of vacancy-type radiation defects with mobile Fe atoms is observed in electron-irradiated *n*-Cz-Si crystals that contain a background or intentionally introduced concentration of Fe_i. This interaction manifests itself experimentally in the presence of an anomalously early stage of annealing (T_{ann} = 100–150°C) of the *A* centers and divacancies with the resulting formation of new electron $E_{0.36}$ ($E_t = E_c - 0.365$ eV, $\sigma_n = 6.8 \times 10^{-15}$ cm^2) and hole $H_{0.18}$ ($E_t = E_v + 0.184$ eV, $\sigma_p = 3.0 \times 10^{-15}$ cm^2) traps.

The estimated activation energy for the early annealing stage for *A* centers was $E_a \approx 0.8$ eV. The trap $E_{0.36}$ was identified with the Fe_iVO complex. We ascertained that the annealing of this complex is accompanied by a stage of reverse annealing of the $E_{0.17}$ trap. We assume that the formation of the $E_{0.34–0.37}$ traps is also related to the interaction of mobile Fe_i atoms with the *A* centers.

We observed the trap $H_{0.18}$ for the first time and identified it as a complex that consisted of a divacancy and an interstitial iron atom (Fe_iV_2). We showed that the defect $H_{0.18}$ is one of the most thermally stable radiation defects in silicon.

ACKNOWLEDGMENTS

I thank F.P. Korshunov for the interest he showed in this study and L.I. Murin for helpful discussions.

This study was supported in part by the Belarussian Foundation for Basic Research, project no. F01-314.

REFERENCES

1. B. O. Kolbensen, H. Cerva, and G. Zoth, Solid State Phenom. **76–77**, 1 (2001).
2. A. A. Istratov and E. R. Weber, Appl. Phys. A **66**, 123 (1998).
3. A. A. Istratov, H. Hieslmair, and E. R. Weber, Appl. Phys. **70**, 489 (2000).
4. G. D. Watkins and J. W. Corbett, Phys. Rev. **121**, 1001 (1961).
5. J. W. Corbett, G. D. Watkins, R. M. Chrenko, and R. S. McDonald, Phys. Rev. **121**, 1051 (1961).
6. G. D. Watkins and J. W. Corbett, Phys. Rev. A **138**, 543 (1965).
7. L. J. Cheng, J. C. Corelli, J. W. Corbett, and G. D. Watkins, Phys. Rev. **152**, 761 (1966).
8. J. W. Walker and C. T. Sah, Phys. Rev. B **7**, 4587 (1973).
9. L. C. Kimerling, Inst. Phys. Conf. Ser., No. 31, 221 (1977).
10. S. D. Brotherton and P. J. Bradley, Appl. Phys. **53**, 5720 (1982).
11. C. E. Barnes, J. Electron. Mater. **8**, 437 (1979).
12. L. F. Makarenko, V. P. Markevich, L. I. Murin, and V. D. Tkachev, Dokl. Akad. Nauk BSSR, No. 11, 988 (1981).
13. I. F. Medvedeva, L. F. Makarenko, V. P. Markevich, and L. I. Murin, Vesti Akad. Nauk Beloruss. SSR, Ser. Fiz.–Mat. Nauk, No. 3, 19 (1991).
14. L. S. Berman and V. B. Shuman, Fiz. Tekh. Poluprovodn. (Leningrad) **10**, 1755 (1976) [Sov. Phys. Semicond. **10**, 1043 (1976)].

15. P. V. Kuchinskiĭ, V. M. Lomako, and L. N. Shakhlevich, Pis'ma Zh. Éksp. Teor. Fiz. **45**, 350 (1987) [JETP Lett. **45**, 445 (1987)].
16. Z. You, M. Gong, J. Chen, and J. W. Corbett, J. Appl. Phys. **63**, 324 (1988).
17. B. A. Komarov, I. F. Medvedeva, L. I. Murin, *et al.*, in *Proceedings of IV International Conference on Interaction of Radiation with Solids* (Minsk, 2001), p. 161.
18. G. Ferenczi, J. Boda, and T. Pavelka, Phys. Status Solidi A **94**, K119 (1986).
19. L. W. Song, B. W. Benson, and G. D. Watkins, Appl. Phys. Lett. **51**, 1155 (1987).
20. L. I. Murin, Phys. Status Solidi A **101**, K107 (1987).
21. P. Pellegrimo, P. Levegue, J. Lalita, *et al.*, Phys. Rev. B **64**, 195211 (2001).
22. B. A. Komarov, V. P. Markevich, L. I. Murin, and T. Sekiguchi, in *Proceedings of 23rd International Conference on Physics of Semiconductors*, Ed. by M. Scheffler and R. Zimmermann (World Sci., Singapore, 1996), p. 2593.
23. I. F. Medvedeva, L. I. Murin, V. P. Markevich, and B. A. Komarov, Vopr. At. Nauki Tekh., Ser.: Radiats. Materialoved. **79** (2), 48 (2001).
24. B. A. Komarov, Vopr. At. Nauki Tekh., Ser.: Radiats. Materialoved. **79** (2), 43 (2001).
25. A. A. Zolotukhin, A. K. Kovalenko, and L. S. Milevskiĭ, Fiz. Tverd. Tela (Leningrad) **13**, 3119 (1971) [Sov. Phys. Solid State **13**, 2621 (1971)].
26. A. A. Lebedev and B. M. Urunbaev, Fiz. Tekh. Poluprovodn. (Leningrad) **15**, 612 (1981) [Sov. Phys. Semicond. **15**, 350 (1981)].
27. K. P. Abdurakhmanov, B. A. Kotov, J. Kreissl, *et al.*, Fiz. Tekh. Poluprovodn. (Leningrad) **19**, 349 (1985) [Sov. Phys. Semicond. **19**, 218 (1985)].
28. S. H. Muller, G. M. Tuynman, E. G. Sieverts, and C. A. Ammerlaan, Phys. Rev. B **25**, 25 (1982).
29. A. V. Vasil'ev, S. A. Smagulova, and L. S. Smirnov, Fiz. Tekh. Poluprovodn. (Leningrad) **20**, 561 (1986) [Sov. Phys. Semicond. **20**, 354 (1986)].
30. V. P. Markevich, A. R. Peaker, S. B. Lastovskii, *et al.*, J. Phys.: Condens. Matter **15**, S2779 (2003).

Translated by A. Spitsyn

Semiconductors, Vol. 38, No. 9, 2004, pp. 1047–1052. Translated from Fizika i Tekhnika Poluprovodnikov, Vol. 38, No. 9, 2004, pp. 1084–1089.

LOW-DIMENSIONAL SYSTEMS

Electrical Properties of Metal–Semiconductor Nanocontacts

N. V. Vostokov and V. I. Shashkin

Institute for Physics of Microstructures, Russian Academy of Sciences, Nizhni Novgorod, 603950 Russia
e-mail: vostokov@ipm.sci-nnov.ru

Submitted July 7, 2003; accepted for publication January 20, 2004

Abstract—Potential distributions around spherical and cylindrical metallic nanocontacts in semiconductors are calculated. Electrical properties of nanocontacts of small characteristic size $a \ll S$ (S is the width of the depletion region in planar geometry) are analyzed. It is shown that, compared to the planar case, nanocontacts have a weaker voltage dependence of the capacitance, a greater decrease in the Schottky barrier height due to the image forces, and a faster response up to frequencies in the terahertz range. © *2004 MAIK "Nauka/Interperiodica".*

1. INTRODUCTION

The study of the properties of small-size metal–semiconductor contacts is currently generating a great deal of interest [1]. This interest is related to the development of probe methods of studying semiconductor structures, the development and fabrication of nanosize Schottky contacts for microwave and terahertz applications, and attempts to form two- or three-dimensional nanocontact arrays as artificial nonlinear media [2–6]. When fabricated by epitaxial methods, such a medium is a multilayer system of quantum dots or metallic nanoparticles introduced into a semiconductor matrix [7, 8]. A widely known example of such a medium is epitaxial GaAs that is grown at a low temperature and contains As nanoclusters [6, 9].

In these structures, the interface of the metal–semiconductor contact is not planar and has a nonzero curvature, the electric field has a different distribution, and its magnitude near the interface with the metal can be much greater than in the planar case. The same situation arises in the case of small-size contacts, where edge effects cannot be disregarded. In this case the potential distribution differs considerably from that in the case of a large planar contact.

Below, we consider two types of contacts, namely, a metallic sphere of radius a and an infinite metallic cylinder of radius a placed in a homogeneous semiconductor (specifically, of n type). To find the distribution of electrostatic potential φ at the contact, we solve the Poisson equation

$$\Delta\varphi = -\frac{4\pi eN}{\varepsilon}, \tag{1}$$

where N is the impurity concentration in a uniformly doped semiconductor, ε is its permittivity, and e is the elementary charge. We use the approximation of full depletion [10] leading to the following boundary conditions at the metallic surface Ω_1 and at the surface Ω_2 bounding the region of full depletion of the semiconductor:

$$\varphi(r)|_{\Omega_1} = 0, \tag{2}$$

$$\varphi(r)|_{\Omega_2} = u_c - u. \tag{3}$$

Here, u_c is the contact potential difference and u is the voltage at the contact. We assume that u_c is the same, irrespective of the size and shape of the contact. Figure 1a shows a cross section of the nanocontact placed into the semiconductor either by a plane passing through the center of the metallic sphere or by a plane normal to the symmetry axis of the metallic cylinder. The boundary conditions are supplemented by the condition defining the shape of the Ω_2 surface,

$$\nabla\varphi(r)|_{\Omega_2} = 0. \tag{4}$$

Such a formulation of the problem makes it possible to calculate the potential distribution around a nanocontact with sufficient accuracy, to determine the contact capacitance and its voltage dependence, and to deter-

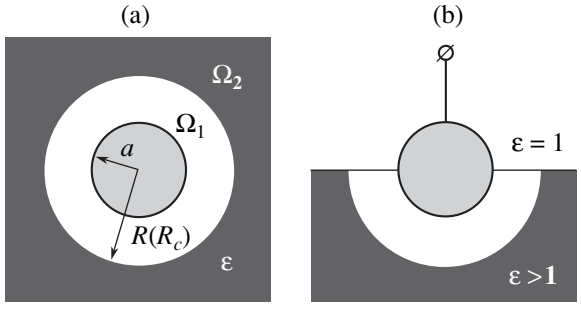

Fig. 1. Cross sections of nanocontacts in the form of a metallic sphere or a metallic cylinder of radius a (a) in a bulk semiconductor and (b) at the boundary of a semi-infinite semiconductor.

1063-7826/04/3809-1047$26.00 © 2004 MAIK "Nauka/Interperiodica"

mine the magnitude of the decrease in the height of the Schottky barrier due to the image forces.

The solution of problem (1)–(4) for $N = 0$ also remains valid for the case in which a metallic sphere or cylinder is half-immersed in the semiconductor, as shown in Fig. 1b. Evidently, if $N \neq 0$ and if the band bending at the interface between the semiconductor and air (free space) may be disregarded, then the solution of the problem of a nanocontact introduced into the bulk of the semiconductor (Fig. 1a) can be approximately reduced to the situation shown in Fig. 1b; i.e., we believe that the results obtained can roughly describe the electrical properties of metallic nanocontacts at the semiconductor surface as well. An example of current interest is contact atomic force microscopy with simultaneous measurement of the current–voltage characteristics through the conducting probe and the sample [5].

2. POTENTIAL DISTRIBUTION AND PROPERTIES OF SPHERICAL CONTACTS

For a metallic sphere of radius a in the semiconductor, we solve Eq. (1) in spherical coordinates with the origin at the center of the sphere with boundary conditions (2)–(4). In this case, Ω_1 is a sphere of radius $r = a$. In view of the symmetry of the problem, Ω_2 is also a sphere of radius $r = R$ (Fig. 1a). The solution is easily found as

$$\varphi(r) = (u_c - u)\left[\frac{a^2}{3S^2}\left(1 - \frac{r^2}{a^2}\right) + \frac{2R^3}{3aS^2}\left(1 - \frac{a}{r}\right)\right]. \quad (5)$$

Here,

$$S = \sqrt{\frac{\varepsilon(u_c - u)}{2\pi eN}}$$

is the width of the region of full depletion in the semiconductor for an infinite planar contact and quantity R is the solution of the equation

$$2R^3 - 3aR^2 - 3aS^2 + a^3 = 0. \quad (6)$$

The only real solution to Eq. (6) is given by the following expression:

$$R = \frac{a}{2} + \frac{a^2}{2\left(2\sqrt{3}\sqrt{3a^2S^4 - a^4S^2} + 6aS^2 - a^3\right)^{1/3}} + \frac{1}{2}\left(2\sqrt{3}\sqrt{3a^2S^4 - a^4S^2} + 6aS^2 - a^3\right)^{1/3}. \quad (7)$$

It is convenient to introduce the width of the region of full depletion in the semiconductor around the metallic sphere, $l = R - a$. For the quantity l, we then obtain the equation

$$a = \frac{2}{3}\frac{l^3}{S^2 - l^2}. \quad (8)$$

It follows from Eq. (8) that if the radius of the sphere $n \longrightarrow \infty$, then $l \longrightarrow S$; this limit corresponds to the transition to the planar problem. As $a \longrightarrow 0$, we have $l \longrightarrow 0$, and as l becomes much smaller than S, we obtain

$$l = \left(\frac{3}{2}aS^2\right)^{1/3} \gg a. \quad (9)$$

The contact capacitance is easily calculated,

$$C(u) = \frac{dQ}{d(u_c - u)} = 4\pi eNR^2\frac{dR}{d(u_c - u)}, \quad (10)$$

where Q is the charge of the depletion area in the semiconductor. Using (6), we obtain

$$C(u) = a\varepsilon\frac{R(u)}{R(u) - a} = a\varepsilon\left(1 + \frac{a}{l(u)}\right). \quad (11)$$

For $a \longrightarrow \infty$, $l \longrightarrow S$, we have

$$C(u) \longrightarrow \frac{a^2\varepsilon}{S(u)} = \frac{\sigma\varepsilon}{4\pi S(u)} \propto (u_c - u)^{1/2},$$

where σ is the area of the sphere of radius a; i.e., we obtain the capacitance of a planar Schottky contact with surface area σ. If $a \ll l < S$, then the quantity $C \approx a\varepsilon$ becomes equal to the capacitance of a sphere in an insulator and does not depend on the applied voltage.

Using (5) and taking into account the potential of interaction of an electron with its image in the metallic sphere, we obtain the electron potential energy

$$V(x) = e(u_c - u) \times \left[\frac{a^2}{3S^2}\frac{x}{a}\left(2 + \frac{x}{a}\right) - \frac{2R^3}{3aS^2}\frac{x}{x + a} - \frac{2c}{x\left(2 + \frac{x}{a}\right)}\right]. \quad (12)$$

Here, $x = r - a$ is the distance from the metallic surface, and

$$c = \frac{e}{4\varepsilon(u_c - u)}$$

is a parameter that has the dimension of length and describes the scale of the potential of image forces. At reverse and small forward voltages for all semiconductors, we have $c < 1$ nm. The third term in the square brackets in (12) is important only for $x \leq c$. Since $c \ll a$, the term $\frac{x}{a}$ in the denominator can be disregarded. Moreover, if we are interested only in the form of the potential energy near the metallic sphere for x smaller than or on the order of a, then for $a \ll S$, we can disregard the first term in the square brackets in (12). Thus, in the vicinity of a reasonably small metallic sphere, we can always disregard the electric field created by the space charge in the semiconductor compared to the

field of the surface charge of the sphere. Thus, for values of x smaller than or on the order of a, we obtain the following approximate expression for the electron potential energy:

$$V(x) \approx -e(u_c - u)\left[g\frac{x}{x+a} + \frac{c}{x}\right]. \quad (13)$$

Here, we introduce the notation

$$g = \frac{2R^3}{3aS^2}.$$

Using (7), we can expand the parameter g into a series in powers of a/S:

$$g = 1 + \left(\frac{3}{2}\frac{a}{S}\right)^{2/3} + \left(\frac{3}{2}\right)^{1/3}\left(\frac{a}{S}\right)^{4/3} + \ldots. \quad (14)$$

It follows that, for $a \ll S$, the parameter $g \approx 1$ and weakly depends on voltage and impurity concentration. In the expression for the lowering of the barrier height due to image forces

$$\Delta V = e(u_c - u)\left(2\sqrt{\frac{cg}{a}} - \frac{c}{a}\right), \quad (15)$$

we can disregard the small term c/a, so

$$\Delta V \approx 2e(u_c - u)\sqrt{\frac{cg}{a}}. \quad (16)$$

Thus, if $a \ll S$, we can assume that $g = 1$ and is independent of the voltage applied to the contact. This is equivalent to disregarding the space charge in the semiconductor. In this case, we have

$$\Delta V = 2e(u_c - u)\sqrt{\frac{c}{a}} = \sqrt{\frac{e^3(u_c - u)}{a\varepsilon}} \propto (u_c - u)^{1/2}. \quad (17)$$

This expression differs from the corresponding dependence for a planar Schottky contact [11]:

$$\Delta V_p = 2e(u_c - u)\sqrt{\frac{2c}{S}} = \left(\frac{8\pi N e^7 (u_c - u)}{\varepsilon^3}\right)^{1/4} \propto (u_c - u)^{1/4}, \quad (18)$$

Comparing (17) and (18), we see that, in the case of a small spherical contact, the decrease in the barrier height ΔV is greater than for a planar contact,

$$\frac{\Delta V_p}{\Delta V} = \sqrt{\frac{2a}{S}} \ll 1,$$

its voltage dependence is stronger, and there is no dependence on the impurity concentration N.

If a is smaller but on the order of S, then the contribution of the electric field of the space charge in the semiconductor to the total field near the potential energy maximum becomes appreciable. Therefore, in expansion (14) we cannot disregard the terms that follow unity. Thus, the quantity g becomes appreciably greater than unity and begins to depend on the voltage and N.

3. POTENTIAL DISTRIBUTION AND PROPERTIES OF CYLINDRICAL CONTACTS

For an infinite metallic cylinder of radius a in the semiconductor, we solve Eq. (1) in cylindrical coordinates (the z axis is the symmetry axis of the cylinder) with conditions (2)–(4). Now Ω_1 is the surface of the cylinder of radius $r = a$, and Ω_2 is the surface of the cylinder of radius $r = R_c$ (Fig. 1a). We obtain the solution

$$\varphi(r) = (u_c - u)\left[\frac{a^2}{2S^2}\left(1 - \frac{r^2}{a^2}\right) + \frac{R_c^2}{S^2}\ln\left(\frac{r}{a}\right)\right], \quad (19)$$

where R_c and the width l_c of the region of full depletion are determined from the equations

$$\frac{R_c^2}{S^2}\ln\left(\frac{R_c}{a}\right) = 1 - \frac{a^2}{2S^2} + \frac{R_c^2}{2S^2}, \quad (20)$$

$$\ln\left(1 + \frac{l_c}{a}\right) = \frac{1}{2} + \frac{2S^2 - a^2}{2(l_c + a)^2}. \quad (21)$$

It follows from (21) that, if the radius of the cylinder $a \longrightarrow \infty$, $l_c \longrightarrow S$. As $a \longrightarrow 0$, l_c tends to zero logarithmically slowly, so $l_c \approx S$ for any physically reasonable values of the radius.

Proceeding in the same way as in the spherical case, we obtain the capacitance per unit length of the cylinder:

$$C(u) = \frac{\varepsilon}{2\ln\left(1 + \frac{l_c(u)}{a}\right)}. \quad (22)$$

As $a \longrightarrow \infty$, we have $l_c \approx S$, and the solution turns into that for a planar Schottky contact. If $a \ll S$, then

$$C(u) \approx \frac{\varepsilon}{2}\left[\ln\frac{l_c(u)}{a}\right]^{-1};$$

this value is slightly voltage-dependent.

Using (19) and taking into account the potential of interaction of an electron with its image in the plane, we obtain the electron potential energy

$$V(x) = e(u_c - u)\left[\frac{a^2}{2S^2}\frac{x}{a}\left(2 + \frac{x}{a}\right) - \frac{R_c^2}{S^2}\ln\left(1 + \frac{x}{a}\right) - \frac{c}{x}\right]. \quad (23)$$

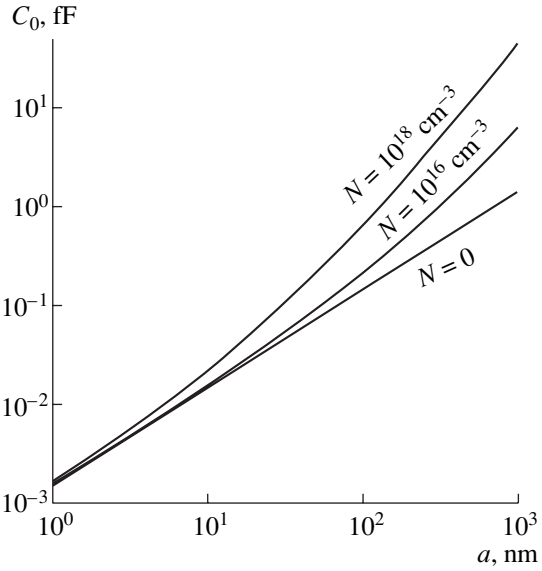

Fig. 2. Capacitance C_0 of a spherical contact (for $u = 0$, $u_c = 0.7$ V, $\varepsilon = 13.1$) as a function of the radius a for different impurity concentrations N.

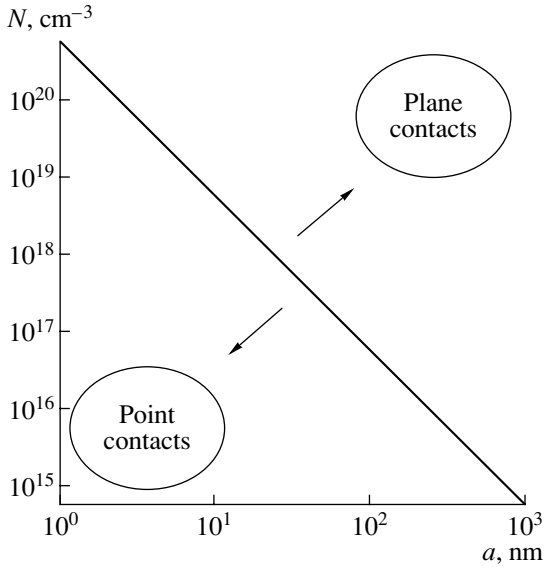

Fig. 3. Plane of the parameters N, a. The straight line corresponds to equality of the radius of the metallic sphere and the width of the depletion region around it ($a = l$). Above and away from this line, the parameters correspond to a planar contact; below and away from the line, $a = l$ corresponds to a point contact.

If $a \ll S$, then for values of x smaller than or on the order of a we obtain

$$V(x) = -e(u_c - u)\left[g_c \ln\left(1 + \frac{x}{a}\right) + \frac{c}{x}\right], \qquad (24)$$

where

$$g_c = \frac{R_c^2}{S^2}.$$

The decrease in the barrier height with allowance for the forces of interaction of images is

$$\Delta V_c \approx 2e(u_c - u)\sqrt{\frac{cg_c}{a}}. \qquad (25)$$

Since $g_c < g$, the decrease in the barrier height is smaller for a cylindrical contact than for a spherical one.

4. DISCUSSION

Evidently, the effects related to nonplanarity or small size are more pronounced in the spherical contact. We will consider their characteristics in more detail.

Figure 2 shows the dependence of the contact capacitance C_0 (for $u = 0$) on the radius of the metallic sphere a for various impurity concentrations N. This dependence is calculated for GaAs ($u_c = 0.7$ V, $\varepsilon = 13.1$) using (7) and (11). It can be seen from Fig. 2 that, for small $a \ll l$, the capacitance is almost independent of the doping level and $C_0 \propto a$. In this case, it follows from (11) that the capacitance C is practically independent of voltage. For $a/l \longrightarrow \infty$, the capacitance C is proportional to the area of the contact, depends on N, and varies with voltage as $C(u) \propto (u_c - u)^{-1/2}$, as in the case of planar geometry. The situation where $a \approx l$ is intermediate. Figure 3 shows the plane of the parameters N and a divided into two parts by the line at which $a = l$ (on this line $l = S\sqrt{\frac{3}{5}}$). As we move away from this line downwards (where $a \ll l$), we come to the domain of parameters in which the impurity concentration plays no role. In contrast, as we move away from this line upwards (where $a \gg l$), the curvature of the contact and the edge effects are not important.

In Fig. 4, we show the dependences of the decrease in the barrier height ΔV on the applied voltage (Fig. 4a) and on the doping impurity concentration (Fig. 4b) for various radii of the sphere. The curves are calculated for GaAs ($u_c = 0.7$ V) using relations (4), (14), and (16). In Fig. 4a, the impurity concentration is $N = 10^{16}$ cm^{-3} [$S(0) = 320$ nm], and in Fig. 4b for all curves we have $u = 0$. We can see from Fig. 4a that the lowering of the barrier height in the case of small-radius spheres is much greater and depends more heavily on voltage than in the planar case ($a = \infty$). For spherical contacts, the dependence of ΔV on the concentration of the doping impurity in Fig. 4b remains weak until the width of the planar depletion region S becomes equal to a.

Finally, we can estimate the speed of response of a metal–semiconductor nanocontact. We calculate the

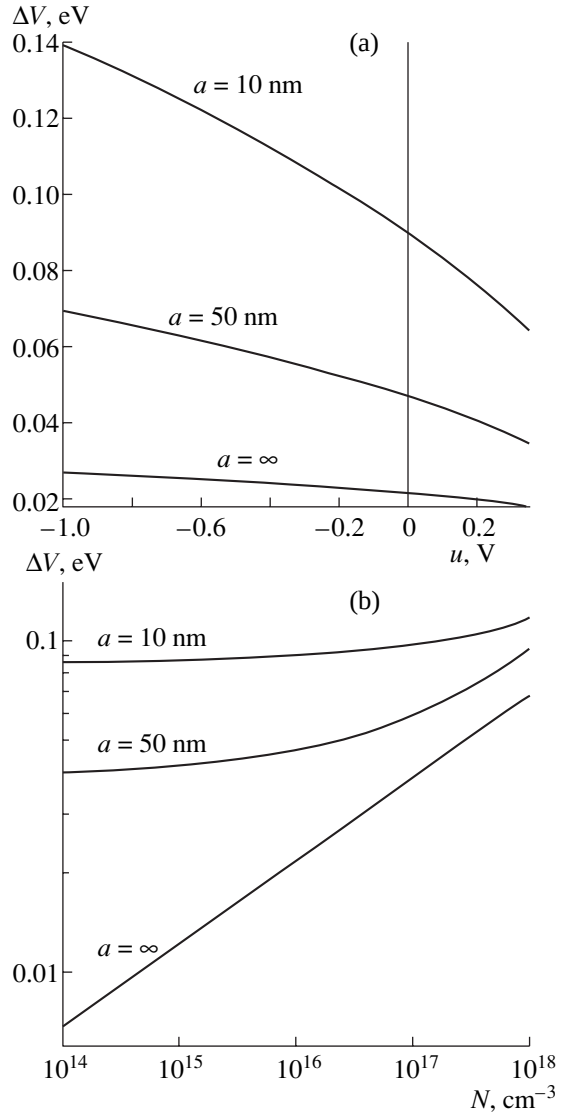

Fig. 4. Dependence of the decrease in the barrier height ΔV for spherical contacts of different radii (a) on the applied voltage ($N = 10^{16}$ cm^{-3}, $u_c = 0.7$ V, $\varepsilon = 13.1$) and (b) on the concentration of the doping impurity ($u = 0$, $u_c = 0.7$ V, $\varepsilon = 13.1$).

dependence of the critical frequency

$$f_C = \frac{1}{2\pi r_S C_0}$$

on the radius a of the sphere for different doping levels [10]. Here, r_S is the spreading resistance of the semiconductor outside the depletion region equal to

$$r_S = \frac{\rho}{4\pi R(0)},$$

where ρ is the resistivity of the semiconductor. For $a \longrightarrow 0$, we have $f_C \propto a^{-2/3}$, and for $a \longrightarrow \infty$, we obtain $f_C \propto a^{-1}$. The results of the calculations for GaAs are shown in Fig. 5. We can see that the critical frequency depends heavily on a and reaches the terahertz range even at relatively low doping levels (~10^{15}–10^{16} cm^{-3}).

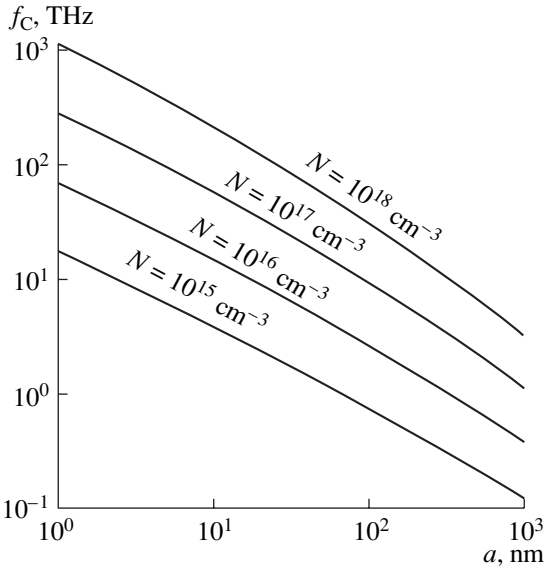

Fig. 5. Dependence of the critical frequency f_C on the radius of the sphere a at different GaAs doping levels ($u_c = 0.7$ V).

5. CONCLUSIONS

We calculated potential distributions in a semiconductor around spherical and cylindrical nanocontacts in the approximation of full depletion. We also analyzed the electrical properties of nanocontacts of small characteristic size $a \ll S$ (S is the width of the depletion region in the planar geometry).

The calculations show that the width of the depletion region around a nanoparticle $l \gg a$, thus ensuring small contact capacitance and its weak dependence on voltage and doping impurity concentration.

Compared to the planar case, a stronger electric field near the metallic nanoparticle produces a greater decrease in the height of the potential barrier due to the image forces and a stronger dependence of the decrease in the barrier height on the applied voltage. The form of the potential near the metal is mainly determined by the field of charges at the metal–semiconductor interface, and the field of the space charge of impurities in the semiconductor is unimportant, thus resulting in a weak dependence of the decrease in the barrier height on the doping level.

The critical frequency of a Schottky nanocontact reaches the terahertz region even at rather low doping levels (~10^{15}–10^{16} cm^{-3}), which is indicative of a fast response.

REFERENCES

1. Takhee Lee, Jia Liu, Nien-Po Chen, *et al.*, J. Nanoparticle Res. **2**, 345 (2000).
2. G. D. J. Smit, S. Rogge, and T. M. Klapwijk, Appl. Phys. Lett. **81**, 3852 (2002).
3. G. D. J. Smit, M. G. Flokstra, S. Rogge, and T. M. Klapwijk, Microelectron. Eng. **64**, 429 (2002).
4. Hideki Hasegawa, Taketomo Sato, and Chinami Kaneshiro, J. Vac. Sci. Technol. B **17**, 1856 (1999).
5. I. Tanaka, I. Kamiya, and H. Sakaki, J. Cryst. Growth **201/202**, 1194 (1999).
6. Kian-Giap Gan, Jin-Wie Shi, Yen-Hung Chen, *et al.*, Appl. Phys. Lett. **80**, 4054 (2002).
7. I. Aberg, K. Deppert, M. H. Magnusson, *et al.*, Appl. Phys. Lett. **80**, 2976 (2002).
8. N. V. Vostokov, V. M. Danil'tsev, M. N. Drozdov, *et al.*, in *Proceedings of Workshop on Nanophotonics* (Nizhni Novgorod, 2003), p. 363.
9. A. C. Warren, J. M. Woodall, J. L. Freeout, *et al.*, Appl. Phys. Lett. **57**, 1331 (1990).
10. S. Sze, *Physics of Semiconductor Devices*, 2nd ed. (Wiley, New York, 1981; Mir, Moscow, 1984).
11. E. H. Rhoderick and R. H. Williams, *Metal–Semiconductor Contacts*, 2nd ed. (Clarendon, Oxford, 1988; Radio i Svyaz', Moscow, 1982).

Translated by I. Zvyagin

Semiconductors, Vol. 38, No. 9, 2004, pp. 1053–1060. Translated from Fizika i Tekhnika Poluprovodnikov, Vol. 38, No. 9, 2004, pp. 1090–1096.

LOW-DIMENSIONAL SYSTEMS

Effect of Electron–Electron and Electron–Hole Collisions on Intraband Population Inversion of Electrons in Stepped Quantum Wells

V. L. Zerova*^, G. G. Zegrya, and L. E. Vorob'ev***

** St. Petersburg State Polytechnical University, St. Petersburg, 195251 Russia*

*** Ioffe Physicotechnical Institute, Russian Academy of Sciences, St. Petersburg, 194021 Russia*

^ e-mail: VZerova@rphf.spbstu.ru

Submitted January 21, 2004; accepted for publication January 26, 2004

Abstract—The effect of intersubband electron–electron (*e–e*) and electron–hole (*e–h*) scattering on intraband population inversion of electrons in a stepped InGaAs/AlGaAs quantum well is investigated. The characteristic times of the most probable *e–e* and *e–h* processes, which affect the electron densities on the excited levels, are calculated for the temperature range 80–300 K. Dependences of these times on the electron and hole density on the ground levels are studied. Temperature dependences of the intraband inversion of population for two nonequilibrium densities are calculated by solving a system of rate equations. It is shown that the intersubband *e–e* and *e–h* scattering only slightly affects the population inversion for electron densities below 1×10^{12} cm^{-2}.

1. INTRODUCTION

Population inversion can be created between the quantum well (QW) subbands in QW lasers for the mid-IR range. The possibility of obtaining intersubband population inversion in QWs is defined primarily by the ratio between the rates of different nonradiative intersubband transitions. This ratio is strongly dependent on the density of nonequilibrium carriers in QWs, which is controlled by the design of the laser and the parameters of its cavity, waveguide, and QWs. At high carrier densities, electron–electron (*e–e*) and electron–hole (*e–h*) scattering can play the role of the main nonradiative processes [1, 2].

In this study, we investigate the effect of intersubband *e–e* and *e–h* scattering on population inversion in the InGaAs/AlGaAs heterostructure suggested in [3] (Fig. 1). Nonequilibrium carriers are generated in wide-gap regions by an electric injection or band-to-band optical excitation. For the injected electrons, the calculated probability of their capture from the continuum to level *e*3 is much higher than that to *e*2. The special configuration of QWs provides a long lifetime of captured electrons on level *e*3 with respect to intersubband scattering with the emission of optical phonons. The lifetime on level *e*2 is small because of the large overlap between the electron wave functions of the second and first levels. Therefore, population inversion arises between levels *e*3 and *e*2. Nonequilibrium electrons and holes are accumulated on levels *e*1 and *hh*1, because in this structure the band-to-band recombination time is much longer than the intersubband relaxation time. The parameters of a stepped QW (Fig. 1) are $z < 0$, the region of the $Al_{0.28}Ga_{0.72}As$ barrier; $0 < z < a$, the $Al_{0.26}Ga_{0.74}As$ layer with width $L_1 = 3.8$ nm; $a < z < b$, the $In_{0.24}Ga_{0.76}As$ strained layer, $L_{NW} = 6.8$ nm; $b < z < c$, the $Al_{0.26}Ga_{0.74}As$ layer, $L_2 = 11.4$ nm; and $z > c$, the region of the $Al_{0.28}Ga_{0.72}As$ barrier [3]. The energies of the electron and heavy-hole levels in this QW are reckoned from the edges of the *c* and *v* bands of the narrow-gap semiconductor; they are $\mathscr{E}_{e1} = 60$ meV, $\mathscr{E}_{e2} = 230$ meV, $\mathscr{E}_{e3} = 346$ meV, $\mathscr{E}_{hh1} = 16$ meV, $\mathscr{E}_{hh2} = 62$ meV, and $\mathscr{E}_{hh3} = 135$ meV.

Preliminary estimates show that the expected threshold current density for intraband emission in this structure is rather high (>10 kA cm^{-2}) [3]. At this current, the density of nonequilibrium carriers in a QW, which defines the rates of *e–e* and *e–h* interactions, can be high. However, if a stimulated band-to-band emission arises in the structure, these densities cease to increase with a rise in current. The band-to-band emission of GaAs-based injection lasers usually corresponds to the near-infrared (NIR) range, and the average threshold current density J_{th}^{NIR} exceeds 0.1 kA cm^{-2}. The threshold carrier density for NIR-stimulated emission can be high. Consequently, the probabilities of intersubband *e–e* and *e–h* scattering may become comparable with the probabilities of intersubband electron–phonon scattering, which can reduce the population inversion between levels *e*3 and *e*2.

In this study, we investigate the effect of intersubband *e–e* and *e–h* scattering on intraband population inversion for different possible densities of nonequilibrium carriers in QWs, corresponding to the threshold of band-to-band emission. It is shown that in these hetero-

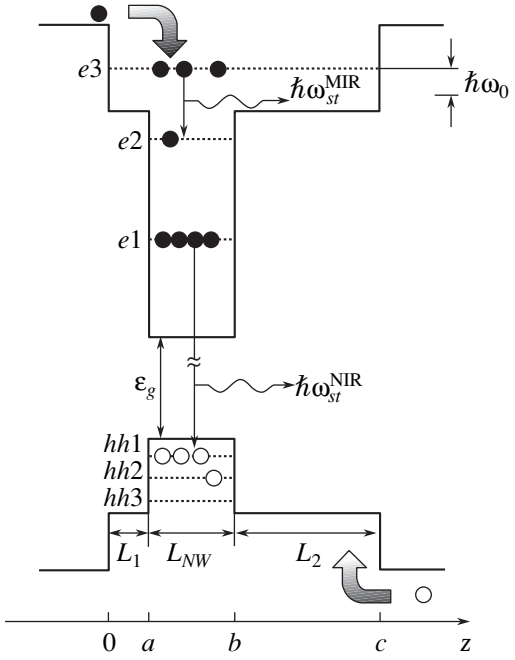

Fig. 1. Potential profile, energy levels of electrons *ei* and heavy holes *hhi*, and stimulated optical transitions in a stepped QW. $\hbar\omega_{st}^{MIR}$ is the energy of intersubband stimulated emission of the mid-IR range; $\hbar\omega_{st}^{NIR}$, the energy of band-to-band near-IR stimulated emission of the near-IR range; and $\hbar\omega_0$, the energy of a polar optical phonon.

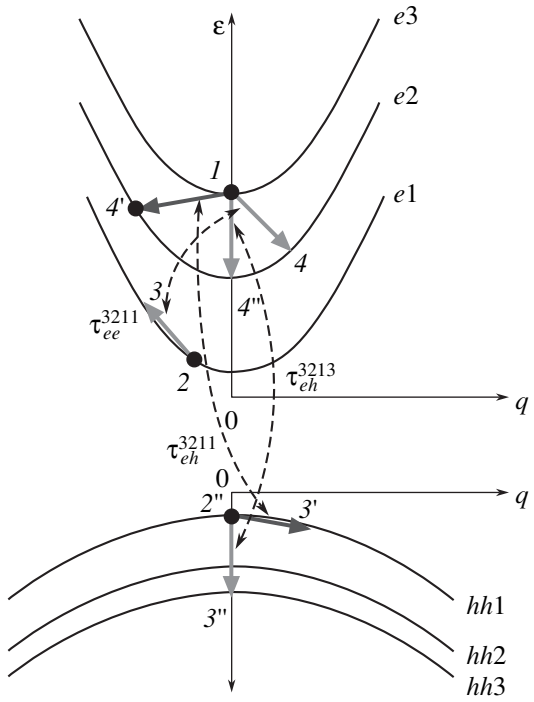

Fig. 2. Principal intersubband *e–e* and *e–h* processes in a stepped QW, which lead to the departure of electrons from the third subband. Numbers *i* = 1, 2, 3, and 4 indicate the initial and final states of interacting carriers for *e–e* transition 3211; *i*' = 1, 2', 3', and 4' indicate the same for *e–h* process 3211; *i*'' = 1, 2', 3'', and 4'', the same for *e–h* process 3213.

structures, at densities ranging up to 5×10^{12} cm^{-2}, the characteristic times of the fastest *e–e* and *e–h* scattering processes are large compared to those for scattering on optical phonons, which determines the population inversion between levels *e*3 and *e*2. This relationship is retained in the temperature range 80–300 K. Thus, we show that the *e–e* and *e–h* processes only slightly affect the population inversion in the heterostructures under study.

2. CALCULATION OF PROBABILITIES OF *e–e* AND *e–h* SCATTERING

Electron–electron and electron–hole collisions can either reduce or enhance the intersubband population inversion of electrons in QWs. The inversion is reduced by the processes in which an electron passes from subband *e*3 to *e*2 (Fig. 2). This transition most probably occurs via interaction with an electron in subband *e*1 or a heavy hole in subband *hh*1, because carriers are accumulated at the lowest levels [4]. In this case, the energy of an electron or hole in the ground subband will increase within the subband. These processes are denoted as 3211. Similar processes that cause the electron transition *e*2 ⟶ *e*1 (2111) empty level *e*2; consequently, they stimulate the inversion.

The probability of processes with an electron transition from the ground subband to higher-lying subbands is low [2, 4], because the energy of these transitions is high (more than 150 meV for the heterostructure under study). The distance between hole subbands is less than that between electron subbands; therefore, along with 3211 and 2111 *e–h* processes, *e–h* processes with intersubband transitions of holes also occur, and their probability is higher. Among these processes, the most probable seems to be the hole transition *hh*1 ⟶ *hh*3 (3213), because its energy is close to that of the electron transition *e*3 ⟶ *e*2. This means that process 3213 may be resonant, and it will proceed with the transfer of a small wave vector. The role of 3212 and 2112 *e–h* processes may also be significant.

To calculate the rates of *e–e* and *e–h* processes, a multiband approximation must be used for the wave functions of carriers [5]. In this situation, the effective Hamiltonian must take into account the admixture of $|\mathbf{p}\rangle$ states of holes to electron $|\mathbf{s}\rangle$ states. This specific feature of the energy spectrum and the wave functions of electrons in QWs is well described by Kane's model [6]. The wave functions and energy spectrum of electrons in stepped QWs can be determined by using Kane's model for each of the quantum-confined layers [4]. In each layer of a stepped QW, the solution to the system of Kane's equations is determined by the poten-

tials of c and v bands and the effective mass of electrons in the material.

In first-order perturbation theory, the rate of Auger processes is given by

$$G = \frac{2\pi}{\hbar}\sum_{\mathbf{q}_1,\mathbf{q}_2,\mathbf{q}_3,\mathbf{q}_4}|M|^2 f(\mathbf{q}_1)f(\mathbf{q}_2)[1-f(\mathbf{q}_3)] \times[1-f(\mathbf{q}_4)]\delta(\mathscr{E}_{q1}+\mathscr{E}_{q2}-\mathscr{E}_{q3}-\mathscr{E}_{q4}), \quad (1)$$

where M is the matrix element of e–e or e–h interaction; $f(\mathbf{q}_i)$, the energy distribution function of electrons with the wave vector $\mathbf{q}_i$; $\mathscr{E}_{q1}$ and $\mathscr{E}_{q2}$, the energies of the initial states; and $\mathscr{E}_{q3}$ and $\mathscr{E}_{q4}$, the energies of the final states. The summation is done over all the initial and final states of electrons.

The matrix element of the Coulomb e–e interaction can be used disregarding the screening [7, 4]. The dispersion law near the bottom of subbands is assumed to be parabolic. At a high carrier density, the distribution function of electrons can be assumed to be quasi-equilibrium within each separate subband [8, 9, 4]. The final states of electrons and holes, which are described by wave vectors $\mathbf{q}_4$ and $\mathbf{q}_3$, are, with high probability, free in all transitions of the types discussed above, and the corresponding filling factors $[1 - f(\mathbf{q}_3)]$ and $[1 - f(\mathbf{q}_4)]$ are close to unity. In the interaction, the conservation laws for the energy and longitudinal component of the wave vector of carriers have the form

$$\mathscr{E}_{q1}+\mathscr{E}_{q2}=\mathscr{E}_{q3}+\mathscr{E}_{q4}, \quad \mathbf{q}_1+\mathbf{q}_2=\mathbf{q}_3+\mathbf{q}_4. \quad (2)$$

As shown in [4], the probability of 3211 and 2111 e–e processes is the highest at certain intermediate energies and wave vectors transferred in the interaction:

$$k_\mathrm{B}T \ll \mathscr{E}_{q3}-\mathscr{E}_{q2} \le \Delta_e, \qquad q_T^e \ll |\mathbf{q}_3-\mathbf{q}_2| \le \sqrt{2m_e\Delta_e/\hbar^2}, \quad (3)$$

where T is the lattice temperature; k_B, the Boltzmann constant; $q_T^2 = \sqrt{2m_e k_\mathrm{B}T/\hbar^2}$, the magnitude of the thermal wave vector of an electron; m_e, the electron effective mass in a narrow-gap semiconductor; and Δ_e, the energy spacing between the subbands among which electrons are redistributed (for transition 3211, $\Delta_e \equiv \Delta_e^{32}$; for 2111, $\Delta_e \equiv \Delta_e^{21}$). Therefore, the following approximations can be used in the calculation of the e–e scattering rate:

$$|\mathbf{q}_4|, |\mathbf{q}_3| \gg |\mathbf{q}_1|, |\mathbf{q}_2|, \quad q_4^2 \approx q_3^2. \quad (4)$$

This conclusion is also valid for 3211 and 3212 e–h processes. In 3213 e–h process in the QWs under study, the energies of electron $e3 \longrightarrow e2$ and hole $hh1 \longrightarrow hh3$ transitions are close ($\Delta_e^{32} \approx \Delta_h^{13}$); therefore this process can proceed with the wave vector unchanged:

$$|\mathbf{q}_1-\mathbf{q}_4| \approx 0. \quad (5)$$

The energy transferred in a 3213 process remains high—on the order of Δ_e. However, unlike 3211 and 3212 processes, the energy conservation law can be obeyed by holes near the bottom of a subband, and there is a great quantity of them.

To calculate the rate of 3211 e–h process G_{eh}^{3211}, we first sum over $\mathbf{q}_4$ in (1) using the Kronecker δ function:

$$G_{eh}^{3211} = \frac{2\pi}{\hbar}\left(\frac{4\pi e^2}{2\pi\varepsilon_0}\right)^2 \sum_{\mathbf{q}_1,\mathbf{q}_2,\mathbf{q}_3}\left|\int_{q_z}\frac{I_z^{14}(q_z)I_z^{23}(q_z)}{(\mathbf{q}_3-\mathbf{q}_2)^2+q_z^2}dq_z\right|^2 \times f(q_1)f(q_2)\delta\left(\frac{\hbar^2q_1^2}{2m_e}+\frac{\hbar^2q_2^2}{2m_h}-\frac{\hbar^2q_3^2}{2}\left(\frac{1}{m_e}+\frac{1}{m_h}\right)+\Delta\right), \quad (6)$$

where m_h is the effective mass of a heavy hole in the narrow-gap semiconductor; q_z, the magnitude of the wave vector transferred in the interaction in the z direction normal to the heterointerface; e, the elementary charge; ε_0, the static dielectric constant of the semiconductor; and the integrals $I_z^{14}(q_z)$ and $I_z^{23}(q_z)$ are defined by the overlap of envelopes of wave functions $\psi_{qi}(z)$ in the z direction of the initial and final states of electrons and holes, respectively:

$$I_z^{14}(q_z) = \int\psi_{q1}^*(z)\psi_{q4}(z)e^{iq_zz}dz, \qquad I_z^{23}(q_z) = \int\psi_{q2}^*(z)\psi_{q3}(z)e^{-iq_zz}dz. \quad (7)$$

We replace the remaining summations (over $\mathbf{q}_1$, $\mathbf{q}_2$, and $\mathbf{q}_3$) by integrations. Owing to approximation (4), the integrand contains no dependences on angles between vectors $\mathbf{q}_1$, $\mathbf{q}_2$, and $\mathbf{q}_3$. We then integrate over q_1^2 with the use of the δ function:

$$G_{eh}^{3211} = \frac{2\pi}{\hbar}\frac{1}{(2\pi)^3}\left(\frac{4\pi e^2}{2\pi\varepsilon_0}\right)^2\frac{2m_e}{\hbar^2} \times\frac{1}{2}\int_{q_{2\min}}^{q_{2\max}}q_2dq_2\int_{q_{3\min}}^{q_{3\max}}q_3dq_3\left|\int_{q_z}\frac{I_z^{14}(q_z)I_z^{23}(q_z)}{q_3^2+q_z^2}dq_z\right|^2\frac{n_3}{N_c} \times\exp\left(-\frac{\hbar^2\alpha(q_2,q_3)}{2m_ek_\mathrm{B}T}\right)\frac{p_1}{N_v}\exp\left(-\frac{\hbar^2q_2^2}{2m_hk_\mathrm{B}T}\right), \quad (8)$$

where p_1 and n_i (i = 2 and 3, respectively, for the electron transitions from subbands $e2$ and $e3$) are the hole and electron densities in subbands to which the initial states of the interacting electron and hole belong; $N_c = m_ek_\mathrm{B}T/\pi\hbar^2$ and $N_v = m_hk_\mathrm{B}T/\pi\hbar^2$, the 2D densities of

states in the conduction and valence bands, respectively; and

$$\alpha(q_2, q_3) = q_3^2\frac{m_e + m_h}{m_h} - q_2^2\frac{m_e}{m_h} - \frac{2m_e\Delta_e}{\hbar^2}. \quad (9)$$

We perform integration over q_2 and q_3 in (8) and over q_z and z numerically. The integration over q_2 will be performed within the limits from $q_{2\min} = 0$ to $q_{2\max} = 2q_T^h$, where $q_T^h = \sqrt{2m_h k_B T/\hbar^2}$ is the thermal wave vector of a hole. The lower limit of integration over q_3 can be found using the inequalities $\alpha(q_2, q_3) \geq 0$ and $q_3 > q_2$:

$$q_{3\min}(q_2) = \sqrt{\frac{m_e}{m_e + m_h}\left(q_2^2 + \frac{2m_h\Delta_e}{\hbar^2}\right)}. \quad (10)$$

The upper limit of integration over q_3 corresponds to the maximum wave vector that can be transferred in the electron transition from state 1 to state 4; it is reckoned from the magnitude of the initial wave vector of hole q_2:

$$q_{3\max}(q_2) = q_2 + \sqrt{\frac{2m_e\Delta_e}{\hbar^2}}. \quad (11)$$

The rate of *e–h* process 2111, G_{eh}^{2111}, and the rates of 3212 and 2112 processes are calculated in the same way.

If we assume $m_h = m_e$ in this calculation, then expressions (8)–(10), which define the rate of *e–h* scattering, are transformed into relations for the *e–e* scattering rate G_{ee}^{3211} in transition 3211, obtained in [4].

Now we calculate the rate of the resonance *e–h* process with the intersubband hole transition 3213. Due to approximation (5), the momentum conservation law (2) for this transition is transformed into $\mathbf{q}_3 = \mathbf{q}_2$. Using the Kronecker function $\delta_{\mathbf{q}_3, \mathbf{q}_2}$, we sum expression (1) over $\mathbf{q}_3$:

$$G_{eh}^{3213} = \frac{2\pi}{\hbar}\left(\frac{4\pi e^2}{2\pi\varepsilon_0}\right)^2 \sum_{q_1, q_2, q_4}\left|\int_{q_z}\frac{I_z^{14}(q_z)I_z^{23}(q_z)}{q_z^2}dq_z\right|^2 \times f(q_1)f(q_2)\delta\left(\frac{\hbar^2 q_1^2}{2m_e} + \frac{\hbar^2 q_4^2}{2m_e} + \Delta_e^{32} - \Delta_h^{13}\right). \quad (12)$$

In contrast to (6), the denominator of the integrand in (12) does not contain the summand $|\mathbf{q}_3 - \mathbf{q}_2|^2$, which results in an increase in G_{eh}^{3213} compared with G_{eh}^{3211}. However, the overlap integral $I^{23}(q_z)$ for intersubband hole transitions is much less than the integral for intrasubband hole transitions, which results in a decrease in G_{eh}^{3213} compared with G_{eh}^{3211}.

Now we pass from the summation in (12) to integration over q_1^2, using the δ function:

$$G_{eh}^{3213} = \frac{2\pi}{\hbar}\frac{1}{(2\pi)^3}\left(\frac{4\pi e^2}{2\pi\varepsilon_0}\right)^2\frac{2m_e}{\hbar^2}\int_{q_2 = 0}^{\infty} q_2 f(q_2)dq_2 \times \int_{q_4 = 0}^{q_{4\max}} q_4 f(\alpha(q_4))dq_4\left|\int_{q_z}\frac{I_z^{14}(q_z)I_z^{23}(q_z)}{q_z^2}dq_z\right|^2, \quad (13)$$

where

$$\alpha(q_4) = q_4^2 - \frac{2m_e(\Delta_e^{32} - \Delta_h^{13})}{\hbar^2}. \quad (14)$$

The remaining integration over q_2 and q_4 can be done analytically and independently of one other. In the case of a Boltzmann distribution, we have

$$\int_{q_2 = 0}^{\infty} q_2 f(q_2)dq_2 = \frac{p_1}{N_v}\frac{m_h k_B T}{\hbar^2}, \quad (15)$$

$$\int_{q_4 = 0}^{q_{4\max}} q_4 f(\alpha(q_4))dq_4 = \frac{n_3}{N_c}\frac{m_e k_B T}{\hbar^2}\left[\exp\left(\frac{\Delta_e^{32} - \Delta_h^{13}}{k_B T}\right) - 1\right], \quad (16)$$

where the upper limit of integration over q_4 is determined from the condition $\alpha(q_4) \geq 0$:

$$q_{4\min}^2 = \frac{2m_e(\Delta_e^{32} - \Delta_h^{13})}{\hbar^2}. \quad (17)$$

Finally, we obtain the rate of the resonant *e–h* process 3213:

$$G_{eh}^{3213} = \frac{2\pi}{\hbar}\frac{1}{(2\pi)^3}\frac{1}{2}\left(\frac{4\pi e^2}{2\pi\varepsilon_0}\right)^2\frac{2m_e}{\hbar^2}\frac{p_1}{N_v}\frac{n_3}{N_c}\frac{m_e k_B T}{\hbar^2} \times \frac{m_h k_B T}{\hbar^2}\left[\exp\left(\frac{\Delta_e^{32} - \Delta_h^{13}}{k_B T}\right) - 1\right]\left|\int_{q_z}\frac{I_z^{14}(q_z)I_z^{23}(q_z)}{q_z^2}dq_z\right|^2. \quad (18)$$

Having calculated the rates of the Auger processes, we can determine the inverse times of *e–h* and *e–e* interactions:

$$\frac{1}{\tau} = \frac{G}{n_i}, \quad (19)$$

where $i = 2, 3$ is the number of the subband containing the initial state of an electron. It appears that the characteristic times τ for *e–h* processes depend on the hole density p_1 on level *hh*1, and for *e–e* processes they depend on the electron density n_1 on level *e*1.

3. RESULTS AND DISCUSSION

Figure 3 shows the calculated temperature dependences of characteristic times of *e–h* and *e–e* interactions τ_{ee}^{3211}, τ_{ee}^{2111}, τ_{eh}^{3211}, τ_{eh}^{2111}, τ_{eh}^{3212}, τ_{eh}^{2112}, and τ_{eh}^{3213} for the heterostructure under study with stepped QWs, for electron and hole densities in the main subbands $n_1 = p_1 = 5 \times 10^{11}$ cm^{-2}. These densities are close to the threshold densities for the onset of band-to-band emission. The *e–h* and *e–e* processes of 2111 type (at T = 80 K, $\tau_{eh}^{2111} \approx 7.8$ ps, $\tau_{ee}^{2111} \approx 8$ ps) have the highest probability. The characteristic times of type 3211 processes are significantly longer (at T = 80 K, $\tau_{eh}^{3211} \approx 70$ ps, $\tau_{ee}^{3211} \approx$ 47 ps). This fact is accounted for by the weak overlapping of the wave functions of states *e*3 and *e*2 and the strong overlapping of the wave functions of states *e*2 and *e*1, because of the stepped shape of the QW. The probabilities of *e–h* processes 3211 and 2111 are close to those for similar *e–e* processes.

The characteristic times τ_{eh}^{3212} and τ_{eh}^{2112} are longer than times τ_{eh}^{3211} and τ_{eh}^{2111}, respectively, due to a weaker overlapping of the wave functions of the initial and final states of holes, compared to those for intrasubband transition.

The characteristic time of the resonant *e–h* scattering τ_{eh}^{3213} is significantly longer than the times τ_{eh}^{3211} and τ_{eh}^{3212}, despite the fact that no wave vector is transferred in 3213 processes. The small probability of these transitions is accounted for by the weak overlapping of the wave functions of states *hh*1 and *hh*3.

Note that, in the temperature range under study at $n_1 = p_1 = 5 \times 10^{11}$ cm^{-2}, the characteristic times of *e–h* and *e–e* processes are significantly longer than the times of the main processes of intersubband ($ei \longrightarrow ej$) scattering of electrons on polar optical phonons, τ_{ph}^{ij} [4]. Their ratio determines the possibility of obtaining intersubband population inversion in a QW. This means that, at the given n_1 and p_1, the intrasubband Auger processes have only a weak impact on the degree of population inversion.

The temperature dependence of the rate of Auger processes is weak; it is defined by the temperature dependence of the distribution function and the limiting magnitudes of wave vectors $\mathbf{q}_2$ and $\mathbf{q}_3$. As the temperature increases, the relationship between the characteristic times τ_{eh}^{3211}, τ_{ee}^{3211}, τ_{eh}^{3212}, $\tau_{eh}^{3213} \gg \tau_{eh}^{2111}$, τ_{ee}^{2111}, τ_{eh}^{2112}, which ensures the weak influence of the Auger processes on the population inversion, is retained.

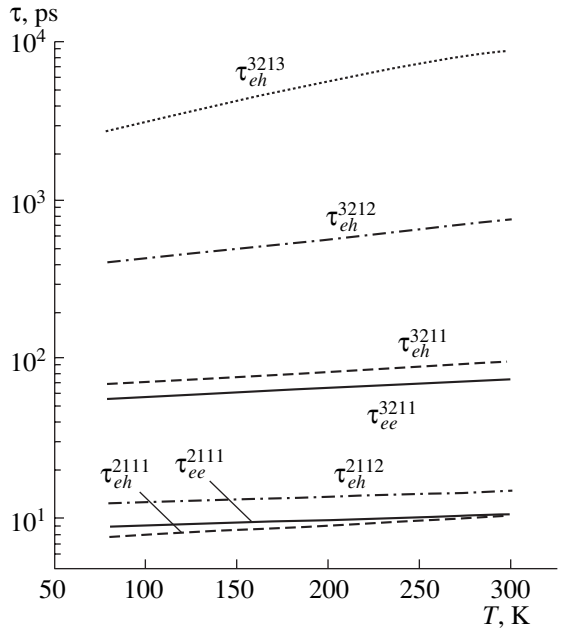

Fig. 3. Temperature dependence of the characteristic times of the main intersubband Auger processes in a stepped QW with nonequilibrium carrier density $n_1 = p_1 \approx 5 \times 10^{11}$ cm^{-2}.

4. CALCULATION OF THE INTERSUBBAND POPULATION INVERSION

To estimate the population inversion n_3–n_2 taking into account *e–e* and *e–h* interactions, we solve the system of rate equations that describe the density of carriers on the QW levels. These equations must include the rates of the main processes of electron–phonon, *e–e*, and *e–h* scattering; the rates of spontaneous and stimulated band-to-band emission in the near-IR range; and the rates of electron capture on QW levels. Note that the processes of spontaneous band-to-band emission must be taken into account at currents J below the threshold current for stimulated band-to-band emission ($J < J_{th}^{\mathrm{NIR}}$). At $J > J_{th}^{\mathrm{NIR}}$, they can be disregarded. As we established above, the main processes of *e–e* and *e–h* scattering are type 2111 and 3211 processes.

The electron capture in a QW is determined mainly by the interaction of electrons with polar optical phonons [3]. In this situation, the injected electrons are, with the highest probability, captured by level *e*3. The coefficients of electron capture in a QW to levels *e*1, *e*2, and *e*3 are $A_1 = 0.03$, $A_2 = 0.07$, and $A_3 = 0.9$ ($A_1 + A_2 + A_3 = 1$), respectively, and they are virtually temperature-independent. The rate of intersubband emission (both spontaneous and stimulated) in the mid-IR range is negligible compared with the rates of the processes listed above, and it can be disregarded in the calculation of population inversion.

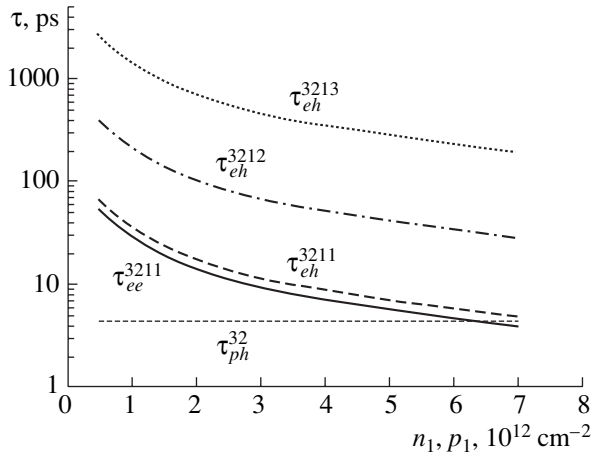

Fig. 4. Characteristic times of *e*–*e* and *e*–*h* scattering in intersubband transitions from the third level at $T = 80$ K as functions of the density $n_1 = p_1$. For comparison, the time of electron–phonon scattering τ_{ph}^{32}, which is independent of n_1 in terms of our model, is shown.

Therefore, in stationary conditions, the system of kinetic equations has the form

$$\frac{dn_3}{dt} = \eta J A_3 - \frac{n_3}{\tau_{ph}^{32}} - \frac{n_3}{\tau_{ph}^{31}} - G_{ee+eh}^{3211}(n_1, n_3) - \frac{n_3}{\tau_{sp}^{e3}} = 0, \quad (20)$$

$$\frac{dn_2}{dt} = \eta J A_2 + \frac{n_3}{\tau_{ph}^{32}} - \frac{n_2}{\tau_{ph}^{21}} + G_{ee+eh}^{3211}(n_1, n_3) - G_{ee+eh}^{2111}(n_1, n_2) - \frac{n_2}{\tau_{sp}^{e2}} = 0, \quad (21)$$

$$\frac{dn_1}{dt} = \eta J A_1 + \frac{n_3}{\tau_{ph}^{31}} + \frac{n_2}{\tau_{ph}^{21}} + G_{ee+eh}^{2111}(n_1, n_2) - \frac{n_1}{\tau_{sp}^{e1}} - B_{1st} N_\nu = 0, \quad (22)$$

where $G_{ee+eh} = G_{ee} + G_{eh}$, $n_1 = p_1$, and J is the driving current density (for optical band-to-band pumping, $J/e = P/h\nu$, where P is the intensity of pumping); the factor η defines the loss of electron–hole pairs in quantum-confined layers and barriers; τ_{sp}^{e1}, τ_{sp}^{e2}, and τ_{sp}^{e3} are the lifetimes on levels with respect to the band-to-band radiative recombination (spontaneous emission); N_ν is the density of photons emitted in band-to-band stimulated emission; and B_{1st} is the proportionality factor.

The last term in (22) describes the depletion of level $e1$ via band-to-band stimulated emission of the near-IR range, which is defined by the characteristic time τ_{st}^{e1}: $B_{1st}N_\nu \propto \frac{n_1}{\tau_{st}^{e1}}$ [10]. This circumstance plays a significant role when currents exceed the threshold for the generation of near-IR emission, because in this case $N_\nu \propto (J/J_{th}^{\mathrm{NIR}} - 1)$. As follows from (22), the number of photons N_ν increases when the number of generated electron–hole pairs increases at $J \le J_{th}^{\mathrm{NIR}}$, whereas the density n_1 remains virtually unchanged.

The density n_1 can be determined from the expression obtained by the summation of Eqs. (20)–(22) for stationary conditions at currents close to the threshold for the band-to-band emission ($J \le J_{th}^{\mathrm{NIR}}$). In this case, $n_3, n_2 \ll n_1$, and $B_{1st}N_\nu \longrightarrow 0$, so we can obtain the density of electrons on the first level near the threshold, n_{1th}:

$$n_{1th} \approx \eta J_{th}^{\mathrm{NIR}} \tau_{sp}^{e1}. \quad (23)$$

Typical values of the characteristic times of spontaneous emission, τ_{sp}^{ei}, in GaAs-based nanostructures are about 1 ns. According to (23), for the given τ_{sp}^{ei}, $\eta = 0.5$ and $J_{th}^{\mathrm{NIR}} = 0.1$–$0.2$ kA cm^{-2}; the density n_{1th} in each QW is $(3$–$6) \times 10^{11}$ cm^{-2}. As the current increases further, $J > J_{th}^{\mathrm{NIR}}$, the density on the first level remains virtually unchanged: $n_1 \approx n_{1th}$.

The threshold density n_1, which is necessary for the onset of band-to-band stimulated emission, can be different, depending on J_{th}^{NIR}, τ_{sp}^{ei}, and η. Figure 4 shows the characteristic times of Auger processes that reduce the electron density in subband $e3$ as functions of n_1. For the Boltzmann distribution function, and disregarding the screening processes, the probabilities (inverse relaxation times) of *e*–*e* and *e*–*h* interactions depend linearly on the density n_1, whereas the probability of electron–phonon scattering $(\tau_{ph}^{32})^{-1}$, calculated under the same approximations, is independent of the electron density in a QW. It can be seen that τ_{ee}^{3211} and τ_{eh}^{3211} become close to τ_{ph}^{32} only at $n_1 > 5 \times 10^{12}$ cm^{-2}, and the impact of the Auger processes on the population inversion becomes considerable. Therefore, in a wide temperature range (room temperature included), at densities $n_1 < 5 \times 10^{12}$ cm^{-2}, the intersubband Auger processes have no significant impact on the intraband population inversion.

Having estimated J_{th}^{NIR}, τ_{sp}^{ei}, and η, and therefore n_1 from (20) and (21), and taking into account (19),

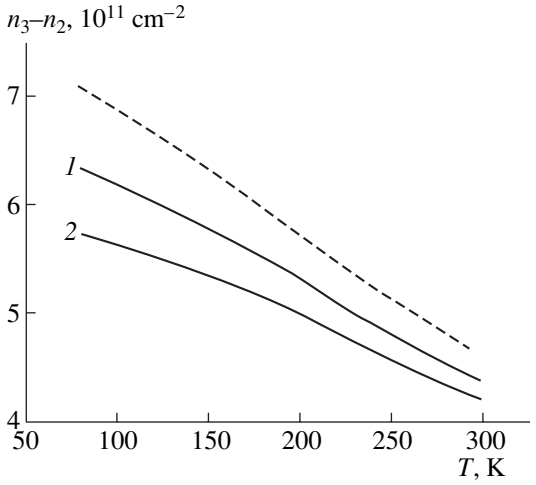

Fig. 5. Population inversion n_3–n_2 vs. temperature; the data were calculated by solving a system of rate equations at the injection current near the threshold for mid-IR emission at $T = 80$ K. Solid lines indicate calculations taking into account electron–phonon and Auger interactions: (*1*) for $n_1 = p_1 = 5 \times 10^{11}$ cm^{-2} and (*2*) for $n_1 = p_1 = 1 \times 10^{12}$ cm^{-2}. Dashed line, calculation taking into account electron–phonon interaction only.

we easily find n_3 and n_2 for the given injection current J:

$$n_3 = \frac{\eta J A_3}{(\tau_{ph}^{32})^{-1} + (\tau_{ph}^{31})^{-1} + (\tau_{ee}^{3211}(n_1))^{-1} + (\tau_{eh}^{3211}(n_1))^{-1}}, \quad (24)$$

$$n_2 = \frac{\eta J A_2 + n_3 \left[(\tau_{ph}^{32})^{-1} + (\tau_{ee}^{3211}(n_1))^{-1} + (\tau_{eh}^{3211}(n_1))^{-1} \right]}{[(\tau_{ph}^{21})^{-1} + (\tau_{ee}^{2111}(n_1))^{-1} + (\tau_{eh}^{2111}(n_1))^{-1}]}. \quad (25)$$

Figure 5 shows the population inversion n_3–n_2 calculated with formulas (24) and (25) for different temperatures at two densities n_1. The calculation was done for an injection current close to the threshold for intersubband emission in the heterostructure under study [3]. At high temperatures, the population inversion decreases, because the absorption of optical phonons increases, but this decrease is insignificant. To reveal the effect of the Auger processes on the population inversion, the same figure also shows the results of a calculation in which only the electron–phonon interaction was taken into account. At a temperature of 80 K, *e*–*e* and *e*–*h* scattering reduces the population inversion by 11% for $n_1 \approx 5 \times 10^{11}$ cm^{-2} and by 19% for $n_1 \approx 1 \times 10^{12}$ cm^{-2}. At 300 K, the reduction in the population inversion is weaker: 5% for $n_1 \approx 5 \times 10^{11}$ cm^{-2} and 9% for $n_1 \approx 1 \times 10^{12}$ cm^{-2}. The threshold current, which is necessary for the observation of the mid-IR emission from the heterostructure, increases in the same proportion.

5. CONCLUSION

We studied the effect of intersubband *e*–*e* and *e*–*h* scattering on the intraband population inversion in stepped InGaAs/AlGaAs QWs. The most probable *e*–*e* and *e*–*h* processes, which modify the electron density on the inversely populated levels *e*3 (3211) and *e*2 (2111), were considered. The calculations show that, for the heterostructure under study, the characteristic times τ_{ee}^{3211} and τ_{eh}^{3211} are large compared to τ_{ee}^{2111} and τ_{eh}^{2111}. This relationship between the characteristic times of intersubband Auger processes is favorable for intraband population inversion between levels *e*3 and *e*2.

We compared the characteristic times of intersubband *e*–*e* and *e*–*h* scattering with the characteristic times of the main processes of intersubband electron–phonon scattering, which determine the possibility of population inversion between levels *e*3 and *e*2 in this heterostructure. This comparison showed that the characteristic times of the Auger processes are much longer than those of the electron–phonon scattering at the expected threshold density of nonequilibrium carriers for band-to-band emission $n_1 = p_1 = 5 \times 10^{11}$ cm^{-2}. Since this density depends on a variety of factors (parameters of the cavity and QWs, laser design, etc.) and can exceed 5×10^{11} cm^{-2}, we analyzed the dependence of the characteristic times of Auger processes and electron–phonon scattering on this density. It was shown that, up to $n_1 \approx 5 \times 10^{12}$ cm^{-2}, the main intersubband *e*–*e* and *e*–*h* processes are slower than the electron–phonon interaction, so they have no significant impact on the intraband population inversion. This conclusion is valid for the temperature range 80–300 K, because of the weak temperature dependence of characteristic times of the Auger processes.

The population inversion n_3–n_2 was calculated considering *e*–*e* and *e*–*h* interactions at different temperatures for two densities n_1, by solving the system of rate equations for a given injection current. The Auger processes reduce the population inversion in the heterostructure under study by 11% at 80 K and by 5% at 300 K, if $n_1 \approx 5 \times 10^{11}$ cm^{-2}. At $n_1 \approx 1 \times 10^{12}$ cm^{-2}, these values increase to 19% and 9%, respectively.

ACKNOWLEDGMENTS

This study was supported in part by the Russian Foundation for Basic Research (project no. 03-02-16719) and by the Ministry of Education of the Russian Federation (grant no. E02-3.4-318).

REFERENCES

1. W. T. Tsang, in *Semiconductors and Semimetals*, Vol. 22: *Light-Wave Communications Technology*, Ed. by W. T. Tsang (Academic, New York, 1985).
2. P. Kinsler, P. Harrison, and R. W. Kelsall, Phys. Rev. B **58**, 4771 (1998).
3. A. Kastalsky, L. E. Vorobjev, D. A. Firsov, *et al.*, IEEE J. Quantum Electron. **37**, 1356 (2001).
4. V. L. Zerova, L. E. Vorob'ev, and G. G. Zegrya, Fiz. Tekh. Poluprovodn. (St. Petersburg) **38**, 716 (2004) [Semiconductors **38**, 689 (2004)].
5. B. L. Gel'mont, Zh. Éksp. Teor. Fiz. **75**, 536 (1978) [Sov. Phys. JETP **48**, 258 (1978)].
6. E. O. Kane, J. Phys. Chem. Solids **1**, 249 (1957).
7. V. V. Mitin, V. A. Kochelap, and M. A. Stroscio, *Quantum Heterostructures* (Cambridge Univ. Press, Cambridge, 1999).
8. S.-C. Lee and I. Galbraith, Phys. Rev. B **55**, R16025 (1997).
9. B. L. Gel'mont, R. I. Lyagushchenko, and I. N. Yassievich, Fiz. Tverd. Tela (Leningrad) **14**, 533 (1972) [Sov. Phys. Solid State **14**, 445 (1972)].

Translated by D. Mashovets

Semiconductors, Vol. 38, No. 9, 2004, pp. 1061–1064. Translated from Fizika i Tekhnika Poluprovodnikov, Vol. 38, No. 9, 2004, pp. 1097–1100.

LOW-DIMENSIONAL SYSTEMS

Calculation of Current–Voltage Characteristics of Gallium Arsenide Symmetric Double-Barrier Resonance Tunneling Structures with Allowance for the Destruction of Electron-Wave Coherence in Quantum Wells

D. V. Pozdnyakov, V. M. Borzdov, and F. F. Komarov

Belarussian State University, Minsk, 220050 Belarus

e-mail: borzdov@bsu.by

Submitted June 16, 2003; accepted for publication February 4, 2004

Abstract—An approach that describes the effect of electron-wave coherence destruction in quantum wells of GaAs-based symmetric double-barrier resonance tunneling structures on their current–voltage characteristics is suggested. Electron scattering by polar optical phonons, ionized impurities, and surface roughness in quantum wells, as well as thermal fluctuations of particle energies, are analyzed as the major factors responsible for coherence destruction. Current–voltage characteristics of GaAs-based symmetric double-barrier resonance tunneling structures are calculated for three-, two-, and one-dimensional electron gas in the emitter and collector of the structure at different temperatures. © *2004 MAIK "Nauka/Interperiodica".*

There are now a number of papers that deal with resonance tunneling of electrons through GaAs-based double-barrier resonance tunneling structures (DBRTSs) (see, e.g., [1–4]). The main reason for this is that such studies form a scientific basis for the development and design of new high-speed semiconductor devices [5, 6].

It is well known that electron scattering has a significant effect on electron resonance tunneling through a system of potential barriers [1, 7–9], since these processes destroy the coherence of electron waves and, therefore, change the resonance tunneling probability. It is also known that one of the most effective methods of describing the effect of scattering on current–voltage (*I–V*) characteristics of the DBRTS is the method based on electron transfer matrices (the matrix approach) [8, 9]. With this method, satisfactory agreement between theoretical results and experimental data has been achieved. However, the disagreement between these results still remains quite significant. We believe that this disagreement may be attributed to the following reasons. First, in [8, 9] only two mechanisms of electron-wave coherence destruction in a quantum well (QW), namely, electron scattering by polar optical phonons and by ionized impurities, were considered, whereas in this case it is also necessary to take into account the other most important charge-carrier scattering mechanisms. Second, in these studies, the electron-wave coherence destruction in a QW was described using the longitudinal component of the electron mean free path. However, for a more adequate description of the interference effects related to electron-wave properties, it is more correct to use the longitudinal coherence length for electron waves in a QW of the DBRTS [10]. Third, the matrix approach is not sufficiently rigorous from the standpoint of the description of electron transport in nonstationary quantum systems [11].

The aim of this study is to revise the model of electron transport suggested in [8] and use it to study the effect of temperature on *I–V* characteristics of the DBRTS with electron gas of different dimensionalities in the emitter and collector of the structure. We consider thermal fluctuations of particle energies, as well as electron scattering by polar optical phonons, ionized impurities, and surface roughness in a QW, as the main causes of the coherence destruction.

We study symmetric $Al_xGa_{1-x}As/GaAs/Al_xGa_{1-x}As$ ($0 \le x \le 1$) DBRTSs, because for such structures one can obtain maximal values of the peak current density retaining a high degree of current variation in the region of negative differential resistance in the *I–V* characteristic [1, 9]. This property is extremely important from the standpoint of practical applications in various DBRTS-based devices [12]. A bulk DBRTS, a quantum-layer-based DBRTS, and a DBRTS based on a quantum wire of rectangular cross section have two-, one-, and zero-dimensional electron gas in the QW formed by potential barriers. Accordingly, we consider them as structures with three-dimensional (3D), two-dimensional (2D), and one-dimensional (1D) electron gas in the emitter and collector.

The potential profile of the structure under study was constructed using the following approximations: (i) outside the region of the QW and the potential barriers, electron transport was assumed to be sequential and incoherent [13]; (ii) in the region of the QW and poten-

1063-7826/04/3809-1061$26.00

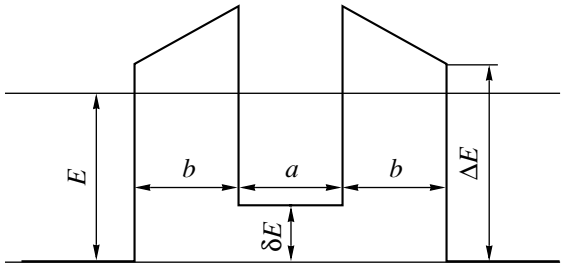

Fig. 1. Potential profile of a double-barrier resonant-tunneling structure.

tial barriers, after the destruction of electron-wave coherence, the equilibrium state with respect to the center of a QW is instantly restored [10]; and (iii) the probability T_g of coherent transmission of electrons through the DBRTS with allowance for the processes of electron-wave coherence destruction is negligible compared with the probability of incoherent capture of electrons in the QW $(1 - R_g)$ [8, 9, 14], where R_g is the probability of coherent reflection of electrons from the DBRTS with allowance for the processes of electron-wave coherence destruction.

The potential profile of the DBRTS has the shape shown in Fig. 1. This shape is conserved for different dimensionalities of electron gas in the emitter and the collector in a wide range of voltages U applied to the structure, since the operating voltage only affects the electron energy distribution in the emitter and collector with respect to the edge of the conduction band in the QW.

In Fig. 1, the following notation is introduced: E is the longitudinal component of the electron energy, ΔE is the potential barrier height, δE is the QW potential that characterizes the cutoff voltage in the I–V characteristic [1, 2, 7, 12], a is the width of the QW, and b is the width of the potential barrier.

According to [15], the quantity ΔE expressed in electronvolts is given by

$$\Delta E = 0.693x + 0.222x^2. \tag{1}$$

In order to find the quantity δE, we used the following approximation:

$$\delta E = (E_F^0 + k_B T)\exp\left(-\frac{2k_B T}{E_F^0}\right). \tag{2}$$

Here, k_B is the Boltzmann constant, T is temperature, E_F^0 is the Fermi energy for a given dimensionality of electron gas in the emitter and collector of the structure (this energy is measured from the ground quantum state of the system in the approximation of infinitesimal activation energy of the donor impurity and $T = 0$ K).

If all electrons in the emitter and collector of the structure are in the ground quantum state, then the average current density through the DBRTS in the quantum limit for 3D, 2D, and 1D electron gas in the emitter and collector (with allowance for the above approximations and for the symmetry of the DBRTS) can be calculated by the formula

$$\begin{aligned} j = {} & \frac{1}{2}\int_0^\infty \left[1 - R_g\left(E + \frac{eU}{2}\right)\right] f\left(E, E_F + \frac{eU}{e}\right) dE \\ & - \frac{1}{2}\int_0^\infty [1 - R_g(E)]\, f\left(E, E_F - \frac{eU}{2}\right) dE, \end{aligned} \tag{3}$$

where e is the elementary charge, E_F is the Fermi energy for a given dimensionality of electron gas in the emitter and collector of the structure and is measured from the ground quantum state of the system, and $f(E, \varepsilon)$ is the function of the average current-density distribution in the longitudinal component of the electron energy, which, according to [2, 7, 13, 16], can be written as

$$f(E, \varepsilon) = \begin{cases} \dfrac{em^* k_B T}{2\pi^2 \hbar^3} \ln[1 + \exp((\varepsilon - E)/(k_{BT}))] \\ \text{for 3D gas,} \\ \dfrac{e\sqrt{2m^* k_B T}}{\pi^2 \hbar^2 L_W} \displaystyle\int_0^\infty \frac{\exp((\varepsilon - E)/(k_B T) - t^2)}{1 + \exp((\varepsilon - E)/(k_B T) - t^2)} dt \\ \text{for 2D gas} \\ \dfrac{e}{\pi\hbar L_W L_H} \dfrac{\exp((\varepsilon - E)/(k_B T))}{1 + \exp((\varepsilon - E)/(k_B T))} \quad \text{for 1D gas.} \end{cases} \tag{4}$$

Here, $\hbar$ is Planck's constant, m^* is the electron effective mass, L_W is the width of the quantum layer or quantum wire, and L_H is the quantum wire height.

The quantity $R_g(\varepsilon)$ was calculated in the usual way as the squared absolute value of the ratio between the amplitude of the electron wave reflected from the DBRTS and that of the incident wave [8]. The processes of electron-wave coherence destruction in a QW were taken into account by introducing a complex electron wave vector in this region, which is equivalent to a Schrödinger equation with complex energy. The latter is convenient for describing nonstationary quantum systems [11]. In this case, according to [10, 11, 13], the longitudinal component of the electron wave vector in the QW is given by the relation

$$k = \begin{cases} \dfrac{1}{\hbar}\sqrt{2m^*(E - \delta E)} + \dfrac{i}{2L}, & E > \delta E, \\ \dfrac{1}{\hbar}\sqrt{2m^*(\delta E - E)}, & E \le \delta E, \end{cases} \tag{5}$$

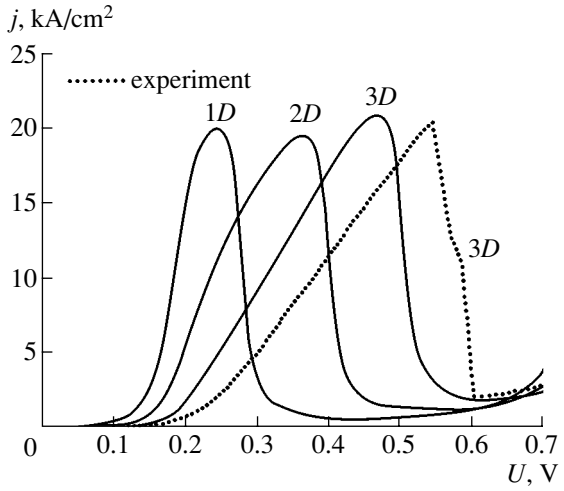

Fig. 2. Current–voltage characteristics of the double-barrier resonant-tunneling structure for different dimensionalities of electron gas in the emitter and collector of the structure at T = 77K.

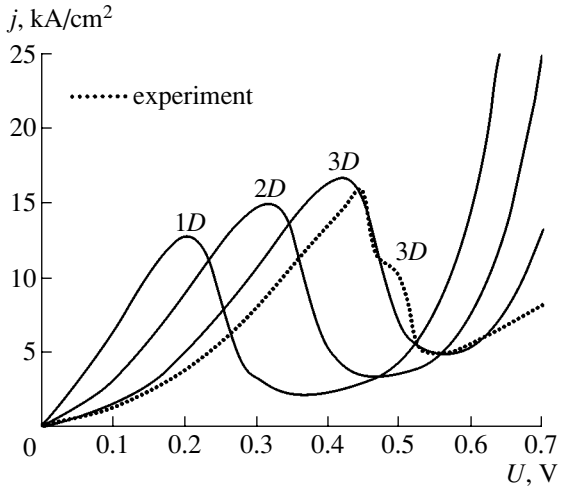

Fig. 3. Current–voltage characteristics of the double-barrier resonant-tunneling structure for different dimensionalities of electron gas in the emitter and collector of the structure at T = 300 K.

where i is the imaginary unit and L is the longitudinal coherence length of electron waves in the QW of the DBRTS.

The longitudinal coherence length of electron waves in the QW of the DBRTS was calculated on the basis of results reported in [10]. In addition, we took into account the equivalence of electron quantum states with a phase shift of electron waves by $\pm n\pi$ (n = 1, 2, 3, …) that arises due to electron scattering by surface roughness. We also included the processes of electron-wave coherence destruction by thermal fluctuations of the electron energy by introducing the corresponding coherence time

$$\tau = \frac{\hbar}{k_B T}. \tag{6}$$

It follows that the longitudinal coherence length L of electron waves in the QW of the DBRTS can be calculated using the expression

$$L = \left(\frac{1}{L_1} + \frac{1}{L_2} + \frac{1}{L_3} + \frac{1}{L_4}\right)^{-1}, \tag{7}$$

where the partial longitudinal coherence lengths of electron waves L_1, L_2, L_3, and L_4 related to thermal electron energy fluctuations, particle scattering by polar optical phonons, ionized impurities, and surface roughness are given by

$$L_1 = \frac{\hbar^2 k}{m^* k_B T}, \tag{8}$$

$$L_2 = \frac{3\pi\hbar k}{m^* \omega}, \tag{9}$$

$$L_3 = \frac{3}{N_L}, \tag{10}$$

$$L_4 = a\left\{\left(\frac{\pi}{2\sigma k}\right)^2 + 3\exp\left[-\frac{2}{5}\left(\frac{\pi}{2\sigma k}\right)^2\right]\right\}. \tag{11}$$

Here, ω is the angular frequency of a polar optical phonon, N_L is the longitudinal linear ionized-impurity concentration in the QW of the DBRTS, and σ is the rms deviation of a rough QW–potential barrier interface from a plane.

In Figs. 2 and 3, we show the experimental I–V characteristics [7] and I–V characteristics of DBRTS calculated using expressions (3) and (4) at different temperatures and dimensionalities of electron gas in the emitter and collector of the structure. The following model parameters were used in the calculation: x = 1, a = 5 nm, b = 2.26 nm, the ionized-impurity concentration in the emitter and collector of the structure $N^+ = 5 \times 10^{24}$ m^{-3}, and the ionized-impurity concentration in the quantum well $N = 10^{22}$ m^{-3}. These parameters correspond to the experimental data [7]. The value of σ was taken to be 0.3 nm [15]. We assumed the transverse dimensions of the quantum wire and the quantum layer to be $L_W = L_H$ = 6 nm, in accordance with the linear concentration of ionized impurities in the emitter and collector of the structure.

It follows from Figs. 2 and 3 that the dimensionality of electron gas in the emitter and collector of the DBRTS, as well as the temperature, can have a significant effect on I–V characteristics. We note that, in contrast to [8, 9], the I–V characteristics that we obtained for a structure with 3D electron gas in the emitter and collector agree well with the experimental results [7] not only quantitatively (the ratio of peak to valley cur-

rents) but also qualitatively (the shape of the *I–V* characteristics).

Thus, in this study we suggested an approach that makes it possible to describe in a simple way the processes of electron-wave coherence destruction in the QW of a DBRTS and their effect on the *I–V* characteristic of the structure. Thus, we can calculate *I–V* characteristics of DBRTS with reduced dimensionality of electron gas in the emitter and collector of the structure without using complicated numerical methods.

REFERENCES

1. A. S. Tager, Élektron. Tekh., Ser. 1: Élektron. SVCh **9** (403), 21 (1987).
2. P. Roblin and W.-R. Liou, Phys. Rev. B **47**, 2146 (1993).
3. M. M. Vrubel' and V. M. Borzdov, Fiz. Tekh. Poluprovodn. (St. Petersburg) **28**, 1852 (1994) [Semiconductors **28**, 1023 (1994)].
4. R. C. Bowen, G. Klimeck, and K. L. Lear, Appl. Phys. Lett. **75**, 1302 (1999).
5. R. T. Bate, Nanotechnology **1** (1), 1 (1990).
6. L. Worschech, S. Reitzenstein, and A. Forchel, Appl. Phys. Lett. **77**, 3662 (2000).
7. Y. Fu, Q. Chen, M. Willander, *et al.*, J. Appl. Phys. **74**, 1874 (1993).
8. V. M. Borzdov, M. M. Vrubel, S. G. Mulyarchik, and A. V. Homich, Phys. Low-Dimens. Semicond. Struct. **7**, 67 (1997).
9. V. M. Borzdov and F. F. Komarov, *Simulation of Electrical Properties of Solid-State Layered Structures in Integrated Electronics* (Belorus. Gos. Univ., Minsk, 1999) [in Russian].
10. D. V. Pozdnyakov, Vestn. Beloruss. Gos. Univ., Ser. 1 **3**, 41 (2002).
11. A. S. Davydov, *Quantum Mechanics*, 2nd ed. (Nauka, Moscow, 1973; Pergamon Press, Oxford, 1976).
12. A. S. Tager, Élektron. Tekh., Ser. 1: Élektron. SVCh **2** (406), 17 (1988).
13. G. Iannaccone and B. Pellegrini, Phys. Rev. B **52**, 17406 (1995).
14. Y. Hu, J. Phys. C: Solid State Phys. **21** (2), L23 (1988).
15. E. X. Ping and H. X. Jiang, Phys. Rev. B **40**, 11792 (1989).
16. N. Zou, Q. Chen, and M. Willander, J. Appl. Phys. **75**, 1829 (1994).

Translated by I. Zvyagin

Semiconductors, Vol. 38, No. 9, 2004, pp. 1065–1073. Translated from Fizika i Tekhnika Poluprovodnikov, Vol. 38, No. 9, 2004, pp. 1101–1109.

LOW-DIMENSIONAL SYSTEMS

Relaxation of Charge Carriers in Quantum Dots with the Involvement of Plasmon–Phonon Modes

A. V. Fedorov and A. V. Baranov

Vavilov State Optical Institute, All-Russia Research Center, Birzhevaya liniya 12, St. Petersburg, 199034 Russia

e-mail: anatoli.fedorov@online.ru

Submitted January 28, 2004; accepted for publication February 16, 2004

Abstract—A new mechanism of intraband relaxation of charge carriers in quantum dots (QDs) incorporated in a heterostructure at a relatively large distance from its doped elements is considered. Relaxation is caused by coupling of the electron subsystem of the QD to plasmon–phonon excitations of doped components of the heterostructure via the electric potential induced by these excitations. It is shown that this interaction with bulk plasmon–LO-phonon modes is possible only due to their spatial dispersion. The performed estimations of relaxation rates have shown that the mechanism under consideration is quite efficient even if the QDs are at a distance as large as 100 nm from the doped regions of the heterostructure. If this distance is about several tens of nanometers, this mechanism can become dominant. *© 2004 MAIK "Nauka/Interperiodica".*

1. INTRODUCTION

Due to the rapid development of nanoelectronics, the design of nanoelectronic devices based on semiconductor quantum dots (QDs) has become a reality. Typical examples of such devices are single-electron transistors [1], quantum bits [2], memory cells [3], and lasers [4]. All of them consist of a large number of structural components including doped semiconductor layers, quantum wires, and substrates. The development of high-performance nanoelectronic devices of this type calls for a deep understanding of the energy and phase relaxation in QDs, since QDs are the main operational elements of these devices.

Until now, the main efforts of researchers in this field were directed toward the study of relaxation processes caused by the interaction with various elementary excitations, which are localized inside the QDs or at their surface. Thus, for example, they studied the effect of quantum-confined and surface optical phonons on electron dynamics in QDs [5–8]. Some studies were concerned with multiphonon relaxation involving longitudinal optical and acoustic phonons [5, 9, 10]. The fast relaxation of charge carriers in QDs was accounted for by the multiphonon mechanism assisted by defects [11–13]. In addition, the Auger process was considered as another efficient mechanism of intraband relaxation in QDs [14, 15].

Actual QD-based devices are complex heterostructures consisting of many structural components such as matrices, QDs, and quantum wells and wires, as well as coating, buffer, and wetting layers. Despite this, relatively few studies have been devoted to the effect of elementary excitations in the surrounding material on electron dynamics in QDs. In addition to the interaction of the electron subsystem of QDs with optical and acoustical phonons in the barrier and the matrix [5, 8, 16–18], researchers studied only the effect of the nearest neighborhood on the electron dynamics in QD. For example, they studied homogeneous broadening of optical transitions, which is caused by elastic Coulomb collisions between free charge carriers of the wetting layer and carriers in QDs [19]. Furthermore, they studied electron dephasing caused by charge fluctuations due to recharging of impurity states via the ensemble of free electrons [2]. However, we may expect that not only free charges of the surrounding medium but also plasmons and plasmon–phonon modes, which are eigenexcitations of the doped components of the heterostructure, interact with the electron subsystem of QDs. It is obvious that, if there is direct contact between QDs and doped components, the carriers in QDs are strongly coupled to excitations in the surrounding material and produce electric fields. However, in many cases, these components (for example, substrates) are at a distance of several tens of nanometers from QDs, and it is not clear a priori how strong the interaction between them is.

A simple electrostatic analysis shows that the electric fields induced by longitudinal bulk waves, irrespective of their origin (longitudinal optical (LO) phonons, plasmons, or plasmon–phonon modes), cannot penetrate into materials with a different permittivity [20, 21]. However, using the example of LO phonons [22, 23], it was shown that phonon dispersion gives rise to exponential tails of the electric field in the other material. We can expect that the same situation takes place in the case of plasmons or plasmon–phonon modes as well. It is due to dispersion that the electric fields induced by longitudinal optical waves can propagate through the interface between the materials and affect the electron subsystem of QDs, thus opening new relax-

1063-7826/04/3809-1065$26.00

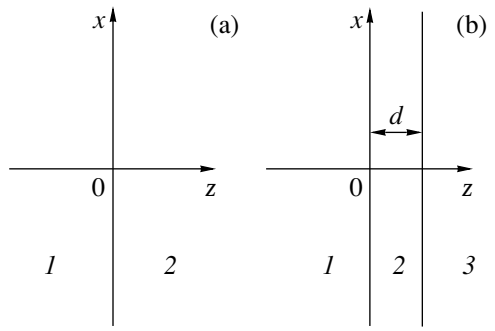

Fig. 1. (a) Single and (b) double heterostructures. Region *1* is the doped semiconductor, region *2* is the intrinsic semiconductor, and region *3* is air.

ation channels. The natural question arises as to whether these fields cause efficient intraband carrier relaxation in QDs in the intrinsic material at relatively large distances from the interface. As far as we know, this problem has not been considered until now.

The aims of this paper are the following:

(i) to construct a theoretical model of the new mechanism of intraband relaxation of charge carriers in QDs, which is caused by the interaction between the carriers and the electric potential induced by bulk plasmon–LO phonon modes of doped components of the heterostructure;

(ii) to estimate the dependence of the rates of intraband relaxation caused by this mechanism on the distance between the QD and the doped component of the heterostructure, on the concentration of doping impurity, and on the design of the heterostructure;

(iii) to discuss possible manifestations of the new relaxation mechanism in optical spectra of heterostructures.

2. COUPLED PLASMON–PHONON MODES IN A SEMICONDUCTOR HETEROSTRUCTURE

2.1. Dielectric Formalism Making No Allowance for Retardation

Before constructing a model of intraband carrier relaxation in QDs located far from the doped components of the heterostructure, let us briefly discuss the plasmon–phonon waves, which are eigenexcitations in doped materials. We will restrict our discussion to excitations that are hybrid states of charge-density fluctuations and optical phonons. Let us first analyze the coupled plasmon–phonon states in the context of a dielectric formalism making no allowance for spatial dispersion of "bare" plasma and phonon waves. To simplify the problem as much as possible with the aim of obtaining the clearest results, we consider two designs of a heterostructure with plane boundaries. These are the so-called single and double heterostructures, which are shown in Fig. 1. We assume that the half-space *1* ($z \le 0$) is filled with a doped semiconductor, for example, of *n* type with concentration n_0; region *2* ($z \le 0$ or ($d \ge z > 0$)) is an intrinsic semiconductor; and half-space *3* ($z > d$) is air with permittivity $\varepsilon_3 = 1$.

It is well known (see, for example, [20, 21]) that, when studying elementary excitations in the context of the dielectric formalism with no allowance for retardation effects, we can restrict our consideration to a single Maxwell equation $\mathrm{div}\mathbf{D} = 0$ for the electric displacement $\mathbf{D} = \varepsilon(\omega)\mathbf{E}$, where $\varepsilon(\omega)$ and $\mathbf{E}$ are the dielectric function and the electric field in the corresponding region of the heterostructure. Using the explicit form of the dielectric functions [21, 24] in regions *1* and *2*,

$$\varepsilon_1(\omega) = \varepsilon_{1\infty}\left(\frac{\omega_{1L}^2 - \omega^2}{\omega_{1T}^2 - \omega^2} - \frac{\omega_p^2}{\omega^2}\right), \quad (1)$$

$$\varepsilon_2(\omega) = \varepsilon_{2\infty}\frac{\omega_{2L}^2 - \omega^2}{\omega_{2T}^2 - \omega^2} \quad (2)$$

and the translation symmetry of the problem in the *xy* plane, it is easy to derive the system of equations for the self-consistent electric potential $\varphi_j(\mathbf{r}, \omega) = \varphi_j(z)\exp(i\mathbf{qx})\exp(-i\omega t)$ for $j = 1, 2, 3$ and $\mathbf{q}, \mathbf{x} \perp z$:

$$\varepsilon_j(\omega)\left(\frac{d^2}{dz^2} - q^2\right)\varphi_j(z) = 0, \quad (3)$$

which describes coupled plasmon–LO-phonon modes. In Eqs. (1)–(3), q is the wave vector lying in the *xy* plane, $\omega_{1(2)L}$ and $\omega_{1(2)T}$ are the frequencies of longitudinal and transverse optical phonons, $\omega_p = (4\pi e^2 n_0/\varepsilon_{1\infty} m)^{1/2}$ is the plasma frequency, m is the electron effective mass, and $\varepsilon_{1(2)\infty}$ is the high-frequency permittivity.

Let us consider the bulk plasmon–LO-phonon excitations. Since these correspond to eigenstates for bulk materials, the dielectric function that corresponds to the doped region of the heterostructure vanishes at the frequencies ω_b of these excitations, $\varepsilon_1(\omega) = 0$. Thus, we obtain two branches of plasmon–LO-phonon oscillations:

$$\omega_{b\pm}^2 = \frac{1}{2}\{\omega_{1L}^2 + \omega_p^2 \pm [(\omega_{1L}^2 + \omega_p^2)^2 - 4\omega_{1T}^2\omega_p^2]^{1/2}\}. \quad (4)$$

In this case, the first of Eqs. (3) is satisfied identically. Assuming that the intrinsic semiconductor is not a resonance medium, i.e., $\varepsilon_2(\omega_{b\pm}) \neq 0$, we derive the electric potential for a single heterostructure in the following form:

$$\varphi(z) = \varphi(0)\begin{cases}\sin(k_z z), & z \le 0,\\ 0, & z > 0,\end{cases} \quad (5)$$

where k_z is the component of the wave vector normal to the interface. For a double heterostructure, the condition that the intrinsic semiconductor is not a resonance

medium is described by the relationship

$$\omega_{b\pm}^2 \neq \frac{\varepsilon_{2\infty}\omega_{2L}^2 + \omega_{2T}^2 \tanh qd}{\varepsilon_{2\infty} + \tanh qd}. \quad (6)$$

If condition (6) is satisfied, we have

$$\varphi(z) = \varphi(0)\begin{cases} \sin k_z z, & z \le 0, \\ 0, & d \ge z > 0, \\ 0, & z > d. \end{cases} \quad (7)$$

It follows from expressions (5) and (7) that, if the dispersion of plasmons and phonons is disregarded and the intrinsic semiconductor is not a resonance medium, the electric potential of bulk plasmon–LO-phonon excitations is concentrated in the doped material.

2.2. The Role of Plasmon Dispersion in the Formation of Plasmon–Phonon Modes

To clarify the effect of plasmon dispersion on the energy spectrum of plasmon–phonon modes and on the electric potential induced by them, we use a combined approach developed by us. This approach is based on the dielectric formalism for the description of optical phonons and on the hydrodynamic approximation for plasma oscillations, which allows us to take into account their dispersion. In the context of this approach, the equation of motion for vibration amplitudes u, which corresponds to optical phonons without spatial dispersion [23], is added to the set of Bloch equations [25] for the potential of hydrodynamic velocity of free charge carriers ψ ($\mathbf{v} = -\nabla\psi$), charge carrier density N, and self-consistent electric potential Φ. The coupling between the phonon and plasmon subsystems is due to the fact that the self-consistent potential is determined by both fluctuations of the free-carrier charge density and the dipole phonon polarization. Accordingly, we derive a system of coupled nonlinear equations, which can be substantially simplified using the standard linearization method (see, for example, [25–27]). We assume that the unperturbed state of the free-carrier gas is characterized by a uniform density n_0 in the doped region of the sample, which is separated from the remaining part by a nontransparent barrier. In this case, in the first order of the perturbation theory in the deviations of ψ, N, Φ, and $\mathbf{u}$ from the equilibrium values $\psi_0 = 0$, n_0, φ_0, and $\mathbf{u}_0 = 0$, we derive the following system of linear equations:

$$\begin{aligned} \frac{\partial\psi}{\partial t} &= -\frac{e}{m}\varphi + \frac{\beta^2}{n_0}n, \\ \frac{\partial n}{\partial t} &= \nabla(n_0\nabla\psi), \\ \nabla\varphi &= \frac{4\pi e}{\varepsilon_\infty}n + \frac{4\pi\alpha}{\varepsilon_\infty}\nabla\mathbf{u}, \\ \rho\frac{\partial^2\mathbf{u}}{\partial t^2} &= -\rho\omega_T^2\mathbf{u} - \alpha\nabla\varphi, \end{aligned} \quad (8)$$

where $\varphi = \Phi - \varphi_0$, $\beta = v_F/\sqrt{3}$ is the propagation velocity of hydrodynamic perturbations in the free-carrier gas, $v_F = (3\pi^2 n_0)^{1/3}\hbar/m$ is the Fermi velocity, $n = N - n_0$, $\alpha = \omega_T[(\varepsilon_0 - \varepsilon_\infty)\rho/4\pi]^{1/2}$, ε_0 is the low-frequency permittivity, and ρ is the mass density of the unit cell of the semiconductor. The following Hamiltonian corresponds to this system of equations:

$$\begin{aligned} H = \int d^3r\Big[&\frac{1}{2}\rho\dot{\mathbf{u}} + \frac{1}{2}\rho\omega_T^2\mathbf{u}^2 + \alpha\mathbf{u}\nabla\varphi \\ &- \frac{\varepsilon_\infty}{8\pi}(\nabla\varphi)^2 + \frac{1}{2}mn_0(\nabla\psi)^2 - e\varphi n + \frac{m\beta^2}{2n_0}n^2\Big]. \end{aligned} \quad (9)$$

Below, we use this Hamiltonian to perform secondary quantization of plasmon–LO-phonon modes.

To find the eigenfrequencies of elementary excitations and electric fields in the inhomogeneous system under study, we consider Eqs. (8) in all regions of the heterostructure assuming as before that the evolution of variables n, ψ, φ, and $\mathbf{u}$ is determined by the exponential function $\exp(-i\omega t)$. In addition, we use the translation symmetry in the xy plane; i.e., we represent the variables $\{n_1(\mathbf{r}), \psi_1(\mathbf{r}), \varphi_j(\mathbf{r}), \mathbf{u}_j(\mathbf{r})\}$ as $\{n_1(z), \psi_1(z), \varphi_j(z), \mathbf{u}_j(z)\}\exp(i\mathbf{qx})$, where the subscript numerates the region of the heterostructure and the two-dimensional wave vector $\mathbf{q}$ and the two-dimensional radius vector $\mathbf{x}$ lie in the xy plane. In this case, for the doped region 1, we derive the following system of equations:

$$\begin{aligned} &\beta^2\frac{d^2n_1(z)}{dz^2} + \left(\omega^2 - \omega_p^2\frac{\varepsilon_{1\infty}}{\varepsilon_{1ph}(\omega)} - \beta^2q^2\right)n_1(z) = 0, \\ &\varepsilon_{1ph}(\omega)\left(\frac{d^2}{dz^2} - q^2\right)\varphi_1(z) = 4\pi e n_1(z), \\ &-i\omega\psi_1(z) = -\frac{e}{m}\varphi_1(z) + \frac{\beta^2}{n_0}n_1(z), \\ &\mathbf{u}_1(z) = \frac{\alpha_1}{\rho_1}\frac{\nabla\varphi_1(z) + i\mathbf{q}\varphi_1(z)}{\omega^2 - \omega_{1T}^2}. \end{aligned} \quad (10)$$

From the first equation of system (10), it follows that, if the parameter

$$k_z^2 = \left(\omega^2 - \omega_p^2\frac{\varepsilon_{1\infty}}{\varepsilon_{1ph}(\omega)} - \beta^2q^2\right)/\beta^2 > 0, \quad (11)$$

we have bulk-plasmon–LO-phonon modes, for which k_z is the z component of the total wave vector $\mathbf{k} = \{k_z, \mathbf{z}\}$. The dispersion relation for these modes for both single

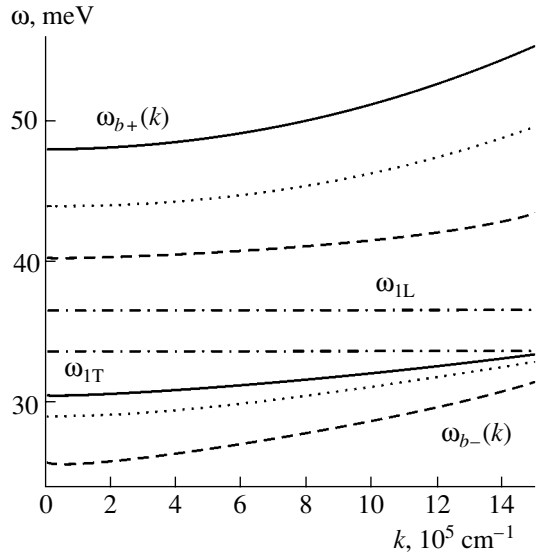

Fig. 2. Dependence of the dispersion relations $\omega_{b\pm}(k)$ of bulk plasmon–phonon modes for GaAs parameters on the concentration of the doping impurity n_0: solid lines correspond to 10^{18}; dotted lines, 0.75×10^{18}; dashed lines, 0.5×10^{18} cm^{-3}. Dash-dotted lines show the energies of longitudinal ω_{1L} and transverse ω_{1T} optical phonons of GaAs.

and double heterostructures is defined by the equations

$$\omega^2_{b\pm}(k) = \frac{1}{2}\{\omega^2_{1L} + \omega^2_p + \beta^2 k^2 \pm [(\omega^2_{1L} + \omega^2_p + \beta^2 k^2)^2] - 4\omega^2_p\omega^2_{1T} - 4\omega^2_{1L}\beta^2 k^2]^{1/2}\}, \quad (12)$$

where $k^2 = k_z^2 + q^2$ (see Fig. 2). We can easily see that, for $\beta \longrightarrow 0$ (i.e., if the dispersion of plasma oscillations is disregarded), Eq. (12) is transformed into Eq. (4).

Below, we assume that the intrinsic semiconductor is not a resonance medium with respect to plasmon–phonon modes, i.e., $\varepsilon_{2ph}(\omega_{b\pm}(k)) \neq 0$. In this case, the equations describing $\mathbf{u}(z)$ in region 2 of the heterostructure and $\varphi(z)$ in regions 2 and 3 take the form

$$\mathbf{u}_2(z) = \frac{\alpha_2}{\rho_2}\frac{\nabla\varphi_2(z) + i\mathbf{q}\varphi_2(z)}{\omega^2 - \omega^2_{2T}},$$

$$\varepsilon_{2ph}(\omega)\left(\frac{d^2}{dz^2} - q^2\right)\varphi_2(z) = 0, \quad (13)$$

$$\left(\frac{d^2}{dz^2} - q^2\right)\varphi_3(z) = 0.$$

We can show that the solution of systems (10) and (13) for a single heterostructure can be written as

$$n_1(z) = C_1 e^{ik_z z} + C_2 e^{-ik_z z},$$

$$\varphi_1(z) = -\frac{4\pi e}{\varepsilon_{1ph}(\omega)k^2}(C_1 e^{ik_z z} + C_2 e^{-ik_z z}) + C_3 e^{qz}, \quad (14)$$

$$\varphi_2(z) = Be^{-qz},$$

for a double heterostructure this solution can be written as

$$n_1(z) = C_1 e^{ik_z z} + C_2 e^{-ik_z z},$$

$$\varphi_1(z) = -\frac{4\pi e}{\varepsilon_{1ph}(\omega)k^2}(C_1 e^{ik_z z} + C_2 e^{-ik_z z}) + C_3 e^{qz}, \quad (15)$$

$$\varphi_2(z) = B_1 e^{-qz} + B_2 e^{qz},$$

$$\varphi_3(z) = Ae^{-qz}.$$

In order to find the coefficients A, B, and C, we assume that the electric potential and the z component of the electric displacement are continuous at the interfaces. Furthermore, we use the fact that the normal component of the hydrodynamic velocity vanishes at the interface $z = 0$; i.e., $v_z = 0$. In this case, for a single heterostructure we have

$$C_3 = ik_z\frac{2m\omega^2}{en_0k^2}\frac{\gamma(\omega)}{ik_z\delta(\omega) - q\gamma(\omega)}C_2, \quad (16)$$

$$C_1 = \frac{ik_z\delta(\omega) + q\gamma(\omega)}{ik_z\delta(\omega) - q\gamma(\omega)}C_2, \quad (17)$$

$$B = -ik_z\frac{2m\beta^2\varepsilon_{1ph}(\omega)}{en_0\varepsilon_{2ph}(\omega)}\frac{\gamma(\omega)}{ik_z\delta(\omega) - q\gamma(\omega)}C_2,$$

where

$$\gamma(\omega) = \frac{\varepsilon_{1\infty}}{\varepsilon_{1ph}(\omega)}\frac{\varepsilon_{2ph}(\omega)}{\varepsilon_{1ph}(\omega) + \varepsilon_{2ph}(\omega)}\omega^2_p, \quad (18)$$

$$\delta(\omega) = \beta^2k^2 + \gamma(\omega). \quad (19)$$

For a double heterostructure, the coefficients C_1 and C_3 are defined by expressions (16) and (17) with renormalized parameters $\gamma(\omega)$ (18) and $\delta(\omega)$ (19), in which $\varepsilon_{2ph}(\omega)$ should be replaced by

$$\varepsilon(\omega) = \frac{\eta_-(\omega)}{\eta_+(\omega)}\varepsilon_{2ph}(\omega), \quad (20)$$

where

$$\eta_\pm(\omega) = 1 \pm \frac{\varepsilon_{2ph}(\omega) - 1}{\varepsilon_{2ph}(\omega) + 1}e^{-2qd}. \quad (21)$$

For a double heterostructure, the coefficients A and B are given by

$$B_1 = -ik_z\frac{2m\beta^2\varepsilon_{1ph}(\omega)}{\eta_+(\omega)en_0\varepsilon(\omega)}\frac{\gamma(\omega)}{ik_z\delta(\omega) - q\gamma(\omega)}C_2,$$

$$B_2 = [\eta_+(\omega) - 1]B_1, \quad A = \frac{2\varepsilon_{2ph}(\omega)}{\varepsilon_{2ph}(\omega) + 1}B_1.$$

The coefficient C_2 for both heterostructures can be determined from the normalization condition.

Thus, as expected, taking into account dispersion of plasma oscillations leads to an important result. In con-

trast to the case considered in the previous subsection, the electric fields induced by bulk-plasmon–LO-phonon modes propagate into the region of heterostructures filled with an intrinsic semiconductor. These fields couple the excitations of a doped semiconductor with electron excitations of the intrinsic material, thus significantly affecting the dynamics of these excitations.

2.3. Secondary Quantization of Plasmon–LO-Phonon Modes

Plasmon–LO-phonon oscillations, which were considered in the previous subsection, induce the electric potential $V(\mathbf{r}) = -e\varphi(\mathbf{r})$, which describes their interaction with other electron excitations. Therefore, for further applications, it is convenient to express $V(\mathbf{r})$ in terms of Bose creation and annihilation operators $b_{\mathbf{k}}^{+}$ and $b_{\mathbf{k}}$ for quasiparticles corresponding to plasmon–LO-phonon modes. For this purpose, we apply the standard procedure of secondary quantization to Hamiltonian (9). This procedure allows us to determine the unknown constants C_2. Accordingly, the Hamiltonian assumes the form $H = \sum \hbar\omega_{b\pm}(k)[b_{\mathbf{k}}^{+}b_{\mathbf{k}} + 1/2]$, and the energy of interaction of electrons with bulk plasmon–phonon modes can be written as

$$V_b(\mathbf{r}) = \sum_{\mathbf{k}} (V_{\mathbf{k}}(z)e^{i\mathbf{qx}}b_{\mathbf{k}} + V_{\mathbf{k}}^{*}(z)e^{-i\mathbf{qx}}b_{\mathbf{k}}^{+}), \qquad (22)$$

where for a single heterostructure

$$V_{\mathbf{k}}(z) = V_k\begin{cases} M_1(\zeta_{\mathbf{k}}e^{ik_z z} + e^{-ik_z z}) - \chi_{\mathbf{k}}\omega^2 e^{qz}, & z \le 0, \\ \chi_{\mathbf{k}}\dfrac{\varepsilon_{1\mathrm{ph}}(\omega)}{\varepsilon_{2\mathrm{ph}}(\omega)}\beta^2 k^2 e^{-qz}, & z > 0, \end{cases} \qquad (23)$$

L^3 is the normalization volume,

$$M_1 = \frac{\varepsilon_{1\mathrm{ph}}(\omega) + \varepsilon_{2\mathrm{ph}}(\omega)}{2\varepsilon_{2\mathrm{ph}}(\omega)},$$

$$\zeta_{\mathbf{k}} = \frac{ik_z\delta(\omega) + q\gamma(\omega)}{ik_z\delta(\omega) - q\gamma(\omega)}, \quad \chi_{\mathbf{k}} = \frac{ik_z}{ik_z\delta(\omega) - q\gamma(\omega)}.$$

Here, for ω, we should use the expressions for eigenfrequencies of bulk plasmon–phonon modes (12), whereas the other parameters are defined by formulas (18) and (19). For a double heterostructure, we have

$$V_{\mathbf{k}}(z) = V_k\begin{cases} M_2(\zeta_{\mathbf{k}}e^{ik_z z} + e^{-ik_z z}) - \chi_{\mathbf{k}}\omega^2 e^{qz}, & z \le 0, \\ M_3\beta^2 k^2[e^{-qz} + (\eta_{+}(\omega) - 1)e^{qz}], & \\ d \ge z > 0, & \\ M_4 M_3\beta^2 k^2 e^{-qz}, & z > d, \end{cases} \qquad (24)$$

$$M_2 = \frac{\varepsilon_{1\mathrm{ph}}(\omega) + \varepsilon(\omega)}{2\varepsilon(\omega)},$$

$$M_3 = \frac{\chi_{\mathbf{k}}}{\eta_{+}(\omega)}\frac{\varepsilon_{1\mathrm{ph}}}{\varepsilon(\omega)},$$

$$M_4 = \frac{2\varepsilon_{2\mathrm{ph}}(\omega)}{\varepsilon_{2\mathrm{ph}}(\omega) + 1}.$$

It should be noted that in this case $\zeta_{\mathbf{k}}$ and $\chi_{\mathbf{k}}$ are expressed in terms of the renormalized parameters $\gamma(\omega)$ and $\delta(\omega)$, while other quantities in expression (24) are defined by formulas (20) and (21).

It follows from expressions (23) and (24) that, formally passing to the problem without dispersion ($\beta \longrightarrow 0$), we find that the electric potential induced by plasmon–phonon oscillations in the intrinsic region of the heterostructure vanishes. This conclusion fully agrees with the results of Subsection 2.1, where it has been shown that, in the absence of dispersion, the electric potential of bulk-plasmon–LO-phonon oscillations is concentrated in the doped material.

3. INTRABAND RELAXATION RATE OF ELECTRON EXCITATIONS IN A QUANTUM DOT

Let us consider the following mechanism of intraband relaxation of electron excitations in QDs. We assume that the QD is located in the undoped region of the heterostructure at a distance a from the interface between the doped and undoped regions. In this case, according to Eq. (22), the electron subsystem of the QD is coupled to plasmon–phonon modes via the electric potential induced by them. As a result, the electron can pass from one state to another emitting a quantum of plasmon–phonon oscillations (Fig. 3).

In the first order of the perturbation theory, we can represent the transition rate of charge carriers in the QD between levels E_2 and E_1 (Fig. 3) with excitation of plasmon–phonon modes with quantum numbers n as

$$W = \frac{2\pi}{\hbar^2}\sum_n |\langle 1|V_n(\mathbf{r})|2\rangle|^2\delta(\Omega - \omega_n),$$

where $|2\rangle$ and $|1\rangle$ are the wave functions of the initial and final states of the charge carrier and $\Omega = (E_2 - E_1)/\hbar$.

In the case of relaxation assisted by bulk plasmon–phonon excitations, the wave vector components k_z and $\mathbf{q}$ form the set of quantum numbers of these excitations. Choosing the origin of coordinates to be linked to the QD, we obtain

$$W_{b\pm} = \frac{2\pi}{\hbar^2}\sum_{k_z,\,\mathbf{q}} |\langle 1|\tilde{V}_{\mathbf{k}}(z)e^{i\mathbf{qx}}|2\rangle|^2 e^{-2qa}\delta(\Omega - \omega_{b\pm}(k)), \qquad (25)$$

where the dispersion relation $\omega_{b\pm}(k)$ is defined by Eq. (12). For simplicity, we restrict our consideration to

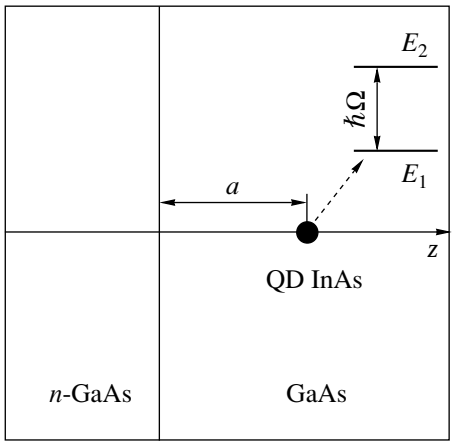

Fig. 3. Schematic diagram of the heterostructure with an InAs QD; the diagram illustrates the energy relaxation of charge carriers in a QD with emission of a quantum of coupled plasmon–phonon excitation. E_1 and E_2 are the electron levels of the QD, $\hbar\Omega$ is the energy gap between the states involved in the relaxation, and a is the distance from the QD to the doped region.

the case of heterostructures whose regions 1 and 2 are filled with the same semiconductor material $\varepsilon_{1ph}(\omega) = \varepsilon_{2ph}(\omega)$. In this case, according to (23) and (24), for a single heterostructure, we have

$$\tilde{V}_{\mathbf{k}}(z) = V_k \chi_{\mathbf{k}} \beta^2 k^2 e^{-qz},$$

and for a double heterostructure, we obtain

$$\tilde{V}_{\mathbf{k}}(z) = V_k \frac{\chi_{\mathbf{k}}}{\eta_-(\omega)} \beta^2 k^2 [e^{-qz} + (\eta_+(\omega) - 1) e^{q(z+2a)}].$$

Further calculations are associated with the choice of the specific model of the QD. Let us consider a spherical QD with radius R_0 under the condition of strong quantum confinement; i.e., we assume that the exciton Bohr radius for the bulk material of the QD is greater than R_0. In this case, if the electron subsystem of the QD is confined by an infinitely high potential barrier, the wave functions and the energy spectrum of electrons are given by

$$\Psi_{nlm}(\mathbf{r}) = Y_{lm}(\theta, \varphi) \sqrt{\frac{2}{R_0^3}} \frac{j_l(\xi_{ml} r/R_0)}{j_{l+1}(\xi_{nl})}, \quad E_{n,l} = \frac{\hbar^2 \xi_{nl}^2}{2mR_0},$$

where ξ_{nl} is the nth root of the lth order spherical Bessel function ($j_l(\xi_{nl}) = 0$). If the potential-barrier height V_0 is finite, the wave functions can be represented as [28]

$$\Psi_{nlm}(\mathbf{r}) = Y_{lm}(\theta, \varphi) R_{nl}(r),$$

$$R_{nl}(r) = \sqrt{\frac{2}{R_0^3}} [j_l^2(x_1) k_{l-1}(x_2) k_{l+1}(x_2) - k_l^2(x_2) j_{l-1}(x_1) j_{l+1}(x_1)]^{-1/2} \times \begin{cases} k_l(x_2) j_l(x_1 r/R_0), & r \le R_0, \\ j_l(x_1) k_l(x_2 r/R_0), & r > R_0, \end{cases}$$

where

$$x_1 = R_0 \sqrt{2m_1 E_{nl}/\hbar^2}, \quad x_2 = R_0 \sqrt{2m_2 (V_0 - E_{nl})/\hbar^2},$$

k_l is the modified spherical Bessel function, m_1 and m_2 are the electron effective masses inside the QD and outside it, and the energies E_{nl} are determined from the secular equation

$$m_2 x_1 k_l(x_2) j_l'(x_1) = m_1 x_2 k_l'(x_2) j_l(x_1).$$

Since electron states are degenerate in the projection of the angular moment m, it is necessary to average expression (25) over initial states with quantum numbers l and n and to sum it over the final states with the same l' and n', i.e., to use the operation

$$\frac{1}{2l+1} \sum_{m, m'}. \tag{26}$$

When calculating matrix elements in Eq. (25), we encounter the quantities

$$\int d\mathbf{r} \Psi^*_{n'l'm'}(\mathbf{r}) (a e^{-qr(\cos\theta - i\sin\theta\cos\varphi)} + b e^{qr(\cos\theta + i\sin\theta\cos\varphi)}) \Psi_{nlm}(\mathbf{r}).$$

Using Clebsch–Gordon coefficients $C^{l'm'}_{lm, l''m''}$ [29], we can transform these quantities into the following form:

$$\sqrt{\frac{2l+1}{2l'+1}} \sum_{p=0}^{\infty} \sum_{t=-p}^{t=p} \frac{J^{(p)}_{n'l', nl} (qR_0)^p}{\sqrt{(p-t)!(p+t)}} \times [(-1)^p i^t a + (-i)^t b] C^{l'0}_{l0, p0} C^{l'm'}_{lm, pt}, \tag{27}$$

where

$$J^{(p)}_{n'l', nl} = \frac{2}{j_{l'+1}(\xi_{n'l'}) j_{l+1}(\xi_{nl})} \int_0^1 dx x^{2+p} j_{l'}(\xi_{n'l'} x) j_l(\xi_{nl} x))$$

for QDs with an infinitely high potential barrier and

$$J^{(p)}_{n'l', nl} = 2A_{n'l'} A_{nl} \left[B^{nl}_{n'l'} \int_0^1 dx x^{2+p} j_{l'}(x_1 x) j_l(x_1 x) + C^{nl}_{n'l'} \int_0^{\infty} dx x^{2+p} k_{l'}(x_2 x) k_l(x_2 x) \right],$$

$$A_{nl} = [j_l^2(x_1) k_{l-1}(x_2) k_{l+1}(x_2) - k_l^2(x_2) j_{l-1}(x_1) j_{l+1}(x_1)]^{-1/2},$$

$$B^{nl}_{n'l'} = k_{l'}(x_2) k_l(x_2), \quad C^{nl}_{n'l'} = j_{l'}(x_1) j_l(x_1)$$

for QDs with a finite potential barrier height V_0.

Since only quantities (27) depend on the quantum numbers m and m', operation (26) can be performed for

the square of their moduli. As a result, we derive the expression

$$(|a|^2 + |b|^2)\sum_{p=0}^{\infty}\frac{(J^{(p)}_{n'l'}C^{l'0}_{l0,\,p0})^2}{(2p+1)!}(2qR_0)^{2p},$$

which determines the selection rules for electron transitions in the QD. Thus, for a single heterostructure, the relaxation rate is

$$W^{(n'l',\,nl)}_{b\pm} = \frac{2m\beta^2q^3(\Omega)}{\pi\hbar n_0}\sum_{p=0}^{\infty}[2R_0q(\Omega)]^{2p}\frac{(J^{(p)}_{n'l'}C^{l'0}_{l0,\,p0})^2}{(2p+1)!} \times\int_0^1\frac{d\tau e^{-2q(\Omega)a\tau}\tau^{2p+1}\sqrt{1-\tau^2}}{1+a_s(\Omega)(1-\tau^2)}, \tag{28}$$

whereas for a double heterostructure, we have

$$W^{(n'l',\,nl)}_{b\pm} = \frac{2m\beta^2q^3(\Omega)}{\pi\hbar n_0}\sum_{p=0}^{\infty}[2R_0q(\Omega)]^{2p}\frac{(J^{(p)}_{n'l'}C^{l'0}_{l0,\,p0})^2}{(2p+1)!} \times\int_0^1\frac{d\tau e^{-2q(\Omega)a\tau}\tau^{2p+1}\sqrt{1-\tau^2}}{1+a_d(\Omega)(1-\tau^2)}\frac{1+(\eta_+(\Omega)-1)^2e^{4q(\Omega)a\tau}}{\eta_-^2(\Omega)}, \tag{29}$$

where

$$a_s(\Omega) = \left[\frac{\Omega\beta q(\Omega)}{\gamma_0(\Omega)}\right]^2,$$

$$a_d(\Omega) = \frac{\beta^2q^2(\Omega)[\beta^2q^2(\Omega)+2\gamma_0(\Omega)\eta_-(\Omega)]}{\gamma_0^2(\Omega)\eta_-^2(\Omega)},$$

$$\gamma_0(\Omega) = \frac{\varepsilon_{1\infty}}{2\varepsilon_{1\mathrm{ph}}(\Omega)}\omega_\mathrm{p}^2,$$

$$\eta_\pm(\Omega) = 1\pm\frac{\varepsilon_{1\mathrm{ph}}(\Omega)-1}{\varepsilon_{1\mathrm{ph}}(\Omega)+1}e^{-2dq(\Omega)\tau},$$

$$q(\Omega) = \frac{1}{\beta}\sqrt{\frac{[\Omega^2-\omega_{b+}^2(0)][\Omega^2-\omega_{b-}^2(0)]}{(\Omega^2-\omega_{1\mathrm{L}}^2)}}.$$

For the upper plasmon–phonon branch $\omega_{b+}(k)$ (Fig. 2), the relationship $\Omega \geq \omega_{b+}(0)$ is valid, whereas, for the lower branch $\omega_{b-}(k)$, the transition frequency Ω is bounded by the double inequality $\omega_{b-}(0) \leq \Omega < \omega_{1\mathrm{T}}$.

Figure 4b shows the dependences of the rates of intraband relaxation (28) in a spherical QD with an infinite potential-barrier height on the energy difference between the lowest initial and final electron states. The QD is incorporated into the single heterostructure at a distance of 50 nm from the doped region. It is assumed that the heterostructure is formed by doped *n*-GaAs and intrinsic GaAs, whereas InAs is the material of the QD (Fig. 3). One can see that the interaction of the electron subsystem of the QD with bulk plasmon–phonon modes results in the emergence of two relaxation windows (L_+ and L_-), whose spectral position depends on the doping impurity concentration, while the widths of the windows are controlled by the dispersion of plasmon–phonon modes. The relaxation window L_+ is formed due to the emission of plasmon–phonon modes belonging to the upper dispersion branch (Fig. 2), and the window L_- corresponds to the emission of plasmon–phonon modes of the lower dispersion branch. Figure 4a shows the dependence of the peak value of the intraband relaxation rates on the distance *a* between the QD and the doped region of the heterostructure. Even for the case $a = 100$ nm, the peak value of the relaxation rate is about 10^8 s^{-1}. Since this value is close to the rates of band-to-band recombination of electron–hole pairs in QDs, the mechanism under consideration can significantly contribute to the total rate of dephasing of optical transitions. As the value of *a* decreases, the rates of intraband relaxation significantly increase (see Fig. 4). At $a = 50$ nm, they are several times greater than 10^9 s^{-1} and attain values of about 10^{11} s^{-1} at $a = 20$ nm.

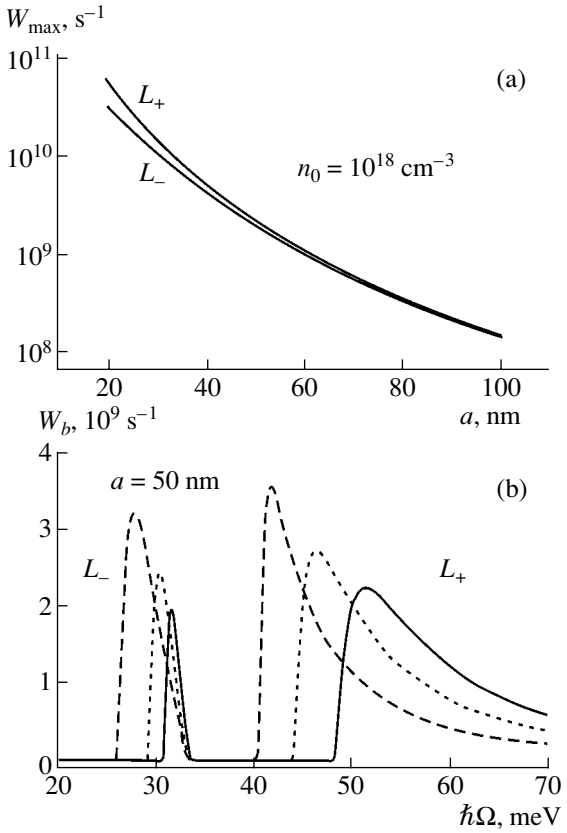

Fig. 4. (a) Peak values of relaxation rates in relation to the distance *a* between the QD and the doped region of the heterostructure. (b) Spectra of the rate of intraband relaxation of charge carriers in a QD incorporated into a single heterostructure for various doping impurity concentrations n_0; the solid line is for 10^{18}; dotted line, 0.75×10^{18}; dashed line, 0.5×10^{18} cm^{-3}. Symbols L_+ and L_- denote the relaxation windows formed due to the emission of bulk plasmon–phonon modes, which belong to the upper and lower dispersion branches, respectively (Fig. 2).

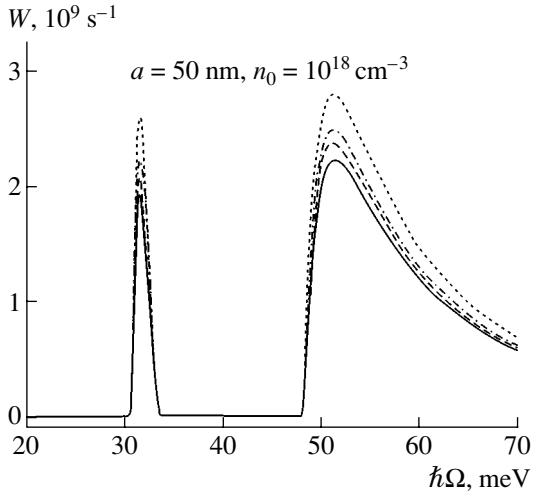

Fig. 5. Spectra of the intraband relaxation rates in a QD incorporated into a single heterostructure (solid line) and into double heterostructures for various thicknesses of the intrinsic layer d: (dashed line) 80, (dash-dotted line) 70, and (dotted line) 60 nm.

These magnitudes are comparable with the rates characteristic of other relaxation mechanisms [7, 15]. Therefore, we may conclude that the mechanism under consideration is quite competitive and should be taken into account both in analyzing the optical spectra of real heterostructures and in designing the corresponding nanoelectronic devices.

To estimate the effect of the heterostructure design on the rate of the intraband relaxation assisted by bulk plasmon–phonon modes, we show in Fig. 5 the spectra $W_{b\pm}^{(n'l', nl)}(\Omega)$ for single and double heterostructures at various thicknesses d of the intrinsic semiconductor layer. The above material parameters were used. One can see that the existence of the second boundary affects the relaxation rates only slightly. Even in the case where the QD is not far from the interface between the intrinsic material and air, the relative increase in relaxation rates is only 25%. The shape and spectral position of the relaxation windows is virtually independent of d.

A similar analysis can also be easily performed for QDs of different shape and with finite potential-barrier height. This analysis shows that all the specific features of the relaxation process considered above are also retained in this case.

4. CONCLUSIONS

We have shown that the existence of dispersion of bulk plasmon–phonon modes leads to the propagation of electric fields induced by these modes from the doped part of the heterostructure to the intrinsic part. As a result, the electron subsystem of the QD located in the intrinsic part of the heterostructure interacts with these electric fields. This interaction leads to the emergence of two new windows of intraband relaxation in QDs. These windows correspond to two branches of dispersion of bulk plasmon–phonon oscillations.

For example, we have considered spherical InAs QDs incorporated into the GaAs heterostructure and estimated the rates of intraband relaxation caused by a new mechanism, depending on the distance a between the QD and the doped substrate as well as on the doping impurity concentration n_0. We have shown that the mechanism under consideration is quite efficient for the characteristic concentrations $n_0 \approx 10^{18}$ cm^{-3} even at relatively large distances a (up to 100 nm). If the distance between the QD and the substrate is several tens of nanometers, the new relaxation mechanism can become dominant. In this case, it becomes possible to control the electron dynamics in the QD, because the spectral position of the relaxation windows depends on the free-carrier concentration in the doped part of the heterostructure. By varying this parameter, we can create a situation in which the relaxation window is in resonance or out of resonance with any intraband transition in the QD. Thus, we can control the populations of photoexcited and lower-energy states of the QD.

The most important question arising in connection with the mechanism of intraband relaxation discussed in this paper is the problem of reliable experimental observation of such processes. To solve this problem, it is necessary to analyze a possible manifestation of intraband relaxation in QDs due to interaction with plasmon–phonon modes of the doped part of the heterostructure in any optical experiment. Thus, for example, relaxation processes in self-assembled QDs are often investigated by the photoluminescence method [10, 30]. Currently, there are preliminary experimental data on the photoluminescence of self-assembled QDs incorporated into a double heterostructure [31]. It follows from these data that a new relaxation mechanism indeed exists and gives rise to two distinct spectral lines, L_+ and L_-.

Since not only bulk but also surface plasmon–phonon excitations can exist in doped elements of the heterostructure, the question of their role in intraband relaxation of charge carriers in QDs is undoubtedly of interest. This interesting problem will be considered in our subsequent study.

ACKNOWLEDGMENTS

This study was supported by the Russian Foundation for Basic Research, project no. 02-02-17311, and by INTAS, project nos. N 01-2100 and N 01-2331.

REFERENCES

1. L. Guo, E. Leobandung, and S. Y. Chou, Science **275**, 649 (1997).
2. T. Itakura and Y. Tokura, Phys. Rev. B **67**, 195320 (2003).

3. K. Yano, T. Ishii, T. Sano, *et al.*, Proc. IEEE **87**, 633 (1999).
4. *Advances in Semiconductor Lasers and Applications to Optoelectronics*, Ed. by M. Dutta and M. A. Stroscio (World Sci., Singapore, 2000).
5. A. V. Baranov, V. Davydov, H.-W. Ren, *et al.*, J. Lumin. **87–89**, 503 (2000).
6. X.-Q. Li and Y. Arakawa, Phys. Rev. B **57**, 12285 (1998).
7. X.-Q. Li, H. Nakayama, and Y. Arakawa, Phys. Rev. B **59**, 5069 (1999).
8. F. Gindele, K. Hild, W. Langbain, and U. Woggon, Phys. Rev. B **60**, 2157 (1999).
9. T. Inoshita and H. Sakaki, Phys. Rev. B **46**, 7260 (1992).
10. R. Heitz, M. Veit, N. N. Ledentsov, *et al.*, Phys. Rev. B **56**, 10435 (1997).
11. P. C. Sercel, Phys. Rev. B **51**, 14532 (1995).
12. D. F. Schroeter, D. F. Griffits, and P. C. Sersel, Phys. Rev. B **54**, 1486 (1996).
13. X.-Q. Li and Y. Arakawa, Phys. Rev. B **56**, 10423 (1997).
14. U. Bockelmann and T. Egeler, Phys. Rev. B **46**, 15574 (1992).
15. A. L. Efros, V. A. Kharchenko, and M. Rosen, Solid State Commun. **93**, 281 (1995).
16. A. V. Fedorov, A. V. Baranov, and Y. Masumoto, Solid State Commun. **122**, 139 (2002).
17. U. Bockelmann and G. Bastard, Phys. Rev. B **42**, 8947 (1990).
18. H. Benisty, Phys. Rev. B **51**, 13281 (1995).
19. A. V. Uskov, K. Nishi, and R. Lang, Appl. Phys. Lett. **74**, 3081 (1999).
20. E. Evans and D. L. Mills, Phys. Rev. B **8**, 4004 (1973).
21. N. Mori and T. Ando, Phys. Rev. B **40**, 6175 (1989).
22. B. K. Ridley, Phys. Rev. B **49**, 17253 (1994).
23. F. Comas, C. Trallero-Giner, and M. Cardona, Phys. Rev. B **56**, 4115 (1997).
24. A. Mooradian and A. L. McWhorter, Phys. Rev. Lett. **19**, 849 (1967).
25. R. H. Ritchie and R. E. Wilems, Phys. Rev. **178**, 372 (1969).
26. J. Harris, Phys. Rev. B **4**, 1022 (1971).
27. L. Kleinman, Phys. Rev. B **7**, 2288 (1973).
28. K. Vahala, IEEE J. Quantum Electron. **24**, 523 (1988).
29. D. A. Varshalovich, A. N. Moskalev, and V. K. Khersonskiĭ, *Quantum Theory of Angular Momentum* (Nauka, Leningrad, 1975; World Sci., Singapore, 1988).
30. K. H. Schmidt, G. Mederios-Ribero, M. Oestreich, *et al.*, Phys. Rev. B **54**, 11346 (1996).
31. A. V. Baranov, A. V. Fedorov, I. D. Rukhlenko, and Y. Masumoto, Phys. Status Solidi C **0**, 1217 (2003).

Translated by N. Korovin

Semiconductors, Vol. 38, No. 9, 2004, pp. 1074–1077. Translated from Fizika i Tekhnika Poluprovodnikov, Vol. 38, No. 9, 2004, pp. 1110–1114.

AMORPHOUS, VITREOUS, AND POROUS SEMICONDUCTORS

Influence of Supramolecular Ordering on Photophysical Properties of Polyamidines

E. L. Aleksandrova*^, M. E. Kompan*, M. M. Dudkina, A. V. Tenkovtsev**, and E. I. Terukov***

** Ioffe Physicotechnical Institute, Russian Academy of Sciences, Politekhnicheskaya ul. 26, St. Petersburg, 194021 Russia*

*** Institute of Macromolecular Compounds, Russian Academy of Sciences, Bol'shoi proezd 31, St. Petersburg, 119004 Russia*

^e-mail: 15lab@hg.macro.ru

Submitted November 24, 2003; accepted for publication November 24, 2003

Abstract—Photosensitive and luminescence properties of some supramolecularly orderable polyamidines are studied. It is shown that the luminescence efficiency of polyamidines, depending on their molecular structure, can more than triply exceed that of widely used organic luminescent semiconductors, i.e., polyphenylenevinylenes. It is assumed that this effect is caused by the fact that polyamidines can form supramolecular structures with π–*n*–H-conjugation. © *2004 MAIK "Nauka/Interperiodica".*

1. INTRODUCTION

The term "supramolecular structures," introduced for the first time by Lehn in 1978, was defined as "complex structures arising from spontaneous association of two or more chemical particles bound by intermolecular forces" [1]. Previously, we showed that polyamidines (PAs) can exhibit photoconductive properties due to the formation of such structures [2] and provide efficient transport of free carriers. The carrier mobility is ~10^{-4} $cm^2/(V\ s)$ [3], which is comparable to that of polyphenylenevinylenes (PPVs) polyconjugated due to (π–π) interactions. In contrast to PPVs, PAs are not polyconjugated polymers. However, they can associate efficiently due to a system of intermolecular hydrogen bonds between amidine groups [2]. This behavior results in the formation of linear and cyclic supramolecular structures, e.g., those shown in Fig. 1. In this case, it may be assumed that the π–*n*–H conjugation in such systems can arise due to π electrons of the carbon–carbon bond, an unshared pair of nitrogen atoms, and the hydrogen bond.

It is well known [1] that the formation of supramolecular ensembles can result in a change in the properties of compounds in the ground and excited states compared to the properties of individual molecules. In many cases, this cooperative process is accompanied by the appearance of new photophysical properties. Such systems can exhibit a number of processes, e.g., excitation energy transfer, photoinduced separation of charges, and so on, which generally do not occur in other cases.

The formation of the system of interchain hydrogen bonds in PA films gives rise to a quasi-conjugated system (Fig. 1a). In this case, the unshared pair of nitrogen atoms of the imine group involved in the hydrogen-bond formation allows us to consider the electronic structure of quasi-conjugated systems as similar to the structure of PPV. The fact that the PA monomeric unit contains a nitrogen atom and donor fragments (oligomethylene and diphenylmethane) with lower ionization potentials than the fragments incorporated in PPV [4] allows us to assume that the PA polymer class can feature higher photosensitivity, photoconductivity, and so on.

Furthermore, the high alkalinity of amidine groups makes it possible to produce ionic complexes of these polymers with low-molecular compounds (electron donors or acceptors) and with dopants that form complexes due to nonvalent bonding. Such modifications allow changes in the photophysical properties of molecular ensembles due to charge transfer in the chains of macromolecules that compose them as a result of the formation of network hydrogen-bound systems with fragments that have significant π conjugation (Fig. 1b). The possibility of introducing (due to complexing) chromophore molecules characterized by high quantum yields of luminescence into the PA matrix extends the range and improves the efficiency of photophysical processes, which is necessary to develop electroluminescence devices based on them.

The aim of this paper is to study the luminescence properties of various PA structures compared to the same characteristics of PPVs, as well as identify the photophysical processes caused by differences in the π–π and π–*n*–H conjugation systems.

2. SAMPLES

We studied a series of polyamidines that had different backbone chain structures and different substituent types in the amidine fragment. The chemical structural

formulas of the polymers studied are given below.

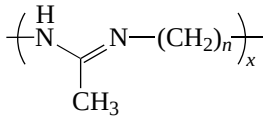

1 (n = 10), **2** (n = 6),

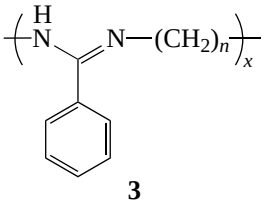

3

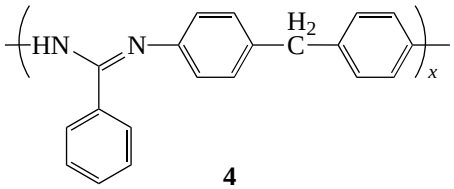

4

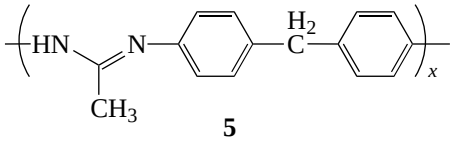

5

These structures were chosen, on the one hand, because of the possibility of studying the effect of the substitutional group (methyl, phenyl) and, accordingly, changes in the hydrogen bond force on the photophysical properties of complexes. Specifically, a systematic increase in the number of π-conjugated fragments, which causes an electron transfer between noncovalently bonded chain units, will make it possible to determine the influence of this factor on the photoconductivity of the system as a whole.

To test the possibility of modifying the PA optical properties, the monomeric fragment (1,5-di(4-oxyphenyl)penta-1,4-dien-3-OH)

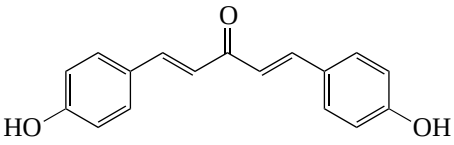

was incorporated into the PA structure.

This compound was chosen as the dopant because this fragment contains a developed chain of polyconjugated bonds that maintain the excitation transfer from the optically active orbitals of the dopant to the main network of supramolecular bonds.

1,5-Di(4-oxyphenyl)penta-1,4-dien-3-on was synthesized using the method described in [5]. Polymers were synthesized using the method in [6].

Polymer complexes were produced by mixing the PA solutions with dopant solutions in ethanol. The prepared solutions were used to cast films onto a rotating substrate using the flow-coating method (3000 rpm, 30 s). The prepared films were then dried in vacuum at room temperature to constant weight. The film thickness was 1–2 μm.

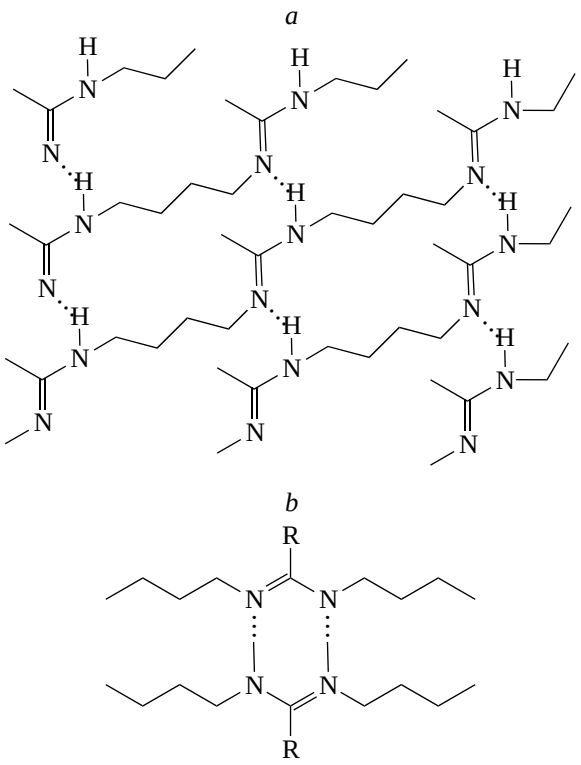

Fig. 1. Linear (*a*) and cyclic (*b*) supramolecular structures of polyamidines.

3. MEASUREMENT TECHNIQUE

The quantum yield η of the charge-carrier photogeneration was measured in the electrophotographic mode in the equienergy spectrum with an average photon flux density of 10^{13} cm^{-2} s^{-1} using the technique described in [7, 8] in the spectral range 400–900 nm with electric field $E = (0.2–1.0)E_0$, where E_0 is the critical field strength for a given material. The measurements were carried out at a temperature below the glass-transition temperature of polymers, at which the photosensitive properties abruptly change due to the destruction of supramolecular structures, as shown in [2] for polymers 4 and 5.

Absorption spectra of the polymers were measured using an SF-20 spectrophotometer.

Luminescence spectra were measured using excitation with a nitrogen laser with a wavelength of ~337 nm and a pulse duration of 6–8 ns. The measurements were carried out for an afterglow time of 1 μs after the excitation pulse at T = 300 K, which is also below the glass-transition temperatures of the polymers.

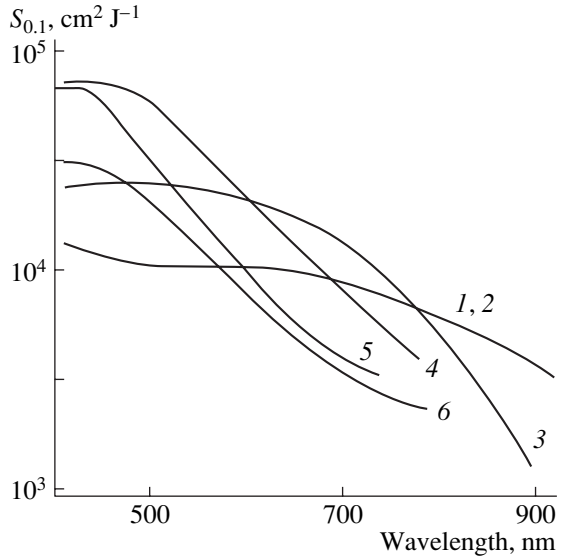

Fig. 2. Polyamidine photosensitivity spectra: (*1*) polymer **1**, (*2*) polymer **2**, (*3*) polymer **3**, (*4*) polymer **5**, (*5*) polymer **4**, and (*6*) PPV.

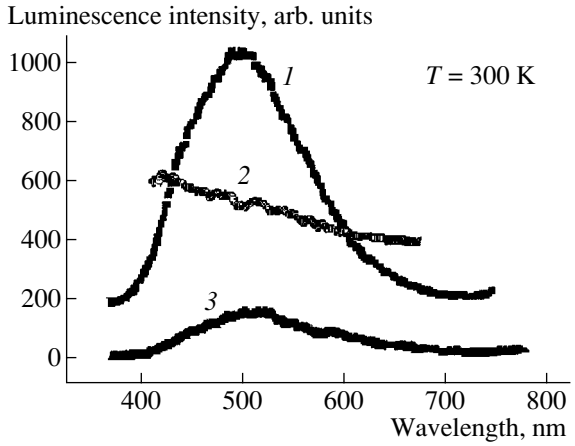

Fig. 3. Polyamidine luminescence spectra: (*1*) polymer **5**, (*2*) polymer **1**, and (*3*) polymer **4**; for clarity, the curves are shifted along the vertical axis by 200 scale units.

4. RESULTS AND DISCUSSION

The measured absorption spectra of the polymers showed that the long-wavelength absorption edge shifts to lower energies as the degree of π conjugation in the monomeric unit increases. In the sequence of polymers **1**, **3**, **4**, and **5**, the long-wavelength edge of the optical-absorption falloff in the region of electron transitions is within 300–400 nm. The largest shift to longer wavelengths was observed for polymer **4**, which contained three phenyl rings. The absorption spectra of the PA films under study contain low-intensity long-wavelength peaks in the visible region, which are absent in the spectra of polymer solutions in ethanol. These bands may be attributed to forbidden transitions in the quasi-conjugated system of hydrogen-bonded amidine groups (Fig. 1). However, this system cannot exist in a solution of proton solvent, specifically, ethanol. Calculation of electric structures of similar molecules using the conventional ZINDO/S method yields similar forbidden absorption bands [9].

Dependence of the relative quantum yield η/η_0 of charge carriers on the number of electrons in the polyamidine conjugation system

Polymer	Number of aromatic fragments in the monomer unit	Absorption peak position, eV	η/η_0
1	0	5.86	1.0
2	0	5.86	1.1
3	1	5.01	0.85
4	3	3.86	4.0
5	2	4.10	2.3

The PA photosensitivity spectra $S_{0.1}(\lambda)$ are shown in Fig. 2. We can see that the photosensitivity $S_{0.1}(\lambda)$ of polymers **1**–**3** decreases steadily from 2×10^4 to 3×10^3 cm^2/J as λ increases from 400 to 950 nm (Fig. 2, curves *1*–*3*). For polymers 4 and 5 (curves *4*, *5*), $S_{0.1}(\lambda)$ is close to 10^5 cm^2/J at $\lambda < 550$ nm and then decreases appreciably with λ. In contrast to the photosensitivity spectra, the spectrum of the quantum yield $\eta(\lambda)$ of carrier photogeneration is almost unchanged in the visible region and decreases steadily at $\lambda > 850$ nm. The value of λ increases in the sequence of polymers **2**–**1**–**3**–**5**–**4**, which correlates with the degree of conjugation and, as expected, increases with the number of aromatic fragments (see table). The photosensitivity spectra (Fig. 2, curve *6*) of PPV that does not form supramolecular structures are characterized by photosensitivity on the order of 10^5 cm^2/J due to stronger absorption in the spectral region $\lambda < 520$ nm, and they have a quantum yield of $(3–10) \times 10^{-2}$, i.e., comparable with η of PA.

The luminescence spectra of PA samples are shown in Fig. 3. We can see that the spectrum of polymer **1** has a peak near 420 nm, while the peaks for polymers **4** and **5** are at 500 nm. The luminescence spectrum of polymer **2** is similar to that of polymer **1**. The decrease in the luminescence maximum energy in going from polymers **1**–**2** to **4**–**5** correlates with the position of the electronic absorption band. In both cases, the observed shift can be accounted for by an increase in the conjugation-chain length due to an increase in the number of aromatic substituents in the PA monomeric unit, as well as a significant decrease in the ionization potential [4]. Note also that the difference of ~0.7 eV between the energies $I(\lambda)$ of the peaks for polymers **1**, **2** and **4**, **5** corresponds to the difference between the ionization potentials of oligomethylene and diphenylmethane fragments (see [4]).

We may therefore assume that the position and intensity of luminescence bands for the samples under

study is controlled by cooperative absorption–emission of an ensemble of supramolecular structures with the π–*n*–H-conjugation system, rather than by the chemical structure of the monomeric unit of the polymer and the length of the π-conjugation system. These structures arise during the ordering of the system as a result of the formation of a hydrogen-bond network between functional groups containing nitrogen atoms. Incorporation of a phenyl substituent into amidine group 4 is, compared to group 5, stoichiometrically unfavorable for the formation of a linear system of hydrogen bonds. This circumstance decreases the luminescence efficiency, despite an increase in the π-conjugation length, which is additional evidence in favor of the crucial role played by π–*n*–H conjugation in the effect under consideration.

It should be noted that the luminescence efficiency of polymer **5** is more than threefold higher (at a comparable excitation power) than that of PPV (Fig. 3, curve *1*) and does not depend on the substrate type (SiO_2, Si, or ITO).

Incorporating chromophore (with an absorption peak at 374 nm) into polymer **1** results in a shift of the luminescence peak to longer wavelengths, from 420 to 500 nm (Fig. 4, curve *2*), as well as an increase in the luminescence intensity to a level several times greater than that of PPV at the same excitation intensity. A study of the thickness dependence of the shape of the luminescence spectra showed that the peak shifts to longer wavelengths with increasing thickness of the polymer layer, which is probably caused by an aggregation of dye molecules. In addition, nonlinear phenomena, in particular, spectral hole burning, were observed in the luminescence band (Fig. 4, inset) of PA sample 1 with chromophore at an excitation power of $\sim 10^3$ W cm^{-2}. This observation is indicative of the long lifetimes of chromophore excited states, which indirectly points to a low rate of nonradiative recombination of excitation in this molecular fragment.

Thus, based on the photosensitivity measurements in the PA samples under study, we can state with confidence the following. The observed photosensitivity and its dependence on the material structure are caused by the supramolecular structure that forms the π–*n*–H-bond network, which provides conductivity with a charge mobility of $\sim 10^{-4}$ cm^2 V^{-1} s^{-1}. At the same time, the appreciable luminescence suggests that the possibility of photoexcited carrier transport over the polymer chain does not give rise to intense processes of nonradiative recombination. Furthermore, we succeeded in demonstrating the possibility of modifying the PA luminescent properties by doping with chromophore (1,5-di(4-oxyphenyl)penta-1,4-dien-3-OH). Remember that doping provided a shift of the band peak by 80 nm and a multifold increase in intensity. All these factors allow us to conclude that PAs have rather high conductivity and do not rank below PPVs in luminescent properties. This give grounds to consider polyamidines as a promising class of materials for the production of organic optoelectronic devices.

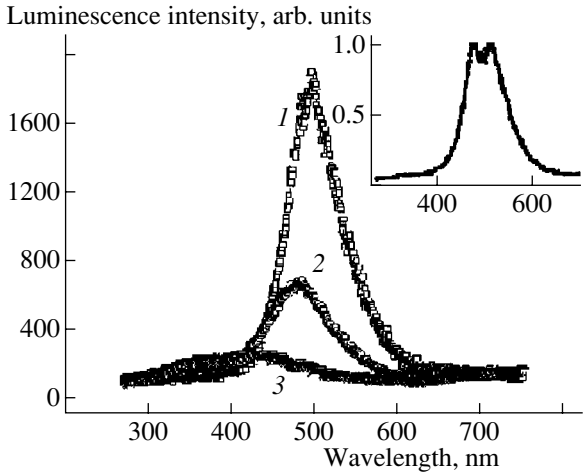

Fig. 4. Luminescence spectra of polymer **1** doped with chromophore (1,5-di(4-oxyphenyl)penta-1,4-dien-3-OH): (*1*, *2*) spectra measured at various point of the sample and (*3*) PPV luminescence at the same absorbed excitation. Inset: example of the luminescence spectrum of the same material at a high excitation intensity, where the line profile is changed due to spectral hole burning.

REFERENCES

1. E. L. Aleksandrova, M. M. Dudkina, and A. V. Ten'kovtsev, Fiz. Tekh. Poluprovodn. (St. Petersburg) **37**, 282 (2003) [Semiconductors **37**, 266 (2003)].
2. E. L. Aleksandrova, L. P. Kazakova, M. M. Dudkina, and A. V. Ten'kovtsev, in *Abstracts of III International Conference on Amorphous and Microcrystalline Semiconductors* (St. Petersburg, 2002), p. 107.
3. J.-M. Lehn, *Supramolecular Chemistry: Concepts and Perspectives* (VCH, Weinheim, 1995; Nauka, Novosibirsk, 1998).
4. L. V. Gurvich, G. V. Karachentsev, and V. N. Kondrat'ev, *Energies for Splitting the Chemical Bonds* (Khimiya, Moscow, 1974) [in Russian].
5. A. V. Tenkovtsev, A. V. Yakimansky, M. M. Dudkina, *et al.*, Macromolecules **34**, 7100 (2001).
6. F. Boehme, C. Klinger, H. Komber, *et al.*, J. Polym. Sci. **36**, 929 (1997).
7. I. A. Akimov, Yu. A. Cherkasov, and M. I. Cherkashin, *Sensitized Photoelectric Effect* (Nauka, Moscow, 1980) [in Russian].
8. E. L. Aleksandrova and Yu. A. Cherkasov, Opt. Spektrosk. **64**, 1047 (1988) [Opt. Spectrosc. **64**, 624 (1988)].
9. http://www.chemistry-software.com/molecmod.htm.

Translated by A. Kazantsev

Semiconductors, Vol. 38, No. 9, 2004, pp. 1078–1080. Translated from Fizika i Tekhnika Poluprovodnikov, Vol. 38, No. 9, 2004, pp. 1115–1117.

AMORPHOUS, VITREOUS, AND POROUS SEMICONDUCTORS

Current Instability with an *S*-Shaped *I–V* Characteristic in Films of a Metal–Polymer Complex of Polyamide Acid with Tb^{+2}

É. A. Lebedev*, M. Ya. Goĭkhman, K. D. Tséndin*, I. V. Podeshvo**, E. I. Terukov*, and V. V. Kudryavtsev****

** Ioffe Physicotechnical Institute, Russian Academy of Sciences, Politekhnicheskaya ul. 26, St. Petersburg, 194021 Russia*

*** Institute of Macromolecular Compounds, Russian Academy of Sciences, Bol'shoi proezd 31, St. Petersburg, 119004 Russia*

Submitted December 30, 2003; accepted for publication January 8, 2004

Abstract—The manifestation of current instability as an *S*-shaped *I–V* characteristic was detected in thin films of a metal–polymer complex of polyamide acid with Tb^{+2}. The current instability characteristics are comparable to those of the switching effect in chalcogenide glasses. The origin of the current instability in the metal–polymer complex may be related to electrothermal switching. The threshold voltage and current in films ~0.1 μm thick are 3–7 V and $(2–1) \times 10^{-2}$ A/cm^2, respectively. © *2004 MAIK "Nauka/Interperiodica".*

Recently, organic polymers have attracted much attention as promising initial materials for developing such optoelectronic devices as field-effect transistors (FETs) and electroluminescent diodes [1, 2]. The high parameters of these devices (emission intensity of electroluminescent diodes and cutoff frequency of FETs) are attained by decreasing the interelectrode distance and applying the highest possible voltage. In this context, we studied the current instabilities limiting the current and applied voltage in thin films of a metal–polymer complex of polyamide acid with Tb^{+2} ions (PAA + Tb^{+2}). The current instabilities are of interest not only because they play an important role in the limitation of the critical field and current but also because they can be used to switch voltage and current.

The polymer (PAA + Tb^{+2}) has attracted much attention due to its thermal stability and luminescence properties. The intensity of luminescence of this polymer is on the same order of magnitude as that of a conjugated polymer of polyphenylvinylene when measured under the same conditions [3].

The polymer (PAA + Tb^{+2}), i.e., polyamide acid with imide and biquinolyl units in the backbone, is a soluble hydrolytically stable polymer that can form films. These films are characterized by high deformation–strength properties and thermal stability up to 180°C. Studies of optical and electrical properties have shown that the long-wavelength optical-absorption edge in (PAA + Tb^{+2}) is significantly smeared and a change in the optical absorption coefficient from 10^2 to 10^3 cm^{-1} occurs approximately in the photon-energy range 2.75–3.00 eV. The peak in the photoluminescence spectrum is at 520 nm (2.4 eV).

The room-temperature dark conductivity is ~10^{-13} Ω^{-1} cm^{-1}. In the temperature range 350–400 K, the conductivity exponentially depends on temperature with an activation energy of ~2.1 eV. At lower temperatures, the dependence deviates from the exponential law [3].

The films under study were obtained by pouring a prepared polymer solution onto glass substrates coated with an indium tin oxide (ITO) layer. They were then dried at a temperature of 100°C to constant weight. The film thickness was 0.1–3 μm. The ITO layer was used as one of the electrodes, and the second electrode was made of either aluminum or graphite.

The *I–V* characteristics were measured at dc and pulsed voltage. Voltage pulses from a GPI-54 oscillator were applied to the sample and an in-series load resistance. The current was determined by measuring the voltage across the load using a two-beam oscilloscope; the voltage across the sample was determined as the difference between applied and load voltages. The pulse duration was 0.1–1 ms. The load resistance was varied from 200 to 10 kΩ.

The measurements showed that the shape of the *I–V* characteristic depends heavily on the film thickness. No significant deviation of the *I–V* characteristics from linearity was observed for films 2–1 μm thick at voltages of up to 50 V. A strong nonlinearity and current instability in the form of an *S*-shaped *I–V* characteristic were observed for layers ~0.1 μm thick. The nonlinearity of the *I–V* characteristics of thin polymeric layers can be caused by space-charge-limited currents [4]. When currents are limited by a space charge, the *I–V* characteristic follows either a power or exponential law, depending on the energy distribution of local states [5].

Figure 1 shows the *I–V* characteristics at voltages below the threshold. For some layers, they can be described by an exponential function (curve *a*); in other cases, the *I–V* characteristics are described by an exponential function with a single exponent only in a limited voltage range (curve *b*).

1063-7826/04/3809-1078$26.00 © 2004 MAIK "Nauka/Interperiodica"

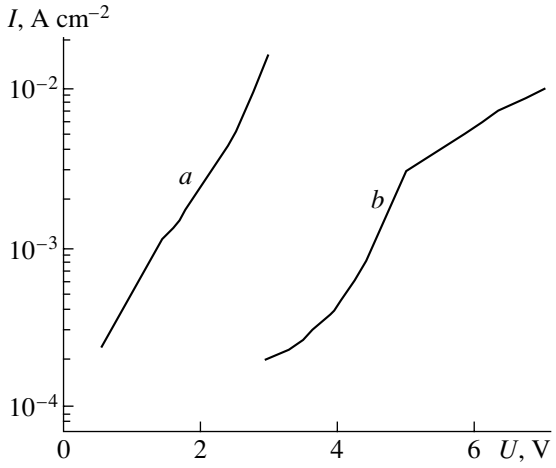

Fig. 1. *I–V* characteristics of 0.1-μm-thick films of a metal–polymer complex of polyamide acid with Tb^{+2} below the threshold voltage for different samples (*a*, *b*).

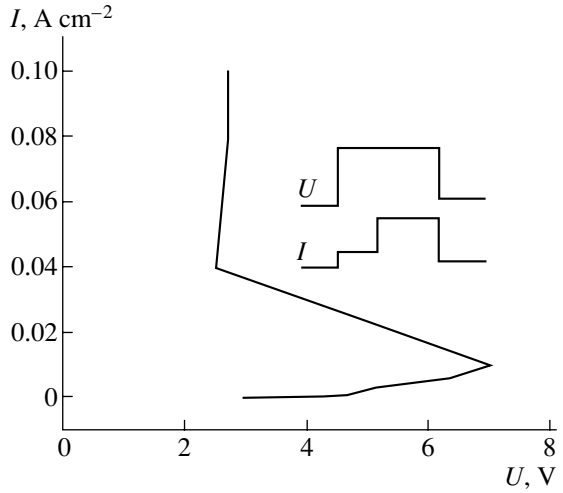

Fig. 2. *S*-shaped *I–V* characteristic of a film of a metal–polymer complex of polyamide acid with Tb^{+2}. Inset: oscillogram of current *I* at threshold voltage *U*; the pulse duration is 1 ms.

In the case of space-charge-limited currents, the exponential dependence is observed for semiconductors with local states uniformly distributed over energies [6]. The steeper dependence observed at lower voltages might be caused by the effect of contacts.

Figure 2 shows the *I–V* characteristic measured for a film 0.1 μm thick. It can be seen that the transition from the high- to the low-resistance state occurs at a threshold voltage of 7 V and a current of 10^{-2} A/cm^2. Note that, in the case of an *S*-shaped *I–V* characteristic, such a transition is generally accompanied by current pinching and the pinch-current density can be much higher than that shown in Fig. 2 (reduced to the electrode area).

The inset to Fig. 2 shows the oscillogram of a current *I* when a threshold voltage *U* is applied. The transition from the high- to the low-resistance state is characterized by a delay of ~0.4 ms at the threshold voltage. The delay decreases abruptly as the voltage increases.

Such an instability is similar to the switching effect observed in chalcogenide glasses [7–9]. This effect consists in rapid and reversible switching from the high- to the low-resistance state of the sample. Under pulsed conditions, chalcogenide glass films withstand as many as 10^{12} switchings without appreciable degradation of their parameters, which is sufficient to use such switches in microelectronic devices.

The stability of (PAA + Tb^{+2}) films is much lower than that of chalcogenide glass films. The degradation of their switching parameters manifests itself as a decrease in the threshold voltage and a change in the *I–V* characteristic at voltages below the threshold.

The simplest form of current instability in solids is electrothermal instability. The main condition for its occurrence is a semiconductor-type temperature dependence of conductivity. Positive feedback, which is necessary for the onset of instability in an *S*-shaped *I–V* characteristic, is established between the processes of increasing temperature and current. The current passing through a sample heats it. If the semiconductor-type temperature dependence of the conductivity in the form $\sigma(T) = \sigma_0 \exp(-\Delta E/kT)$ occurs at rather high activation energies $\Delta E/kT$, an increase in temperature causes an increase in the conductivity, which results in a further increase in the current. We estimated the characteristics of electrothermal instability as was done for chalcogenide glasses [10] by solving the system of equations

$$\sigma(T)SU^2/L = \lambda L(T - T_0), \quad (1a)$$

$$[d\sigma(T)/dT]SU^2/L = \lambda L, \quad (1b)$$

where the left- and right-hand sides in Eq. (1a) describe the heat release and heat removal, respectively; *S* is the active-region area; *L* is the film thickness; *U* is the voltage across the sample; *T* and T_0 are the temperatures of the sample and the surrounding medium, respectively; and λ is the factor of external heat removal.

In the case under consideration, the *I–V* characteristics are nonlinear. We will take into account this factor by writing the conductivity as a function of voltage: $\sigma(T, U)$. The value of σ and its dependence on voltage are controlled by a specific electronic mechanism that changes the conductivity in an electric field.

The samples with the *I–V* characteristics shown in Fig. 1 had conductivity $\sigma(T, U) = 2 \times 10^{-8}\ \Omega^{-1}\ \text{cm}^{-1}$ at $U = 3$–7 V for $L \approx 0.1$ μm. Estimation of their threshold voltage using formulas (1a) and (1b) yielded ~5–10 V. These values are close to the experimentally observed values (3–7 V).

In organic polymers, electric switching can exhibit very different characteristics [11, 12]; however, its mechanism is mainly associated with the displacement

of polymer chain fragments [13, 14]. In the case under consideration, the good agreement between the calculated and experimental data suggest that the observed *S* shape is caused by the electrothermal mechanism, which takes into account the nonlinearity of *I–V* characteristics.

In this case, the factor of displacement of structural units should not be ruled out. Upon switching, this factor should be especially pronounced in the low-resistance state. On the one hand, this may limit the increase in temperature; on the other hand, the switching characteristics may change.

ACKNOWLEDGMENTS

This study was supported by the St. Petersburg Scientific Center, Russian Academy of Sciences, within the program "Metal–Polymer Complexes and Luminescent Materials Based on Them."

REFERENCES

1. J. H. Burroughes, C. A. Jones, and R. H. Friend, Nature **335**, 137 (1988).
2. D. D. C. Bradley, Synth. Met. **54**, 401 (1993).
3. É. A. Lebedev, M. Ya. Goĭkhman, M. E. Kompan, *et al.*, Fiz. Tekh. Poluprovodn. (St. Petersburg) **37**, 844 (2003) [Semiconductors **37**, 816 (2003)].
4. S. Karg, M. Meir, and W. Riess, J. Appl. Phys. **82**, 1951 (1997).
5. A. Rose, *Concepts in Photoconductivity and Allied Problems* (Interscience, New York, 1963; Mir, Moscow, 1966).
6. I. L. Hartke, Phys. Rev. **125**, 1177 (1962).
7. B. T. Kolomiets and É. A. Lebedev, Radiotekh. Élektron. (Moscow) **8**, 2097 (1963).
8. S. R. Ovshinshky, Phys. Rev. Lett. **21**, 1450 (1968).
9. B. T. Kolomiets, É. A. Lebedev, and I. A. Taksami, Fiz. Tekh. Poluprovodn. (Leningrad) **3**, 731 (1969) [Sov. Phys. Semicond. **3**, 621 (1969)].
10. B. T. Kolomiets, É. A. Lebedev, and K. D. Tséndin, Fiz. Tekh. Poluprovodn. (Leningrad) **5**, 1568 (1971) [Sov. Phys. Semicond. **5**, 1369 (1971)].
11. Th. Frauenheim, C. Hamann, and M. Muller, Phys. Status Solidi A **86**, 735 (1984).
12. V. M. Arkhangorodskiĭ, A. N. Ionov, V. M. Tuchkevich, and I. S. Shlimak, Pis'ma Zh. Éksp. Teor. Fiz. **51**, 56 (1990) [JETP Lett. **51**, 67 (1990)].
13. I. Shlimak and M. S. Shur, in *Proceedings of 23rd International Conference on Physics of Semiconductors*, Ed. by M. Scheffler and R. Zimmermann (World Sci., Singapore, 1996), p. 3347.
14. N. A. Poklonskiĭ, E. F. Kislyakov, D. I. Sagaĭdak, *et al.*, Pis'ma Zh. Tekh. Fiz. **27** (5), 17 (2001) [Tech. Phys. Lett. **27**, 180 (2001)].

Translated by A. Kazantsev

Semiconductors, Vol. 38, No. 9, 2004, pp. 1081–1083. Translated from Fizika i Tekhnika Poluprovodnikov, Vol. 38, No. 9, 2004, pp. 1118–1120.

AMORPHOUS, VITREOUS, AND POROUS SEMICONDUCTORS

Carrier Drift Mobility in Porous Silicon Carbide

L. P. Kazakova^, M. G. Mynbaeva, and K. D. Mynbaev

Ioffe Physicotechnical Institute, Russian Academy of Sciences, St. Petersburg, 194021 Russia

^ e-mail: Kazakova@mail.ioffe.ru

Submitted December 22, 2003; accepted for publication January 26, 2004

Abstract—The time-of-flight technique was used to determine the drift mobilities of electrons and holes in porous silicon carbide produced by surface anodization of *n*-type 4*H*-SiC wafers. The electron and hole mobilities at 300 K in an electric field of 10^4 V/cm were $\mu_e = 6 \times 10^{-3}$ and $\mu_h = 3 \times 10^{-3}$ cm^2 V^{-1} s^{-1}, respectively. The low values of the mobilities are accounted for by carrier capture in localized states. © *2004 MAIK "Nauka/Interperiodica".*

Porous SiC (*PSC*) is presently regarded as a material that may expand the field of application of silicon carbide in microelectronics. It has been reported that *PSC* has high resistivity [1, 2] and low effective carrier density [3], while carrier transport in *PSC* has virtually not been studied at all. However, the problem of transport mechanisms in *PSC* is becoming a matter of current interest owing to, among other things, the prospects for using this material in device structures [4].

This paper reports the results obtained in studying one of the main transport parameters in *PSC*: the carrier drift mobility μ. The study was performed by measuring the transit time of carriers across a sample [5]. The time-of-flight technique makes it possible to determine the mobility in materials in which it is difficult to interpret the results obtained in measuring this parameter by the conventional methods (e.g., using the Hall effect), because the kinetic Boltzmann equation is inapplicable at low values of μ [6]. Previously, this technique was successfully used in studies of semiconductors with a disordered structure [7], and in more recent years, it was applied to porous silicon [8–10].

PSC layers were produced by surface anodization of *n*-type 4*H*-SiC wafers in an aqueous solution of hydrofluoric acid using the procedure described in [4]. The anodization current density was 8 mA/cm^2. A part of each wafer was closed with a mask during anodization. According to scanning electron microscopy (SEM), the resulting *PSC* layers had a thickness of 5 μm. The samples for time-of-flight measurements had a sandwich-type structure. A semitransparent aluminum film of area 9 mm^2 deposited in a vacuum served as the upper electrode. The unanodized part of the SiC wafer was used as the lower electrode.

Carriers were injected into a *PSC* sample in the vicinity of the upper electrode with a pulse of light with a wavelength of 0.337 μm, produced by an ILGI-503 laser. The pulse width was 8 ns. A pulsed voltage (pulse width 1 ms) was applied to a sample with a delay of ~100 μs between the instant of voltage application and the pulse of light. The time constant of the measuring circuit was considerably shorter than the transit time. The measurements were carried out at room temperature in the strong-injection mode, in which the influence of the electric field of the drifting carrier packet could not be disregarded. In these conditions, a space-charge-limited current (SCLC) flows in the sample [11].

Figure 1 shows oscillograms of the photocurrent, which were observed in the drift of electrons (Fig. 1a) and holes (Fig. 1b) in a *PSC* layer. It can be seen that the shape of the oscillograms of the transient photocurrent $I(t)$ is typical of the SCLC mode. The dependence $I(t)$ was characterized by the initial (I_0) and maximum (I_m) currents. The occurrence of the SCLC mode was indicated by the experimentally observed quadratic dependence of the current on voltage and its independence from the intensity of the injecting light. The time t_m corresponding to the maximum photocurrent varied in inverse proportion to the voltage U applied to the sample. As is well known [11], the carrier drift mobility can be determined in this measurement mode in two ways: from the transit time and from the photocurrent.

In the first case, the drift mobility was calculated using the formula

$$\mu = L^2/t_T U, \qquad (1)$$

where t_T is the transit time of carriers across the sample under conditions of weak injection, which is related to t_m by the expression $t_m = 0.8t_T$ [11].

In the second case, the drift mobility can be found from the expression for the initial current density under SCLC conditions [11]:

$$j_0 = I_0/S = \mu\varepsilon U^2/(2.25 \times 10^{13} L^3) \text{ A/cm}^2, \qquad (2)$$

where ε is the dielectric constant.

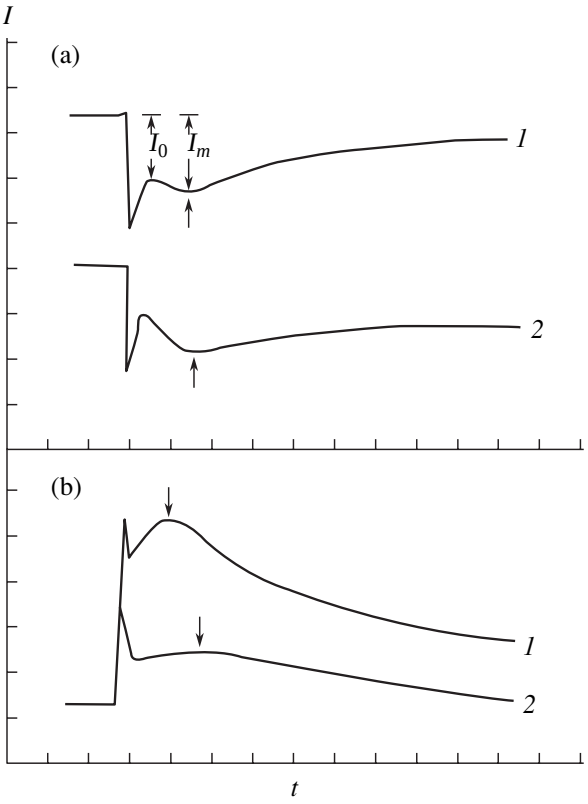

Fig. 1. Oscillograms of the transient photocurrent $I(t)$, which correspond to drift of (a) electrons and (b) holes in a 5-μm-thick *PSC* layer. Voltage U: (a) (*1*) 10 and (*2*) 5 V; (b) (*1*) 6 and (*2*) 4 V. Scale of t axis: (a) (*1*) 2 and (*2*) 5 μs/div; (b) (*1*, *2*) 10 μs/div. Scale of I axis: (a) (*1*) 65 and (*2*) 10 μA/div; (b) (*1*, *2*) 5 μA/div. The arrows show the instant of time t_m.

The drift mobilities of electrons (μ_e) and holes (μ_h), obtained using formula (1), are shown in Fig. 2 in relation to the applied voltage. It can be seen that, at $F = 10^4$ V/cm, $\mu_e = 6 \times 10^{-3}$ cm^2 V^{-1} s^{-1} and $\mu_h = 3 \times 10^{-3}$ cm^2 V^{-1} s^{-1} and the mobility increases with increasing voltage U.

The established dependence of the drift mobility on the electric field strength may indicate that carrier transport in *PSC* is dispersive, in which case a strongly spatially broadened carrier packet drifts in a sample [6]. Such a type of transport may account for the fact that the I_m/I_0 ratio found from the experimental $I(t)$ curves was smaller than the value of 2.7 that corresponds to the ideal SCLC mode [9, 12].

As the carrier drift mobilities were calculated by formula (1), formula (2) was used to determine the value of ε. Substitution of the known values of I_0, S, μ, L, and U into expression (2) yielded $\varepsilon \approx 4$. It should be noted that the resulting value of ε is close to that established for porous Si [8].

The type of the dependences $I(t)$ and $\mu(F)$ in *PSC* was also close to that obtained in porous Si, and the low

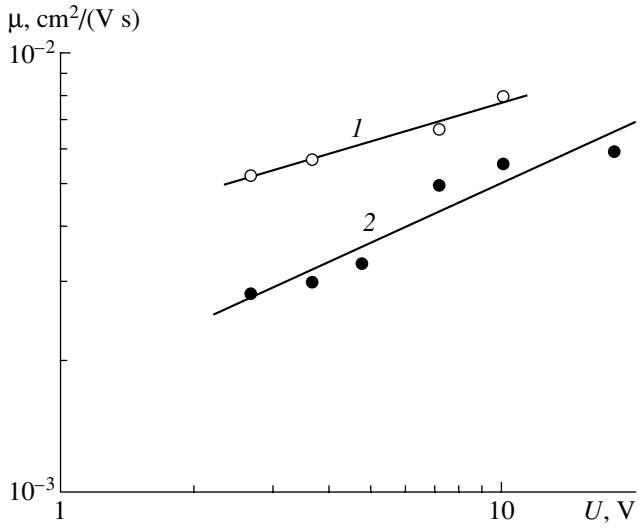

Fig. 2. Drift mobility of (*1*) electrons and (*2*) holes vs. the voltage across a 5-μm-thick *PSC* layer.

drift mobilities in *PSC* are of the same order of magnitude [8–10]. This suggests that the carrier transport in *PSC*, like that in porous Si [5, 6], is controlled by capture in localized states. For this type of transport, the motion of carriers in the allowed band with a high mobility μ_0, which corresponds to ohmic conductivity, is limited by multiple capture in traps. In *PSC*, localized states may appear, for example, on the well-developed surface of the forming pores. The dispersive nature of the transport suggests that the localized states are distributed over energy.

The conclusion drawn here agrees with the data of [13], where the conclusion that localized states are formed in *PSC* was based on the results obtained in measuring the capacitance–voltage characteristics of Schottky barriers formed on *PSC*.

This study was supported in part by NICOP (Naval International Cooperative Opportunities in Science and Technology program), grant no. 00014-01-1-0828, and also in part by a program of the Ministry of Science and Education of the Russian Federation.

REFERENCES

1. A. O. Konstantinov, C. I. Harris, and E. Janzen, Appl. Phys. Lett. **65**, 2699 (1994).
2. S. Zangooie, P. O. A. Persson, and J. N. Hilfiker, Mater. Sci. Forum **338–348**, 537 (2000).
3. S. Soloviev, T. Das, and T. S. Sudarshan, Electrochem. Solid-State Lett. **6**, G22 (2003).
4. M. Mynbaeva, Mater. Res. Soc. Symp. Proc. **742**, 303 (2003).
5. W. E. Spear, J. Non-Cryst. Solids **1**, 197 (1969).

6. N. F. Mott and E. A. Davis, *Electronic Processes in Non-Crystalline Materials*, 2nd ed. (Clarendon Press, Oxford, 1979; Mir, Moscow, 1982).
7. É. A. Lebedev and L. P. Kazakova, in *Electronic Phenomena in Chalcogenide Vitreous Semiconductors*, Ed. by K. D. Tséndin (Nauka, St. Petersburg, 1996), Chap. 4, p. 141.
8. L. P. Kazakova, A. A. Lebedev, and É. A. Lebedev, Fiz. Tekh. Poluprovodn. (St. Petersburg) **31**, 609 (1997) [Semiconductors **31**, 517 (1997)].
9. N. S. Averkiev, L. P. Kazakova, É. A. Lebedev, and N. N. Smirnova, Fiz. Tekh. Poluprovodn. (St. Petersburg) **35**, 609 (2001) [Semiconductors **35**, 588 (2001)].
10. N. S. Averkiev, L. P. Kazakova, and N. N. Smirnova, Fiz. Tekh. Poluprovodn. (St. Petersburg) **36**, 355 (2002) [Semiconductors **36**, 336 (2002)].
11. M. A. Lampert and P. Mark, *Current Injection in Solids* (Academic, New York, 1970; Mir, Moscow, 1973).
12. M. Silver, E. Snow, D. Wesson, and K. Okamoto, J. Non-Cryst. Solids **66**, 237 (1984).
13. P. A. Ivanov, M. G. Mynbaeva, and S. E. Saddow, Semicond. Sci. Technol. **19**, 319 (2004).

Translated by M. Tagirdzhanov

Semiconductors, Vol. 38, No. 9, 2004, pp. 1084–1087. Translated from Fizika i Tekhnika Poluprovodnikov, Vol. 38, No. 9, 2004, pp. 1121–1124.

AMORPHOUS, VITREOUS, AND POROUS SEMICONDUCTORS

Quartz Microtubes Based on Macroporous Silicon

E. V. Astrova*^, T. N. Borovinskaya*, T. S. Perova, and M. V. Zamoryanskaya***

** Ioffe Physicotechnical Institute, Russian Academy of Sciences, St. Petersburg, 194021 Russia*

*** University of Dublin, Trinity College, Dublin 2, Ireland*

^ e-mail: east@mail.ioffe.ru

Submitted February 9, 2004; accepted for publication February 11, 2004

Abstract—The conditions under which quartz microtubes 5–10 μm in diameter are formed in the course of structuring oxidized macroporous silicon are reported. It is shown that microtubes with a closed bottom can be fixed in a vertical position at equal distances from one another in correspondence with the "lattice" of macroporous silicon and may be of interest as test tubes for a single-chip microlaboratory. In a disordered state, long, thin quartz microtubes form a "glass wool." It is found that the microtubes and the glass wool exhibit high-intensity photo- and cathodoluminescence with the highest intensity in the green spectral range. © *2004 MAIK "Nauka/Interperiodica".*

1. INTRODUCTION

Interest in macroporous silicon (*ma*-Si), which has the form of an ordered lattice of vertical channels in a single-crystal silicon wafer, is steadily growing. This is due to the development of technology and the appearance of new possibilities for the application of *ma*-Si [1, 2]. In the present study, macroporous silicon with a layer of a thermal oxide on the inner surface of the channels was etched with a hot alkali, which actively reacts with silicon but does not dissolve the SiO_2 layer, to give thin-walled quartz microtubes. It was found that these tubes exhibit strong greenish luminescence when excited with the UV light of a mercury lamp. Their optical properties were studied.

2. FABRICATION OF MICROTUBES

An 80–180-μm layer of macroporous silicon was formed in *n*-Si(100) wafers with a thickness of 200 μm and a resistivity of 15 Ω cm using the standard technology [3]. Seed pits that served as macropore nucleation centers were arranged in a triangular lattice with a period of 12 μm. The diameter of the channels formed upon anodization was 4 μm. Using repeated cycles of oxidation and oxide dissolution, their diameter was increased to ~9 μm. The oxide formed in the last oxidation stage (1100°C, H_2O) was not removed. Quartz microtubes were obtained by patterning macroporous silicon. Figure 1 shows microtubes formed by etching windows on the front side of a wafer. First, the oxide was removed from the inner surface of channels through the photoresist mask within a round window, and then the sample was etched with a 30% KOH solution at $T = 65$°C to a depth that exceeded the thickness of the porous layer. Microtubes were preserved at the edges of the window. They were hanging on incompletely etched remains of silicon walls, which fastened them to the porous layer. The tubes were closed at their bottom ends; i.e., they were shaped like test tubes. The length of the tubes was equal to the depth of the macropores (80 μm in the case in question), their diameter was determined by the channel diameter (9 μm), and the wall thickness corresponded to the thickness of the SiO_2 layer (63 μm).

In alkaline etching of the back side of the wafer [4] (with a window opened in the substrate in the process), the bottom parts of the quartz tubes were uncovered, whereas their upper parts remained embedded in the *ma*-Si matrix. This yielded an ordered system of vertically standing microtubes with closed bottom ends (Fig. 2a). In addition to the vertically standing tubes, a reddish wool appeared in many cases as the etchant penetrated deep into the porous layer from the substrate side. This wool was virtually unetchable in the alkali and dissolved rather slowly in HF. An electron-microscopic study demonstrated that the wool is composed of fallen and tangled microtubes (Fig. 2b). It is an insulator, which makes it difficult to study using a scanning electron microscope. Similarly to separate microtubes, this wool exhibits strong photoluminescence (PL).

A silicon-based light-emitting material is usually obtained by electrochemical or chemical etching in an HF solution (nanoporous silicon) [5] or by introducing nanoscale silicon inclusions into the SiO_2 matrix [6]. In the case of quartz microtubes or glass wool, luminescence appeared when oxidized *ma*-Si was treated with a hot alkali. The reddish coloration of the glass wool suggests that the oxide contains an excess amount of silicon. To answer the question of why light is emitted by quartz microtubes, it is appropriate to compare their characteristics with the optical properties of nanoporous silicon and SiO_2.

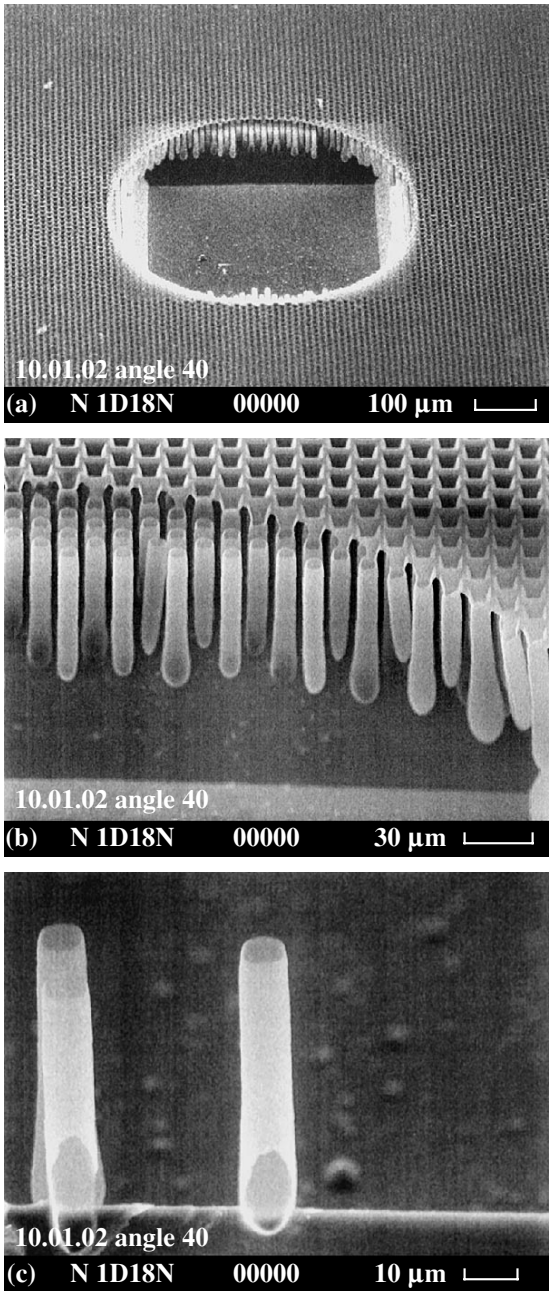

Fig. 1. Quartz microtubes on the periphery of a window in a sample of macroporous silicon: (a–c) SEM images on different scales.

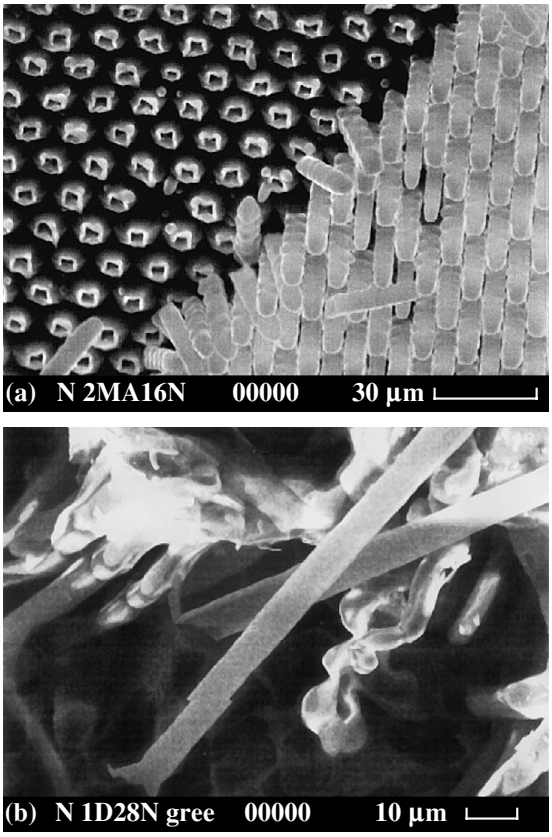

Fig. 2. Quartz microtubes in the form of (a) vertically standing test tubes and (b) glass wool. In both cases, the SEM images were obtained from the back side of the wafer.

2. EXPERIMENTAL PROCEDURE

The optical properties of the microtubes were examined using photo- and cathodoluminescence, as well as IR spectroscopy. PL spectra were studied on a Renishaw micro-Raman system 1000 setup, which provided a spatial resolution of <1 μm. A Laser Physics Reliant 150M Ar^+ laser operating at a wavelength of 514 nm served as the excitation source. The PL spectra were recorded at room temperature with a CCD camera (resolution ~1 cm^{-1}). The excitation power was maintained up to a maximum of 0.5 mW, because a higher-intensity illumination led to the destruction of tubes. The use of a microscope in the confocal mode made it possible to obtain spectra of both a single tube and a bundle of tubes (wool). The resulting PL spectrum was multiplied with the normalization curve obtained by recording the spectrum of a calibrated source of white light.

Cathodoluminescence (CL) spectra were measured on a Camebax electron-beam microanalyzer coupled with an optical spectrometer of original design. The spectra were excited with a 5-keV electron beam with a current of 15 nA. The width of the CL generation area was 1–3 μm. The spectra were recorded in the range 1.5—5.0 eV at room temperature.

IR spectra were recorded on a Bio-Rad 6000 Fourier spectrometer equipped with a UMA-500 IR microscope with a resolution of 4 and 8 cm^{-1}. A cadmium–mercury–tellurium photodetector operating in the spectral range 5000–700 cm^{-1} was used to record the spectra.

3. RESULTS AND DISCUSSION

Figure 3 shows PL spectra of the wool and separate tubes. For comparison are shown PL spectra of nanop-

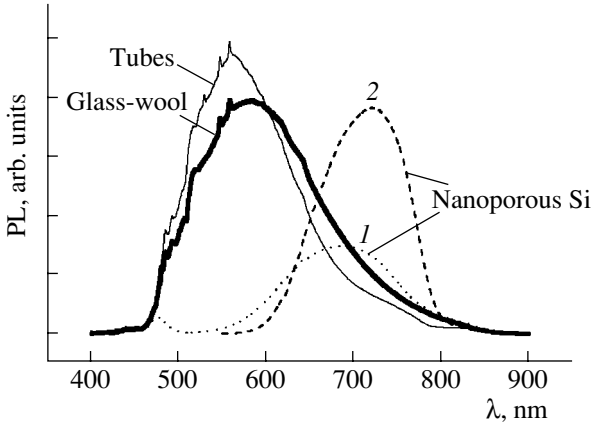

Fig. 3. PL spectra of separate microtubes and a bundle of tubes in the form of wool. For comparison are shown spectra of unoxidized nanoporous silicon (samples *1* and *2*) obtained under the same conditions.

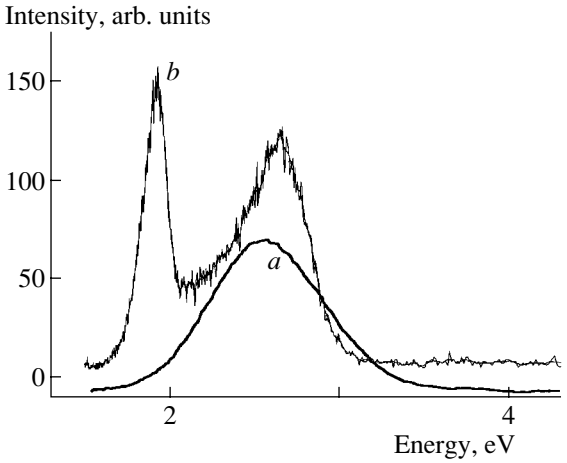

Fig. 4. CL spectra of (*a*) glass wool and (*b*) amorphous SiO_2.

orous silicon obtained in an HF : H_2O : C_2H_5OH = 2 : 1 : 1 solution at a current density of j = 20 mA/cm^2 (curve *1*) and in the same solution with the addition of $NaNO_2$ at j = 16 mA/cm^2 (curve *2*). It can be seen that the PL spectrum of the tubes is shifted to shorter wavelengths compared with the spectrum of "ordinary" nanoporous silicon, which is perceived by the eye as a greenish white glow when excited with UV radiation. The PL from the thermal oxide has an intensity that is several orders of magnitude lower and is shifted to even shorter wavelengths. It is known that the PL from light-emitting nanoporous silicon has several bands [6]. The red band, which is peaked at $h\nu$ = 1.5–1.9 eV, is due to silicon nanocrystallites and correlates with their size, whereas the blue band ($h\nu$ = 2.6–2.7 eV) is associated with SiO_2 [7]. The kinetics of the second band is distinguished by short decay times. It was demonstrated in [8] that a short-wavelength light is necessary to excite blue PL, which was not provided by the argon laser used in the experiment. A study of how nanoporous silicon is oxidized [7–9] has shown that the intensity of the blue band grows in the course of oxidation and, in the end, significantly exceeds the intensity of the red band. Thus, the PL from the microtubes is differs considerably from the PL associated with the as-prepared nanoporous silicon and has a shorter-wavelength component, which is more characteristic of SiO_2 or oxidized nanoporous silicon. The CL method is more suitable for a study of this component.

The electron excitation of the glass wool yielded the spectrum shown in Fig. 4. Despite the mild conditions of CL excitation, both the emission intensity and the outward appearance of the material changed in the course of spectral measurements (as observed with an optical microscope in the latter case). This modification occurred because of the heating of the irradiated microvolume of the sample, which is due to the low heat conductivity of the wool. In contrast to the typical CL spectrum of SiO_2, the spectrum of this wool does not contain bands at 1.9 and 2.7 eV.

In accordance with published data, several bands are observed at 1.9, 2.2, 2.7, and 4.3 eV when studying the PL and CL from amorphous SiO_2 [10, 11]. These bands are commonly related to intrinsic defects in SiO_2. The green band at 2.2 eV is characteristic of oxygen-deficient oxides, which contain a doubly coordinated silicon atom. Presently, the nature of this band has no definitive interpretation. A similar CL spectrum has been observed previously by the authors in thin natural oxide on silicon [12], in electron-beam-modified amorphous SiO_2 [13], and in oxide materials with silicon clusters [14].

The IR absorption spectra measured for different parts of a sample (in the regions with and without tubes) are shown in Fig. 5. It can be seen that spectrum *1* mainly contains bands typical of a thermal oxide of stoichiometric composition [15]. These are the bands associated with Si–O–Si stretching vibrations (~810 cm^{-1}), asymmetric bending vibrations (*AS1*) at ~1080 cm^{-1} (TO mode of Si–O–Si vibrations), and a broad shoulder at ~1200 cm^{-1}. The latter spectral feature results from the superposition of bands associated with asymmetric bending vibrations (*AS2*) of Si–O–Si and the TO mode (at ~1235 cm^{-1}) of the LO mode at 1080 cm^{-1}. Other bands associated with C–H and C–O bending vibrations are possibly due to the presence of trace amounts of ethanol, which was added to the electrolyte at the anodization stage in fabricating the macroporous layer. In addition, the spectrum contains a number of repetitive double bands, which are designated by asterisks. Similar bands also appeared in Raman spectra observed on the background of photoluminescence. The authors believe that these bands may belong to microcavity modes in SiO_2 tubes; however, a more detailed analysis of this phenomenon requires a separate study.

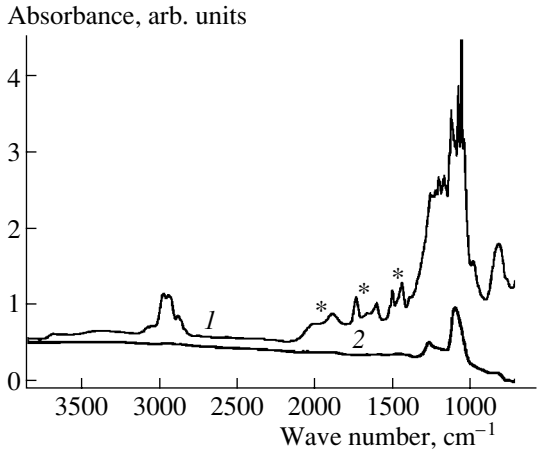

Fig. 5. IR absorption spectra recorded for different parts of a sample: (*1*) region with microtubes and (*2*) substrate.

The data obtained suggest that the microtube walls are composed of SiO_2 that contains defects in the form of excess silicon atoms. The reason for their appearance should be presumably sought in the difference between the oxidation processes within the *ma*-Si channels and on the planar silicon surface.

4. CONCLUSION

Thus, quartz microtubes 5–10 μm in diameter and up to 100 μm long, closed at one end like test tubes, were obtained for the first time. These test tubes are of interest because they are transparent in the visible spectral range and about a million of these test tubes can be fabricated in a single chip. Objects of this kind may find application as microreactors for combinatorial chemistry, in biochips, and in other similar fields.

It was found for the first time that alkaline etching of oxidized *ma*-Si gives rise to high-intensity photo- and cathodoluminescence with the highest intensity in the green part of the spectrum, which may be attributed to structural defects in SiO_2.

ACKNOWLEDGMENTS

The authors are grateful to A. Nashchekin for performing the electron-microscopic studies and to D. Potapova and S. Solosin for carrying out the PL experiments. This study was supported by INTAS (grant no. 01-0642), the "Physics of Solid-State Nanostructures" program of the Ministry of Science and Technology of the Russian Federation, the "Optics and Laser Physics" program of the Russian Academy of Sciences, and the Presidential Program for the Support of Scientific Schools (NSh 758-2003.2).

REFERENCES

1. V. Lehmann, *Electrochemistry of Silicon: Instrumentation, Science, Materials, and Applications* (Wiley–WCH, Weinheim, 2002).
2. H. Foll, M. Christophersen, J. Carstensen, and G. Haase, Mater. Sci. Eng. R **39**, 93 (2002).
3. V. Lehmann and H. Foll, J. Electrochem. Soc. **137**, 653 (1990).
4. E. V. Astrova, T. N. Borovinskaya, V. A. Tolmachev, and T. S. Perova, Fiz. Tekh. Poluprovodn. (St. Petersburg) **38**, 1125 (2004) [Semiconductors **38**, 1088 (2004)].
5. L. T. Canham, Appl. Phys. Lett. **57**, 1046 (1990).
6. O. Bisi, Stefano Ossicini, and L. Pavesi, Surf. Sci. Rep. **38**, 1 (2000).
7. L. Tsybeskov, Ju. V. Vandyshev, and P. M. Fauchet, Phys. Rev. B **49**, 7821 (1994).
8. A. Kux, D. Kovalev, and F. Koch, Appl. Phys. Lett. **66**, 49 (1995).
9. A. J. Kontkievicz, A. M. Kontkievicz, J. Siejka, *et al.*, Appl. Phys. Lett. **65**, 1436 (1994).
10. J. H. Stathis and M. A. Kastner, Phys. Rev. B **35**, 2972 (1987).
11. A. R. Silin' and A. N. Trukhin, *Point Defects and Elementary Excitations in Crystalline and Vitreous SiO_2* (Zinatne, Riga, 1985) [in Russian].
12. M. V. Zamoryanskaya, V. I. Sokolov, I. M. Kotina, and S. G. Konnikov, in *Proceedings of 7th International Symposium on Silicon Nitride and Silicon Dioxide Thin Insulating Films* (Paris, 2003), p. 348.
13. M. V. Zamoryanskaya and V. I. Sokolov, Mater. Res. Soc. Symp. Proc. **737** (F.3.40), 1 (2003).
14. C. Diaz-Guerra, D. A. Kurdyukov, J. Piqueras, *et al.*, J. Appl. Phys. **89**, 2720 (2001).
15. P. G. Pai, S. S. Chao, Y. Takagi, and G. Lucovsky, J. Vac. Sci. Technol. A **4**, 689 (1986).

Translated by M. Tagirdzhanov

Semiconductors, Vol. 38, No. 9, 2004, pp. 1088–1091. Translated from Fizika i Tekhnika Poluprovodnikov, Vol. 38, No. 9, 2004, pp. 1125–1128.

AMORPHOUS, VITREOUS, AND POROUS SEMICONDUCTORS

Technique for Patterning Macroporous Silicon and the Fabrication of Bars of 2D Photonic Crystals with Vertical Walls

E. V. Astrova*^, T. N. Borovinskaya*, V. A. Tolmachev*, and T. S. Perova**

** Ioffe Physicotechnical Institute, Russian Academy of Sciences, St. Petersburg, 194021 Russia*

*** University of Dublin, Trinity College, Dublin 2, Ireland*

^ e-mail: east@mail.ioffe.ru

Submitted February 9, 2004; accepted for publication February 11, 2004

Abstract—A new technological process for fabricating structures with vertical walls in a thick layer of macroporous silicon on a substrate is reported. The problem of photolithography has been solved by patterning on the back side of the wafer. As a result, the silicon substrate itself serves as a mask through which certain parts of the porous layer are removed. Narrow and high bars of macroporous silicon, aligned with macropore rows, have been fabricated. The 2D photonic crystals obtained have been used for in-coupling of light in the direction perpendicular to the channel axes and for recording IR spectra. © *2004 MAIK "Nauka/Interperiodica".*

1. INTRODUCTION

A technique for fabricating an ordered "lattice" of deep channels with vertical walls was first suggested in [1]. The process involves opening windows in the oxide mask on the surface of *n*-Si(100) by means of photolithography, alkaline etching of pits across the mask, and anodization in an HF solution under illumination from the back side of the wafer. The resulting layer of macroporous silicon (*ma*-Si) contains cylindrical (or square in cross section) channels (macropores) 1 to 10 μm in diameter and up to 300 μm deep, formed at the place of the pits. A necessary condition for these channels to be formed is the uniform distribution of the nucleation centers over the entire anodization area and the appropriate relationship between the substrate resistivity and the lattice period of the phototemplate [2]. A rather wide transition layer is formed at the boundary between the macroporous region and that part of the wafer that was not subjected to anodization. Within this layer, the regular structure is distorted (pores are branching, have different depths, and so on).

Various application fields of *ma*-Si [3] frequently require that separate regions of macroporous silicon, with sharp edges and vertical walls, be created on a substrate. In particular, the input of light into a 2D photonic crystal requires fabrication of narrow bars oriented in a certain way with respect to the lattice of the initial *ma*-Si. The first study to address this problem [4] demonstrated that attempts to create a pattern in *ma*-Si with the use of a positive or negative photoresist are unsuccessful. Therefore, the technique suggested in the communication mentioned above included a complex process that assumes the deposition of silicon nitride onto the inner surface of channels, pore filling with polycrystalline silicon or aluminum, and the formation of a pattern on the front side of the wafer. This process, which was named the Ottow process, allowed one to remove certain parts of the *ma*-Si layer to obtain narrow bars with vertical walls on the substrate. Structures of this kind were used in [5, 6] to study the optical properties of photonic crystals.

This paper reports on a simpler process for creating *ma*-Si regions with vertical walls, which is based on masking pores with only a thermal oxide and the formation of a pattern on the back side of the wafer. In con-

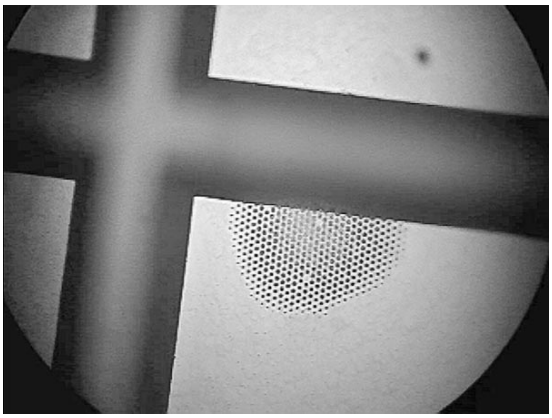

Fig. 1. Image of the back side of a wafer at the initial stage of pore opening. A small region in which the pore bottoms have already opened can be seen. (Optical microscope.)

1063-7826/04/3809-1088$26.00 © 2004 MAIK "Nauka/Interperiodica"

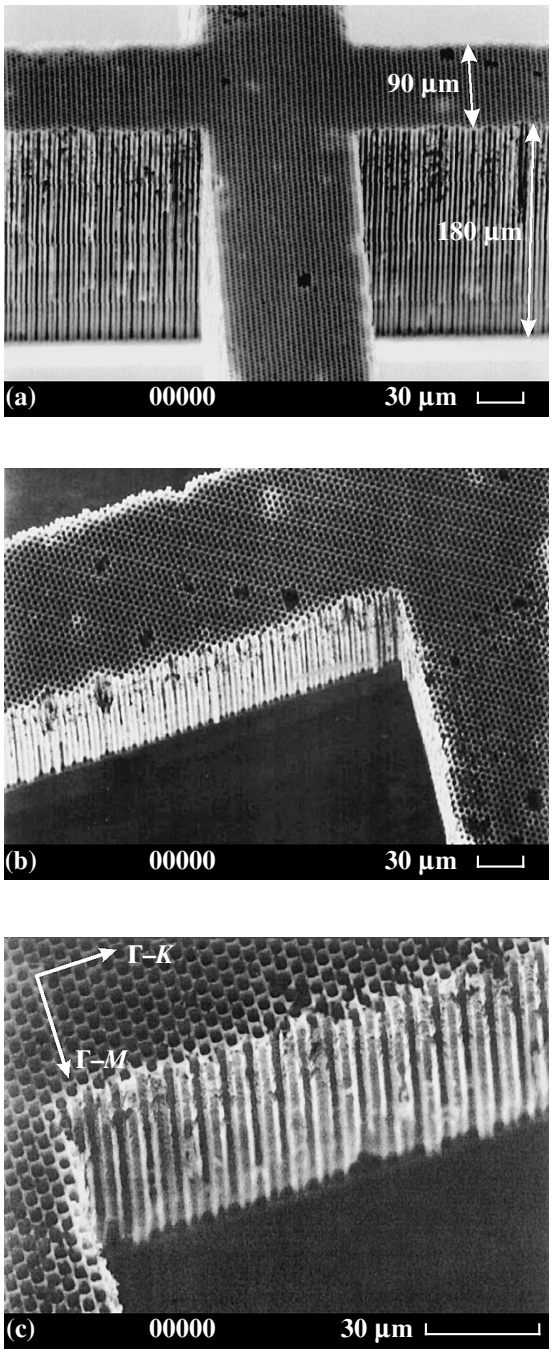

Fig. 2. Macroporous silicon bars with vertical walls: (a, b) SEM images obtained at different angles of view and (c) principal directions in the triangular lattice of the photonic crystal.

trast to the Ottow method, the structures formed have no common substrate, which is also structured. The resulting bars of macroporous silicon were used to introduce light perpendicularly to the axis of the channels, which made it possible to measure reflection spectra with an IR microscope and to determine the position of the photonic gap.

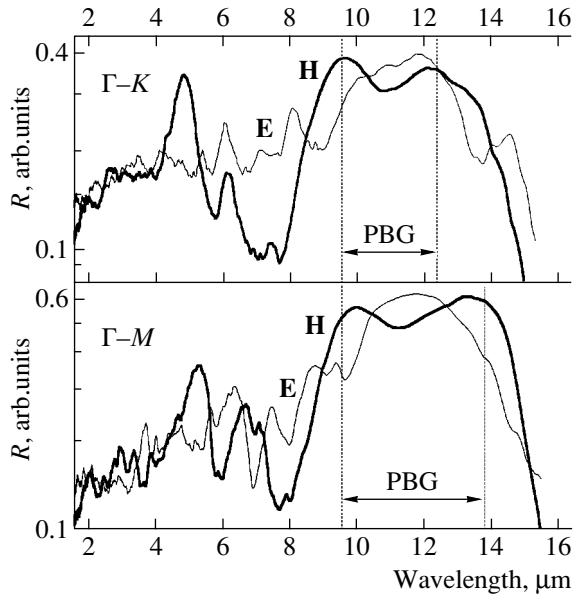

Fig. 3. Reflection spectra for two directions in the photonic crystal, Γ–*K* and Γ–*M*, and two polarizations of light: perpendicular (**H**) and parallel (**E**) to the axis of channels.

2. TECHNOLOGICAL PROCEDURE FOR FABRICATING MACROPOROUS SILICON BARS

The starting *n*-type Si(100) wafers (ρ = 5 Ω cm) were cut into 20×20 mm^2 squares, which were thinned to 200 μm and polished on both sides. Further operations are clear from the schematic of the process shown below. After thermal oxidation, a through alkaline etching of the alignment marks was performed (stage *2*). Then a triangular lattice of seed pits with a period A = 4 μm was formed and photoelectrochemical etching was carried out to a depth of 170–180 μm (stages *3*, *4*). The pits were removed by polishing the front side, and the sample was oxidized in water vapor at T = 1200°C for 70 min. Photolithography was used to open square windows in the oxide on the back side of the wafer; the sides of the squares were oriented along the rows of macropores (stage *5*). A minor bending of the oxidized wafer was elastic and could be eliminated by suction to the table in the mask aligner. Anisotropic alkaline etching was performed through the thus opened windows, so that the substrate was locally removed to the depth that the porous layer needed to reach (stage *6*). Here, the ability of the thermal oxide to protect the inner surface of pores during etching in a KOH solution was used. The initial stage of pore opening can be seen in Fig. 1. Further operations consisted in the removal of the oxide from the inner surface of the pores through the squares opened on the back side of the wafer (stage *7*) and subsequent dissolution of the thin silicon walls between the pores in the window area (stage *8*). In the final stage, the oxide was removed from the pores in an

HF solution. If it was necessary to make the porosity higher, additional oxidation with subsequent dissolution of SiO_2 was used. In the process, narrow bars of *ma*-Si did not undergo any noticeable deformation, unlike the nonstructured porous layer.

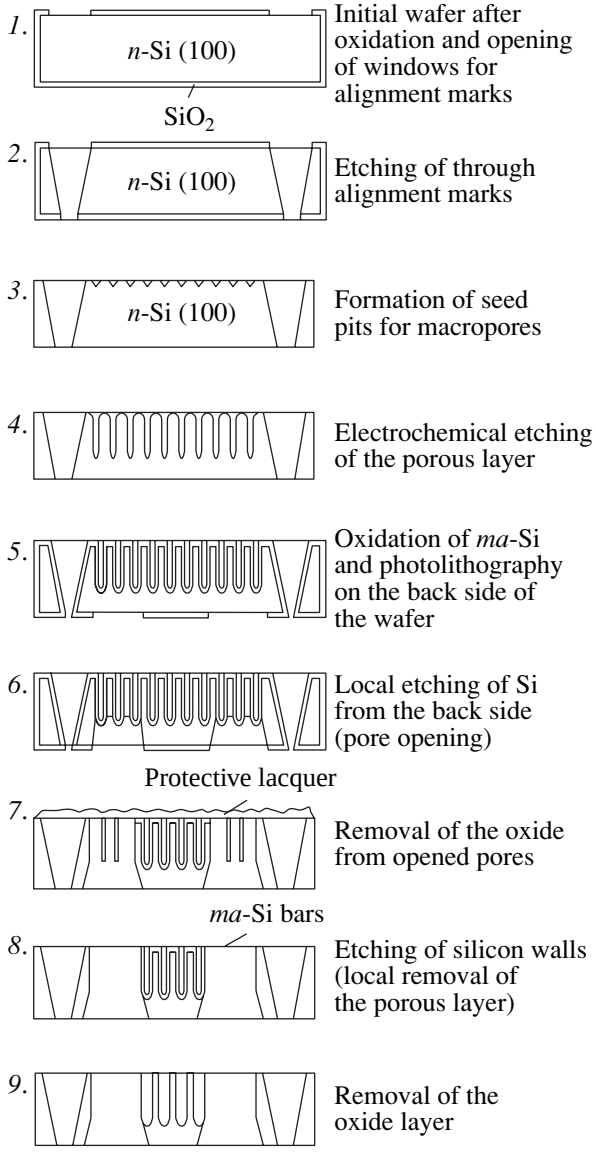

As a result, through square windows separated by crosses of narrow bars of a macroporous layer on the substrate were produced in the wafer. Electron-microscopic images of these bars, obtained at different angles of view, are shown in Figs. 2a, 2b, and 2c. It can be seen that the *ma*-Si bars formed have vertical walls and are oriented along the macropore rows. They are about 90 μm wide (22–26 rows, depending on the direction in the lattice) and 200 μm high (180 μm porous layer + 20 μm substrate).

3. SPECTRA OF PHOTONIC CRYSTALS

The *ma*-Si bars obtained are oriented in mutually perpendicular directions, which correspond to the Γ–*K* and Γ–*M* directions in the reciprocal space of the 2D triangular lattice of *ma*-Si (see Fig. 2c). They are particularly suitable for optical characterization of photonic crystals. The *ma*-Si bars were oxidized three times, and the oxide was dissolved the same number of times. As a result, the channel diameter increased from 1.7 to 3.4 μm and the ratio between the channel radius and the lattice constant was as high as $r/A = 0.425$, which gives reason to believe that a complete photonic gap was formed [7]. Reflection spectra were measured on a Bio-Rad 6000 FTIR spectrometer equipped with a UMA-500 IR microscope, at an aperture of 100×100 μm^2. The incident light was focused with the microscope onto the lateral side of a *ma*-Si bar, with the wave vector of light directed perpendicularly to the axis of the channels. The measurements were performed with a spectral resolution of 8 cm^{-1} at 64 scans. To obtain spectra in polarized light, a polarizer was placed in front of the input window of the photodetector.

Figure 3 shows reflection spectra recorded for different directions in the crystal at two orthogonal polarizations of light. The spectra contain broad regions of high reflection (up to ~60%), centered at around 11 μm, which correspond to the principal photonic gap. The gaps for light polarized perpendicularly to the channels (*H* polarization) are somewhat wider than those for light polarized along the channels (*E* polarization), which is consistent with the results of calculations [7] for a triangular lattice of cylindrical channels in a material with a dielectric constant ($\varepsilon = 11.4$) close to that in the present study.

4. CONCLUSION

Thus, a technological procedure for obtaining structures based on the ordered lattice of macroporous silicon has been developed. This method does not require an intricate process of pore filling and surface planarization prior to photolithography. Instead, the photolithography is done on the back side of the wafer. The structures with deep vertical walls, obtained using the technique suggested, can be used to fabricate components for micromechanics and microphotonics. The application of the technology is demonstrated by the example of fabricating narrow bars of a 2D photonic crystal, on which IR reflection spectra have been studied.

ACKNOWLEDGMENTS

The authors are grateful to A. Nashchekin and Yu. Pilyugina for help in obtaining SEM images and preparing the illustrative material. The study was supported by INTAS (grant no. 01-0642), the "Physics of

Solid-State Nanostructures" program of the Ministry of Science and Technology of the Russian Federation, the "Optics and Laser Physics" program of the Russian Academy of Sciences, and the Presidential Program for Support of Scientific Schools (NSh 758-2003.2).

REFERENCES

1. V. Lehmann and H. Foll, J. Electrochem. Soc. **137**, 653 (1990).
2. V. Lehmann and U. Gruning, Thin Solid Films **297**, 13 (1997).
3. H. Foll, M. Christophersen, J. Carstensen, and G. Haase, Mater. Sci. Eng. R **39**, 93 (2002).
4. S. Ottow, V. Lehmann, and H. Foll, J. Electrochem. Soc. **146**, 385 (1996).
5. U. Gruning, V. Lehmann, S. Ottow, and K. Busch, Appl. Phys. Lett. **68**, 747 (1996).
6. S. W. Leonard, H. M. van Driel, K. Busch, *et al.*, Appl. Phys. Lett. **75**, 3063 (1999).
7. J. D. Joannopoulos, R. D. Meade, and R. D. Winn, *Photonic Crystals: Molding the Flow of Light* (Princeton Univ. Press, Princeton, 1995), Appendix C, p. 125.

Translated by M. Tagirdzhanov

Semiconductors, Vol. 38, No. 9, 2004, pp. 1092–1098. Translated from Fizika i Tekhnika Poluprovodnikov, Vol. 38, No. 9, 2004, pp. 1129–1134.

PHYSICS OF SEMICONDUCTOR DEVICES

A Study of Deep Levels in CdHgTe by Analyzing the Tunneling Current of Photodiodes

V. I. Turinov

NPO Istok, Fryazino, Moscow oblast, 141190 Russia

Submitted August 21, 2003; accepted for publication October 17, 2003

Abstract—The energy positions of the levels $E_t - E_v$ in the band gap and their concentration N_t were determined from studies of tunneling current J_t via these levels in photodiodes based on $Cd_xHg_{1-x}Te$. The shallow acceptor levels $E_t - E_v$ = 8–12 eV introduced by singly charged vacancies V_{Hg}^{+} are observed in the band gap of almost all photodiodes. Deep levels $E_t = E_v + 0.26E_g$ that manifest themselves as recombination states are observed in a number of photodiodes. Even deeper levels ($E_t = E_v + 0.6E_g$) are also observed, which can act as either recombination states or deep traps with a small cross section for the capture of holes. © *2004 MAIK "Nauka/Interperiodica".*

Singly charged vacancies V_{Hg}^{+} introduce shallow acceptor levels E_t into the band gap of $Cd_xHg_{1-x}Te$ ternary semiconductor compounds; these levels are located near the top of the valence band E_v [1]. According to different publications, the experimentally determined energy positions of these shallow acceptor levels range from $E_t - E_v = (12.5 \pm 2)$ meV for a composition with $x = 0.215$ to $E_t - E_v$ = 9.2–10.8 meV for $x = 0.225$ [2]. There are also data on levels with $E_t - E_v$ = 15 meV [1] and 5 meV [3]. Impurity atoms can also introduce levels with this energy position [4]. Deep levels acting mostly as recombination states are more interesting from the standpoint of the effect the position of the level has on the electrical parameters of photodiodes. It is believed that levels with $E_t - E_v \approx 60$ meV (band gap $E_g \approx 100$ meV at $T = 78$ K) are introduced by doubly charged mercury vacancies V_{Hg}^{++} [1]. Jones *et al.* [5] systematized the results of studying $Cd_xHg_{1-x}Te$ samples by deep-level transient spectroscopy (DLTS) and derived the dependences of $E_t - E_v$ on the composition (x) as $E_t = E_v + 0.4E_g$ and $E_t = E_v + 0.75E_g$ for undoped $Cd_xHg_{1-x}Te$. According to the model suggested by Jones *et al.* [6], centers with $E_t = E_v + 0.4E_g$ and $E_v + 0.75E_g$ can be thought of as interstitial Hg, Si, and C atoms; Cl atoms at Hg lattice sites; and antisite defects (Te atoms in the metal sublattice). According to data obtained using DLTS (see [7] and other publications by the same authors), in the $Cd_xHg_{1-x}Te$ samples with E_g = 96 meV, the donor level has the ionization energy $E_t - E_v$ = 43 meV and the acceptor level has $E_t - E_v$ = 35 meV [7–11]. Levels with $E_t - E_v$ = 46 and 52 meV were observed in the band gap of $Cd_xHg_{1-x}Te$ with x = 0.219 [8].

The band-to-band tunneling current I_t [9], tunneling current via impurity levels J_t [10], and tunneling current over the surface [11] are observed in photodiodes based on narrow-gap $Cd_xHg_{1-x}Te$ even when relatively low reverse-bias voltages are applied. The surface tunneling current is typically stimulated under a special metal electrode deposited on an insulator layer above the space-charge region (SCR) of the junction where this region outcrops. The results of preliminary studies of differential resistance R_d in a number of photodiodes were reported in my previous publication [12]. These results were treated in the context of a model of a single tunneling current I_t. It was found later as a result of a more detailed study that there was a transition range of bias voltages U at which the current–voltage (I–V) characteristics had slightly different slopes from those typical of the I_t current where J_t currents are active. Dependences $J_t(U)$ for the tunneling current via levels (which are, as a rule, levels of intrinsic point defects in $Cd_xHg_{1-x}Te$) can be used to determine the energy positions of these levels, and this task was undertaken in this paper. We studied photodiodes fabricated on the basis of p-$Cd_xHg_{1-x}Te$ samples whose parameters (measured at $T = 78$ K) are listed in the table. The base n^+-type region was doped by implanting Zn^{++} ions with energy E = 120 keV and a dose of 1×10^{15} cm^{-2}. According to estimations, the depth of n^+–p junctions was ~0.5–0.8 μm. Zinc sulfide films were used as masks and protective coatings. The ohmic contact to the n^+-type region was formed by sputtering deposition of indium, and that to the p-type region was formed by electrochemical deposition of gold. The $Cd_xHg_{1-x}Te$ samples with equal hole concentration p (for example, samples A1 and A2 in the table) were obtained from the same starting sample (A) with n-type conductivity. Sample A was cut into smaller sizes, and subsequent annealing that converted these smaller samples to

Parameters of photodiodes based on $Cd_xHg_{1-x}Te$

$Cd_xHg_{1-x}Te$ sample (p at 78 K)	Photodiode no.	λ_{co}, μm	$R_{d\,max}$, kΩ/ –U, mV	p_p, 10^{16} cm^{-3}	C, pF (U = 0)	U_{bi}, mV	$E_t - E_v$, meV	N_t', 10^{15} cm^{-3}
A1 A2 (1.1×10^{15} cm^{-3})	2	10.0	5.6/405	1.3	171.6	47.3	38	0.18
	4	9.9	37/300	0.8	120.5	42.5	32	0.11
	5	9.8	55/135	0.6	132.9	35.6	8	0.37
	7	–	18.4/50	0.25	91.7	27.8	12	0.4
B3 B4 (1.5×10^{16} cm^{-3})	9	–	35/135	0.3	73.5	43.2	40	0.26
	11	9.8	23/150	0.22	–	25.9	72	19
	12	10.1	1200/160	1.2	118.2	60.2	36	0.18
	14	9.9	32/126	0.11	63.7	29.4	76	9.0
C1 (1×10^{16} cm^{-3})	3	10.1	3.6/130	0.4	151.9	24.8	8/32	0.036/0.046
	18	10.8	8.7/90	1.5	217.3	32.6	36	0.22
	21	9.94	16.2/68	3.5	237	42.9	38	5.1
D1 D2 (1.8×10^{16} cm^{-3})	10	11.6	12/65	1.0	–	–	8	0.5
	13	11.48	23.5/48	–	–	–	36	0.46
	15	11.29	17.6/49	–	–	–	8	0.24
	16	11.28	27/69	–	–	–	36	0.19
	17	–	16.2/50	–	–	–	28	0.9
G1 (2.8×10^{16} cm^{-3})	8	–	15/47	1.1	235	26.3	22	0.077
	19	11.48	20.6/50	1.0	212.3	27.1	8/58	0.2/0.56
	20	11.8	15/47	0.37	147.9	24.1	8/42	0.35/0.35

Note: The diameter of n^+–p junctions was defined by a photomask and equaled 300 μm.

p-type conductivity was performed under the same temperature conditions (see [13]). Due to technological features of the fabrication of n^+–p junctions, it was not possible to tell from which specific sample (for example, A1 or A2) the photodiodes 2, 4, 5, and 7 were fabricated. These photodiodes were therefore combined into the same group in the table.

The expression for the tunneling current via the impurity levels is written as [10]

$$J_t = qN_t'\left(\frac{\pi^2}{\hbar^3}\right)m_n^* W_t^2 \exp\left[-\frac{4(2m_n^*)^{1/2}}{3\hbar q\mathscr{E}_m}(E_g - E_t)^{3/2}\right] \times \int_0^{\alpha}\left[1 - \exp\left(-\frac{E}{\bar{E}_t}\right)\right]dE, \quad (1)$$

where E is the tunneling-electron energy reckoned from the top of the valence band E_v on the n^+-type side of the junction; q is the elementary charge; $\hbar$ is the reduced Planck constant; m_n^* is the effective electron mass in the conduction band; the matrix element of transition from the valence band to the impurity level $E_t - E_v$ is $W_t^2 = 1.2 \times 10^{-23}$ eV^2 cm^3 [14]; $\mathscr{E}_m = qN_aW/\varepsilon_0\varepsilon_s$ is the maximum value of the electric field in an abrupt junction (in our case, the n^+–p junction) and depends only on the parameters N_a (the acceptor concentration in the lightly doped p-type region) and W (the SCR width); ε_0 and ε_s are the permittivity of free space and the relative permittivity of the semiconductor, respectively; E_g is the semiconductor band gap; $\alpha = \zeta_p + \zeta_n - qU - E_t - E_g$, where ζ_p and ζ_n are the Fermi levels in the p- and n^+-type regions, respectively; U is the bias voltage applied to the junction; $N_t' = N_t/\{1 + (1/2)\exp[(-E_g + E_t - \zeta_p)/k_0T]\}$ is the effective density of the levels filled with electrons (N_t is the total concentration of the levels); and $\bar{E}_t = \hbar F_t/\{[2m_n^*(E_g - E_t)]^{1/2}\}$, where $F_t = q\mathscr{E}$ is the force of the electric field $\mathscr{E}$ that acts on an electron that resides at the level $E_t - E_v$ in the band gap within the SCR of the junction. The integral in expression (1) is on the order of unity, so there is no need to calculate this integral.

Substituting $m_n^*/m_0 = 0.075E_g$ [eV] and $\mathscr{E}_m = (2qN_aU_t/\varepsilon_0\varepsilon_s)^{1/2}$ ($U_t = U_{bi} + U$, where U_{bi} is the built-in potential) into expression (1), we obtain

$$J_t = 8.9 \times 10^{-25}N_t'[E_g^{3/2}/(E_g - E_t)^{3/2}] \times \exp[-4.3 \times 10^{-10}E_g^{1/2}(E_g - E_t)^{3/2}/N_a^{1/2}U_t^{1/2}], \quad (2)$$

where the quantity J_t is expressed in A/cm^2.

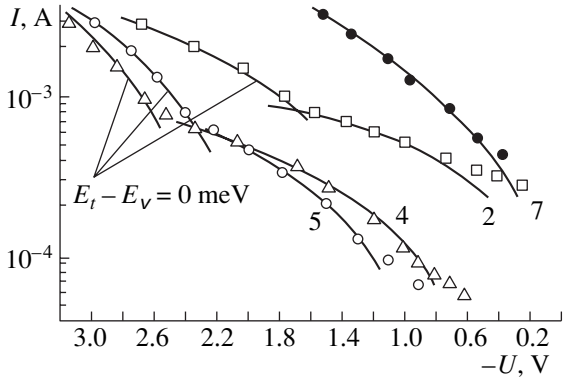

Fig. 1. Current–voltage characteristics of photodiodes based on $Cd_xHg_{1-x}Te$ with $x = 0.222$: the tunneling-current components J_t are shown. Samples A1 and A2; numerals (2, 4, 5, 7) by the curves are diode numbers.

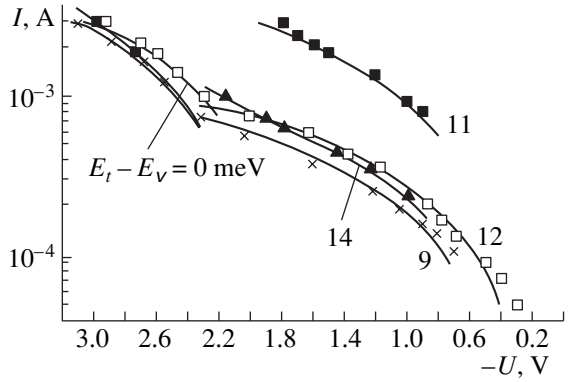

Fig. 2. Current–voltage characteristics of photodiodes based on $Cd_xHg_{1-x}Te$ with $x = 0.217$: the tunneling-current components J_t are shown. Samples B3 and B4; numerals (9, 11, 12, 14) by the curves are photodiode numbers.

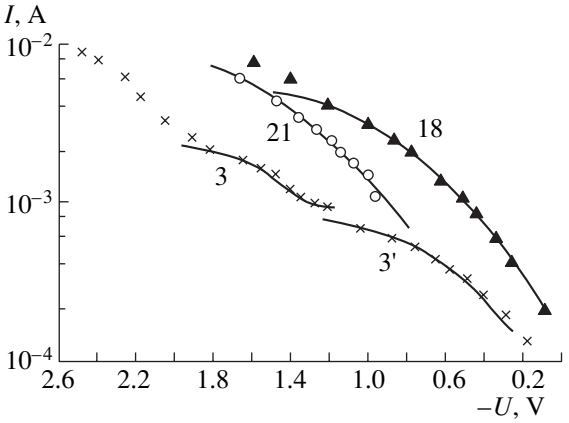

Fig. 3. Current–voltage characteristics of photodiodes based on $Cd_xHg_{1-x}Te$ with $x = 0.215$; the tunneling-current components J_t are shown. Sample C1; numerals (3, 3', 18, 21) by the curves are diode numbers.

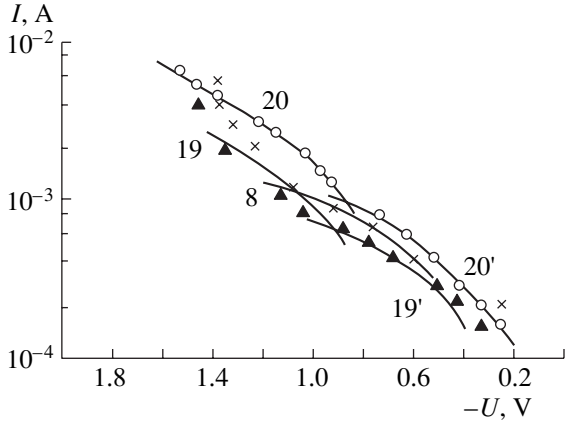

Fig. 4. Current–voltage characteristics of photodiodes based on $Cd_xHg_{1-x}Te$ with $x = 0.219$; the tunneling-current components J_t are shown. Sample G1; numerals (8, 19, 19', 20, 20') by the curves are diode numbers.

In expression (2), two parameters (N_t' and $E_t - E_v$) are unknown. The values of these parameters can be determined by varying them and attaining agreement between the theoretical (2) and experimental *I–V* characteristics of photodiodes in the range of the bias voltages *U* at which the tunneling current via impurity levels is observed. The values of $N_a = p_p$ and U_{bi} were determined from the capacitance–voltage (*C–V*) characteristics of the n^+–*p* junctions. The values of E_g at 78 K were obtained from spectral characteristics of photosensitivity as E_g [eV] = $1.24/\lambda_{co}$ [μm], where λ_{co} is the cutoff wavelength of the photodiode's spectral characteristic at a level of 0.5 of the photosensitivity peak (see table).

Examining the reverse portions of experimental *I–V* characteristics *I*(*U*) plotted on a log–log scale, it is difficult to separate the currents I_t and J_t since they have slopes that differ only slightly. Therefore, in Figs. 1–5, the reverse *I–V* characteristics are plotted on a semilogarithmic scale for the ranges of *U* where the tunneling currents J_t are prevalent. At $E_t - E_v = 0$, the voltage dependences of J_t coincide with those of I_t. In the table, we list the values of $E_t - E_v$ and N_t' determined from these *I–V* characteristics. The corresponding values of $E_t - E_v$ and N_t' in the cases where two levels are observed are listed in the form of fractions (separated by a slash).

In $Cd_xHg_{1-x}Te$ solid solutions [16], the valence bands E_{vi} are formed from the *p* levels of Te atoms, whereas the conduction band is formed from the *s* levels of the metal, Hg, and Cd atoms. In the Kane model [17], which adequately describes narrow-gap semiconductor compounds such as InSb and $Cd_xHg_{1-x}Te$ and is based on the (**kp**) approximation of the perturbation theory, the wave functions of the valence bands E_{vi} and the conduction band E_c are formed from a mixture of the *p* and *s* functions. If the electron wave vector **k** = 0

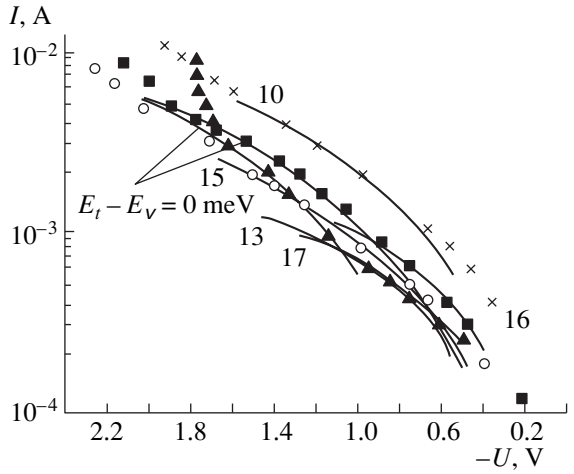

Fig. 5. Current–voltage characteristics of photodiodes based on $Cd_xHg_{1-x}Te$ with $x = 0.214$; the tunneling-current components J_t are shown. Samples D1 and D2; numerals (10, 13, 15, 16, 17) by the curves are photodiode numbers.

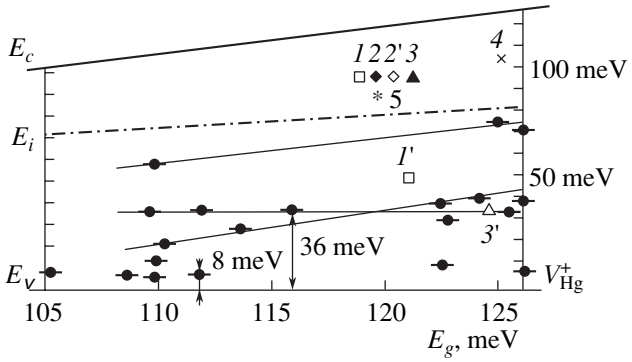

Fig. 6. Energy diagram of electrically active levels in $Cd_xHg_{1-x}Te$. $Cd_xHg_{1-x}Te$ samples: (*1*, *1'*) A1, (*2*, *2'*) A2, (*3*, *3'*) C1, (*4*) C2, and (*5*) B1. Data (*1*–*5*) were obtained before annealing and data (*1'*–*3'*) were obtained after annealing. Other points represent data for the photodiodes listed in the table.

(at the center of the Brillouin zone), the wave functions E_c exhibit only the symmetry of *s* functions; i.e., the E_c band consists of only the *s* levels of Hg and Cd in the vicinity of $\mathbf{k} = 0$. The wave functions of the bands E_{vi} at $\mathbf{k} = 0$ exhibit only the symmetry of *p* functions, whereas the band E_{v1} (the heavy-hole band that largely controls all electrical parameters of the material with *p*-type conductivity) exhibits the symmetry of *p* functions also at $\mathbf{k} \neq 0$; i.e., the E_{v1} band consists exclusively of the *p* levels of Te atoms. When electrically active intrinsic point defects are formed (for example, V_{Hg} or V_{Cd}), the Hg and Cd atoms leave the corresponding lattice sites and bring with them the *s* electrons, so that the uncompensated Te atoms capture electrons in order to recover the electroneutrality (the *p* levels of Te atoms are split off from the E_{vi} bands, whereas the captured electron is collectivized by neighboring Te atoms). In other words, the V_{Hg} and V_{Cd} vacancies act as acceptors. The levels of the above acceptors, although split off from the corresponding bands, are still related to these bands; the energy gap ΔE in reference to the related band varies as, for example, the temperature or composition (x) varies. Using the dependence $\Delta E(x)$, one can determine to which band a particular level is related. This reasoning is illustrated by the energy diagram (Fig. 6). The levels with $E_t - E_v = 8$ meV are related to E_v (the *p* levels of Te and the vacancies V_{Hg}^+). The diagram indicates that some of the levels with an ionization energy of ~36 meV are related to the band E_c in the form of the dependence $E_t \approx E_v + 0.26E_g$, whereas $E_t - E_v$ is independent of composition for some other levels. Thus, in the group of levels under consideration, there are those that are unrelated to the centers studied previously [1, 6]. These new centers may be the vacancies V_{Te}. It is believed that the V_{Te} vacancies are also recombination centers [18, 19]. Finally, the deep levels with $E_t - E_v = 58$, 72, and 76 meV are related to the E_c band and fit the dependence $E_t = E_v + 0.6E_g$, which is close to the dependence $E_t = E_v + 0.75E_g$ [5]. It is worth noting that the levels with $E_t - E_v = 79$ meV observed by Cotton *et al.* [20] can be related [20] to the surface states. This inference may be true in our studies but only for photodiode 11, since the surface diffusion current in the channel I_{ds} [22] was prevalent in the reverse portion of the *I*–*V* characteristic (see Fig. 2 in [21]) of this photodiode at voltages $U \approx -(50–200)$ meV. However, this identification is inconsistent with the data reported previously [21] (Fig. 4): we did not observe the characteristic spreading of the junction over the surface as U varied (the spectral characteristics and dependences of the signal on the coordinate in the sensitive area of photodiode 18 serve as an example [21]). The shape of the spectral characteristic of photodiode 19 in the short-wavelength region (see Fig. 5 in [21]), a slight spreading of the reverse-biased junction (see Fig. 4 in [21]), and the *I*–*V* characteristic (see Fig. 3 in [21]) indicate that the role of the surface is no more important than in other photodiodes. The larger capacitance $C(U = 0)$ of photodiode 19 compared to that, for example, of photodiode 14, which incorporates the levels with the same position ($E_t \approx E_v + 0.6E_g$), is caused by the fact that these photodiodes differ in $\lambda_{co}(E_g)$ and $N_a = p_p$ (see table). This difference in N_a (for the same concentration of the donor doping impurity N_a introduced into the n^+-type layer) leads to the fact that the width of the junction SCR $W = (2\varepsilon_s\varepsilon_0 U_{bi}/qN_a)^{1/2}$ in photodiode 19 is smaller than in photodiode 14 by a factor of approximately 3 for comparable U_{bi}. Accordingly, the capacitances of these photodiodes differ by the same factor. These data are inconsistent with the assumption that the levels $E_t \approx E_v + 0.6E_g$ are related to the surface states. Direct studies of the ZnS–CdHgTe structures did not confirm the presence of local levels with this energy

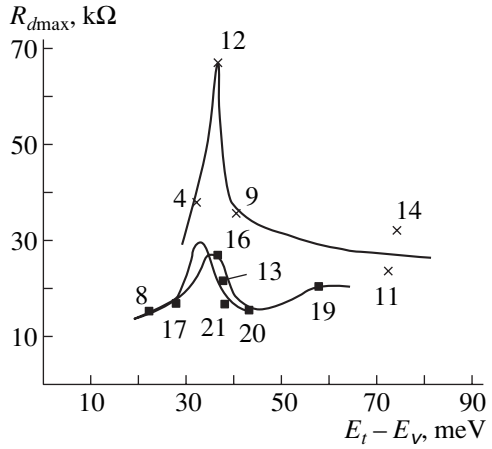

Fig. 7. Dependence of $R_{d\max}$ for photodiodes based on $Cd_xHg_{1-x}Te$ on the energy positions of recombination levels. The data refer to the photodiodes listed in the table.

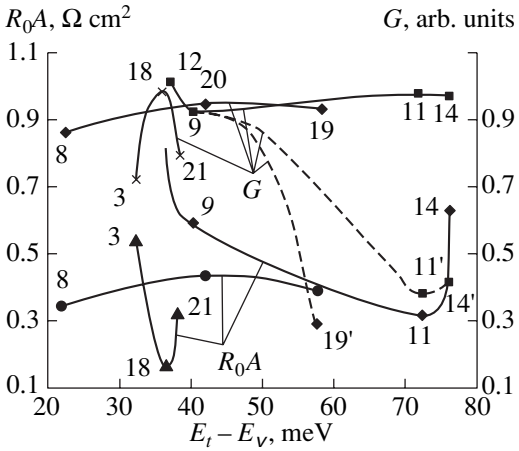

Fig. 8. Dependences of R_0A for photodiodes based on $Cd_xHg_{1-x}Te$ and the recombination probability G on the energy position of the levels $E_t - E_v$.

position at the interface either [23]. Consequently, these levels are introduced by centers that are located in the bulk of the CdHgTe material itself and are related either to an impurity or to intrinsic point defects. In order to identify the origin of these levels, further research is needed using, for example, nuclear magnetic resonance or X-ray structure analysis. In Fig. 6, we also show levels determined from temperature dependences of the resistivity $\rho_0(T)$ of the samples before and after annealing (see Table 1 in [13]).

In Fig. 7, we show the dependence of $R_{d\max}$ on the position $E_t - E_v$ of the levels ($R_{d\max}$ is the highest differential resistance observed in the reverse portion of the *I–V* characteristic of photodiodes; the voltages corresponding to the maximum values of R_d are listed in the table). The peak in $R_{d\max}$ is attained at the kink of two alternating prevalent currents, I_{ds} or I_s (the surface generation–recombination current in a short surface channel [24]) or the J_t current (see [21], Figs. 1–3). The current J_t flows directly via the levels $E_t - E_v$ (2). The current I_{ds} also depends on the energy position of the recombination level $E_t - E_v$. However, this dependence is indirect and involves the electron lifetime τ_n in the surface layer with a thickness on the order of the electron diffusion length. The dependence of the current I_s on the energy $E_t - E_v$ is also indirect and involves the surface-recombination velocity S, since the effective diffusion length of the charge carriers L_{eff} in the surface layer depends on both S and τ_n in the semiconductor bulk:

$$\frac{1}{L_{\text{eff}}^2} = \frac{1}{L_{\text{vol}}^2} + \frac{2S}{dD}, \quad L_{\text{vol}}^2 = D\tau_n,$$

where D is the diffusion coefficient of charge carriers and d is the thickness of the sample.

At first glance, the data shown in Fig. 7 can be used to conclude that the levels with $E_t - E_v \approx 0.4E_g$ are not recombination states. The recombination levels are located higher in the band gap, which is indicated by the sharp decrease in $R_{d\max}$ at $E_t - E_v > 40$ meV. For photodiodes with larger values of λ_{co}, this dependence is not clearly pronounced and the peak of $R_{d\max}$ is presumably shifted to smaller values of $E_t - E_v$ (Fig. 7, dashed line).

In order to clarify the situation, we performed the following experiments and calculations. We determined the charge-carrier diffusion lengths L_n from the forward portion of the *I–V* characteristic; the values of L_n were used to estimate the electron lifetime τ_n in the *p*-type base. Thus, for example, this estimation yielded $\tau_n = 2.6 \times 10^{-8}$ s for the photodiode 5 based on sample B3. As a result of measuring the lifetime using ultrashort pulses of a CO_2 laser for the same photodiode 5, we obtained $\tau_n = 5 \times 10^{-8}$ s, i.e., twice the value mentioned above. The hole lifetime in the initial sample B3 after thermal conversion to *p*-type conductivity was $\tau_p = 1 \times 10^{-7}$ s; i.e., $\tau_n < \tau_p$ in this *p*-type sample. In this case, the lifetime according to the Shockley–Read mechanism of recombination $\tau_{S-R} = (\mu_n\tau_n + \mu_p\tau_p)/(\mu_n + \mu_p)$ is controlled by electrons. In $Cd_xHg_{1-x}Te$ with $x \approx 0.2$ at $T \approx 78$ K, two mechanisms of recombination are prevalent, i.e., the Shockley–Read and Auger types [25] with lifetimes τ_{S-R} and τ_A, respectively; we have $\tau_n = \tau_{S-R}\tau_A/(\tau_{S-R} + \tau_A)$. For $p(78\text{ K}) \approx 2 \times 10^{16}$ cm^{-3}, $\tau_A \approx 7 \times 10^{-8}$ s [25]. Therefore, assuming that $\tau_n = 5 \times 10^{-8}$ s, we obtain $\tau_{S-R} \approx 1.8 \times 10^{-7}$ s; i.e., the lifetime of photogenerated charge carriers τ_n in the *p*-type base of n^+–*p* junctions and all photodiode parameters are governed mainly by Auger recombination. The contribution of Shockley–Read recombination to τ_n is smaller by approximately a factor of 2. Therefore, the dependence of the photodiode parameters on the recombination-center concentration N_t and the level energies $E_t - E_v$ is

weak, even for the most sensitive parameter R_0A (the specific differential resistance at $U = 0$) (Fig. 8). At the same time, $R_{d\max}$ determined at the interface between two mechanisms of currents depends more heavily on the concentration of free charge carriers p_p (photodiodes 9, 11, 12, and 14; see table and Fig. 7), which is characteristic of Auger recombination.

The important energy level for Shockley–Read recombination is the demarcation level E_D related to the minority charge carriers. The demarcation level is located between the level of capture for minority charge carriers and the level of recombination centers with concentration N_r and controls the probability of electron capture by a center occupied with a hole. This probability is equal to the probability that the hole will return to the valence band under the effect of the thermal energy. For a semiconductor in the state of equilibrium, the Fermi level is the same for electrons and holes and acts as the demarcation level. If the equilibrium is violated (for example, by applying a bias U), ζ_p and E_D do not coincide any longer. All the levels located between ζ_p and E_D are basically recombination states, whereas the levels located between ζ_p and E_c and between E_D and E_v are predominantly traps. Using the transport equations [26], we obtain the following expression for the demarcation-level energy:

$$E_D = E_F + \frac{3}{2}kT\ln\left(\frac{m_p^*}{m_n^*}\right) + kT\ln\left(\frac{\gamma_p}{\gamma_n}\right),$$
$$\gamma_n = \sigma_n\langle V_n\rangle, \quad \gamma_p = \sigma_p\langle V_p\rangle, \qquad (3)$$
$$\langle V_n\rangle = \left(\frac{8kT}{\pi m_n^*}\right)^{1/2}, \quad \langle V_p\rangle = \left(\frac{8kT}{\pi m_p^*}\right)^{1/2}.$$

Here, γ_n and γ_p are defined as the probabilities of capturing an electron and a hole, which have the mean thermal velocities $\langle V_n\rangle$ and $\langle V_p\rangle$, from the valence (conduction) band by an unoccupied (occupied) center with a energy level E_r; σ_n and σ_p are the effective capture cross sections for an electron and a hole, respectively.

It can be seen from expression (3) that the energy E_D depends heavily on the type of center owing to the term with recombination coefficients. In undoped $Cd_xHg_{1-x}Te$, we have $\sigma_n \approx 10^{-15}$–$10^{-16}$ cm^2 and $\sigma_p \approx 10^{-17}$–$10^{-18}$ cm^2 for the level $E_t = E_v + 0.4E_g$, while we have $\sigma_n \approx 10^{-16}$ cm^2 and $\sigma_p \approx 10^{-17}$–$10^{-20}$ cm^2 for the level $E_t = E_v + 0.75E_g$ [5]. We use these parameters of recombination centers to estimate the probability of recombination at the levels $E_t = E_v + 0.26E_g$ and $E_t = E_v + 0.6E_g$. We assume that $m_p^* = 0.55m_0$; we also assume that the dependence of effective electron mass on E_g is given, as usual, by $m_n^* = 0.075E_gm_0$ (here, E_g is expressed in electronvolts) [15].

We estimate the probability of recombination at the level E_t as $G = E_D/E_t$ for $E_t > E_D$ and as $G = E_t/E_D$ for $E_t < E_D$. For photodiode 8 with the energy level $E_t - E_v =$ 22 meV, we have $E_D = 26$ meV even if σ_n exceeds σ_p by three orders of magnitude; i.e., this level does not fall within the interval between $\zeta_p = 44$ meV and E_D and, thus, should be considered a trap. All the remaining levels with $E_t = E_v + 0.26E_g$ fall within the interval between ζ_p and E_D and can be considered recombination levels. The large spread in the values of σ_n and σ_p used in our calculations for the levels $E_t = E_v + 0.6E_g$ shows that these levels can be attributed to recombination centers if the difference between the values of σ_n and σ_p is relatively small. For example, at $\sigma_n/\sigma_p = 10$, we have $\zeta_p = 66$ meV and $E_D = 78$ meV at $E_t - E_v =$ 76 meV for photodiode 14. However, if we assume in calculations that $\sigma_n/\sigma_p = 10^4$ (Fig. 8, dashed lines; photodiodes 11, 14, and 19), these levels should be considered traps, whereas we obtain $E_D = 31$ meV for the same photodiode 14'.

As can be seen from Fig. 8, there is a satisfactory correlation between the dependences of the experimental values of R_0A limited by the generation–recombination processes and the values of G on $E_t - E_v$. For photodiode 11, the reduced value of R_0A (Fig. 8) is caused by the elevated value of the current I_{ds} (see Fig. 2 in [21]).

Thus, $Cd_xHg_{1-x}Te$ photodiodes were used to study the tunneling current J_t via the levels in the band gap; the energy positions $E_t - E_v$ and concentrations N_t' of these levels were determined. Shallow acceptor levels with $E_t - E_v = 8$–12 meV attributed to singly charged vacancies V_{Hg}^+ [1] were present in the band gap of almost all the photodiodes. These levels are traps and are not involved in recombination processes. However, the tunneling current J_t flows via these levels at high bias voltages. Deep levels with $E_t = E_v + 0.26E_g$ were observed in a number of diodes; these levels act as recombination states. The possible origin of these levels was suggested by Jones *et al.* [6]. In addition, even deeper levels with an energy of $E_t = E_v + 0.6E_g$ and a concentration N_t' much higher than that of other levels were found. These levels can functionally act as either recombination levels or deep traps with a small cross section of hole capture σ_p. The unusual peak observed in the dependence of $R_{d\max}$ in photodiodes on $E_t - E_v$ is caused by a change in the mechanisms of current rather than by recombination at the levels.

REFERENCES

1. M. A. Kinch, J. Vac. Sci. Technol. **21**, 215 (1982).
2. E. Finkman and Y. Nemirovsky, J. Appl. Phys. **59**, 1205 (1986).
3. B. Schlicht, A. Alpsancar, G. Nimtz, and N. F. Schroeder, in *Proceedings of 4th International Conference on Physics of Narrow-Gap Semiconductors* (Springer, Berlin, 1981), p. 439.
4. R. Fastow and Y. Nemirovsky, J. Vac. Sci. Technol. A **8**, 1245 (1990).

5. C. E. Jones, V. Nair, J. Lingquist, and D. L. Polla, J. Vac. Sci. Technol. **21**, 187 (1982).
6. C. E. Jones, K. James, J. Merz, *et al.*, J. Vac. Sci. Technol. A **3**, 131 (1985).
7. D. L. Polla and C. E. Jones, J. Appl. Phys. **52**, 5118 (1981).
8. D. L. Polla and C. E. Jones, J. Appl. Phys. **51**, 6233 (1980).
9. P. K. Chakraborty, Solid-State Electron. **34**, 665 (1991).
10. J. Y. Wong, IEEE Trans. Electron Devices **27**, 48 (1980).
11. W. W. Anderson and H. J. Hoffman, J. Vac. Sci. Technol. A **1**, 1730 (1983).
12. V. I. Turinov, Élektron. Tekh., Ser. 11: Lazer. Tekh. Optoélektron. **4**, 61 (1989).
13. P. V. Biryulin, V. I. Kosheleva, and V. I. Turinov, Fiz. Tekh. Poluprovodn. (St. Petersburg) **38** (2004) (in press).
14. C. T. Sah, Phys. Rev. **123**, 1594 (1961).
15. M. A. Kinch and D. D. Buss, J. Phys. Chem. Solids Suppl. 1 **32**, 461 (1971).
16. H. Overhof, Phys. Status Solidi B **43**, 315 (1971).
17. E. O. Kane, J. Phys. Chem. Solids **1**, 249 (1957).
18. M. Y. Pines and O. M. Stafsudd, Infrared Phys. **20**, 73 (1979).
19. M. A. Berding, A. Sher, and A.-B. Chen, J. Vac. Sci. Technol. A **5**, 3009 (1987).
20. V. A. Cotton, J. A. Wilson, and C. E. Jones, J. Appl. Phys. **58**, 2208 (1985).
21. P. V. Biryulin, V. I. Turinov, and E. B. Yakimov, Fiz. Tekh. Poluprovodn. (St. Petersburg) **38**, 890 (2004) [Semiconductors **38**, 480 (2004)].
22. M. Cutler and H. M. Bath, Proc. IRE **45**, 39 (1957).
23. P. V. Biryulin, S. A. Dudko, S. A. Konovalov, *et al.*, Fiz. Tekh. Poluprovodn. (St. Petersburg) **37**, 1431 (2003) [Semiconductors **37**, 1383 (2003)].
24. S. P. Tobin, S. Iwasa, and T. Tredwell, IEEE Trans. Electron Devices **27**, 43 (1980).
25. T. N. Casselman, J. Appl. Phys. **52**, 848 (1981).
26. M. A. Kinch, M. J. Brau, and A. Simmons, J. Appl. Phys. **44**, 1649 (1973).

Translated by A. Spitsyn

Semiconductors, Vol. 38, No. 9, 2004, pp. 1099–1104. Translated from Fizika i Tekhnika Poluprovodnikov, Vol. 38, No. 9, 2004, pp. 1135–1140.

PHYSICS OF SEMICONDUCTOR DEVICES

Lasing in Cd(Zn)Se/ZnMgSSe Heterostructures Pumped by Nitrogen and InGaN/GaN Lasers

I. V. Sedova*^, S. V. Sorokin*, A. A. Toropov*, V. A. Kaĭgorodov*, S. V. Ivanov*, P. S. Kop'ev*, E. V. Lutsenko, V. N. Pavlovskii**, V. Z. Zubelevich**, A. L. Gurskii**, G. P. Yablonskii**, Y. Dikme***, H. Kalisch***, A. Szymakowski***, R. H. Jansen***, B. Schineller****, and M. Heuken******

** Ioffe Physicotechnical Institute, Russian Academy of Sciences, St. Petersburg, 194021 Russia*

*** Stepanov Institute of Physics, Belarussian Academy of Sciences, Minsk, 220072 Belarus*

**** Institut für Theoretische Elektrotechnik, RWTH, Aachen, Germany*

***** AIXTRON AG, Aachen, Germany*

^e-mail: irina@beam.ioffe.rssi.ru

Submitted December 22, 2003; accepted for publication December 25, 2003

Abstract—Photoluminescence and lasing at a wavelength of λ = 510–530 nm (green spectral region) in Cd(Zn)Se/ZnMgSSe structures with a different design of the active region are studied in a wide range of temperatures and nitrogen laser pump intensities. A minimal lasing threshold of 10 kW/cm^2, a maximal external quantum efficiency of 12%, and a maximal output power of 20 W were obtained for the structure with the active region composed of three ZnSe quantum wells with fractional-monolayer CdSe inserts. The lasers exhibited a high temperature stability of the lasing threshold (characteristic temperature T_0 = 330 K up to 100°C). For the first time, an integrated converter composed of a green Cd(Zn)Se/ZnMgSSe laser optically pumped by a blue InGaN/GaN laser that is grown on a Si (111) substrate and incorporates multiple quantum wells is suggested and studied. © *2004 MAIK "Nauka/Interperiodica".*

INTRODUCTION

In recent years, much attention has been given to the development of commercial semiconductor lasers and light-emitting devices operating in the blue–green spectral region, which are needed in projection-laser TV systems, short-range fiber-optic communication lines employing plastic fibers, high-quality color printers, and many other laser applications. As before, heterostructures based on wide-gap II–VI semiconductors are the most promising candidates to be employed for the manufacture of green lasers. However, despite continuous efforts, the industrial production of an injection laser based on II–VI compounds is still a problem. Until now, the considerable efforts to optimize ZnSe laser diodes have failed to yield any appreciable increase in their service life. The record of 400 h of continuous-wave operation at room temperature (attained by the Sony Corporation) remains unbroken [1].

Among other semiconductors, III–N compounds are the main competitors of II–VI compounds for optoelectronic applications. In 1996, metal-organic vapor-phase epitaxy was used to fabricate laser diodes with InGaN multiple quantum wells on sapphire substrates with a wavelength of λ = 417 nm and a threshold current density of 4 kA/cm^2 [2] in the pulsed lasing mode. The maximal wavelength of the InGaN/GaN diodes in continuous-wave operation is now λ = 460 nm at room temperature [3]. However, the use of nitride-based semiconductor structures to obtain stimulated green radiation is problematic due to serious difficulties in forming InGaN quantum wells (QWs) with low defect concentration and high indium content, which are necessary to obtain the wavelength required [4, 5].

At the beginning of the 1990s, along with wide-gap II–VI semiconductors, heterostructures based on phosphides of Group-III elements were studied as a material for devices emitting in the green–blue spectral region. The minimal wavelength attained with an AlGaInP laser was 555 nm in the continuous-wave mode at T = 77 K [6]. The results obtained at room temperature were 615 and 607 nm in the continuous-wave [7] and pulsed modes [8], respectively. However, the fabrication of AlGaP/AlGaInP laser diodes faces a number of problems, the main one being the specific behavior of the band structure of $(Al_xGa_{1-x})_{0.52}In_{0.48}P$ solid solutions, which are lattice-matched to GaAs. As x varies from 0 to 1, the $(Al_xGa_{1-x})_{0.52}In_{0.48}P$ solid solution is transformed from a direct-gap semiconductor into an indirect-gap semiconductor. This transformation occurs at $x \approx 0.50$. At this point, the indirect gap width is only E_g = 2.33 eV [9] and is almost independent of x, thus, precluding an increase in E_g of the active region, which considerably worsens the electron confinement in AlGaN/AlGaInP heterostructures with QWs.

Therefore, despite difficulties that are primarily related to the extremely low activation energy of defect

formation, which is typical of the majority of wide-gap II–VI materials [10], only ZnSe heterostructures hold promise for the commercial production of green lasers.

In the late 1990s, a new design of the active region of II–VI laser structures was proposed with the aim of prolonging their lifetime and eliminating the main cause of the fast degradation of laser diodes—nonradiative recombination via defects in the active region, which is favorable for their further formation [11–13].

The mechanism underlying the slow degradation of ZnSe-based laser structures is largely explained by the presence of point defects, which diffuse into the active region mainly from the doped upper *p*-type region [14] and are related to the compensating donor centers, i.e., nitrogen interstitial atoms responsible for the instability of the electrical characteristics of ZnSe:N [15]. Furthermore, the shallow nitrogen acceptor is itself also metastable, which is apparent when, in certain conditions, the acceptor transforms into an interstitial center that forms a mobile charged complex with a selenium vacancy [16].

Therefore, semiconductor lasers with pulsed optical pumping and lasers driven by an electron beam [17], which do not require a *p*–*n* junction and ohmic contacts and, thus, avoid the problems that limit the lifetime of injection lasers, still attract considerable interest and are promising for progress toward the green spectral region, where no lasers based on other compounds can operate.

In this study, we investigate the luminescent and lasing properties of Cd(Zn)Se/ZnMgSSe heterostructures with different configurations of the active region. The main parameters of lasing are determined, such as the threshold pump-power density, the external quantum efficiency, the characteristic temperature, and the output power. For the first time, we carried out optical pumping of a ZnSe heterostructure by the radiation of an optically pumped InGaN/GaN laser.

EXPERIMENTAL

Structures in the (Zn,Mg)(S,Se) systems for optically pumped lasers were grown pseudomorphically by molecular-beam epitaxy (MBE) on (001) GaAs substrates at a growth temperature of 270–280°C. The structures include the bottom and the top confining $Zn_{0.9}Mg_{0.1}S_{0.15}Se_{0.85}$ layers with a thickness of 0.7 and 0.2 μm, respectively; a symmetrical waveguide shaped like a short-period superlattice (SL) of $ZnS_{0.14}Se_{0.86}$ (15 Å)/ZnSe(18 Å) with a total thickness of 0.2 μm; and an active region based on CdSe quantum discs that are self-organized within 2.5 monolayers of CdSe deposited on a ZnSe surface as a result of the elastic relaxation of strain induced by a mismatch of the lattice parameters ($\Delta a/a \approx 7\%$). Structure *A* contains one plane of CdSe quantum discs in the middle of a 10-nm-thick ZnSe QW. Structure *B* consists of three isolated ZnSe QWs that include inserts of CdSe quantum discs, which have the same rated thickness as those in structure *A*. These QWs are located in the SL waveguide, which is expanded to 0.4 μm. The special features of growing an active region based on CdSe quantum discs by MBE are described in detail in [11, 13]. For comparison, a similar structure is grown for this study (structure *C*), but with its active region in the form of a conventional single ZnCdSe QW. The use of nonuniformly stressed short-period SL enables us to improve the electron confinement of holes along with the optimal optical confinement, enhance the efficiency of the carrier collection and the resistance of the entire structure to stresses, and protect the active region from the penetration and development of extended and point defects [12, 17].

Blue lasers in an InGaN/GaN system ($\lambda \approx 455$ nm), which are used for the optical pumping of Cd(Zn)Se/ZnMgSSe lasers, were grown by metal-organic vapor-phase epitaxy at low pressures on (111) *n*-Si substrates by AIXTRON AG (Germany) [18]. GaN/AlGaN/AlN buffer layers served to relieve the appearing stress. The active region consisted of ten InGaN QWs, which were overgrown with a 50-nm-thick GaN layer.

As a source of optical excitation, we employed either a continuous-wave He–Cd laser (wavelength $\lambda_{exc} = 325$ nm, intensity $I_{exc} = 0.5$–20 W/cm^2) or a pulsed N_2 laser (wavelength $\lambda_{exc} = 337.1$ nm, pulse duration $\tau_p = 8$ ns, repetition rate $\nu = 10^3$ Hz, and $I_{exc} = 5$–1500 kW/cm^2) in the temperature range 77–593 K.

RESULTS AND DISCUSSION

Photoluminescence was studied at a low (5 W/cm^2) and a high (from 6 to 400 kW/cm^2) level of excitation of the structures at room temperature and at the liquid-nitrogen temperature. As expected [13], the structures with CdSe quantum-disc inserts feature appreciably higher efficiency of spontaneous emission compared to the reference QW structure (Fig. 1). The relationship between the intensities of emission from the active region and the waveguide layers, $I(\mathrm{QW})/I(\mathrm{SL}) > 10^3$, is indicative of an efficient electron confinement of nonequilibrium carriers at room temperature. Even at high excitation (above 400 kW/cm^2), luminescence from the active region remains dominant.

The lasing characteristics were studied over wide ranges of temperature and excitation intensity. For the long-cavity lasers ($L \approx 400$ μm and longer), the minimal lasing threshold ($I_{th} = 10$ kW/cm^2) was detected in the structure whose active region contained three ZnSe QWs with CdSe quantum discs. The structure with a single CdSe quantum-disc plane had a slightly higher threshold ($I_{th} = 12$–15 kW/cm^2), while the threshold of the reference ZnCdSe/ZnSe QW structure was three to four times higher than that in the CdSe quantum-disc structures (Fig. 2). Such a difference in the lasing thresholds is primarily accounted for by the structure of the active region. In structures with an active region

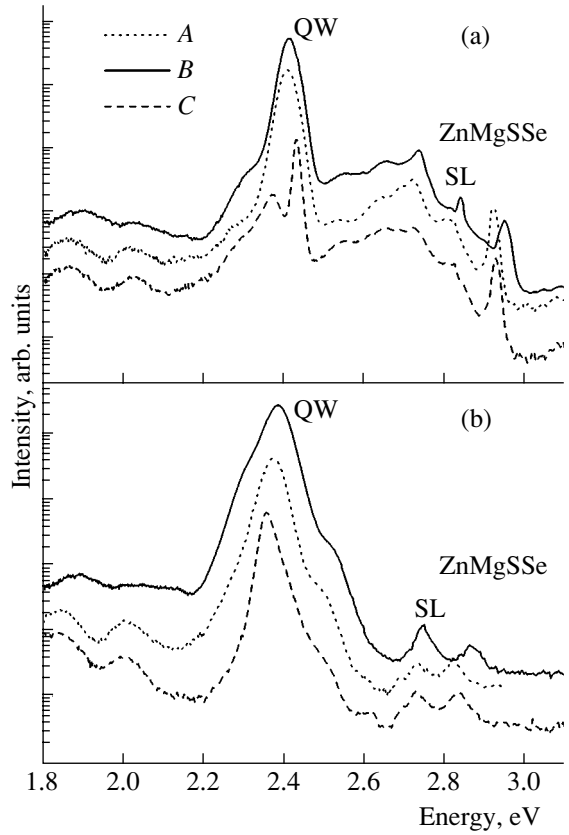

Fig. 1. Photoluminescence spectra of *A*, *B*, and *C* structures at a low level of excitation with a continuous-wave He–Cd laser (λ_{exc} = 325 nm, I_{exc} = 5 W/cm^2) at (a) liquid-nitrogen and (b) room temperatures.

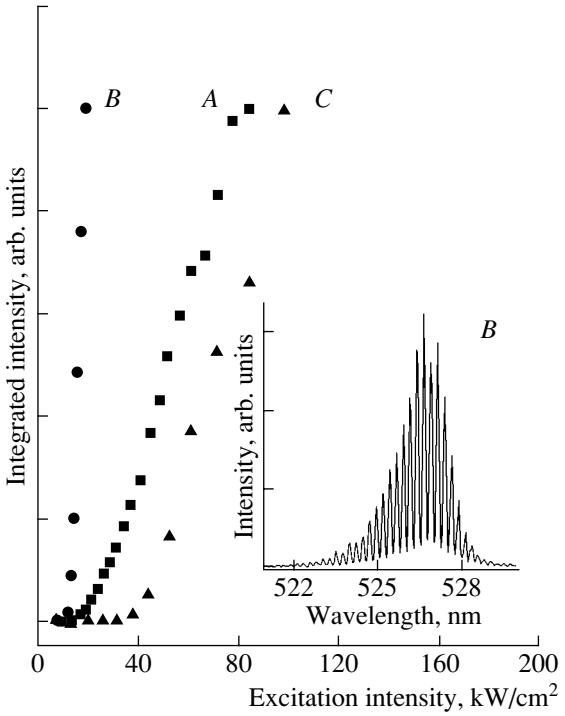

Fig. 2. Threshold characteristics of lasers based on *A*, *B*, and *C* structures with long cavities under excitation by N_2 laser at room temperature: L = (*A*, *C*) 430 and (*B*) 440 μm. The inset: the oscillation spectrum of a laser based on structure *B* with a short cavity (L = 100 μm).

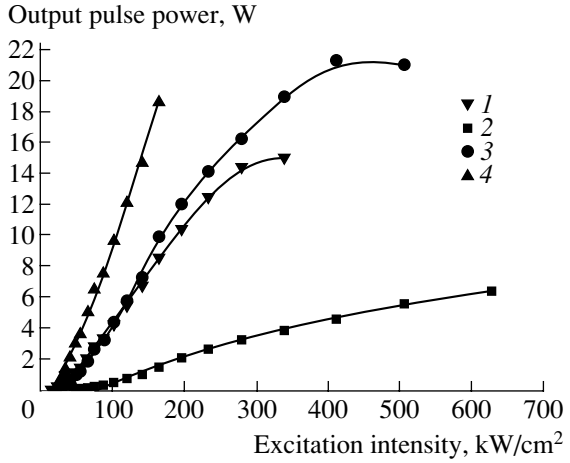

Fig. 3. Output power of lasers with different cavity length L vs. N_2-laser excitation intensity at room temperature: (*1*) structure *A*, L = 580 μm; (*2–4*) structure *B*, L = (*2*) 185, (*3*) 330, and (*4*) 830 μm.

consisting of coherent CdSe-enriched islands in a ZnSe matrix, an efficient localization of carriers in these nanoislands precludes their migration to defect-rich regions where they can be involved in nonradiative recombination, thus, enhancing the rate of the generation of defects in the active region [13]. An increase in the number of CdSe quantum-disc inserts (structure *B*) improves optical confinement in the structure and results in the thickening of the entire active region, which leads to a further decrease in the lasing threshold. The inset in Fig. 2 shows a clearly resolved mode structure in the spectrum of a laser based on a structure with multiple quantum-disc inserts and a comparably short cavity (cavity length L < 150 μm). Note, however, that shortening the cavity to 100 μm increases the lasing threshold significantly.

All the structures under study have a symmetrical waveguide, in which the optical confinement factor is at a maximum for the zero (fundamental) mode. The analysis of the spectral–angular distribution of lasing indicated that the far-field radiation of all structures is characterized by a single central spot, which is an indication of fundamental-mode lasing [19]. The angular divergence of radiation at the half-maximum of intensity ranged from 20° to 25° for all the structures.

Figure 3 shows the dependences of the output power of lasers with different cavity length on the excitation intensity. In the structures with three fractional-monolayer CdSe inserts, no noticeable degradation of lasing was observed up to pump intensities 20–30 times greater than the threshold. The highest pulsed power (more than 20 W) was obtained in this structure for a cavity length of 330 μm.

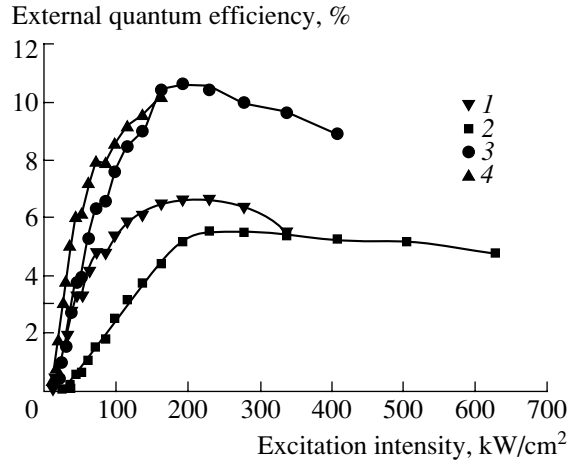

Fig. 4. External quantum efficiency of lasers with different cavity length vs. N_2-laser excitation intensity at room temperature: (*1*) structure *A*, L = 580 μm; (*2–4*) structure *B*, L = (*2*) 185, (*3*) 330, and (*4*) 830 μm.

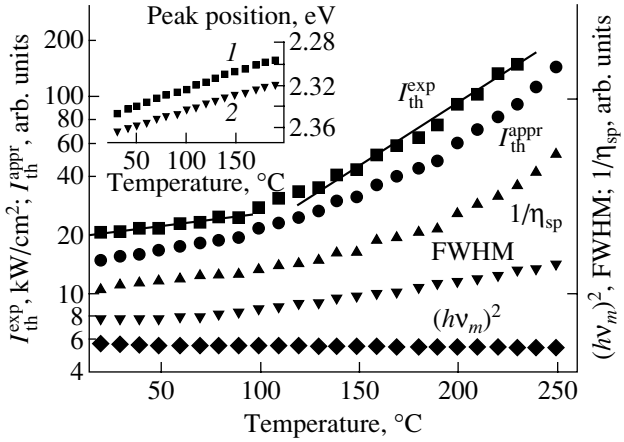

Fig. 5. Experimental temperature dependences and the related approximation according to [21] of the threshold pump power (I_{th}^{exp} and I_{th}^{appr}) for a laser based on structure *B*; temperature dependences of the inverse quantum efficiency of spontaneous radiation $1/\eta_{sp}$, the PL half-width (FWHM), and the squared energy of photons $(h\nu_m)^2$. Inset: temperature dependence of the lasing peak position (*1*) at a low level of excitation by a He–Cd laser and (*2*) at a threshold excitation of the same structure by an N_2 laser.

Measuring the output power in absolute units, we could estimate the external quantum efficiency, which is one of the most important characteristics of a laser. It can be seen from Fig. 4 that, as soon as the lasing threshold is exceeded, the external quantum efficiency of the studied structures rapidly increases with excitation intensity and ultimately attains a maximum (more than 11% for structure *B*). The decrease in efficiency observed with a further growth of the pump power is caused by an increase in the losses due to charge-carrier scattering, the overheating of the active region, the saturation of amplification, and probably the degradation of the structure.

For the structure with multiple CdSe quantum-disc inserts, lasing without any degradation was observed up to 230°C, which is a very high operation temperature for semiconductor lasers. The lasing threshold of structure *B* as a function of temperature is shown in Fig. 5. This dependence is typical of quantum-confinement lasers: it consists of two ascending exponential portions and a kink at a temperature in the range 100–120°C. The characteristic temperature T_0 = 330 and 68 K at operation temperatures below 100°C and above 120°C, respectively. It is known that the temperature dependence of the lasing threshold of semiconductor lasers is largely controlled by the quantum confinement of carriers in the active region [20], which is due to a decrease in the number of degrees of freedom for nonequilibrium charge carriers (NCC). The high value T_0 = 330 K is characteristic of quantum-well heterostructures with 3D quantum confinement of carriers, which is indicative of the effective localization of NCC in cadmium-enriched quantum discs at temperatures below 100°C.

We investigated the factors that increase the lasing threshold. As is well known, the threshold lasing power depends directly on the squared energy of the emitted photon $(h\nu_m)^2$, the photoluminescence line half-width (FWHM), and the inverse quantum efficiency $1/\eta_{sp}$ [21]. We measured the temperature dependences of the PL $h\nu_m$ peak position at a low level of excitation and at the threshold power of excitation (Fig. 5, inset). Both dependences indicate a temperature shift of the band gap in the active region. Thus, the contribution of the position of the PL peak to an increase in the threshold power density is fairly small. As determined directly from the spectra, the PL band width FWHM also increases with temperature only slightly (which suggests a small spread in the CdSe quantum-disc sizes) and has only a small effect on the lasing threshold. The greatest contribution to the temperature increase in the lasing threshold is made by the quantum efficiency of spontaneous emission η_{sp}, which is defined as the ratio of the integrated intensity of the PL spectrum to the pump power density. A decrease in the internal efficiency with temperature evidently results from the reduction of the electron confinement, as well as from the increasing probability of nonradiative recombination and an increase in the internal losses.

The luminescence spectra of CdSe quantum-disc heterostructures at room temperature suggest that a pronounced maximum of excitation efficiency exists in the spectral range 440–460 nm, which closely correlates with the absorption range in an ZnSe/ZnSSe waveguide, where carriers are effectively transported to CdSe quantum discs perpendicularly to the superlattice layers at 300 K. The efficiency of absorption in the confining ZnMgSSe layers is considerably lower both because of their distant position and because of appreciable fluctuations of the potential and capture of carri-

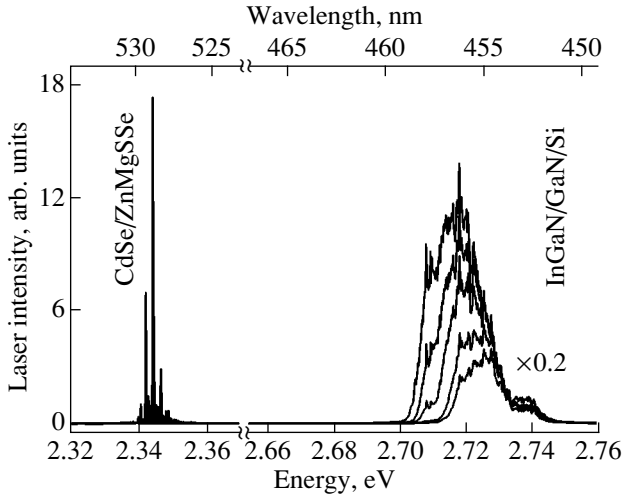

Fig. 6. Lasing spectrum of a CdSe/ZnMgSSe laser optically pumped by an InGaN/GaN laser.

ers by nonradiative recombination centers. Therefore, for lasers with CdSe quantum discs in ZnSe QWs, optical pumping by radiation with a wavelength of ~450 nm should be more efficient and have a lower threshold than that by nitrogen laser radiation (λ = 337.1 nm).

For the optical pumping of CdSe/ZnMgSSe structures, we employed InGaN/GaN lasers with multiple QWs grown on sapphire (Al_2O_3) and silicon (Si) substrates with a nitrogen laser pump and an operation range of 420–470 nm [22, 23]. Lasing in the structure with an active region in the form of CdSe inserts in ZnSe at room temperature was attained using the InGaN/GaN laser grown on a (111) Si substrate and operating in the range 452–458 nm. Lasers on silicon substrates provide higher efficiency in the same wavelength range compared to lasers grown on sapphire. An increase in the number of the buffer layers used for the relaxation of stress resulting from the growth on a mismatched substrate allows one to improve the quality of the active region and to reduce the lasing threshold to I_{th} = 30 kW/cm^2 for a wavelength of 455 nm. Such lasers are characterized by high temperature stability (with T_0 = 195 K) in the range 20–225°C. Their highest quantum efficiency and peak pulsed power are 5% and 30 W, respectively.

The excitation of a laser based on II–VI compounds was carried out in transverse geometry without using any intermediate optical elements. Setting the CdSe/ZnMgSSe laser nearer to the cavity of the InGaN/GaN laser results, first, in an intense luminescence and then (at ~200 μm), with an increase in the pump power density, in lasing. The scattered fraction of the nitrogen laser radiation accounted for less than 0.1% of the InGaN/GaN laser intensity.

A distinct mode structure is seen in the lasing spectrum of a CdSe/ZnMgSSe laser that is optically pumped by a multiple-QW InGaN/GaN laser (Fig. 6).

CONCLUSION

Optically pumped Cd(Zn)Se/ZnMgSSe laser structures with different designs of the active region were grown by molecular-beam epitaxy. For all of the structures, lasing was obtained in a wide range of temperatures and pump intensities without any sign of significant degradation. The top performance was observed in the structure whose active region included three CdSe quantum-disc planes. The resulting external quantum efficiency (12%), the characteristic temperature (330 K in the temperature range to 100°C), and the peak power (20 W) are the best values among the data available from the literature for optical lasers based on II–VI compounds. For the first time, the optical pumping of a CdSe/ZnMgSSe laser was carried out by an optically pumped InGaN/GaN laser with multiple QWs grown on a (111) Si substrate.

The results obtained allow one to consider the possibility of applying GaN-based injection lasers as optical pump sources to obtain a compact integrated InGaN/GaN–Cd(Zn)Se/ZnMgSSe laser converter operating in the green spectral region.

ACKNOWLEDGMENTS

This study was supported by the “Physics of Solid Nanostructures” program of the Russian Ministry of Science and Education; INTAS; the Russian Foundation for Basic Research, project no. 03-02-17563; and the Belarussian–Russian project M-15.

S.V. Ivanov acknowledges the support of the Foundation for the Promotion of National Science.

REFERENCES

1. E. Kato, H. Noguchi, M. Nagai, *et al.*, Electron. Lett. **34**, 282 (1998).
2. S. Nakamura, M. Senoh, S. Nagahama, *et al.*, Jpn. J. Appl. Phys. **35**, L74 (1996).
3. S. Nagahama, T. Yanamoto, M. Sano, and T. Mukai, Appl. Phys. Lett. **79**, 1948 (2001).
4. Y. Narukawa, Y. Kawakami, M. Funato, *et al.*, Appl. Phys. Lett. **70**, 981 (1997).
5. P. G. Eliseev, M. Osinski, J. Lee, *et al.*, J. Electron. Mater. **29**, 332 (2000).
6. A. Valster, M. N. Finke, M. J. B. Boermans, *et al.*, in *Proceedings of 12th IEEE International Semiconductor Laser Conference* (Davos, 1990), PD-12.
7. H. Hamada, K. Tominaga, M. Shono, *et al.*, Electron. Lett. **28**, 18334 (1992).
8. Y. Kaneko, I. Nomura, K. Kishino, and A. Kikuchi, J. Appl. Phys. **74**, 819 (1993).
9. D. J. Mowbray, O. P. Kowalski, M. Hopkinson, *et al.*, Appl. Phys. Lett. **65**, 213 (1994).
10. C. J. Verie, J. Electron. Mater. **27**, 782 (1998).
11. S. V. Ivanov, A. A. Toropov, T. V. Shubina, *et al.*, J. Appl. Phys. **83**, 3168 (1998).
12. S. V. Ivanov, A. A. Toropov, S. V. Sorokin, *et al.*, Appl. Phys. Lett. **73**, 2104 (1998).

13. S. V. Ivanov, A. A. Toropov, S. V. Sorokin, *et al.*, Appl. Phys. Lett. **74**, 498 (1999).
14. D. Albert, J. Nurberger, V. Hock, *et al.*, Appl. Phys. Lett. **74**, 1957 (1999).
15. V. N. Jmerik, S. V. Sorokin, T. V. Shubina, *et al.*, J. Cryst. Growth **214/215**, 502 (2000).
16. S. Gundel, D. Albert, J. Nürberger, and W. Faschinger, Phys. Rev. B **60**, R16271 (1999).
17. M. M. Zverev, S. V. Sorokin, I. V. Sedova, *et al.*, Phys. Status Solidi B **229**, 1025 (2002); A. V. Ankudinov, A. N. Titkov, T. V. Shubina, *et al.*, Appl. Phys. Lett. **75**, 2626 (1999).
18. E. V. Lutsenko, V. N. Pavlovskii, V. Z. Zubialevich, *et al.*, Phys. Status Solidi C **0**, 272 (2002).
19. T. Asano, M. Takeya, T. Tojyo, *et al.*, Appl. Phys. Lett. **80**, 3497 (2002).
20. Y. Arakawa and H. Sakaki, Appl. Phys. Lett. **40**, 939 (1982).
21. N. C. Casey, Jr. and M. B. Panish, *Heterostructure Lasers* (Academic, New York, 1978; Mir, Moscow, 1981), Part A.
22. G. P. Yablonskii and M. Heuken, in *Proceedings of NATO Advanced Research Workshop on Towards the First Silicon Laser, Trento, Italy, 2002*, Ed. by L. Pavesi, S. Gaponenko, and L. Dal Negro (Kluwer Academic, Dordercht, 2003), NATO Sci. Ser. II: Math. Phys. Chem., Vol. 93, p. 455.
23. G. P. Yablonskii, E. V. Lutsenko, V. N. Pavlovskii, *et al.*, Appl. Phys. Lett. **79**, 1953 (2001).

Translated by A. Sidorova

Semiconductors, Vol. 38, No. 9, 2004, pp. 1105–1110. Translated from Fizika i Tekhnika Poluprovodnikov, Vol. 38, No. 9, 2004, pp. 1141–1146.

PHYSICS OF SEMICONDUCTOR DEVICES

Characteristics of Planar Diodes Based on Heavily Doped GaAs/AlAs Superlattices in the Terahertz Frequency Region

D. G. Pavel'ev*, N. V. Demarina*, Yu. I. Koshurinov*, A. P. Vasil'ev, E. S. Semenova**, A. E. Zhukov**, and V. M. Ustinov****

** Lobachevsky State University, pr. Gagarina 23, Nizhni Novgorod, 603950 Russia*
e-mail: demarina@rf.unn.ru

*** Ioffe Physicotechnical Institute, Russian Academy of Sciences, Politekhnicheskaya ul. 26, St. Petersburg, 194021 Russia*

Submitted January 19, 2004; accepted for publication January 26, 2004

Abstract—Characteristics of ohmic InGaAs contacts in planar diodes based on semiconductor superlattices with a small-area active region (1–10 μm^2) are studied. The diodes were formed on the basis of short (18 or 30 periods) heavily doped (10^{18} cm^{-3}) GaAs/AlAs superlattices with a miniband width of 24.4 meV. The reduced resistance of the ohmic contact was equal to 2×10^{-7} Ω cm^2 at room temperature. It is shown that the properties of fabricated planar diodes make it possible to use these diodes later on in semiconductor devices that operate in the terahertz frequency region in a wide temperature range (4–300 K). © *2004 MAIK "Nauka/Interperiodica".*

1. INTRODUCTION

Planar semiconductor diodes with a Schottky barrier are now widely used in uncooled semiconductor devices that operate in the gigahertz frequency region [1–7]. However, in order to use diodes with a Schottky barrier in the terahertz region, it is necessary to increase the highest attainable frequency f_p of the diode's operation (the frequency that specifies the upper bound of the operating frequency range of the diode), which is difficult because of a number of existing restrictions. On the one hand, the highest attainable frequency is controlled directly by special features of physical processes that occur in the semiconductor's structure, in particular, by transit-time effects due to the flight of electrons through the active region. For example, the transit time for the best diodes is ~1 ps [6]. On the other hand, the highest attainable frequency is limited to a great extent by the effect of parasitic diode capacitance C and diode series resistance R_s ($f_p = 1/2\pi R_s C$), which consists of the resistances of the semiconductor bulk, contact connections, and diode leads. The capacitance of a diode with a Schottky barrier and with an active-region area of about several square micrometers is no less than 3 fF at present [4–6]. Reducing the diode's series resistance by increasing the doping level of the semiconductor is limited by the concentration 5×10^{17} cm^{-3} [5, 6].

Shorter response times and smaller values of capacitance can be attained by fabricating planar diodes on the basis of semiconductor superlattices (SLs) [8, 9]. Superlattices also exhibit a current–voltage (I–V) characteristic that includes a portion with a negative differential conductance [10]; this portion is retained up to frequencies of 1 THz [11]. The combination of these properties makes SLs a very attractive object of study, since oscillators, frequency multipliers, detectors, and mixers based on SLs can be used to fabricate new solid-state sources and detectors of electromagnetic radiation in the terahertz frequency region.

An increase in the highest attainable frequencies of diodes based on SLs by reducing the diode's series resistance requires an increase in the degree of doping of the structure and a decrease in the structure's length. One can decrease the capacitance by reducing the active-region area of the diode. The latter, in turn, inevitably leads to an undesirable increase in the diode's series resistance due to an increase in the resistance of the ohmic contact to the SL. The Au–Ge eutectic is typically used as an ohmic contact to SLs based on the GaAs/AlAs heterostructure [8, 9, 12]. This eutectic is deposited (with subsequent fusion) onto a heavily doped n^+-GaAs layer. The contact of Au–Ge alloy with n^+-GaAs at room temperature has a reduced resistance (the product of the contact resistance by the contact area) that is no lower than 10^{-6} Ω cm^2 [13–15], which is caused by inhomogeneities in the fused layer [13]. The use of these contacts in diodes with a small active-region area (several square micrometers) leads to a considerable increase in the series resistance of the diode's structure.

In this paper, we report the results of studying the possibility of reducing the contact resistance of planar diodes fabricated on the basis of heavily doped GaAs/AlAs SLs by using a layer of InGaAs ternary compound grown by molecular-beam epitaxy to form the ohmic contacts. We also describe a method for determining the reduced resistance of a small-area ohmic contact. It is shown that the reduced resistance of these contacts is 2×10^{-7} Ω cm^2 on average.

1063-7826/04/3809-1105$26.00

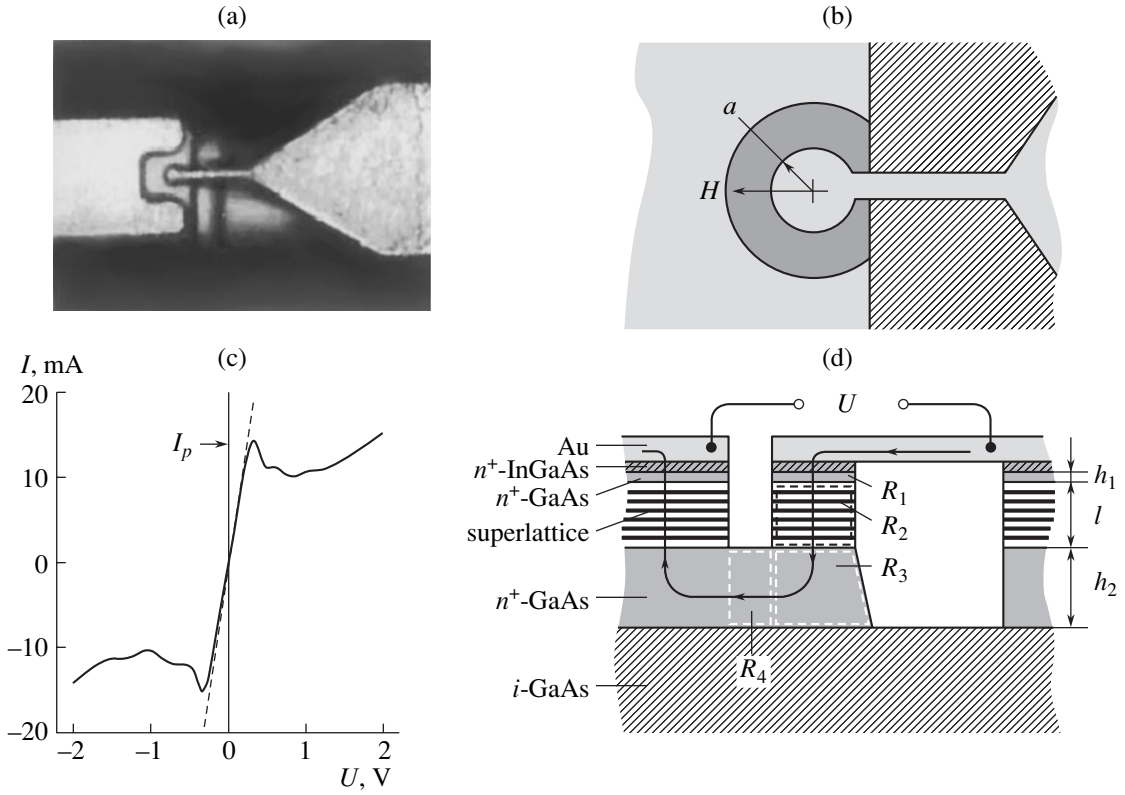

Fig. 1. Planar diode based on the GaAs/AlAs superlattice. (a) A microphotograph of the planar diode; (b) schematic representation of the planar diode: plan view (upper panel) and cross section of the diode structure (lower panel); and (c) the current–voltage characteristic of the planar diode based on a superlattice that includes 18 periods and has an active-region area of 5 μm^2.

2. SAMPLES

For our studies, we fabricated planar diodes based on GaAs/AlAs SLs with a small area (1–10 μm^2) of the active region. In Fig. 1a we show the microphotograph of the planar diode. A schematic representation of the diode (plan view and cross section) is shown in Fig. 1b. We used a semi-insulating GaAs layer as the substrate for growing sequentially a heavily doped n^+-GaAs layer (donor impurity concentration 6×10^{18} cm^{-3}), a GaAs/AlAs superlattice with gradient layers that separated it from the n^+-GaAs layers, a heavily doped n^+-GaAs layer (donor impurity concentration 6×10^{18} cm^{-3}), and an InGaAs layer (the molar fraction of InAs and the donor impurity concentration varied linearly over the layer thickness from 5 to 50% and from 6×10^{18} to 10^{19} cm^{-3}, respectively). Metallization (Au) for the diode leads was formed using electrochemical deposition through a photoresist mask.

The SLs consisted of 18 or 30 periods that corresponded to lengths of 0.112 and 0.186 μm, respectively. Each period included 18 GaAs monolayers (potential wells for electrons) and 4 AlAs monolayers (potential barriers) and was 6.22 nm long. The width of the first SL miniband was estimated using the Kronig–Penney model [16] with modified boundary conditions [17] and was found to be 24.4 meV. The SL was doped with a donor impurity with a concentration of 10^{18} cm^{-3}. Note that using SLs with a larger barrier width would increase the diode resistance and reduce the currents that flow through the diode. A study of such SLs is of no interest for the purposes of fabricating devices that operate in a wide frequency range and are based on these SLs. A decrease in the barrier width in turn causes the SL resistance to decrease. As a result, most of the voltage applied to the diode would drop across the series resistance of the diode.

The structures were grown by molecular-beam epitaxy on semi-insulating GaAs substrates with (100) orientation in a Riber 32P system. The growth rates of the AlAs and GaAs binary components were calibrated using an analysis of the X-ray rocking curves in a wide range of angles in the vicinity of the (004) reflection from the test GaAs/AlAs SLs. The growth rates were about 1 monolayer/s for GaAs and 0.5 monolayer/s for AlAs. Silicon was used as the donor doping impurity.

The structure of the fabricated planar diode included two ohmic contacts of different area that were located at the upper SL boundary so that they were parallel to the SL layers. If the voltage U is applied to this diode (Fig. 1b), the current I flows from the small-area contact through the heavily doped n^+-GaAs layer, then through the second heavily doped n^+-GaAs layer, and finally flows (again through the SL) into the ohmic con-

tact with a larger area. The direction of the current flow is indicated by the arrow in the schematic representation of the diode's cross section (Fig. 1b, bottom).

3. A METHOD FOR DETERMINING THE DIODE PARAMETERS

The use of the long-line method [18] for determining the resistance of ohmic contacts would result in an underestimation of the contact resistance in the diode structures. For example, this underestimation may be caused by the fact that the sizes of the inhomogeneities formed at the metal–semiconductor interface are found to be comparable to the contact diameter. As a result, the contribution of these inhomogeneities to the contact resistance cannot be disregarded. The four-point probe method [18] requires the formation of contacts with an area as small as in the case of contacts to the diode. On the one hand, this requirement is labor-intensive, and on the other, given the complexity of the technological process, it does not ensure the fabrication of contacts that have properties similar to those of the ohmic contacts to the diode. Therefore, in order to determine the ohmic-contact resistance, we used fabricated diodes; specifically, the voltage applied to a diode was expressed in terms of the current that flowed through the diode and the diode's resistance. Calculation and measurement of the resistances of various regions of the diode's structure made it possible to determine the resistance of the small-area ohmic contact.

The expression for the voltage applied to the diode is written as

$$U = IR, \tag{1}$$

where

$$R = R_K + R_1 + R_2 + R_3 + R_4 + R_p.$$

Thus, the total resistance of the diode R is the sum of the resistance R_K of the ohmic contact with the radius a; the resistance of the small-area SL R_2; the resistances R_1, R_3, and R_4 of the n^+-GaAs layers; and the resistance R_p of the contact system that consists of two movable probes and connecting wires. The resistance of the SL includes the resistance of the regular SL R_{SL} and the resistance of gradient layers $R_{gr\text{-}SL}$; i.e., $R_2 = R_{SL} + R_{gr\text{-}SL}$. A gradient layer is a sequence of alternating GaAs and AlAs layers with the layer thickness decreasing (GaAs) or increasing (AlAs) as one moves from the n^+-type layer to the regular SL. The resistance of the SL, the resistance of the n^+-type layer located under the large-area ohmic contact, and the resistance of this contact can be disregarded owing to the large cross-sectional area (compared to the area of the second contact). It can be seen from expression (1) that, in order to find R_K, we must determine R, R_{SL}, $R_{gr\text{-}SL}$, R_1, R_3, R_4, and R_p.

The total resistance R was determined from the I–V characteristic of the planar diode. A typical dependence of the diode current on the applied voltage is shown in Fig. 1c. As the voltage increases, the current first increases to a certain maximum value; a further increase in the voltage is accompanied by a very rapid decrease in the current. This behavior probably indicates that the electric field in the SL's structure is homogeneous only at low applied voltages and becomes inhomogeneous at higher voltages. As a result, a strong-field region (domain) appears in the system, which can be either static or mobile. The initial portion of the I–V characteristic was approximated with a linear dependence (Fig. 1c) that made it possible to determine the total resistance of the diode at low voltages.

The resistances R_1, R_3, and R_4 related to the heavily doped n^+-type layers under the contact and in the region between the contacts were calculated using the following formulas [3]:

$$R_1 = \rho_{n^+}\frac{h_1}{\pi a^2}, \quad R_3 = \frac{\rho_{n^+}}{2\pi a}\arctan\frac{h_2}{a} + \frac{\rho_{n^+}}{4\pi h_2}, \tag{2}$$
$$R_4 = \frac{\rho_{n^+}}{(4/3)\pi h_2}\ln\frac{H}{a}.$$

Here, ρ_{n^+} is the resistivity of the n^+-type layer; h_1 and h_2 are the thicknesses of the n^+-type layers above and underneath the SL, respectively; and H is the distance from the center of the small-area ohmic contact to the edge of the contact with the larger area (Fig. 1b).

The resistance of the contact system R_p was estimated experimentally and was found to be 2.5 Ω.

In order to determine the resistance of the SL using the Monte Carlo method [19], we calculated the dependence of the electron drift velocity on the electric-field strength. The main mechanisms of scattering were considered to be the scattering of electrons by acoustic phonons, polar optical phonons, ionized impurity atoms, and imperfections at the interfaces between the layers. The probability of electron scattering was calculated according to the Fermi golden rule [20] using the matrix elements for bulk GaAs [21, 22] in order to describe the interaction of electrons with acoustic and polar-optical phonons and with ionized-impurity atoms. The traditional model (described, e.g., in [23]) was used to calculate the probability of scattering by imperfections at the interface between the SL layers. The total scattering frequency required to calculate the free-path time in the Monte Carlo simulation of electron motion was calculated by integrating the scattering probability over all possible final electron states taking into account the dispersion relation for electron energy in the SL:

$$\varepsilon = \frac{\Delta}{2}(1 - \cos k_z d) + \frac{\hbar^2}{2m}(k_x^2 + k_y^2), \tag{3}$$

where k_z and k_x are the electron wave-vector components that are parallel to the SL axis, k_y is the corresponding component perpendicular to the SL axis, Δ is the miniband width, d is the SL period, m is the effec-

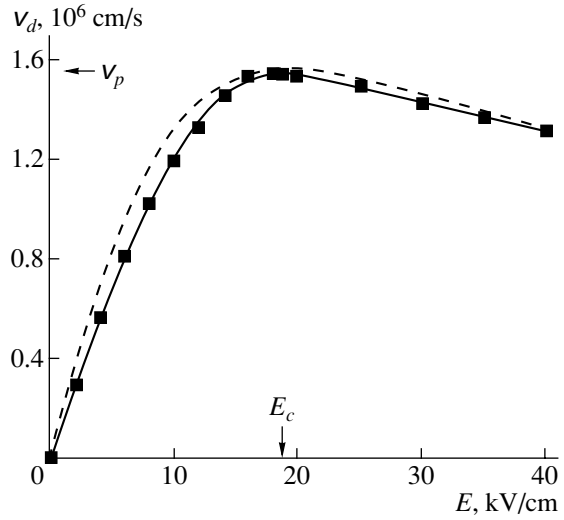

Fig. 2. Dependence of the electron drift velocity v_d on the electric-field strength E in the superlattice under consideration: the results of the Monte Carlo calculation (the solid line) and the approximation using formula (4) (dashed line).

tive mass of an electron for its motion in the direction perpendicular to the SL axis, and $\hbar$ is Planck's constant.

The possibility of electron scattering to neighboring Brillouin minizones was taken into account in the calculation of the total scattering frequency. Integration with respect to all possible final electron states in the reciprocal-lattice space was performed not only over the first Brillouin minizone but also over neighboring minizones. All the material parameters that were necessary to calculate the scattering frequencies were chosen to be the same as for bulk GaAs [18].

The obtained dependence of the drift velocity on the electric field is shown in Fig. 2. A decrease in the drift velocity of electrons v_d with increasing electric-field strength E at $E > E_c$, where E_c is the critical electric-field strength, is caused by the fact that electrons can reach the edge of the Brillouin minizone in the reciprocal-lattice space. At this edge, electrons undergo Bragg reflection. The calculated characteristic was approximated by a dependence that was similar to that suggested previously by Esaki and Tsu [10]:

$$v_d(E) = 2v_p\frac{(E/E_c)}{1+(E/E_c)^{1.7}}, \tag{4}$$

where E is the electric-field strength, the critical field $E_c = 19$ kV/cm, and $v_p = 1.5\times10^6$ cm/s is the highest drift velocity of electrons in the SL. The drift mobility of charge carriers in an electric field can be written as

$$\mu_d = \frac{dv_d(E)}{dE} = 2\frac{v_p}{E_c}\frac{1-0.7(E/E_c)^{1.7}}{[1+(E/E_c)^{1.7}]^2}, \tag{5}$$

so that the electron mobility in a weak field is given by

$$\mu = \left.\frac{dv_d(E)}{dE}\right|_{E\to 0} = 2\frac{v_p}{E_c}. \tag{6}$$

The SL resistance is then expressed as

$$R_{SL} = \frac{1}{qn\mu}\frac{l}{S}, \tag{7}$$

where q is the elementary charge, n is the charge-carrier concentration in the SL, l is the SL length, and $S = \pi a^2$ is the SL area (the same as the ohmic-contact area).

The resistance of the SL gradient layers was calculated using an expression similar to (7), in which the concentration n_{gr} and mobility μ_{gr} of charge carriers in the SL gradient layers and, accordingly, the length l_{gr} of the SL gradient layers were used.

The final expression for the ohmic-contact resistance is written as

$$\begin{aligned} R_K = R &- \frac{1}{qn\mu}\frac{l}{S} - \frac{1}{qn_{gr}\mu_{gr}}\frac{l_{gr}}{S} - \rho_{n^+}\frac{h_1}{\pi a^2} \\ &- \frac{\rho_{n^+}}{2\pi a}\operatorname{arctanh}\frac{h_2}{a} - \frac{\rho_{n^+}}{4\pi h_2} - \frac{\rho_{n^+}}{(4/3)\pi h_2}\ln\frac{H}{a} - R_p. \end{aligned} \tag{8}$$

The parameters of the SL gradient layers were determined by averaging over the layers and were $n_{gr} = 4\times10^{18}$ cm^{-3}, $\mu_{gr} = 450$ cm^2/(V s), and $l_{gr} = 4.8\times10^{-6}$ cm. The contact area was calculated on the basis of the average value of the highest current density $j_p = 2.5\times10^5$ A/cm^2 using the expression $S = I_p/j_p$, where I_p is the maximum current through the diode (Fig. 1c). The diode geometric parameters were $h_1 = 0.1$ μm, $h_2 = 1.5$ μm, and $H = 20$ μm; the resistivity of the n^+-type layer was equal to $\rho_{n^+} = 10^{-3}$ Ω cm.

4. RESULTS AND DISCUSSION

Calculated values of the contact resistance R_K for structures with different areas S are shown in Fig. 3 (upper panel). Diodes with an active-region area ranging from 2 to 6 μm^2 prevail in the set of devices (60 in total) under consideration. The contact resistance decreases as $1/S$ with increasing area; therefore, it makes sense to consider the reduced resistance $R_K\times S$ of the contact. The dependence of the reduced resistance of the contact on the contact area is shown in the lower panel of Fig. 3. Averaging over different diodes in the group yields an average value of the contact resistance of approximately 2×10^{-7} Ω cm^2. This value of the contact resistance agrees well with the corresponding values for ohmic contacts formed using molecular-beam epitaxy on the basis of $Ga_{1-x}In_xAs$ (5×10^{-7} Ω cm^2) [24] and InAs (1.2×10^{-7} Ω cm^2) [7].

In Fig. 3 (inset) the ohmic-contact resistance R_K is compared with the SL resistance R_2 and the resistance

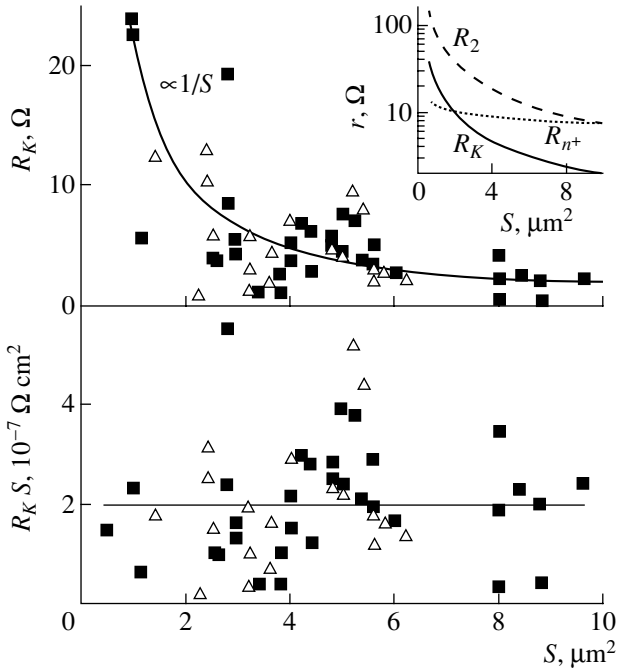

Fig. 3. Upper panel: dependence of the ohmic-contact resistance on the contact area for diodes with a superlattice with 18 periods (triangles) and 30 periods (squares); this dependence (solid line) was obtained by processing the experimental data and by averaging over the entire set of diodes. Lower panel: dependence of the reduced ohmic-contact resistance on the contact area; this dependence was obtained by processing the experimental data and averaging over the entire set of diodes (the same symbols as in the upper panel). Inset: dependences of the contact resistance (solid line), the superlattice resistance (dashed line), and the resistance of the n^+-type diode layer (dotted line) on the active-region area.

of the n^+-type layers $R_{n^+} = R_1 + R_3 + R_4$. For diodes with an active-region area smaller than 2 μm^2, the resistance of the n^+-type layers is lower than that of the ohmic contact owing to the strong dependence of the latter on the area. The total series resistance of the diode ($R_K + R_{n^+}$) is found to be much lower than the SL resistance. As the active-region area S increases, the contact resistance decreases rapidly, whereas the resistance of the n^+-type layers varies only slightly and becomes comparable to the SL resistance at $S = 10$ μm^2. Thus, using ternary compound InGaAs to form ohmic contacts in planar diodes based on the GaAs/AlAs SL made it possible to significantly reduce the series resistance of the diode compared to that for diodes with ohmic contacts based on the Au–Ge alloy. It is worth noting that the highest attainable operating frequency of these diodes (for example, diodes with an active-region area of 4 μm^2) based on an SL with 30 periods is about 6 THz.

The fabricated planar diodes were tested in the circuits of frequency multipliers with a large multiplication factor [25]. The observed output-signal spectra of planar diodes exposed to microwave radiation with a frequency of 20 GHz included components in the range 0.3–1.0 THz.

It is worth noting that the resistance of an ohmic contact based on the Au–Ge alloy increases with decreasing temperature, so that the contact becomes rectifying at cryogenic temperatures [15]. A contact layer formed on heavily doped GaAs and based on the InGaAs ternary compound does not incorporate a barrier. The use of this contact layer in diodes based on GaAs/AlAs SLs would make it possible to operate these diodes in a wide temperature range (4–300 K). The latter circumstance is especially important since it is well known [26] that the parameters of semiconductor devices depend heavily on temperature, which is caused by variation in the charge-carrier mobility with temperature and variation in the relation between various mechanisms of electron emission from contacts. For example, GaAs diodes with a Schottky barrier become inoperative when cooled to 4 K. An appreciable decrease in the intensity of electron scattering by optical phonons with decreasing temperature in diodes based on semiconductor SLs leads to an increase in the extent of the portion with negative differential conductance in the I–V characteristic. We may expect this circumstance to improve the main parameters of devices based on superlattices in operation at low temperatures and widen the operating frequency range. At the same time, the ability of diodes to operate in a wide temperature range can be used to analyze the dynamics of electrons in superlattices at various temperatures.

5. CONCLUSION

We discussed the characteristics of fabricated planar diodes based on heavily doped GaAs/AlAs short-period superlattices. The use of heavily doped thin InGaAs layers in the structures significantly reduces the resistance of ohmic contacts and makes it possible to extend the highest attainable frequency of diode operation to the terahertz region.

ACKNOWLEDGMENTS

This study was supported by the project "Microwave Devices of THz Frequency Range Based on GaAs/AlAs Superlattices" and by the Russian Foundation for Basic Research (project no. 03-02-17088).

REFERENCES

1. *Microwave Semiconductor Devices and Their Circuit Applications*, Ed. by H. A. Watson (McGraw-Hill, New York, 1969; Mir, Moscow, 1972).
2. *Spectroscopic Techniques for Far-Infrared, Submillimeter and Millimeter Waves*, Ed. by D. H. Martin (North-Holland, Amsterdam, 1967; Mir, Moscow, 1970).
3. J. A. Calviello, IEEE Trans. Electron Devices **26**, 1273 (1979).

4. F. Lewen, R. Gendriesh, I. Pak, *et al.*, Rev. Sci. Instrum. **69**, 32 (1998).
5. F. Maiwald, F. Lewen, B. Vowinkel, *et al.*, IEEE Microwave Guid. Wave Lett. **9**, 198 (1999).
6. F. Maiwald, F. Lewen, V. Ahrens, *et al.*, J. Mol. Spectrosc. **202**, 166 (2000).
7. C.-I. Lin, A. Vogt, M. Rodriguez-Gironéz, *et al.*, Annual Report (Technische Univ., Darmstadt, 1998), p. 33; http://www.hf.e-technik.tudarmstadt.de/forschung/jahreberichte/JB1998/index.php.
8. S. Brandl, E. Schomburg, R. Scheuerer, *et al.*, Appl. Phys. Lett. **73**, 3117 (1998).
9. E. Schomburg, K. Hofbeck, R. Scheuerer, *et al.*, Phys. Rev. B **65**, 155320 (2002).
10. L. Esaki and R. Tsu, IBM J. Res. Dev. **14**, 61 (1970).
11. S. Winnerl, E. Schomburg, J. Grenzer, *et al.*, Phys. Rev. B **56**, 10303 (1997).
12. N. Braslau, J. B. Gunn, and J. L. Staples, Solid-State Electron. **10**, 381 (1967).
13. N. Braslau, J. Vac. Sci. Technol. **19**, 803 (1981).
14. C. P. Lee, Electron. Lett. **12**, 406 (1981).
15. K. A. Jones, E. H. Linfield, and J. E. F. Frost, Appl. Phys. Lett. **69**, 4197 (1996).
16. R. de L. Kronig and W. G. Penney, Proc. R. Soc. London, Ser. A **130**, 499 (1931).
17. G. Bastard, *Wave Mechanics Applied to Semiconductor Heterostructures* (Physique, Les Ulis Cedex, 1988).
18. M. Shur, *GaAs Devices and Circuits* (Plenum, New York, 1987; Mir, Moscow, 1991).
19. C. Jacoboni and L. Reggiani, Rev. Mod. Phys. **55**, 645 (1983).
20. L. D. Landau and E. M. Lifshitz, *Course of Theoretical Physics*, Vol. 3: *Quantum Mechanics: Non-Relativistic Theory*, 4th ed. (Nauka, Moscow, 1989; Pergamon Press, Oxford, 1977).
21. W. Fawcett, D. A. Boardman, and S. Swain, J. Phys. Chem. Solids **31**, 1963 (1970).
22. J. G. Ruch and W. Fawcett, J. Appl. Phys. **41**, 3843 (1970).
23. A. Wacker and A.-P. Jauho, Superlattices Microstruct. **23**, 297 (1998).
24. J. M. Woodall, J. L. Freeouf, G. D. Pettit, *et al.*, J. Vac. Sci. Technol. **19**, 626 (1981).
25. D. G. Pavel'ev, Yu. I. Koshurinov, A. P. Vasil'ev, *et al.*, in *Proceedings of Workshop on Nanophotonics* (IFM RAN, Nizhni Novgorod, 2002), p. 116.
26. S. Sze, *Physics of Semiconductor Devices*, 2nd ed. (Wiley, New York, 1981; Mir, Moscow, 1984), Vols. 1, 2.

Translated by A. Spitsyn

Semiconductors, Vol. 38, No. 9, 2004, pp. 1111–1114. Translated from Fizika i Tekhnika Poluprovodnikov, Vol. 38, No. 9, 2004, pp. 1147–1150.

PHYSICS OF SEMICONDUCTOR DEVICES

Behavior of Graded-Gap Detectors of Ionizing Radiation under Irradiation with Alpha Particles

L. Dapkus, K. Požela, J. Požela, A. Čilėnas, V. Jucienė, and V. Jasutis

Institute of Semiconductor Physics, Vilnius, 2600 Lithuania

Submitted February 25, 2004; accepted for publication February 26, 2004

Abstract—The effect of irradiation with α particles on the current and optical responses of graded-gap $Al_xGa_{1-x}As/GaAs$ detectors of α particles and X-ray photons is studied. It is established that a reduction in both the current and optical response is caused by an increase in the rate of nonradiative recombination as the dose of α-particle radiation increases. © *2004 MAIK "Nauka/Interperiodica".*

1. INTRODUCTION

Graded-gap *p*-$Al_xGa_{1-x}As$/*n*-GaAs heterostructures are used as detectors of ionizing radiation with both a current [1–4] and an optical [5–8] response.

In the case of a current response, the graded-gap field is used for collection of the charge generated by ionizing radiation in the bulk of the graded-gap layer. In this situation, the charge-collection efficiency is governed by the parameter

$$\beta = t_{dr}/\tau_{rec}, \quad (1)$$

where τ_{rec} is the lifetime of charge carriers and t_{dr} is the time of drift of nonequilibrium charge carriers through the graded-gap layer.

In the case of an optical response, the detector sensitivity is governed by the quantum yield of conversion of ionizing radiation to optical radiation and by the efficiency of extraction of the latter radiation through the wide-gap window of the graded-gap crystal. The internal quantum yield

$$\eta = \frac{1}{1 + \tau_r/\tau_{nr}} \quad (2)$$

depends on the ratio between the rates of radiative (τ_r^{-1}) and nonradiative (τ_{nr}^{-1}) recombination processes.

In both cases, the detector-operation efficiency is governed by the lifetime of nonequilibrium charge carriers; this lifetime can be affected by various defects that are produced in a crystal exposed to ionizing radiation. It is important that the detector's optical response can either increase or decrease as the radiation dose increases, depending on variations in the rates of the radiative and nonradiative recombination processes [9].

In this paper, we report the results of studying the effect of irradiation with α particles on the characteristics of graded-gap $Al_xGa_{1-x}As$ detectors of α particles and X-ray photons.

2. AN ANALYSIS OF THE ALPHA-PARTICLE SPECTRUM

It has been shown [4, 10] that a graded-gap structure can be used as a detector of α particles that acts without an applied external bias. In this study, we used a graded-gap *n*-GaAs/*p*-$Al_xGa_{1-x}As$/p^+-GaAs heterostructure for detecting the α particles. A 25-μm-thick graded-gap *p*-$Al_xGa_{1-x}As$ layer was grown on the p^+-GaAs substrate; an *n*-GaAs layer with a thickness of no less than 2 μm was then grown on the narrow-gap side of the graded-gap layer. The detector area (1 mm^2) was smaller than the area of the α-particle source (^{241}Am). The electron–hole pairs generated in the crystal were pulled by the graded-gap field to the *p*-$Al_xGa_{1-x}As$/*n*-GaAs junction, where they were separated. We measured the current response that corresponded to the magnitude of the collected charge. The 5.48-MeV α particles are completely absorbed in the 25-μm-thick graded-gap *p*-$Al_xGa_{1-x}As$ layer. With the parameter *x* varying from 0 to 0.35 over the layer thickness, the graded-gap field 120 V/cm ensures an electron-drift velocity of 5×10^5 cm/s and a time of electron drift through the entire layer of $t_{dr} \lesssim 5$ ns. If the lifetime of nonequilibrium charge carriers $\tau_{rec} > 10^{-8}$ s, the aforementioned very short t_{dr} ensures 100% efficiency for the collection of the charge generated in the layer, without applying any external voltage to the $Al_xGa_{1-x}As$ layer. The experimentally determined efficiency of the charge collection was close to 100% in a lightly doped *p*-$Al_xGa_{1-x}As$/*n*-GaAs structure irradiated with X-ray photons from a source with a copper anode if the structure under consideration was not preliminarily irradiated with α particles.

The high efficiency of charge collection ensures a good resolution (5%) of the spectral line that corresponds to 5.48-MeV α particles in the experimentally determined pulse-height spectrum for the current response of the structure irradiated with α particles (see Fig. 1).

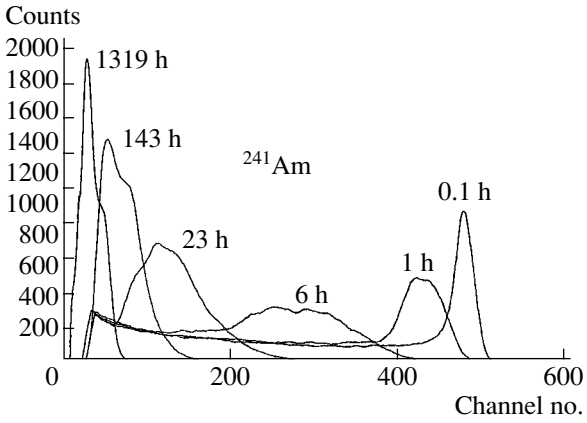

Fig. 1. Amplitude spectra of the current response of a graded-gap detector to irradiation with α particles for various doses of preliminary irradiation with α particles (source: ^{241}Am isotope). The duration of irradiation is indicated in hours.

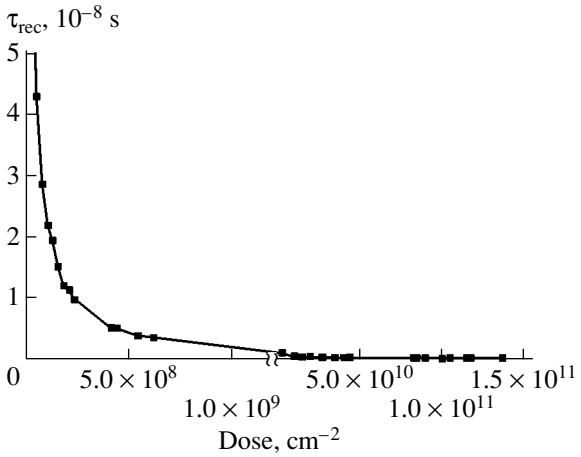

Fig. 2. Lifetime of nonequilibrium charge carriers τ_{rec} in the graded-gap structure as a function of the α-particle dose. The radiation intensity corresponds to the dose 1.04×10^8 cm^{-2} per hour.

Further irradiation of the $Al_xGa_{1-x}As$ layer with α particles reduces the recombination time of electron–hole pairs τ_{rec} and, as a result, reduces the magnitude of the collected charge.

A variation in the amplitude a_α of the collected charge as a result of irradiation with α particles with respect to the amplitude a_0 in the absence of preliminary irradiation is governed by the variation in the quantity τ_{rec}:

$$\frac{a_\alpha}{a_0} = \frac{\tau_{rec}}{t_{dr}}[1 - \exp(-t_{dr}/\tau_{rec})]. \quad (3)$$

In Fig. 1 we show the pulse-height spectrum of collected charge measured for various doses of irradiation with α particles. As can be seen, a drastic decrease in the amplitude a_α of collected charge is observed even after irradiation with relatively low doses of α particles. An appreciable initial decrease in the amplitude a_α of collected charge is also related to the fact that the largest charge is generated at the end of the α-particle track if the narrow-gap side of the structure is irradiated. As the charge-carrier lifetime decreases, the charge carriers at the track end are first to be excluded from collection in the narrow-gap part of the structure.

Measurements of variations in the current-response amplitude of the structure exposed to irradiation with X-ray photons in relation to the dose of preliminary irradiation with α particles confirmed that the efficiency of charge collection in the graded-gap layer decreased as a result of a decrease in the lifetime of charge carriers.

Variations in the charge-carrier lifetime calculated from experimental data using formula (3) are shown in Fig. 2. As can be seen, the defects produced in the $Al_xGa_{1-x}As$ crystal as a result of irradiation with α particles sharply reduce the lifetime of nonequilibrium charge carriers.

If the α-particle dose exceeds $n_d = 10^8$ cm^{-2}, the crystal cannot even be used for studying the spectrum of α particles. However, the $Al_xGa_{1-x}As$/GaAs structure can still be used as the counter of all α particles even if the α-particle dose exceeds $n_d = 10^{11}$ cm^{-2} (see Fig. 1); i.e., the $Al_xGa_{1-x}As$ structure is a radiation-resistant device like an α-particle counter.

3. LUMINESCENCE OF THE GRADED-GAP LAYER EXPOSED TO X-RAY RADIATION

The optical response of the detector to X-ray radiation is controlled by competition between the radiative and nonradiative recombination processes. This response manifests itself in luminescence through the wide-gap part of the graded-gap $Al_xGa_{1-x}As$ layer. Irradiation with α particles increases the rates of both the radiative and nonradiative recombination processes. Detectors with optical response can be found to be more radiation-resistant.

In order to study the luminescence induced by X-ray photons, we grew the wafers of a graded-gap $Al_xGa_{1-x}As$ semiconductor with an area of 5×6 mm^2, a thickness of 90 μm, and a composition gradient corresponding to the variation in x from 0 to 0.2.

The luminescence was observed from the wide-gap side of the wafer using a charge-coupled device (CCD) camera. The luminescence was excited by radiation from an X-ray source with a Cu anode (characteristic line at 8 keV). The absorption coefficient of X-ray photons with this energy is $\mu \approx 400$ cm^{-1} in $Al_xGa_{1-x}As$ [7]. The luminescence induced by X-ray photons was excited in the ~(25–30)-μm-thick wafer layer that adjoined the surface exposed to the X-ray radiation.

An α-particle source (^{241}Am) with an area of 1×2 mm^2 was installed near the center of the surface of the graded-gap wafer. Since the area of the source was

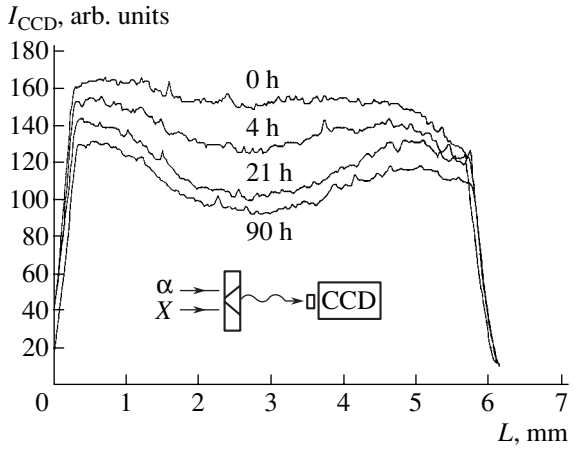

Fig. 3. Coordinate dependence of the intensity of luminescence excited by X-ray radiation in relation to the dose of α particles (the duration of irradiation is indicated in hours). The inset illustrates the method of measurements: the luminescence is excited by X-ray photons incident on the narrow-gap side of the crystal and is observed from the wide-gap side using a CCD camera; during preliminary irradiation, α particles were incident on the narrow-gap side of the structure.

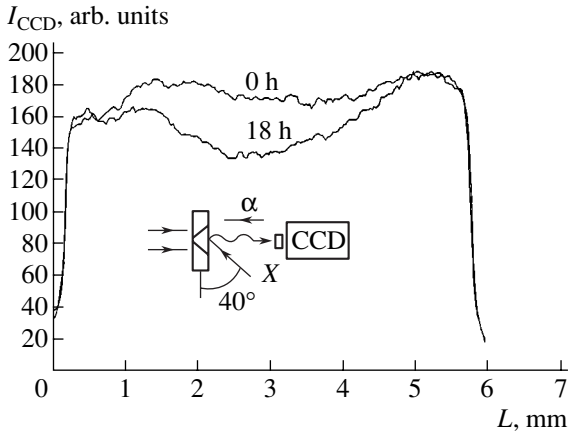

Fig. 4. Coordinate dependence of the intensity of luminescence excited by X-ray photons incident on the wide-gap side of the crystal in relation to the dose of α particles incident on the wide-gap side (the duration of irradiation is indicated in hours). The narrow-gap side of the graded-gap structure was preliminarily irradiated with α particles for 90 h (inset: schematic representation of the experiment).

smaller than that of the $Al_xGa_{1-x}As$ graded-gap wafer, the intensity of irradiation with α particles and, consequently, the dose of radiation were two orders of magnitude lower at the periphery of the sample than at the center of the wafer (directly below the source).

In Fig. 3 we show the dependence of the intensity of luminescence excited by X-ray photons I_{CCD} incident on the narrow-gap side of the structure on the dose of α particles incident on the same side. The luminescence intensity was detected as a function of the coordinate L.

Studies of the luminescence showed that emission comes from the surface layer with a thickness of 20–25 μm in the narrow-gap part of the crystal where the α particles and X-ray photons are absorbed.

The luminescence, which is excited by X-ray photons that penetrate to a depth of ~25 μm in the wide-gap part of the structure and is emitted through the wide-gap window, does not depend on the dose of α particles incident on the narrow-gap side of the structure (Fig. 4). The α particles are stopped at a depth of 20 μm and do not reach the wide-gap side of the wafer, whose thickness is 90 μm.

The dependence of the intensity of luminescence (as observed using the CCD camera) excited by X-ray radiation on the coordinate L is accounted for by the coordinate dependence of the dose of α particles. At the periphery of the wafer, where the radiation dose is several tens of times lower than the dose at the center of the wafer, the intensity of luminescence excited by X-ray photons is almost independent of irradiation with α particles.

The luminescence intensity decreases with increasing radiation dose at the center of the wafer. However, the observed decrease is much smaller than that in the case of the current response (Fig. 1). We attribute this circumstance to the fact that the current response is governed by the total rate of the radiative and nonradiative recombination processes, whereas the optical response (luminescence) depends on the ratio τ_r/τ_{nr} [see expression (2)].

A comparison of the variation of the current-response amplitude with that of the optical-response amplitude as a result of irradiation with α particles for 90 h makes it possible to find that the radiative-recombination rate increases by an order of magnitude. However, the luminescence intensity still decreases by a factor of 1.5 as a result of an increase in the rate of nonradiative recombination. This decrease is much smaller (by a factor of 5) than that in the current response as a result of irradiation with α particles for 90 h (Fig. 1).

Consequently, the detectors with an optical response are much more radiation-resistant than those with a current response.

4. CONCLUSIONS

Irradiation of a graded-gap $Al_xGa_{1-x}As$ layer with α particles leads to an increase in the rates of the radiative and nonradiative recombination of excess charge carriers generated in the layer by ionizing radiation (X-ray radiation and α particles).

As a result, the current response of the graded-gap detector is reduced by an order of magnitude after irradiation with a dose higher than 10^{10} cm^{-2}. The intensity of the optical response (the luminescence excited by X-ray photons) also decreases with increasing radiation dose owing to a dominant increase in the rate of nonradiative recombination, although the radiative-recombi-

nation rate increases. The intensity of the luminescence excited by X-ray radiation decreases only by a factor of 1.5 as a result of irradiation with a dose of 10^{10} cm^{-2} α particles.

ACKNOWLEDGMENTS

This study was supported by the Lithuanian State Foundation for Science and Education ("CERN-Vilnius-RD" program).

REFERENCES

1. A. S. Volkov, Fiz. Tekh. Poluprovodn. (Leningrad) **15**, 1105 (1981) [Sov. Phys. Semicond. **15**, 636 (1981)].
2. J. Požela, K. Požela, A. Šilėnas, *et al.*, Fiz. Tekh. Poluprovodn. (St. Petersburg) **36**, 124 (2002) [Semiconductors **36**, 116 (2002)].
3. A. Šilėnas, J. Požela, K. M. Smith, *et al.*, Nucl. Instrum. Methods Phys. Res. A **487**, 54 (2002).
4. V. M. Andreev, V. N. Blinov, V. A. Nosenko, *et al.*, Fiz. Tekh. Poluprovodn. (Leningrad) **8**, 1227 (1974) [Sov. Phys. Semicond. **8**, 798 (1974)].
5. A. S. Volkov and G. V. Tsarenkov, Fiz. Tekh. Poluprovodn. (Leningrad) **11**, 1709 (1977) [Sov. Phys. Semicond. **11**, 1004 (1977)].
6. J. Požela, K. Požela, A. Šilėnas, *et al.*, Nucl. Instrum. Methods Phys. Res. A **460**, 41 (2001).
7. J. Požela, K. Požela, A. Šilėnas, *et al.*, Nucl. Instrum. Methods Phys. Res. A **460**, 119 (2001).
8. K. Požela, J. Požela, L. Dapkus, *et al.*, Nucl. Instrum. Methods Phys. Res. A **466**, 58 (2001).
9. W. Lu, Y. L. Ji, G. B. Chen, *et al.*, Appl. Phys. Lett. **83**, 4300 (2003).
10. A. Šilėnas, K. Požela, L. Dapkus, *et al.*, Nucl. Instrum. Methods Phys. Res. A **509**, 30 (2003).

Translated by A. Spitsyn

Semiconductors, Vol. 38, No. 9, 2004, pp. 987–991. Translated from Fizika i Tekhnika Poluprovodnikov, Vol. 38, No. 9, 2004, pp. 1025–1029.

ATOMIC STRUCTURE AND NONELECTRONIC PROPERTIES OF SEMICONDUCTORS

Certain Features of Ga Diffusion in ZnS Powders

Yu. Yu. Bacherikov^, I. P. Vorona, S. V. Optasyuk, V. E. Rodionov, and A. A. Stadnik

Institute of Semiconductor Physics, National Academy of Sciences of Ukraine, Kiev, 03028 Ukraine

^e-mail: YuYu@isp.kiev.ua

Submitted December 25, 2003; accepted for publication February 5, 2004

Abstract—Spectra of photoluminescence and electron spin resonance were investigated for ZnS powders annealed in the presence of metallic Ga with limited access of atmospheric air. Analysis of these spectra showed that there was no Ga impurity in the annealed ZnS powders. It was established that subsequent free access of air to annealed ZnS:Ga promotes active Ga introduction into the ZnS lattice. A mechanism of Ga diffusion in ZnS is suggested. © *2004 MAIK "Nauka/Interperiodica".*

1. INTRODUCTION

Gallium is widely used as a coactivator of radiative transitions in ZnS-based phosphors [1–6]. However, despite extensive research, the problems of the origin of radiative centers, which are significantly affected by Ga or involve Ga as part of them, and the mechanisms of electron transitions still remain unsolved.

The aim of this study was to gain insight into the effect of Ga doping on ZnS luminescence characteristics, as well as Ga diffusion and incorporation into the lattice of ZnS powder, including the role of oxygen in these processes.

2. EXPERIMENTAL

We annealed ZnS powders (ETO.035.295 TU) at 800°C with limited access of atmospheric air. To restrict the access of air, we used a gas valve made of activated carbon. The annealing time was 3 h. To dope ZnS with Ga, we annealed ZnS powder in the presence of metallic Ga.

Photoluminescence (PL) spectra were measured using an SDL-2 system at room temperature. To excite PL, we used an LGI-23 nitrogen laser radiation with $\lambda = 337$ nm.

Electron spin resonance (ESR) spectra were measured at room temperature by a Radiopan ESR spectrometer operating in the 3-cm wavelength range. The magnetic field was modulated with an amplitude of 0.2 mT and a frequency of 100 kHz. The ESR spectra were recorded at a microwave power of about 10 mW, i.e., below the saturation level. The magnetic field was monitored by an NMR gage, which provided an accuracy of magnetic field measurements better than 0.1 mT.

The PL and ESR spectra were repeatedly measured at room temperature after 150 h, during which the samples were kept under conditions providing free access of air.

3. RESULTS

As can be seen from Fig. 1, the PL spectrum of an original unannealed ZnS powder (curve *1*) represents a rather broad complicated band with an emission peak at $\lambda \approx 500$ nm and a half-width of 100 nm. The annealing of this powder at 800°C results in a decrease in the half-width to 73 nm and a modification of the spectral shape of the band due to a decrease in the intensity of the lines forming the short-wavelength tail (curve *2*). In Fig. 1, this modification looks like a shift of the short-wavelength band tail at a fixed position of the long-wavelength tail, which eventually results in a shift of the peak position of the band ($\lambda_{max} = 515$ nm). The annealing of the powder at the same temperature in the presence of Ga induces a slight additional decrease (up to 66 nm) in the half-width of the line (curve *3*). As in the previous case, the half-width varies due to the short-wavelength tail of the PL band, which also produces a

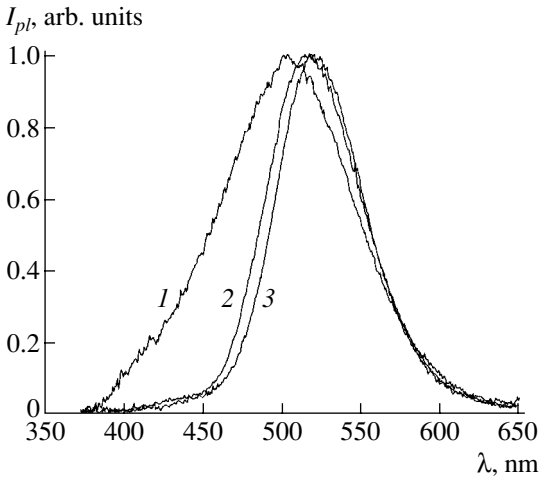

Fig. 1. PL spectra: (*1*) unannealed ZnS powder; (*2*) ZnS powders annealed at 800°C; and (*3*) ZnS powders annealed at 800°C in the presence of Ga.

1063-7826/04/3809-0987$26.00 © 2004 MAIK "Nauka/Interperiodica"

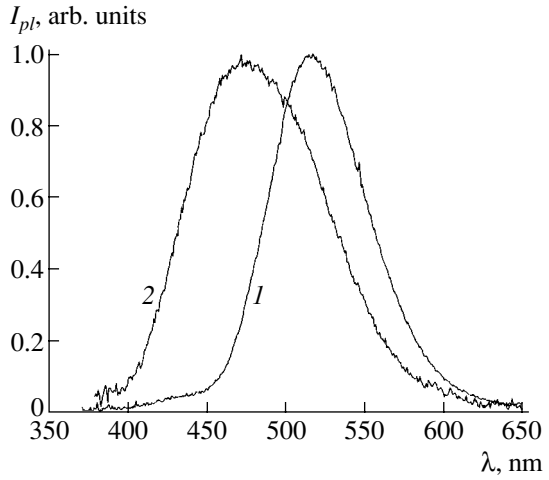

Fig. 2. PL spectra: (*1*) ZnS powder annealed at 800°C in the presence of Ga without access of atmospheric air after annealing and (*2*) the same powders after free access of air to the powder for 150 h.

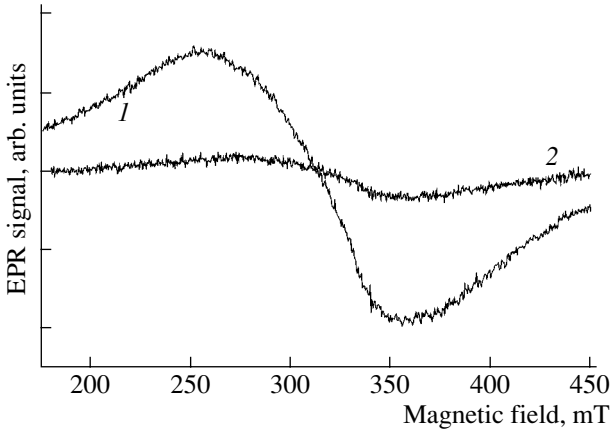

Fig. 3. ESR spectra: (*1*) ZnS powder annealed at 800°C in the presence of Ga without access of air after annealing and (*2*) the same powders after free access of air to the powder for 150 h.

shift in the peak position (λ_{max} = 520 nm). For all three cases, the long-wavelength tails of PL bands practically coincide. Such a change in the spectral characteristic of PL indicates that the PL bands are not elementary for either the original or the annealed ZnS powders.

In previous publications, the band at λ_{max} = 520 nm was usually associated with the presence of oxygen or a copper impurity. However, Grasser *et al.* [7], who studied the reversible transformation of the luminescence from blue to green in high-purity zinc sulfide, attributed these modifications in the spectrum to changes in the sulfur sublattice.

An interesting feature of the behavior of annealed powders is the presence of afterglow. The afterglow of ZnS after annealing lasts a few seconds. Annealing of ZnS with Ga increases the duration of the afterglow to ~60 s.

If we keep the samples without free access of air, the afterglow duration and spectral properties of the annealed powder remain unchanged for more than ~300 h.

Free access of air to the annealed ZnS powder produced no change in the spectral characteristics of the material, in contrast to the case where ZnS was annealed with Ga. The access of air for 150 h to the ZnS powder annealed with Ga results in significant changes in the PL spectrum (Fig. 2). The main peak of the PL spectrum (curve *2*) is shifted to the short-wavelength region (λ_{max} = 471 nm). In addition, the shape of the tail of the PL band indicates the presence of at least one more line in the region of ~500 nm. In [1–4], the band with λ_{max} = 471 nm was associated with the presence of Ga in ZnS. Furthermore, the access of air to the powder annealed with Ga decreased the duration of the PL afterglow to ~3–5 s.

In the original zinc sulfide powder, no ESR spectrum is observed. In the ESR spectrum of both annealed ZnS powders (both undoped and doped with Ga), a broad line ($\Delta H \approx 90$ mT) with $g \approx 2.15$ (Fig. 3) appears. The form of the ESR spectrum corresponds to typical ESR spectra of dangling bonds at the surface and grain boundaries. After keeping both powders in air, the ESR spectrum intensity significantly decreases without distortion.

4. DISCUSSION

We can easily explain the spectral redistribution of PL intensity after the annealing of the samples investigated if we assume that the PL spectra of the original and the annealed ZnS powders are not elementary. In this case, the annealing of the samples decreases the intensity of short-wavelength bands and practically does not affect the long-wavelength bands.

To explain the reasons why the long-wavelength bands are independent of the annealing conditions, we must know the nature of these bands. The band with λ_{max} = 520 nm is frequently associated with the presence of oxygen or copper in zinc sulfide [8]. However, in our experiments, we did not intentionally introduce copper during the annealing and we tried to minimize the access of oxygen. Therefore, in our case, the origin of these bands apparently cannot be definitively associated with the presence of these impurities in ZnS. There are also other models for this PL band. For example, Grasser *et al.* [7] studied the reversible transformation of the luminescence from blue to green in high-purity zinc sulfide and assumed that this band was related to changes in the sulfur sublattice.

As can be seen from the above experimental results, the annealing of zinc sulfide at T = 800°C produces an increase in the intensity of the PL band with λ_{max} = 520 nm. This is accompanied by the appearance of a

broad and intense line in the ESR spectrum (see Fig. 3), which indicates that a large number of dangling bonds are formed at the surface and at grain boundaries.

Thus, we believe that the increase in the PL-band intensity (after annealing at $T = 800°C$) is induced by two factors. On the one hand, the thermal annealing of the powder results in the fact that the surface of the material is cleaned of a number of radicals and compounds formed with elemental air components [9]. This reduces the surface reactivity and, thus, decreases surface nonradiative losses. On the other hand, it is well known [8] that sulfur is a volatile component of zinc sulfide. This results in sulfur desorption from the surface of the material and an increase in the sulfur vacancy concentration (V_S) during the thermal treatment of ZnS. According to [10], sulfur vacancies are involved in the radiative recombination responsible for the PL band with $\lambda_{max} = 520$ nm, and an increase in the concentration V_S results in an increase in the intensity of this band.

A similar situation is also observed for ZnS powder annealed in the presence of metallic Ga. Thus, the annealing of the ZnS powder with Ga at $T = 800°C$ also increases the intensity of the PL band with $\lambda_{max} = 520$ nm without changing the shape of the PL spectrum. The PL spectra obtained involve no luminescence lines characteristic of ZnS with Ga [1–4]. This observation indicates that some of the processes are similar in both cases: high temperature leads to the desorption of spurious radicals and sulfur from the surface of ZnS and to the formation of a layer with an excess of Zn at the surface. Thus, we may assume that the presence of Ga during annealing either induces no substantial Zn diffusion in the bulk of ZnS or (we believe that this is less probable) leads to a position of Ga in the ZnS lattice that does not appear in the PL. This position of Ga atoms in the ZnS lattice cannot be interstitial. Interstitial Ga atoms have an uncompensated valence electron and would appear in ESR spectra. Certainly, it is possible that Ga occupies an interstitial site in the form of a complex like Cu_2S, whose presence in ZnS is associated with the appearance of "yellow" and "red" radiative centers. However, this assumption does not explain what prevents Ga from occupying Zn sites in this case, as observed for ZnS doped with Ga compounds [11].

It is well known that a molecule of gas interacting with the surface of a solid can be in the preadsorption state weakly bound to the surface so that it diffuses over the surface until it forms a stronger bond [12, 13]. This weakly bound state most adequately corresponds to physical adsorption, which precedes the diffusion. In our case, the annealing of ZnS in the presence of Ga most likely results in the physical adsorption of Ga on the surface of powder particles without its further penetration into the material. This can be explained by the absence of chemical affinity between Ga and Zn, i.e., by the appearance of a chemical potential gradient [14] limiting the diffusion of doping atoms into the ZnS lattice. An activation barrier is probably formed, thus preventing Ga from penetrating the material even if the thermal energy is $E_T^1 = 3/2kT = 139$ meV. The above requirements are best satisfied by capillary condensation [15], where the adsorption predominantly occurs at internal grain surfaces, filling the pores, cracks, etc.

Another distinction between powders annealed with and without gallium is the duration of the afterglow. As was mentioned, for pure ZnS powder, the duration of the PL afterglow does not change appreciably after annealing, while ZnS annealing in the presence of Ga increases the afterglow duration to ~60 s. This behavior enables us to conclude that the presence of Ga during the annealing of ZnS at $T = 800$ K results either in the activation of deep traps already existing in the material or in the formation of new deep traps. These traps capture a part of the excited carriers and can increase the afterglow duration from several seconds ($\tau \approx 3$ s for ZnS annealed without Ga) to tens of seconds.

Once τ is known, we can estimate the depth of deep levels. The probability of carrier release from a trap per unit time is given by the expression [16]

$$P = 1/\tau = s\exp(-E_\tau/kT), \qquad s = N_B v \sigma_t, \tag{1}$$

where E_τ is the depth of the trap level, τ is the carrier dwelling time in a trap, N_B is the density of states in the band into which the carriers pass, v is the carrier thermal velocity, and σ_t is the cross section for carrier capture by a trap.

A typical value of s for ZnS is 10^8 s^{-1} [16]. Using formula (1), we can estimate E_τ at room temperature ($T = 293$ K); this quantity lies in the range of ~0.57 ± 0.05 eV. Such a low accuracy in the estimation of E_τ is caused by disregarding a number of processes, such as the repeated capture of already released carriers by traps and others.

We believe that the energy corresponding to the V'_{Zn} acceptor level [4] fits the given interval of E_τ best. Gallium adsorbed on the powder surface or located at an interstitial site most likely initiates a certain reconstruction of the ZnS structure during the annealing of the material. Due to an increase in sulfur vacancy concentration in the material, the Zn position at the lattice sites becomes unstable. It is therefore quite possible that some of the Zn atoms pass from their positions at lattice sites to interstitial sites, thus increasing the V_{Zn} concentration and, of course, the concentration of interstitial Zn. However, the authors of [17], having investigated the luminescence of ZnS with a high concentration of V'_{Zn}, do not discuss its kinetic features, which they could hardly not have noticed. We believe that a high concentration of V'_{Zn} is a necessary, but not sufficient, condition for a long afterglow of the band $\lambda_{max} = 520$ nm. Free-electron transitions to V'_{Zn} levels compete with transi-

tions to shallow levels with a large capture cross section; the vacancies V_S play an active role in the formation of these levels. We believe that the presence of either surface or interstitial gallium also affects shallow traps, forcing them to migrate through the material. These traps probably annihilate when they mix, decreasing their concentration, and the remaining traps are arranged so that their contribution to electrical properties of the material sharply decreases.

Thus, in the band gap of ZnS, Ga atoms generate effective deep levels ($E_\tau \approx 0.57$ eV), which play the role of traps.

The long-term exposure of the samples to air (we believe that here the presence of oxygen plays the key role) results in a substantial modification of the PL spectra and kinetics ($\tau \longrightarrow 3$ s). As mentioned above, in this case the PL spectrum peaks at $\lambda_{max} = 471$ nm. This band is associated with the presence of Ga in ZnS [1]. The authors of [3, 4] assumed that the model of the *CA* center in nonactivated ZnS is apparently similar to the model of blue luminescence centers in ZnS activated by subgroup-IIIB elements. The luminescence of these centers is induced by the recombination of electrons captured by shallow donors Ga_{Zn}^{*} and holes at the *A* centers of the $\{V_{Zn}''Ga_{Zn}^{*}\}$ type. In the case of nonactivated ZnS, a *CA* center can include an interstitial Ga as a donor for Zn_i and an *A* center $\{V_{Zn}''Ga_i^{*}\}$ as an acceptor. Prener and Williams [4] assumed that this luminescence center is the association of a doubly ionized zinc vacancy $(V_{Zn})^{2-}$ and an ionized donor impurity Ga_{Zn}^{+} located at a neighboring lattice site. It is believed [4] that such a complex (designated as $(V_{Zn^-}Ga_{Zn})^-$ with a negative effective charge behaves like a compensated singly ionized acceptor, which introduces a level (filled by an electron) into the band gap near the valence band.

Thus, we may assume that the annealing of ZnS powder at $T = 800$°C with limited access of air in the presence of metallic Ga with subsequent prolonged ($t =$ 150 h) passivation in air results in the doping of ZnS with Ga. However, we note that only atmospheric passivation leads to the incorporation of Ga in the ZnS lattice. This passivation process is confirmed by the ESR studies of our samples. The access of air strongly decreases the intensity of the ESR spectrum (see Fig. 3), which indicates that the number of paramagnetic centers significantly decreases (i.e., the dangling bonds are healed due to the interaction of the surface with Ga atoms and residual gases or water molecules).

We draw attention to the fact that Ga diffuses at room temperature, i.e., at $E_T^2 = 38$ meV; this value is approximately four times smaller than E_T^1. There are several factors that can explain such behavior. The chemisorption of air components on the surface of grains in the powder results in a regrouping of all chemical bonds, thus lowering the activation barrier. Previously, the effect of extraneous adsorbed atoms on the migration rate during self-diffusion and heterodiffusion was repeatedly studied [18–20]. The authors of [18, 19] showed that oxygen and water increase the self-diffusion rate in metals. In [20], it was shown that even a small amount of oxygen and nitrogen increases the diffusion activation energy by a factor of 1.5. Another factor, although not so crucial, is "poisoning" the adsorption centers, which leads to an acceleration of diffusion. One more factor may be the formation of chemical compounds with the diffusing atoms.

Finally, we note that gallium diffusion in a zinc sulfide lattice at room temperature is not accompanied by intense penetration of oxygen into the material. This is confirmed by the absence of PL bands with $\lambda \approx 435$ nm, which is characteristic of a ZnS:O solid solution [21].

Previously, in research on the doping of ZnS with Ga, doping with compounds that contain Ga was mainly considered [11]. In this study, we investigated the diffusion of metallic Ga in ZnS. The above results have shown that these two cases are radically different. We believe that the main difference is that Ga atoms are not introduced to ZnS lattice sites in the absence of extraneous adsorbed atoms, which can affect both the diffusion rate and the rate of Zn replacement by Ga in ZnS. The subsequent access of air (even at room temperature) to ZnS powder results in an intense introduction of Ga atoms into the Zn sublattice.

REFERENCES

1. J. S. Prener and D. J. Weil, J. Electrochem. Soc. **103**, 342 (1956).
2. *Physics and Chemistry of II–VI Compounds*, Ed. by M. Aven and J. S. Prener (North-Holland, Amsterdam, 1967; Mir, Moscow, 1970).
3. J. E. Nicholls, J. J. Davis, and B. C. Cavenott, J. Phys. C: Solid State Phys. **12**, 378 (1979).
4. J. S. Prener and F. E. Williams, J. Chem. Phys. **25**, 361 (1956).
5. K. Urabe and S. Shionoya, J. Phys. Soc. Jpn. **24**, 543 (1968).
6. A. N. Georgobiani, Tr. Fiz. Inst. im. P. N. Lebedeva, Akad. Nauk SSSR **59**, 38 (1972).
7. R. Grasser, A. Scharmann, and W. Schwedes, Z. Phys. **20**, 235 (1975).
8. N. K. Morozova and V. A. Kuznetsov, *Zinc Sulfide. Production and Optical Properties*, Ed. by M. V. Fok (Nauka, Moscow, 1987) [in Russian].
9. V. F. Kharlamov, L. Yu. Frolenkova, and T. S. Rogozhina, Zh. Tekh. Fiz. **71** (10), 90 (2001) [Tech. Phys. **46**, 1294 (2001)].
10. N. P. Golubeva and M. V. Fok, Zh. Prikl. Spektrosk. **43**, 940 (1985).
11. M. A. Il'ina, V. B. Gutan, and A. M. Gurvich, Zh. Prikl. Spektrosk. **14**, 838 (1971).

12. M. W. Roberts and C. S. McKee, *Chemistry of the Metal–Gas Interface* (Clarendon, New York, 1978; Mir, Moscow, 1981).
13. Yu. G. Ptushinskiĭ and V. A. Chuĭkov, Poverkhnost, No. 9, 5 (1992).
14. A. Zangwill, *Physics at Surfaces* (Cambridge Univ. Press, Cambridge, 1988; Mir, Moscow, 1990).
15. J.-E. Germain, *Catalyse Hétérogéné* (Dunod, Paris, 1959; Mir, Moscow, 1961).
16. J. I. Pankove, *Optical Processes in Semiconductors* (Prentice Hall, Englewood Cliffs, N.J., 1971; Mir, Moscow, 1973).
17. A. P. Georgobiani, M. B. Kotlyarevskiĭ, and V. N. Mikhalenko, Izv. Akad. Nauk SSSR, Neorg. Mater. **17**, 1329 (1981).
18. G. B. Abdullaev and T. O. Dzhafarov, *Diffusion of Atoms in Semiconductor Structures* (Atomizdat, Moscow, 1980) [in Russian].
19. *Atomic Diffusion in Semiconductors*, Ed. by D. Shaw (Plenum, London, 1973; Mir, Moscow, 1975).
20. B. A. Nesterenko and O. V. Snitko, *Physical Properties of Atomic-Clean Surface of Semiconductors* (Naukova Dumka, Kiev, 1983) [in Russian].
21. N. K. Morozova and M. M. Veselkova, Zh. Prikl. Spektrosk. **29**, 366 (1978).

Translated by V. Bukhanov

Semiconductors, Vol. 38, No. 9, 2004, pp. 992–995. Translated from Fizika i Tekhnika Poluprovodnikov, Vol. 38, No. 9, 2004, pp. 1030–1033.

ELECTRONIC AND OPTICAL PROPERTIES OF SEMICONDUCTORS

Impact-Ionization Autosolitons in Compensated Silicon

A. M. Musaev

Institute of Physics, Dagestan Scientific Center, Russian Academy of Sciences, ul. 26 Bakinskikh Komissarov 94, Makhachkala, 367003 Russia

e-mail: akhmed-musaev@yandex.ru

Submitted November 27, 2003; accepted for publication December 30, 2003

Abstract—Autosolitons with self-production of charge carriers upon impact ionization of deep acceptor levels of indium in silicon in strong electric fields at a temperature of 77 K have been revealed experimentally and studied. A model of autosoliton excitation is proposed in which the free-carrier concentration plays the role of an activator and the carrier temperature plays the role of an inhibitor. Autosolitons arise because the region of high carrier concentration at the autosoliton center does not spread due to the balance between the diffusion flux from the autosoliton center and the thermal diffusion flux. © *2004 MAIK "Nauka/Interperiodica".*

It was shown theoretically [1] that spatially localized dissipative structures (autosolitons) can be excited by an external perturbation in an active nonlinear system characterized by diffusion in the region of a stable uniform state. Autosolitons can be found in the general (mathematical) class of active systems in which diffusion occurs and whose properties are determined by nonlinear differential diffusion equations. However, the physical mechanisms of autosoliton formation are fairly diverse. Semiconductors and semiconductor structures are the most appropriate model systems with an active kinetic medium—nonequilibrium electron–hole plasma—for studying the kinetics of formation and evolution of autosolitons.

Ionization autosolitons were studied experimentally in [2–4]. It was shown in [2] that the electron–hole plasma obtained by impact ionization in *n*-GaAs films is stratified into either current filaments (dense electron–hole plasma) or electric-field striations (loose electron–hole plasma). Spike autosolitons excited by a localized light pulse in (*p*–*i*–*n*)-Si structures were studied in [3]. Pulsing autosolitons in Si with self-production of charge carriers upon impact ionization of excitons in a strong electric field were investigated in [4].

In this paper, we report the results of experimentally detecting and studying autosolitons with self-production of charge carriers upon impact ionization of deep acceptor levels of In (ionization energy $\varepsilon_h = 0.16$ eV) in Si in strong electric fields at 77 K.

We investigated compensated *p*-Si⟨In⟩ samples with a difference in the concentrations of acceptors and donors of $N_A - N_D = 6.0 \times 10^{12}$ cm^{-3}, cut in the form of rectangular plates. The crystallographic orientation of the samples and the measurement scheme are shown in Fig. 1. Ohmic (p^+–p) contacts were formed by deposition of aluminum with its subsequent alloying or by alloying aluminum foil. Such contacts eliminate the effect of their transition characteristics on the kinetics of the current evolution upon generation–recombination processes in the sample bulk [5]. In this case, the following condition must be satisfied: $\tau < \tau_t$, where τ is the characteristic evolution time of the generation–recombination process and τ_t is the time of passage of charge carriers through the sample. To eliminate surface effects, the contacts on the opposite faces were deposited such that a distance of 0.25 mm was left between the contact and face boundaries. Dynamic current–voltage (*I*–*V*) characteristics were measured by applying single sawtooth voltage pulses with different slopes of the leading edge to samples in the voltage-

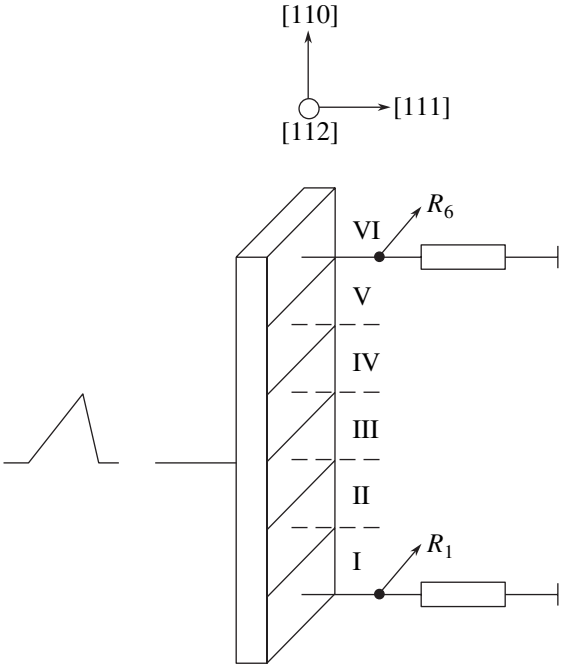

Fig. 1. Measurement scheme and sample orientation; (R_1–R_6) are load resistors.

source mode. The time instability of current was studied using dc voltage pulses with widths of up to 50 μs. The nonuniformity of the current density distribution over the sample cross section was studied by sectioning the cathode contact (see Fig. 1).

At low temperatures, the main mechanism leading to an increase in the conductivity of silicon with deep impurity levels in strong electric fields is impact ionization, which occurs in electric fields in the range 10^3–10^4 V/cm [5]. Some other mechanisms may also lead to an increase in the carrier concentration with increasing electric field: injection of minority carriers and (when the current is limited by a space charge) injection of majority carriers. A substantial factor is also the increase in the hole concentration upon thermally assisted field generation of charge carriers, which increases with increasing electric field (as a result of the Pool–Frenkel effect). In this case, the electric field changes the maximum height of the energy barrier by

$$\Delta\varepsilon = -e/(eE/\pi\kappa)^{1/2}, \quad (1)$$

where E is the electric field strength, κ is the permittivity of silicon, and e is the elementary charge. The dependence of the thermally assisted field generation rate on the electric field is an exponential function of the quantity $\Delta\varepsilon/kT$, which, in the case under consideration (attracting centers), has the form [5]

$$\Delta\varepsilon/kT = -0.84(E/10^4)^{1/2}(300\ \text{K}/T_0), \quad (2)$$

where T_0 is the lattice temperature and k is the Boltzmann constant.

Analysis of the increase in the carrier concentration as the electric field increases at different rates shows that the role of the Pool–Frenkel effect is insignificant if the voltage increases at a rate of no less than 40 V/μs. The reason is that the temperature of the sample does not have time to increase significantly over such a short period (adiabatic conditions). At the same time, with an increase in Joule heating, the role of this effect increases.

The concentration of free carriers at field strengths that are sufficient for efficient impact ionization is determined from the conditions of the balance between the rates of capture, impact ionization, and thermally assisted field generation.

The impact ionization rate is defined as

$$G = p(p^\varepsilon/p)\sigma_i v^\varepsilon N_g, \quad (3)$$

where p^ε/p is the fraction of free holes with energies exceeding the energy of impurity levels, v^ε is the rate corresponding to the energy of impurity levels $(2\varepsilon_h/m)^{1/2}$, N_g is the concentration of unionized impurities, and σ_i is the impact-ionization cross section.

The free-hole capture rate can be written as

$$R = p\sigma_h v_{\text{th}} N_c, \quad (4)$$

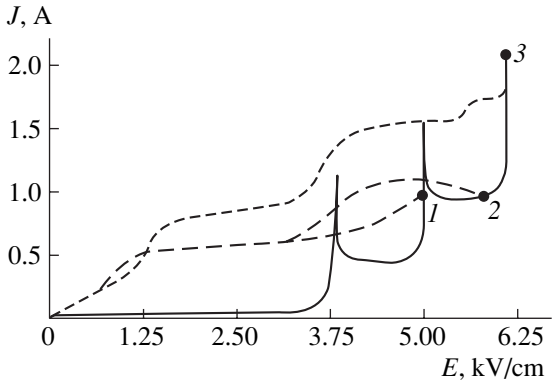

Fig. 2. Dynamic current–voltage characteristic of the sample. Dashed lines show the reverse *I–V* characteristics at different values of the applied sawtooth voltage; *1–3* are the return points.

where σ_h is the capture cross section, $v_{\text{th}} = (2kT_0/m)^{1/2}$ is the hole thermal velocity, and N_c is the concentration of ionized impurities. The cross section σ_h of hole capture by an ionized In atom at 77 K is 7×10^{-14} cm^2; it decreases with increasing temperature. In strong electric fields, the capture cross section decreases due to two different factors. First, the average energy of carriers increases ($T > T_0$) and, accordingly, the number of particles at the bottom of the conduction band decreases, which directly controls the capture. Second, bound states with binding energies lower than the energy of impurity centers ε_h decay in strong electric fields [6].

In this case, the main mechanism responsible for the increase in the majority-carrier concentration is the impact ionization of impurities. Figure 2 shows a typical dynamic *I–V* characteristic $J(E)$ obtained with a growth rate of sawtooth voltage of 50 V/μs. A typical feature of this characteristic is the presence of current peaks that arise stepwise with increasing electric field. Figure 3 shows the *I–V* characteristics for different parts (I, II, V) of the sample (obtained by sectioning the cathode contact; see Fig. 1). It can be seen that the peaks indicating a stepwise increase in the current correspond to different parts of the sample; these peaks are similar in shape and electric characteristics. With a decrease in the growth rate of the sawtooth voltage, the *I–V* characteristic gradually changes. In this case, the ionization potential of impurities decreases and the dependence $J(E)$ is not so sharp, which is explained by Joule heating of the lattice and thermally assisted field ionization of the impurities. In other words, as the lattice temperature increases, thermally assisted field ionization occurs rather than impact ionization. We believe that this phenomenon also accounts for the specific features of the *I–V* characteristic recorded with decreasing voltage, i.e., the hysteresis that occurs when the electric field decreases. Figure 2 shows the hysteresis of the *I–V* characteristic for sawtooth voltage pulses of different amplitudes. The results of measurements show the fol-

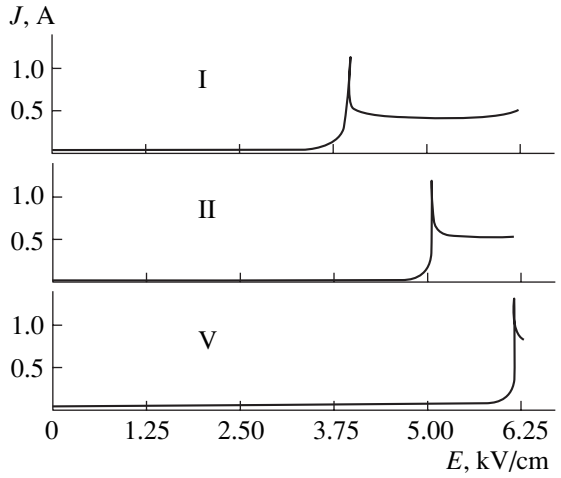

Fig. 3. Dynamic current–voltage characteristics of parts I, II, and V of the sample with a split cathode contact.

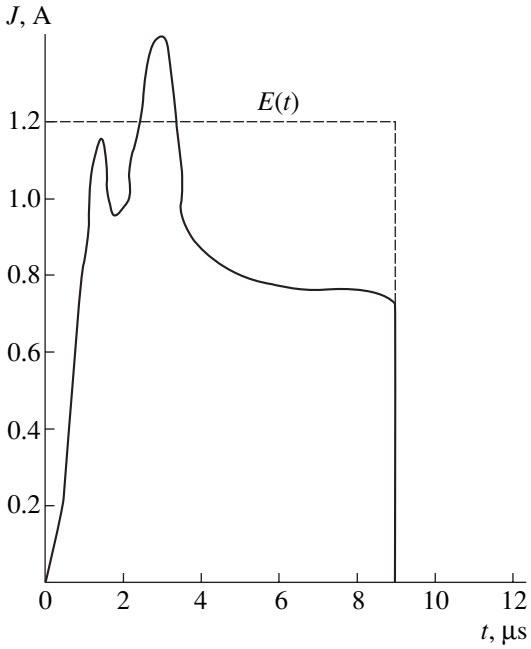

Fig. 4. Oscillogram of a current through the sample at E = 5 kV/cm.

lowing: the higher the losses in the ionization region, the lower the voltages at which the hole concentration begins to decrease. With electric fields weaker than the impact-ionization field, the Pool–Frenkel effect plays a certain role, which is, however, not very significant. As was shown in [7], at low temperatures, the hole concentration in In-doped Si increases by no more than a factor of 3 with an increase in the electric field from 10^2 to 4×10^3 V/cm.

Figure 4 shows the change in the current J with time t when pulses of electric field $E(t)$ with an amplitude sufficient for the ionization of impurities are applied to the sample. As can be seen from the oscillogram, when the field applied exceeds the impact-ionization field, the current through the sample changes in a stepwise manner. The decrease in the current is related to the decrease in the carrier mobility, which, in turn, is due to the scattering of holes by phonons upon Joule heating of the ionization region. In Si, at temperatures above 77 K and with an electric field applied, the scattering of carriers by the deformation acoustic and optical potentials is dominant and the mobility decreases with increasing field. This is confirmed by the temperature dependences of the sample conductivity for different values of the applied field.

The results obtained make it possible to consistently interpret the observed phenomena in terms of the model of a static longitudinal autosoliton with local self-production of charge carriers (developed in [1]). Both nonuniform distribution of impurities and inhomogeneities of other types that lead to impact ionization in local regions of size X may initiate spontaneous excitation of autosolitons. The stability of autosolitons is related to the scattering of charge carriers by ionized impurities (since the distance between the centers of impurities is much smaller than the transverse size of an autosoliton) and by phonons in the region of size X where autosolitons exist. In the stratification mechanism under consideration, the concentration of free charge carriers p plays the role of an activator and the carrier temperature plays the role of an inhibitor. The positive feedback over the activator is due to the increase in the ionization rate of deep impurity levels with increasing hole concentration (the ionization rate is a sharply rising function of carrier concentration). The damping role of the inhibitor is related to a decrease in the temperature of carriers upon their scattering by ionized impurities and phonons, which limits the impact ionization rate. In this case, the increase in the temperature in the regions where autosolitons exist leads to an even larger decrease in the carrier energy.

The distributions of the carrier concentration and carrier energy flux in an autosoliton in the system under consideration are given by the expressions

$$\partial p/\partial t = e^{-1}\mathrm{div}\, J_h + G + G_T - R, \quad (5)$$

$$\partial(pT)/\partial t = -\mathrm{div}\, J_\varepsilon + W + P, \quad (6)$$

$$J_h = ep\nu_h - eD_h\nabla N, \quad J_\varepsilon = -\chi\nabla - 2EJ_h/e,$$

$$W = \sigma_0(T/T_0)^{1/2}E^2, \quad P = pT(T-T_0)/\tau_\varepsilon T,$$

where J_h is the hole current density, J_ε is the hole energy flux, W is the power density supplied to the system of charge carriers, P is the power transferred from the system of carriers to the lattice, p is the carrier concentration, T is the carrier temperature, E is the electric field strength, T_0 is the lattice temperature, D_h is the hole diffusivity, ν_h is the hole drift velocity, σ_0 is the conductivity, and τ_ε is the hole-energy relaxation time.

In this model, the electric field strength is a bifurcation parameter, $\alpha = \tau_p/\tau_T \ll 1$, and the ratio $\beta = L_p/L$, depending on the parameters of the system, can be either larger or smaller than unity. Here, τ_p and L_p are the characteristic time and length of a change in the carrier concentration and τ_T and L_T are the characteristic time and length of a change in the average carrier temperature.

The time intervals during which the current peaks are formed in the time dependences (Fig. 4) (these peaks are due to the local impact ionization and are controlled by the time of settling of thermal equilibrium upon adiabatic heating of the autosoliton region of size X) can be used to estimate the characteristic size of an autosoliton. The parameters of the region where heating occurs can be expressed in the form $\tau \sim X^2/\chi$ [8], where χ is the thermal diffusivity of silicon. Assuming that $\tau = 1.0$ μs and $\chi = 0.238$ cm^2/s (which corresponds to a thermal-conductivity coefficient of 0.2 cal cm^{-1} s^{-1} K^{-1}, a density of 2.32 g/cm^3, and a specific heat of 0.181 cal g^{-1} K^{-1}), we obtain $X \approx 7$ μm.

ACKNOWLEDGMENTS

This study was supported by the Russian Foundation for Basic Research, project no. 02-02-17888.

REFERENCES

1. B. S. Kerner and V. V. Osipov, *Autosolitons: A New Approach to Problems of Self-Organization and Turbulence* (Nauka, Moscow, 1991; Kluwer, Dordrecht, 1994).
2. B. S. Kerner and V. F. Sinkevich, Pis'ma Zh. Éksp. Teor. Fiz. **36**, 359 (1982) [JETP Lett. **36**, 436 (1982)].
3. V. N. Vashchenko, B. S. Kerner, V. V. Osipov, and V. F. Sinkevich, Fiz. Tekh. Poluprovodn. (Leningrad) **24**, 1705 (1990) [Sov. Phys. Semicond. **24**, 1065 (1990)].
4. A. M. Musaev, Fiz. Tekh. Poluprovodn. (St. Petersburg) **33**, 1183 (1999) [Semiconductors **33**, 1076 (1999)].
5. A. G. Milnes, *Deep Impurities in Semiconductors* (Wiley, New York, 1973; Mir, Moscow, 1977).
6. É. É. Godik, Yu. A. Kuritsyn, and V. P. Sinis, Fiz. Tekh. Poluprovodn. (Leningrad) **12**, 351 (1978) [Sov. Phys. Semicond. **12**, 203 (1978)].
7. A. E. McCombs, Int. J. Electron. **32**, 361 (1972).
8. H. S. Carslaw and J. C. Jaeger, *Conduction of Heat in Solids*, 2nd ed. (Clarendon Press, Oxford, 1959; Nauka, Moscow, 1964).

Translated by Yu. Sin'kov

Semiconductors, Vol. 38, No. 9, 2004, pp. 996–997. Translated from Fizika i Tekhnika Poluprovodnikov, Vol. 38, No. 9, 2004, pp. 1034–1035.

ELECTRONIC AND OPTICAL PROPERTIES OF SEMICONDUCTORS

Effect of Vacuum Annealing on the Edge Luminescence of Undoped Zinc Selenide

V. P. Makhniĭ, A. M. Sletov, and I. V. Tkachenko

Fed'kovich State University, ul. Kotsyubinskogo 2, Chernovtsy, 58012 Ukraine

e-mail: oe-dpt.@chnu.cv.ua; e-mail: LSlyotov@mail.ru

Submitted January 8, 2004; accepted for publication February 5, 2004

Abstract—It has been established experimentally that vacuum annealing of undoped ZnSe crystals in the temperature range 700–1200 K leads to a significant increase in the intensity of the blue luminescence band and suppression of the red-orange band. A model for defect formation is proposed to explain the observed characteristics. © *2004 MAIK "Nauka/Interperiodica".*

Interest in radiative properties of zinc selenide is mainly related to the possibility of using this material in light-emitting diodes operating in the blue spectral range [1]. In most cases, fabrication of these devices includes various kinds of heat treatment, which inevitably lead to a reconstruction of the ensemble of intrinsic point defects. This reconstruction, in turn, not only changes the properties of the starting material but also affects the characteristics of the impurity atoms: their solubility and position in the lattice, the charge state, and so on. These factors in particular account for the similarity of (or difference in) the emission spectra of ZnSe crystals that contain dopants of different (or the same) type [2–4]. In this context, it is important to know the effect of thermal treatment on the radiative properties of zinc selenide. It is expedient to perform such studies with undoped samples.

Bulk ZnSe crystals were grown by the Bridgman method from a stoichiometric melt under pressure of an inert gas. At room temperature, they have low ($\sim 10^{-10}\ \Omega^{-1}\ cm^{-1}$) electronic conductivity and the emission spectrum contains red-orange (*R*) and blue (*B*) bands (Fig. 1). Photoluminescence (PL) was excited by a nitrogen laser with $\lambda_m = 0.337$ μm, and PL spectra were recorded automatically using an MDR-23 grating monochromator and a conventional lock-in detection system [5]. The emission spectra reported here were corrected with regard to the nonlinearities of the measuring elements. They were plotted in the following coordinates: number of photons in a unit energy interval N_ω–photon energy $\hbar\omega$. Rocking curves of the samples were recorded on a double-crystal spectrometer using Cu K_α radiation. The samples were annealed in quartz cells (evacuated to 10^{-4} Torr and sealed) in the temperature range T_a = 600–1200 K with a step of 100 K. The annealing time at each value of T_a was 1 h.

The investigations performed show that the annealing most significantly affects the emission efficiency of individual bands. This is illustrated by the data listed in the table. These data indicate that the intensity of the red band I_R abruptly decreases with increasing temperature and that this band is not observed at all at $T_a \geq 900$ K. In contrast, the intensity of the blue band I_B increases with increasing annealing temperature, tending to saturation at $T_a \geq 900$ K. In this range of T_a, the half-widths of the blue luminescence band and the rocking curve ($\Delta\hbar\omega_B$ and $\Delta\theta$, respectively) have the smallest values. The decrease in the half-width of the rocking curve indicates that the structural quality of the surface layers of annealed samples improves in comparison with the starting samples, for which $\Delta\theta$ is significantly larger (Fig. 2).

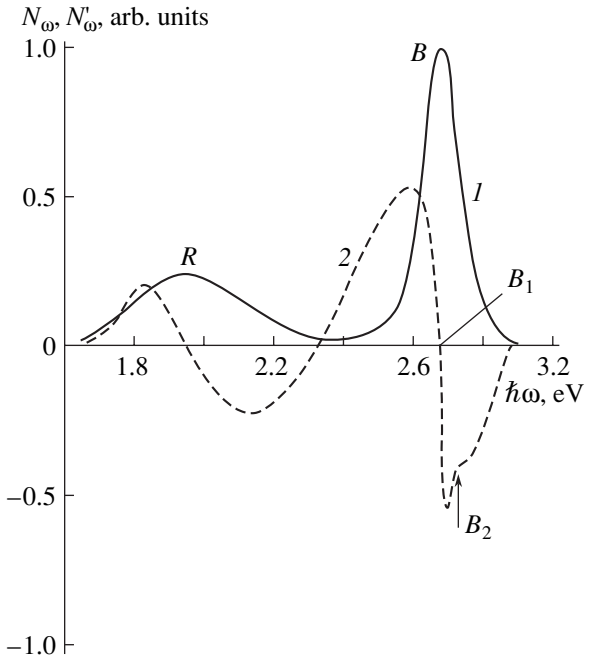

Fig. 1. (1) PL spectrum and (2) differential PL spectrum of starting ZnSe crystals at 300 K.

1063-7826/04/3809-0996$26.00 © 2004 MAIK "Nauka/Interperiodica"

Table

Parameter	Starting sample	T_a, K					
		700	800	900	1000	1100	1200
I_B, arb. units	180	240	260	360	350	420	400
I_R, arb. units	40	15	10	–	–	–	–
$\Delta\hbar\omega_B$, eV	0.2	0.15	0.13	0.1	0.1	0.12	0.12

To explain the dependences observed, the mechanisms of formation of intrinsic point defects (which are actually responsible for the evolution of the luminescence characteristics) should be analyzed. The *R* band in the spectra of undoped ZnSe crystals is due to the recombination in donor–acceptor pairs, which consist of negative doubly charged zinc vacancies V''_{Zn} and positive singly charged selen vacancies $V^{\bullet}_{Se}$ [2–4]. The large half-width of the blue band is indicative of its complex structure, which can be revealed in difference PL spectra (Fig. 1). The point of intersection of the curve N'_{ω} with the abscissa axis corresponds to the peak of the B_1 band. The energy position of the peak $\hbar\omega_1 \approx 2.68$ eV and its independence of the excitation level are indicative of recombination via shallow centers, which are generally related to Se vacancies in *n*-ZnSe [3]. The inflection at $\hbar\omega \approx 2.7$ eV on the curve N'_{ω} corresponds to the peak of the B_2 band, which is due to interband transitions. The ratio of the band intensities I_{B_2}/I_{B_1} at T_a = const, as one would expect [6], increases with increasing excitation level.

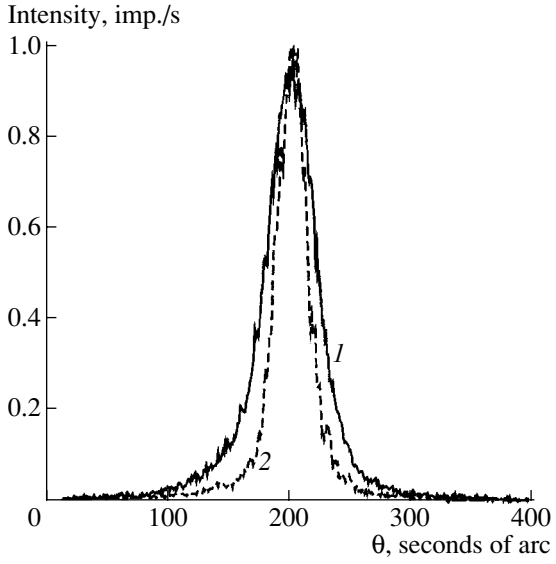

Fig. 2. Rocking curves of (1) a starting ZnSe crystal and (2) a ZnSe crystal annealed at 1000 K.

An increase in the annealing temperature should enhance the diffusion processes and, as a result, lead to a reconstruction of the ensemble of intrinsic point defects. At high temperatures, defects (predominantly weakly bound interstitials) migrate from the bulk of a crystal to its faces to recombine with the corresponding vacancies. The probability of such recombination is proportional to the diffusivity in the first-order approximation. If we assume that the diffusivity of zinc exceeds that of selen, the surface layers should be depleted of Zn vacancies after annealing. This depletion will lead to a decrease in the number of $V''_{Zn}V^{\bullet}_{Se}$ associates, and, accordingly, to an increase in the concentration of Se vacancies due to their escape from donor–acceptor pairs. Thus, the above processes, on the one hand, suppress the red-orange band and, on the other, increase the intensity of the blue band. It is reasonable to suggest that the difference between I_R and I_B should increase with increasing T_a, which is observed experimentally (see table). The fact that the number of Zn vacancies decreases is also confirmed by the improvement of the structural quality of surface layers, which manifests itself in narrower rocking curves (Fig. 2).

To conclude, we should note that chemical etching of the surface layers formed due to the annealing almost completely restores the characteristics of the PL and the rocking curves. In addition, the results reported indicate the possibility of relatively simple control of the structural quality and the emission spectrum of the surface layers of undoped ZnSe crystals.

REFERENCES

1. A. N. Georgobiani and M. B. Kotlyarevskiĭ, Izv. Akad. Nauk SSSR, Ser. Fiz. **49**, 1916 (1985).
2. *Physics of II–IV Compounds*, Ed. by A. N. Georgobiani and M. K. Sheĭnkman (Nauka, Moscow, 1986) [in Russian].
3. D. D. Nedeoglo and A. V. Simashkevich, *Electrical and Luminescent Properties of Zinc Selenide* (Shtiintsa, Chisinau, 1984) [in Russian].
4. V. I. Gavrilenko, A. M. Grekhov, D. V. Korbutyak, and V. G. Litovchenko, *Optical Properties of Semiconductors* (Naukova Dumka, Kiev, 1987) [in Russian].
5. V. P. Makhniĭ, *Principles and Methods of Modulation Spectroscopy* (Ruta, Chernivtsi, 2001) [in Ukrainian].
6. V. P. Gribkovskiĭ, *The Theory of Absorption and Emission of Light by Semiconductors* (Nauka i Tekhnika, Minsk, 1975) [in Russian].

Translated by Yu. Sin'kov

Semiconductors, Vol. 38, No. 9, 2004, pp. 998–1000. Translated from Fizika i Tekhnika Poluprovodnikov, Vol. 38, No. 9, 2004, pp. 1036–1038.

ELECTRONIC AND OPTICAL PROPERTIES OF SEMICONDUCTORS

Low-Frequency Noise in Gallium Nitride Epitaxial Layers with Different Degrees of Order of Mosaic Structure

N. M. Shmidt*, M. E. Levinshteĭn*^, W. V. Lundin*, A. I. Besyul'kin*, P. S. Kop'ev*, S. L. Rumyantsev, N. Pala**, and M. S. Shur****

** Ioffe Physicotechnical Institute, Russian Academy of Sciences, Politekhnicheskaya ul. 26, St. Petersburg, 194021 Russia*
^e-mail: melev@nimis.ioffe.rssi.ru

*** Department of Electrical, Computer, and Systems Engineering, Cll 9017, Rensselaer Polytechnic Institute, Troy, NY 12180-3590, USA*

Submitted January 30, 2004; accepted for publication February 26, 2004

Abstract—The correlation between the noise level $1/f$ and the degree of mosaic-structure order in gallium nitride epitaxial layers was studied for the first time. Samples with a doping level of $N_d - N_a \approx 8 \times 10^{16}$ cm^{-3} and a relatively high degree of order were characterized by the Hooge parameter $\alpha \approx 1.5 \times 10^{-3}$. This value is unprecedently low for thin GaN epitaxial films. The Hooge parameter was significantly higher for samples with $N_d - N_a \approx 1.1 \times 10^{18}$ cm^{-3} and a low degree of order despite the fact that α generally decreases with increasing doping level at the same degree of order. Thus, the degree of mosaic-structure order affects not only the optical and electrical characteristics but also the fluctuation parameters of GaN epitaxial layers. © *2004 MAIK "Nauka/Interperiodica".*

1. INTRODUCTION

Devices based on gallium nitride (GaN) are now considered among the most promising devices in various fields of electronics: short-wavelength light-emitting devices, solar-blind ultraviolet photodetectors, high-speed high-power transistors, and others [1–5].

A distinctive feature of the nitrides of Group-III elements is a system of extended defects with a high dislocation density and a mosaic (columnar, domain) structure [6]. As was shown previously, the variety of structural features of these compounds can be quantitatively characterized using such system parameters as the degree Δ of mosaic-structure order, the degree of violation of general and local symmetry, and the degree of self-organization of the system of extended defects [7]. In this case, the lower the values of Δ, the better the mosaic structure is ordered.

Comparative studies of structural properties of epitaxial layers with various values of Δ showed that coherent matching of mosaic structure domains with the formation of dilatational boundaries is mainly observed in layers with a well-ordered mosaic structure ($\Delta < 0.340$). Epitaxial layers with a poorly ordered mosaic structure ($\Delta > 0.350$) are characterized by the preferential formation of dislocation walls at domain boundaries. In the case of intermediate values of Δ, both boundary types coexist in various ratios [8].

The optical and electrical properties of layers, as well as carrier-transport mechanisms, differ significantly for layers with different Δ [9]. Layers with a well-ordered mosaic structure are characterized by the classical temperature dependence of conductivity: the conductivity increases with temperature T in the low-temperature range, peaks, and then drops with a further increase in T due to phonon scattering. For layers with a poorly ordered mosaic structure, the temperature dependence of the conductivity differs significantly from this classical form and is similar to the corresponding dependences for low-dimensional structures [10].

It is well known that the noise $1/f$ is one of the most sensitive indicators of structural disorder for semiconductors (see, e.g., [11]). However, to our knowledge, no attempts to ascertain the correlation between the degree of mosaic-structure order in GaN and the $1/f$ noise level have been undertaken.

In this study, the correlation between the $1/f$ noise level and the degree of mosaic-structure order in GaN epitaxial layers is considered for the first time.

2. EXPERIMENTAL

The studies were carried out with *n*-GaN epitaxial layers grown on (0001) sapphire substrates by metal–organic chemical vapor deposition (MOCVD). The layers differed from each other in the growth conditions for the buffer layer, the degree Δ of mosaic-structure order, the electron mobility μ and density n; they were characterized by the following parameters.

Layer *A*-598 had a high degree of structural order ($\Delta = 0.320$). At room temperature, its electron density and Hall mobility were $n = N_d - N_a \approx 8 \times 10^{16}$ cm^{-3} and $\mu = 600$ cm^2 V^{-1} s^{-1}, respectively. The layer thickness was $t = 4$ μm.

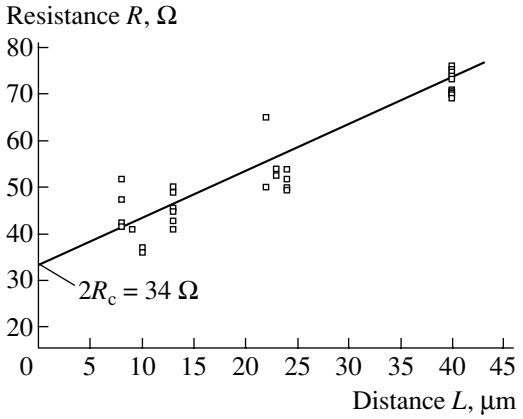

Fig. 1. Dependence of the resistance of samples R on the distance L between contacts (for plate *A*).

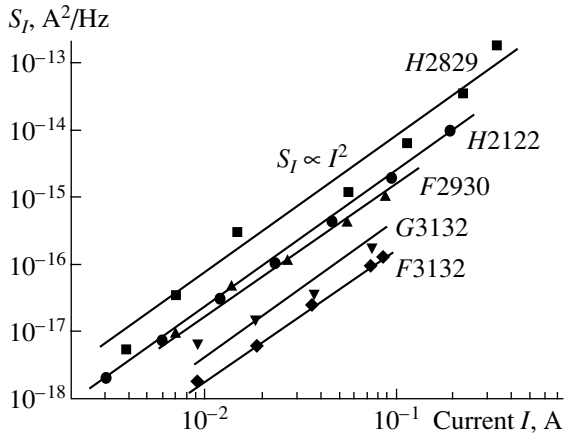

Fig. 2. Dependences of the noise spectral density S_I on the current I for several samples of wafer *B*. The analysis frequency is f = 6 Hz. Solid lines correspond to the relation $S_I \propto I^2$.

Layer *B*-1261 was characterized by Δ = 0.350. Its electron density and Hall mobility at room temperature were $n = N_d - N_a \approx 10^{18}$ cm^{-3} and μ = 200 cm^2 V^{-1} s^{-1}, respectively. The layer thickness was t = 3 μm.

The degree of mosaic-structure order was determined by multifractal analysis: processing the data obtained in the study of the layer surface using atomic-force microscopy (as described in [7]).

Ohmic contacts shaped like parallel strips of length W = 240 μm were formed on each layer. The distances between the strips were $5 < L < 41$ μm. The low-frequency noise was measured in the linear mode (with a low voltage applied to the samples under study) in the frequency range 1–10 kHz using tungsten probes with tips ~10 μm in diameter. A special procedure for "fitting" the probe to the contact surfaces provided a low transition resistance between the probe and the metal contacts.

2. RESULTS AND DISCUSSION

Several tens of samples with different L were studied for both layers *A* and *B*. The *I*–*V* characteristics of all the samples were linear in the current range studied (~2×10^{-3}–0.2 A). The measurements on samples with different distances L made it possible to determine the contact resistance and (independent of the Hall data) the layer conductance σ. For example, Fig. 1 shows the results of the corresponding measurements for wafer *A*.

The dependence $R(L)$, extrapolated to L = 0, determines the double contact resistance $2R_c$ = 34 Ω. The measured value of $2R_c$ corresponds to the contact resistivity $r_c \approx 4$ Ω mm, which seems to be quite a reasonable value for an electron density of $n \approx 8 \times 10^{16}$ cm^{-3} and planar contacts. Similar measurements for wafer *B* yield $2R_c$ = 8.4 Ω ($r_c \approx 1$ Ω mm). The smaller value of r_c can obviously be explained by the higher value of n in wafer *B* ($n \approx 10^{18}$ cm^{-3}) [12].

As is well known, the averaged GaN conductivity σ can be determined by the slope of the dependence $R(L)$. The value of σ determined from Fig. 1,

$$\sigma = \frac{L}{(R - 2R_c)tW}$$

is σ = 11 Ω^{-1} cm^{-1}, which is reasonably consistent with the results of measurements before deposition of strip contacts: $\sigma_0 \approx 8$ Ω^{-1} cm^{-1}. For wafer *B*, similar measurements yield σ ≈ 30 Ω^{-1} cm^{-1} ($\sigma_0 \approx 32$ Ω^{-1} cm^{-1}).

The room-temperature noise in all the measured samples was described by $1/f^\gamma$ with γ close to unity (flicker noise). The spectral density S_I of the current noise was proportional to the squared current in the entire current range: $S_I \propto I^2$. For example, Fig. 2 shows the dependences $S_I(I)$ for several samples (wafer *B*), measured at an analysis frequency of 6 Hz.

Generally, the noise characteristics of various devices and materials are estimated by the dimensionless Hooge parameter α [13]:

$$\alpha = \frac{S_I}{I^2} fN, \qquad (1)$$

where f is the frequency of analysis and N is the total number of carriers in a sample.

The parameter α is very sensitive to the structural quality of a material (see, e.g., [14]). For Si films of high structural quality, typical values of α are in the range 10^{-4}–10^{-5}. For GaAs epitaxial films, typical values of α are 10^{-3}–10^{-5}. For GaN films of standard quality with concentration $N_d - N_a \approx 10^{17}$ cm^{-3}, the values of α are generally much higher: 10^{-2}–1 [14]. As was shown in [15], the doping of GaN films with silicon to $N_d - N_a \approx 10^{18}$ cm^{-3} substantially decreases the value of α (to 2×10^{-3}). One would therefore expect the Hooge parameter for film *B* (at the same structural disorder) to be much lower than for film *A*.

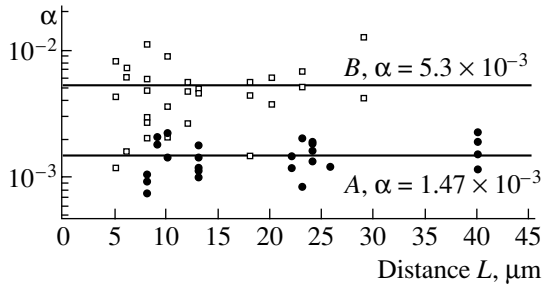

Fig. 3. Hooge parameter α for samples prepared on films *A* and *B*.

Figure 3 shows the values of α calculated using expression (1) for a large number of samples prepared from both films. It can be seen that the experimental result completely contradicts the prediction based on the assumption of identical structural quality of the films. The result obtained seems to be even more convincing since, according to estimations, the contact noise (especially in the samples with a short distance *L*) should contribute significantly to the total noise of the structures (thus, the measured values of α represent an "upper" estimate). Meanwhile, as mentioned above, the resistance of contacts to the samples prepared on film *A* is significantly higher than that of the samples on film *B*. It should be concluded that the contribution of the contact noise to the total noise is larger than that of samples made on film *B*. Therefore, the difference between the *volume* noise $1/f$ in samples of types *A* and *B* is even larger than what follows from Fig. 3.

We note that even the "upper" estimate for the Hooge parameter in samples prepared on plate *A* is a record low value for thin epitaxial GaN films [14].

ACKNOWLEDGMENTS

This study was supported by the Russian Foundation for Basic Research, project nos. 02-02-16496 and 02-02-17619.

REFERENCES

1. V. Adivarahan, M. Gaevski, W. H. Sun, *et al.*, IEEE Trans. Electron Devices **24**, 541 (2003).
2. M. S. Shur and M. Asif Khan, Semicond. Semimet. **57**, 407 (2002).
3. R. J. Trew, Proc. IEEE **90**, 1032 (2002).
4. V. Kumar, W. Lu, R. Schwindt, *et al.*, IEEE Electron Device Lett. **23**, 455 (2002).
5. X. Hu, A. Koudymov, G. Simin, *et al.*, Appl. Phys. Lett. **79**, 2832 (2001).
6. F. A. Ponce, MRS Bull. **22**, 51 (1997).
7. N. V. Shmidt, A. G. Kolmakov, A. D. Kryzhanovsky, *et al.*, Inst. Phys. Conf. Ser. **169**, 303 (2001).
8. A. V. Ankudinov, A. G. Kolmakov, V. V. Lundin, *et al.*, in *Abstract of VI Conference on the Physics of Semiconductors* (St. Petersburg, 2003), p. 92.
9. N. M. Shmidt, A. I. Besulkin, M. S. Dunaevsky, *et al.*, J. Phys.: Condens. Matter **14**, 13025 (2002).
10. N. M. Shmidt, V. V. Emtsev, A. G. Kolmakov, *et al.*, Nanotechnology **12**, 471 (2001).
11. M. E. Levinshtein, S. L. Rumyantsev, M. S. Shur, *et al.*, IEE Proc. G: Circuits, Devices Syst. **149**, 32 (2002) [Special Issue: *Selected Topics on Noise in Semiconductor Devices*].
12. M. Shur, *GaAs Devices and Circuits* (Plenum, New York, 1987; Mir, Moscow, 1991).
13. F. N. Hooge, T. G. M. Kleinpenning, and L. K. J. Vandamme, Rep. Prog. Phys. **44**, 479 (1981).
14. M. E. Levinshtein, A. A. Balandin, S. L. Rumyantsev, and M. S. Shur, in *Noise and Fluctuations Control in Electronic Devices*, Ed. by A. Balandin (Am. Sci., Riverside, 2002).
15. S. L. Rumyantsev, N. Pala, M. S. Shur, *et al.*, Electron. Lett. **37**, 720 (2001).

Translated by A. Kazantsev